SYNTHESIS AND CHARACTERIZATION OF TRANSITION METAL DOPED SOLID OXIDE FUEL CELL CATHODES

by

Ayşenur Eslem Kısa

B.S., Chemistry, Middle East Technical University, 2012

Submitted to the Institute for Graduate Studies in
Science and Engineering in partial fulfillment of
the requirements for the degree of
Master of Science

Graduate Program in Chemistry
Bogazici University
2015

Dedicated to my dear family

ACKNOWLEDGEMENTS

On this auspicious occasion I give profound thanks to all concerned who have extended their selfless guidance to assist in completing my master thesis. First and foremost, I would like to express my deepest appreciation to my thesis advisor Assist. Prof. Oktay Demircan whose intelligence, diligence, enthusiasm and philosophy have had a big impact on me, not only in my research but also in my daily life. Dr. Demircan is a scientist who, by the most sincere care, gave me rays of hope and aspiration to accomplish this thesis. I thank Dr. Demircan for showing me the beauty of science. Whenever I got stuck with my research, he was always available to provide kind help with lots of encouragement and inspiration. This gave me a lot of strength and motivated me going through some of the difficult days. Dr. Demircan also made me realize and believe that most questions can be answered in a 'simpler' way by a careful theoretical argument. Sometimes an insightful analysis with a deep understanding is much more effective, efficient, and full of beauty.

I would like to express my heartfelt gratitude to Prof. Viktorya Aviyente and Assoc. Prof. Selmiye Alkan Gürsel for being in my thesis committee.

Without the various support from the colleagues, this work would not be complete. Therefore I express my sincere gratitude to following colleagues: I thank Elif Kılıç İyilik, Kübra Avrupalı and Aktan Polat for helping me in the darkest times and for their friendly atmosphere.

I gratefully acknowledge the financial support by the TUBITAK under grant numbers of 214Z094 and 112M279 and also Boğaziçi University Research and Development Center for XRD and XPS analysis. I would also like to extend my appreciation to all members of the Department of Chemistry at Boğaziçi University and as well as to other departments for their essential contributions.

Last but not least, I would like to add a special thanks to my dear family members, my father Ali Kısa, my mother Dilek Kısa and sisters Erva and Hümeyra. It is their selfless support and understanding that made me go through my master life, which is full of ups and downs. You made me the person that I am and I am proud to have such a great family. I love you all. I thank my fiancé Muhammed Erkam Özbudak for his loving support and understanding whenever this work absorbed a substantial amount of my time and energy.

ABSTRACT

SYNTHESIS AND CHARACTERIZATION OF TRANSITION METAL DOPED SOLID OXIDE FUEL CELL CATHODES

Fuel cells have become of great interest as a potential economical and clean candidate for alternative and environmental friendly power generation services. There are several types of fuel cells with large differences in application, size, cost and operating temperature range. Solid Oxide Fuel Cell (SOFC) is a high temperature fuel cell, dealing with generation of power as well as heat. This study explains a number of experimental studies on the cathode of the SOFC. The emphasis is on two important aspects, the effect of different cathode materials on the electrochemical performance of the electrode and the kinetics of the oxygen reduction reaction (ORR). The main purpose of the thesis is to progress a novel and high quality cathode materials for SOFCs working at intermediate temperature (500°C<T) range. It is aimed to develop the alternative for the conventional IT-SOFC cathode materials with better mixed ionic-electronic conductivity, high electrochemical activity and good oxygen reducing with better efficiency. The production of novel cathode electrodes used in IT-SOFC is aimed to employ cheaper metals (Ti, Fe, Co, Cr, Mn, V, B and Gd) by using superior properties of perovskite structure. The study concerned a comparison is made between four different cathode materials under identical conditions. The cathode types investigated LV3SF ($La_{0.57}V_{0.03}Sr_{0.4}FeO_{3-\delta}$), LG10SC ($La_{0.5}Gd_{0.1}Sr_{0.4}CoO_{3-\delta}$), LV05SM ($La_{0.595}V_{0.005}Sr_{0.4}MnO_{3-\delta}$) and LV05SC ($La_{0.595}V_{0.005}Sr_{0.4}CoO_{3-\delta}$) were successfully synthesized by sol-gel process and are characterized with XRD (X-Ray Diffraction) and XPS (X-Ray Photoelectron Spectrosopy). For electrical conductivity measurements, four-probe conductivity method was performed. Also for the electrochemical characterization of the electrodes impedance measurements were completed. Of the four cathodes, the LV05SC on YSZ showed the highest are area specific resistance. The results for other cathode materials were in good agreement with literature.

ÖZET

GEÇİŞ METALİ KATKILI KATI OKSİT YAKIT HÜCRESİ KATOT ELEKTRODU SENTEZİ VE KARAKTERİZASYONU

Yakıt hücreleri, alternatif ve çevre dostu enerji üretim hizmetleri için potansiyel ekonomik ve temiz bir aday olarak büyük ilgi görmüştür. Yakıt hücrelerinin uygulama, boyut, maliyet ve çalışma sıcaklık aralığı gibi özelliklerde içinde büyük farklılıklarla pek çok türevi vardır. Katı Oksit Yakıt Hücresi (KOYH) ısı ve güç üretimi ile ilgilenen yüksek sıcaklıkta çalışan bir yakıt hücresidir. Bu çalışma, KOYH katodu için yapılan bir dizi deneysel çalışmayı açıklar. Vurgulanan iki önemli yön ise farklı katot malzemelerinin elektrotun elektrokimyasal performansına etkisi ve oksijen indirgeme reaksiyonunun (ORR) kinetiği üzerinedir. Bu tezin temel amacı, orta sıcaklıkta çalışan (500°C<T) KOYH için yeni ve üstün nitelikli katot elektrotlarının geliştirilmesidir. Orta Sıcaklık Katı Oksit Yakıt Hücresinde (OS-KOYH) kullanılan geleneksel katot malzemesi yerine yüksek elektrokimyasal aktiviteye sahip ve daha iyi bir verimle oksijen indirgeyebilen karma iyonik-elektronik iletken malzemeler hazırlayarak kullanılması hedeflenmiştir. Özellikle perovskit yapısının üstün özelliklerinden faydalanılarak, daha ucuz ve düşük değerli metaller (Ti, Fe, Co, Cr, Mn, V, B ve Gd) kullanılarak yüksek verimlilik gösterebilen OS-KOYH elektrotlarının üretiminin değerlendirilmesi amaçlanmıştır. İlgili çalışmada aynı koşullar altında dört farklı katot malzemesi arasında karşılaştırma yapılmıştır. Geliştirilen LV3SF ($La_{0.57}V_{0.03}Sr_{0.4}FeO_{3-\delta}$), LG10SC ($La_{0.5}Gd_{0.1}Sr_{0.4}CoO_{3-\delta}$), LV05SM ($La_{0.595}V_{0.005}Sr_{0.4}MnO_{3-\delta}$) ve LV05SC ($La_{0.595}V_{0.005}Sr_{0.4}CoO_{3-\delta}$) katot türleri başarılı bir şekilde sol-jel yöntemi ile sentezlenmiştir ve XRD (X-Işını Kırınımı) ve XPS (X-Işını Fotoelektron Spektroskopisi) ile karakterize edilmiştir. Elektrik iletkenliği için dört-nokta iletkenlik yöntemi kullanılmıştır. Ayrıca elektrotların elektrokimyasal karakterizasyonu için ise impedans ölçümleri tamamlanmıştır. Geliştirilen dört katot malzemesi içinde YSZ üzerinde LV05SC malzemesi en yüksek alan spesifik direnç göstermiştir. Diğer malzemeler için ölçüm sonuçları literatür ile uyumludur.

TABLE OF CONTENTS

ACKNOWLEDGEMENTS iv

ABSTRACT v

ÖZET vi

LIST OF FIGURES ix

LIST OF TABLES xvii

1. INTRODUCTION 1

1.1. Energy Sources 1

1.2. Fuel Cells 2

1.3. Solid Oxide Fuel Cell (SOFC) 3

1.3.1. Materials for SOFC components 5

1.3.1.1. Anode 6

1.3.1.2. Electrolyte 6

1.3.1.3. Cathode 7

1.3.2. Electrochemical Impedance Spectroscopy 14

1.4. Scope of the thesis 17

2. EXPERIMENTAL 20

2.1. Sol-Gel Process 20

2.1.1. Fabrication of SOFC material powders with sol-gel process 22

2.2. Rectangular bar preparation for four-probe conductivity measurements 39

2.3. Symmetric cell production for electrochemical impedance analysis 39

2.4. Tape casting and screen-printing tecniques for intermediate-temperature SOFC material preparation 40

3. RESULTS & DISCUSSION 44

3.1. X-Ray Diffraction (XRD) Results 44

3.2. X-Ray Photoeletron Spectroscopy (XPS) Results ...……..…….53

3.3. Electrical Conductivity – Four Probe Measurement Results ...……..…….66

3.4. Electrochemical Impedance Spectroscopy (EIS) Results ...……..…..81

4. FUTURE WORK 162

5. CONCLUSION ...……..164

REFERENCES 167

LIST OF FIGURES

Figure 1.1. Schematic representation of SOFC working principle 5

Figure 1.2. Current - voltage curve of a working SOFC 8

Figure 1.3. Crystal structure of 'ideal' cubic perovskite ABO_3 11

Figure 1.4. Schematic represenatiton of saddle point 13

Figure 1.5. Outlines of possible reaction paths of the oxygen reduction and incorporation reaction and some possible rate determining steps ..……..14

Figure 1.6. Sinusoidal current response in a linear system 16

Figure 1.7. Schematic representation of EIS Nyquist plot 17

Figure 2.1. Outline of sol-gel processing 21

Figure 2.2. A flow scheme illustrating the processing procedure for LSM powder synthesis 24

Figure 2.3. Schematic view for tape-casting process 41

Figure 2.4. Doctor blade profile in tape casting procedure 41

Figure 3.1. X-Ray Diffraction pattern of LSM sample 45

Figure 3.2. XRD patterns of $La_{0.6-x}V_xSr_{0.4}CoO_{3-\delta}$ (x= 0.005 – 0.1) powder calcined at 1100 ^oC in air for 2h 45

Figure 3.3. Powder XRD patterns of the as-synthesized $La_{0.595}V_{0.005}Sr_{0.4}CoO_{3-\delta}$ 46

Figure 3.4. Powder X-Ray Diffraction patterns of the as-synthesized $La_{0.6-x}V_xSr_{0.4}FeO_{3-\delta}$ with different V-doping amount 47

Figure 3.5. X-Ray Diffraction pattern of as-prepared $La_{0.57}V_{0.03}Sr_{0.4}FeO_3$ 48

Figure 3.6. XRD patterns of $La_{0.6-x}V_xSr_{0.4}MnO_{3-\delta}$ (x= 0.005 – 0.1) samples 49

Figure 3.7. X-Ray Diffraction data for $La_{0.595}V_{0.005}Sr_{0.4}MnO_3$ 50

Figure 3.8. XRD pattern of as-synthesized $La_{0.5}Gd_{0.1}Sr_{0.4}CoO_3$ powder 51

Figure 3.9. XRD peaks of $La_{0.6-x}V_xSr_{0.4}CrO_{3-\delta}$ (x = 0.005, 0.01, 0.02, 0.03, 0.04, 0.1) samples 51

Figure 3.10. X-Ray Diffraction patterns for $La_{0.6-x}V_xSr_{0.4}TiO_{3-\delta}$ (x = 0.005, 0.01, 0.02, 0.03, 0.04, 0.1) 52

Figure 3.11. XRD patterns of $La_{0.6}Sr_{0.4}VO_3$ cathode powder 53

Figure 3.12. XPS survey spectrum of the LV05SC powder 55

Figure 3.13. The La3d core level XP spectra of LV05SC 55

Figure 3.14. The V2p core level XP spectra of LV05SC 56
Figure 3.15. The Sr3d core level XP spectra of LV05SC 56
Figure 3.16. The Co2p core level XP spectra of LV05SC 57
Figure 3.17. XPS spectra survey analysis at room temperature for LV05SM samples ...58
Figure 3.18. XPS spectra of La3d for LV05SM sample 58
Figure 3.19. XPS spectra of V2p for LV05SM sample 59
Figure 3.20. XPS spectra of Sr3d for LV05SM sample 59
Figure 3.21. XPS spectra of Mn2p for LV05SM sample 60
Figure 3.22. XPS survey spectrum of the LV3SF powder 61
Figure 3.23. XPS spectra of La3d for LV3SF sample 61
Figure 3.24. The V2p core level XP spectra of LV3SF 62
Figure 3.25. The Sr3d core level XP spectra of LV3SF 62
Figure 3.26. The Fe2p core level XP spectra of LV3SF 63
Figure 3.27. XPS survey spectrum of the LG10SC powder 63
Figure 3.28. XPS spectra of La3d for LG10SC sample 64
Figure 3.29. XPS spectra of Gd4d for LG10SC sample 64
Figure 3.30. XPS spectra of Sr3d for LG10SC sample 65
Figure 3.31. XPS spectra of Co2p for LG10SC sample 65
Figure 3.32. Temperature dependance of the electrical conductivity of LV05SC sample sintered at 1100 ^{o}C 67
Figure 3.33. Comparison of the total conductivity of various cobalt containing perovskite related materials in air 68
Figure 3.34. Temperature dependance of the electrical conductivity of LV3SF sample sintered at 1100 ^{o}C 70
Figure 3.35. Electrical conductivity of $La_{0.57}V_{0.03}Sr_{0.4}FeO_{3-\delta}$ (LV3SF) compared with conventional iron containing cathode materials 71
Figure 3.36. Temperature dependance of the electrical conductivity of LV05SM sample sintered at 1100 ^{o}C 72
Figure 3.37. Electrical conductivity of $La_{0.595}V_{0.005}Sr_{0.4}MnO_{3-\delta}$ (LV05SM) compared with manganese containing conventional cathode materials 74
Figure 3.38. Temperature dependance of the electrical conductivity of LG10SC sample sintered at 1100 ^{o}C 75

Figure 3.39. Electrical conductivity of $La_{0.5}Gd_{0.1}Sr_{0.4}CoO_{3-\delta}$ (LG10SC) compared with cobalt containing conventional cathode materials 76
Figure 3.40. The electrical conductivity values of a) LV05SM, b) LV05SC, c) LV3SF, d) LG10SC 78
Figure 3.41. Electrical conductivity of LV05SM, LV3SF, LV05SC and LG10SC samples in comparison 80
Figure 3.42. Complex impedance plots for LV05SM/YSZ/LV05SM symmetric cell at between 400-800 °C for different oxygen partial pressures 82
Figure 3.43. Typical EIS of a symmetric LV05SM/YSZ/LV05SM cell measured at 600 °C while fixing the oxygen partial pressure between 1 – 25% 83
Figure 3.44. Impedance spectra of LV05SM cathode measured in 3% O_2 – 97% N_2 at various temperatures with data fitting 84
Figure 3.45. Impedance spectra of LV05SM cathode measured in 10% O_2 – 90% N_2 at various temperatures with data fitting 85
Figure 3.46. Impedance spectra of LV05SM cathode measured in 15% O_2 – 85% N_2 at various temperatures with data fitting 85
Figure 3.47. Impedance spectra of LV05SM cathode measured in 25% O_2- 75% N_2 at various temperatures with data fitting 86
Figure 3.48. The equivalent circuits used for fitting the impedance data for a) 500 - 600 °C b) 400, 700 and 800 °C 86
Figure 3.49. The relations of polarization resistance to PO_2 of corresponding ORR processes on the cathode 90
Figure 3.50. Dependence of three resistances at high, medium and low frequency on oxygen partial pressure for LV05SM/YSZ interface between 400-800 °C (a) R_1; (b) R_2; (c) R_3 and (d) $R_2 + R_3$ 91
Figure 3.51. The dependence of ASR of the LV05SM/YSZ interface as a function of oxygen partial pressure at different temperatures 92
Figure 3.52. Complex impedance plots for LV05SM/GDC/LV05SM symmetric cell at between 400-800 °C for different oxygen partial pressures 93
Figure 3.53. Typical EIS of a symmetric LV05SM/GDC/LV05SM cell measured at 600 °C while fixing the oxygen partial pressure between 1 – 25% 94

Figure 3.54. Experimental and fit Nyquist plots for a symmetrical LV05SM/GDC/LV05SM cell measured at 3% O_2 – 97% N_2 between 400 – 800 ºC …….95
Figure 3.55. Experimental and fit Nyquist plots for a symmetrical LV05SM/GDC/LV05SM cell measured at 10% O_2 – 90% N_2 between 400 – 800 ºC ……...96
Figure 3.56. Experimental and fit Nyquist plots for a symmetrical LV05SM/GDC/LV05SM cell measured at 15% O_2 – 85% N_2 between 400 – 800 ºC ……96
Figure 3.57. Experimental and fit Nyquist plots for a symmetrical LV05SM/GDC/LV05SM cell measured at 25% O_2 – 75% N_2 between 400 – 800 ºC ……...97
Figure 3.58. The equivalent circuits adopted for fitting the impedance data for a) 400 – 500 ºC b) 600, 700 and 800ºC …….....97
Figure 3.59. Dependence of three resistances at high, medium and low frequency on oxygen partial pressure for LV05SM/GDC interface between 400 - 800 °C (a) R_1; (b) R_2; (c) R_3 and (d) $R_2 + R_3$ …….....102
Figure 3.60. The dependence of the area specific resistance of the LV05SM/GDC interface as a function of PO_2 at different temperatures …….103
Figure 3.61. Complex impedance plots for LV05SC/YSZ/LV05SC symmetric cell at between 400-800 °C for different oxygen partial pressures ……....104
Figure 3.62. Typical EIS of a symmetric LV05SC/YSZ/LV05SC cell measured at 600 ºC while fixing the oxygen partial pressure between 1 – 25% ……105
Figure 3.63. Experimental and fit Nyquist plots for a symmetrical LV05SC/YSZ/LV05SC cell measured at 3% O_2 – 97%N_2 between 400 – 800 ºC …….106
Figure 3.64. Experimental and fit Nyquist plots for a symmetrical LV05SC/YSZ/LV05SC cell measured at 10% O_2 – 90%N_2 between 400 – 800 ºC ……106
Figure 3.65. Experimental and fit Nyquist plots for a symmetrical LV05SC/YSZ/LV05SC cell measured at 15% O_2 – 85%N_2 between 400 – 800 ºC ……107
Figure 3.66. Experimental and fit Nyquist plots for a symmetrical LV05SC/YSZ/LV05SC cell measured at 25% O_2 – 75%N_2 between 400 – 800 ºC ……107
Figure 3.67. The equivalent circuits adopted for fitting the impedance data for a) 400 – 500 ºC b) 600 - 700 ºC …….....108
Figure 3.68. Dependence of three resistances at high, medium and low frequency on oxygen partial pressure for LV05SC/YSZ interface between 400 - 800 °C (a) R_1; (b) R_2; (c) R_3 and (d) $R_2 + R_3$ ……...……...112

Figure 3.69. The dependence of the area specific resistance of the LV05SC/YSZ interface as a function of oxygen partial pressure at different temperatures 113
Figure 3.70. Complex impedance plots for LV05SC/GDC/LV05SC symmetric cell at between 400 - 800 °C for different oxygen partial pressures 114
Figure 3.71. Typical EIS of a symmetric LV05SC/GDC/LV05SC cell measured at 600 ºC while fixing the oxygen partial pressure between 1 – 25% 115
Figure 3.72. Experimental and fit Nyquist plots for a symmetrical LV05SC/GDC/LV05SC cell measured at 3% O_2 – 97%N_2 between 400 – 800 ºC 116
Figure 3.73. Experimental and fit Nyquist plots for a symmetrical LV05SC/GDC/LV05SC cell measured at 10% O_2 – 90%N_2 between 400 – 800 ºC 116
Figure 3.74. Experimental and fit Nyquist plots for a symmetrical LV05SC/GDC/LV05SC cell measured at 15% O_2 – 85%N_2 between 400 – 800 ºC 117
Figure 3.75. Experimental and fit Nyquist plots for a symmetrical LV05SC/GDC/LV05SC cell measured at 25% O_2 – 75%N_2 between 400 – 800 ºC 117
Figure 3.76. The equivalent circuits adopted for fitting the impedance data for a) 400 ºC b) 500 - 800 ºC 118
Figure 3.77. Dependence of three resistances at high, medium and low frequency on oxygen partial pressure for LV05SC/GDC interface between 400 - 800 °C (a) R_1; (b) R_2; (c) R_3 and (d) $R_2 + R_3$ 122
Figure 3.78. The dependence of the area specific resistance of the LV05SC/ GDC interface as a function of PO_2 at different temperatures 122
Figure 3.79. Complex impedance plots for LV3SF/YSZ/LV3SF symmetric cell at between 400 - 800 °C for different oxygen partial pressures 123
Figure 3.80. Typical EIS of a symmetric LV3SF/YSZ/LV3SF cell measured at 600 ºC while fixing the oxygen partial pressure between 1 – 25% 124
Figure 3.81. Experimental and fit Nyquist plots for a symmetrical LV3SF/YSZ/LV3SF cell measured at 3% O_2 – 97%N_2 between 400 – 800 ºC 125
Figure 3.82. Experimental and fit Nyquist plots for a symmetrical LV3SF/YSZ/LV3SF cell measured at 10% O_2 – 90%N_2 between 400 – 800 ºC 126
Figure 3.83. Experimental and fit Nyquist plots for a symmetrical LV3SF/YSZ/LV3SF cell measured at 15% O_2 – 85%N_2 between 400 – 800 ºC 126

Figure 3.84. Experimental and fit Nyquist plots for a symmetrical LV3SF/YSZ/LV3SF cell measured at 25% O_2 – 75%N_2 between 400 – 800 ºC 127
Figure 3.85. The equivalent circuits adopted for fitting the impedance data for a) 400, 600, 700 and 800 ºC b) 500 ºC 127
Figure 3.86. Dependence of three resistances at high, medium and low frequency on oxygen partial pressure for LV3SF/YSZ interface between 400-800 °C (a) R_1; (b) R_2; (c) R_3 and (d) $R_2 + R_3$ 131
Figure 3.87. The dependence of the area specific resistance of the LV3SF/YSZ interface as a function of oxygen partial pressure at different temperatures 132
Figure 3.88. Complex impedance plots for LV3SF/GDC/LV3SF symmetric cell at between 400-800 °C for different oxygen partial pressures 133
Figure 3.89. Typical EIS of a symmetric LV3SF/GDC/LV3SF cell measured at 500 ºC while fixing the oxygen partial pressure between 1 – 25% 134
Figure 3.90. Experimental and fit Nyquist plots for a symmetrical LV3SF/GDC/LV3SF cell measured at 3% O_2 – 97%N_2 between 400 – 800 ºC 135
Figure 3.91. Experimental and fit Nyquist plots for a symmetrical LV3SF/GDC/LV3SF cell measured at 10% O_2 – 90%N_2 between 400 – 800 ºC 135
Figure 3.92. Experimental and fit Nyquist plots for a symmetrical LV3SF/GDC/LV3SF cell measured at 15% O_2 – 85%N_2 between 400 – 800 ºC 136
Figure 3.93. Experimental and fit Nyquist plots for a symmetrical LV3SF/GDC/LV3SF cell measured at 25% O_2 – 75%N_2 between 400 – 800 ºC 136
Figure 3.94. The equivalent circuits adopted for fitting the impedance data for a) 400 – 600 ºC b) 700 - 800 ºC 137
Figure 3.95. Dependence of three resistances at high, medium and low frequency on oxygen partial pressure for LV3SF/GDC interface between 400 - 800 °C (a) R_1; (b) R_2; (c) R_3 and (d) $R_2 + R_3$ 141
Figure 3.96. The dependence of the area specific resistance of the LV3SF/ GDC interface as a function of oxygen partial pressure at different temperatures 141
Figure 3.97. Complex impedance plots for LG10SC/YSZ/LG10SC symmetric cell at between 400-800 °C for different oxygen partial pressures 142
Figure 3.98. Typical EIS of a symmetric LG10SC/YSZ/LG10SC cell measured at 600 ºC while fixing the oxygen partial pressure between 1 – 25% 143

Figure 3.99. Experimental and fit Nyquist plots for symmetrical LG10SC/YSZ/LG10SC cell measured at 3% O_2 – 97%N_2 between 400 – 800 ºC ……..144
Figure 3.100. Experimental and fit Nyquist plots for symmetrical LG10SC/YSZ/LG10SC cell measured at 10% O_2 – 90%N_2 between 400 – 800 ºC ……144
Figure 3.101. Experimental and fit Nyquist plots for symmetrical LG10SC/YSZ/LG10SC cell measured at 15% O_2 – 85%N_2 between 400 – 800 ºC ……145
Figure 3.102. Experimental and fit Nyquist plots for symmetrical LG10SC/YSZ/LG10SC cell measured at 25% O_2 – 75%N_2 between 400 – 800 ºC ……145
Figure 3.103. The equivalent circuits adopted for fitting the impedance data for a) 400 - 500 ºC b) 600 - 800 ºC ……...146
Figure 3.104. Dependence of three resistances at high, medium and low frequency on oxygen partial pressure for LG10SC/YSZ interface between 400 - 800 °C (a) R_1; (b) R_2; (c) R_3 and (d) $R_2 + R_3$ ……150
Figure 3.105. The dependence of the area specific resistance of the LG10SC/YSZ interface as a function of PO_2 at different temperatures ……...151
Figure 3.106. Complex impedance plots for LG10SC/GDC/LG10SC symmetric cell at between 400-800 °C for different oxygen partial pressures ……152
Figure 3.107. Typical EIS of a symmetric LG10SC/GDC/LG10SC cell measured at 600 ºC while fixing the oxygen partial pressure between 1 – 25% …….153
Figure 3.108. Experimental and fit Nyquist plots for symmetrical LG10SC/GDC/LG10SC cell measured at 3% O_2 – 97%N_2 between 400 – 800 ºC …….....154
Figure 3.109. Experimental and fit Nyquist plots for symmetrical LG10SC/GDC/LG10SC cell measured at 10% O_2 – 90%N_2 between 400 – 800 ºC ……154
Figure 3.110. Experimental and fit Nyquist plots for symmetrical LG10SC/GDC/LG10SC cell measured at 15% O_2 – 85%N_2 between 400 – 800 ºC ……155
Figure 3.111. Experimental and fit Nyquist plots for symmetrical LG10SC/GDC/LG10SC cell measured at 25% O_2 – 75%N_2 between 400 – 800 ºC ……155
Figure 3.112. The equivalent circuits adopted for fitting the impedance data for a) 400 ºC b) 500 - 800 ºC …….....156
Figure 3.113. Dependence of three resistances at high, medium and low frequency on oxygen partial pressure for LG10SC/GDC interface between 400 - 800 °C (a) R_1; (b) R_2; (c) R_3 and (d) $R_2 + R_3$ …….....159

Figure 3.114. The dependence of the area specific resistance of the LG10SC/GDC interface as a function of PO_2 at different temperatures 160

LIST OF TABLES

Table 1.1. Types of the fuel cells and their typical characteristic ……....2

Table 3.1. Calculated σ_{max}, $\sigma_{800^{o}C}$ and E_a of specimens sintered at 1100 ^{o}C ……69

Table 3.2. Calculated σ_{max}, $\sigma_{800^{o}C}$ and E_a of specimens sintered at 1100 ^{o}C ……71

Table 3.3. Calculated σ_{max}, $\sigma_{800^{o}C}$ and E_a of specimens sintered at 1100 ^{o}C ……....75

Table 3.4. Calculated σ_{max}, $\sigma_{800^{o}C}$ and E_a of specimens sintered at 1100 ^{o}C ……77

Table 3.5. The fitting parameters as a function of temperature for LV05SM/YSZ/LV05SM in PO_2 88

Table 3.6. The fitting parameters as a function of temperature for LV05SM/GDC/LV05SM in PO_2 ……99

Table 3.7. The fitting parameters as a function of temperature for LV05SC/YSZ/LV05SC in PO_2 ……...……... 109

Table 3.8. The fitting parameters as a function of temperature for LV05SC/GDC/LV05SC in PO_2 ……. 119

Table 3.9. The fitting parameters as a function of temperature for LV3SF/YSZ/LV3SF in PO_2 ……...……129

Table 3.10. The fitting parameters as a function of temperature for LV3SF/GDC/LV3SF in PO_2 ……...138

Table 3.11. The fitting parameters as a function of temperature for LG10SC/YSZ/LG10SC in PO_2 ……..……..... 147

Table 3.12. The fitting parameters as a function of temperature for LG10SC/GDC/LG10SC in PO_2 ……...… 157

1. INTRODUCTION

1.1. Energy Sources

Mainly two kinds of energy sources are available today, namely renewable and non-renewable energy. When the source of energy is immense after utilizing, it is called renewable energy like wind energy, solar energy, tidal and wave energy, biomass, hydropower energy, geothermal energy, etc. Utilizing a non-renewable energy source results to its exhaustion. A great thing to stand behind about renewable energy is that these kinds of sources do not emit any green house gases to the atmosphere. In contrast, non-renewable energy sources such as coal, natural gas and petroleum when employed add to green house gases, which is the main problem in global warming. The accelerated growth of population and industrialization of mankind has resulted in a serious demand in energy supply. The considerable decrease in non-renewable energy sources is one of the hot topics in worldwide concern. Fossil fuels provide 80% of the total energy consumption, and oil will only continue for 40 years, natural gas has 60 years and coal about 200 years [1]. The worldwide energy demand is assumed to be about 13 terawatts (TW) by 2050 [2]. So, in order to meet this demand, innovative approaches must be designed and developed.

On the contrary to the enormous pace of technological change in areas such as computing and health care, the technology in power generation has stayed still over the last 50 years. Nowadays, most of the electricity is still produced by thermal power plants, where heat from the combustion of fuel is converted into the mechanical energy, which is subsequently converted to electrical energy. In a power plant, nearly ⅔ of the energy in the fuel stays unused and is lost as waste heat. According to the World Energy Council Report, only 2% improvement (from 32% to 34%) in thermal power generation efficiency was succeeded worldwide from 1990 to 2008 [3].

1.2. Fuel Cells

Considering the environmental concerns, the search and development of new and cleaner power generation technologies are in topical issue. Fuel cells are one such technology. Attention on these alternative energy conversion devices has increased quickly in recent years, while the main principles of fuel cell operation are recognized since the early experiments of Schönbein and Grove in the first half of the 19^{th} century [4]. A fuel cell can be defined as a unit in which the reactants and the products are continuously supplied and removed.

Unlike heat engines, fuel cells directly convert the chemical energy stored by the fuel into the electrical energy. This direct conversion of chemical to electrical energy, without linking a thermal engine as in conventional methods of power generation, offers the chance for much better efficiencies unconstrained by Carnot's Law. There are several types of fuel cells exist today, all operating with the same principle. In contrast to rechargeable batteries, in fuel cells the fuel and the oxidant are constantly supplied to electrodes and the chemical reaction products are removed from them, so providing continuous operation. Mainly the cell is based on an electronically insulating, gas tight electrolyte that only transfers charge in the form of ions. Two electrodes on each sides of the electrolyte adapt the reduction of oxygen for the cathode side and the oxidation of the fuel for the anode side, respectively. For the reaction to be completed, the produced electrons at the fuel electrode are delivered through an external circuit.

Table 1.1. Types of the fuel cells and their typical characteristics.

Fuel Cell	AFC	PEMFC	PAFC	MCFC	SOFC
Charge Carrier	OH^-	H^+	H^+	CO^{2-}	O^{2-}
Electrolyte	KOH	Nafion	H_3PO_4	$Li_2CO_3 + K_2CO_3$	$Zr_2 + Y_2O_3$
$T_{operation}$ (°C)	100	80	200	650	650-850
Fuel	Pure H_2	Pure H_2	Pure H_2	H_2, CO, CH_4	H_2, CO, CH_4

A variety of fuel cells are in different stages of development. The most common classification of fuel cells is by the type of electrolyte used in the cells and includes 1) alkaline fuel cell (AFC), 2) polymer electrolyte membrane fuel cell (PEFC), 3) phosphoric acid fuel cell (PAFC), 4) molten carbonate fuel cell (MCFC), and 5) solid oxide fuel cell (SOFC) summarized in Table 1.1. Broadly, the choice of electrolyte determines the operating temperature range of the fuel cell. The operating temperature and useful life of a fuel cell specifies the properties of materials used in the cell components (i.e., electrodes, electrolyte, interconnect, current collector, etc.). By far the greatest research interest throughout the world has focused on Proton Exchange Membrane Fuel Cells (PEMFCs) and Solid Oxide Fuel Cells (SOFCs).

1.3. Solid Oxide Fuel Cell

Numerous different technological insights of the fuel cell idea are being considered nowadays, and the Solid Oxide Fuel Cell (SOFC) is regarded as one of the most promising one. In this type of fuel cell, an ionically conducting oxide membrane separates the reactant gases. The electrolyte material is generally an oxide ion conductor like doped ZrO_2 and a porous strontium-doped $LaMnO_{3\pm\delta}$ (LSM) cathode and a porous Ni/YSZ cermet (ceramic-metallic composite) anode. Since the charge carrier is oxide ion, SOFCs provide flexibility in the sense of fuel gas with high efficiency. Whereas, for instance, low temperature Polymer Electrolyte Membrane (PEM) fuel cells are usually restricted to the conversion of pure hydrogen as fuel, the high temperature SOFC is much more tolerant in this respect and can be operated with natural gas, biogas, syngas or other fuels. Efficiencies for this type of fuel cell can reach up to 70% [5].

SOFC technology is very favorable from the materials viewpoint and has potential benefits in the following qualities [6]:

- It has higher electrical efficiency, ~60%, compared to ~40% for low temperature cells.
- SOFCs do not need expensive noble metals such as platinum instead of low cost electrode materials.

- Not only hydrogen the purity of which does not matter but also a large variety of fuels can be used including natural gas, biogas, and hydrocarbon fuels without preliminary reforming.
- The high operating temperature of SOFCs produces ”high quality” heat, which can be utilized efficiently in CHP-units (combined heat and power). This can additionally increase the overall energy efficiency.

SOFCs are composed of all-solid-state materials, which are ceramic materials due to the high temperatures required for the operation. Cells are being assembled in many different arrangements, such as planar button cell, flat-plates cells, tubular cells or rolled tubes. A SOFC consists of two electrodes (the anode and the cathode) sandwiched around a solid electrolyte (Figure 1.1). Oxidant (air) is fed to the cathode where it is electrochemically reduced by electrons from the external circuit:

$$O_2(g) + 4e^- \rightarrow 2O^{2-} \quad (1.1)$$

Fuel (H_2, syngas, CO, CH_4, etc.) is fed to the anode, where it undergoes an oxidation reaction and releases electrons to the external circuit:

$$H_2(g) + O^{2-} \rightarrow H_2O(g) + 2e^- \quad (1.2)$$

$$CO(g) + O^{2-} \rightarrow CO_2(g) + 2e^- \quad (1.3)$$

or, in the case of hydrocarbon fuels,

$$C_nH_{2n+2} + (3n+1)O^{2-} \rightarrow nCO_2(g) + (n+1)H_2O + 2(3n+1)e^- \quad (1.4)$$

The classical SOFC concept, which has already been developed to technological maturity, is schematically shown in Figure 1.1. The porous electrodes (anode for fuel, cathode for oxidant) are separated by a gas-tight electrolyte. With the help of electrons the oxygen in the oxidant (e.g. air, O_2) is reduced to oxide ions O^{2-} at the cathode side (Equation 1.1). The produced oxide ions are merged into the electrolyte material, which is the responsible part for the oxide ion transport and hence allows only the ions to travel through towards anode side. Oxide ions combine with the fuel (e.g. H_2, CH_4, CO) to form water and if carbon-containing fuels are involved, CO_2 is produced as the end product. During this oxidation step of fuel (Equation 1.2, 1.3 and 1.4) electrons are released and

transport via an external circuit to the cathode side that is the where reduction of the oxygen proceeds.

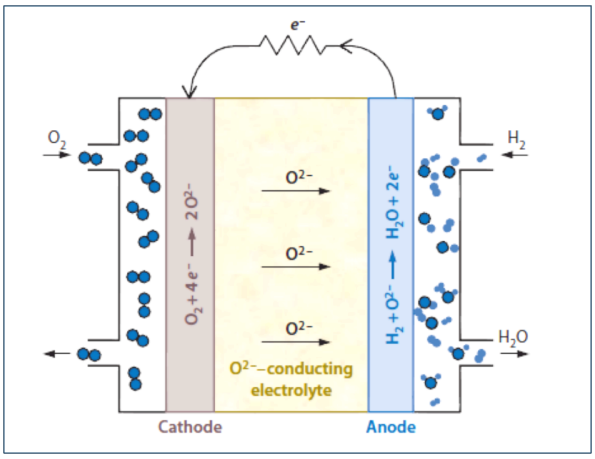

Figure 1.1. Schematic representation of SOFC working principle.

Therefore, electrical power can be produced from the fuel cell. The common principle of fuel cells and batteries resides the separations of reduction and oxidation by an ionically conducting material, driving the electrons to flow via an external circuit. Since the voltage produced by one of these cells is only about 1 V, multiple cells are to be combined to form a fuel cell stack for substantial applications.

1.3.1. Materials for SOFC Components

The main components of a fuel cell are the electrolyte, the anode, the cathode and the interconnect materials. Each element operates several functions in the fuel cell and has to fulfill certain requirements such as: proper stability in terms of chemical, phase, morphological, and dimensional in oxidizing and reducing atmosphere, similar thermal expansion coefficients (TEC), chemical compatibility within each components, having

proper type of conductivity, dense gas tight electrolyte material and porous cathode and anode to allow gas transport to the reaction sites.

1.3.1.1. Anode: The fuel electrode (anode) must be stable in reducing conditions of the fuel and have enough porosity to allow the transport of the oxidized fuel. Moreover, since the composition of fuel changes during the operation, the anode must be non-oxidized. The literature on anode materials for SOFCs is very extensive. In this part of the cell the fuel oxidation takes place:

$$O^{2-} + H_2 \rightarrow H_2O + 2e^- \quad (1.5)$$

The most significant requirements for the anode are long-term stability, matching thermal expansion coefficient with the electrolyte, supporting both electronic and ionic conductivity and high catalytic activity to promote the formation of water [7]. Transition metals can be used as SOFC anode materials such as Nickel (Ni). Nickel is used due to its excellent catalytic characteristics for breaking hydrogen bonds in the fuel (oxidation reaction of the hydrogen) and the low reactivity with other cell components [8]. Fuel electrodes are fabricated from composite powder mixtures of electrolyte material such as YSZ, GDC or SDC and nickel oxide NiO. During the start-up phase of the cell by the prevailing fuel atmosphere, the nickel oxide is then commonly reduced to nickel metal. The reason for forming a matrix of YSZ around the nickel particles is to stabilize the porosity of the electrode structure, to extend the reaction zone by increasing the triple phase boundaries (TPB), and also to provide a thermal expansion coefficient comparable to those of the other cell materials. Other candidate anode materials under investigation include cobalt-YSZ, ruthenium-YSZ, and mixed conducting oxides based on Y_2O_3-ZrO_2-TiO_2 solid solutions [9].

1.3.1.2. Electrolyte: A SOFC uses a solid oxide ion conductor as the electrolyte material. This material should be electronically insulating and have sufficient ionic conductivity for oxide (O^{2-}) ions at operating temperature. Moreover, having suitable thermal expansion coefficient, chemical and physical compatibility with electrode materials are also important. The conventional electrolyte is made of Yttria Stabilized Zirconia ((Y_2O_3)0.08 –

(ZrO_2)0.92), abbreviated as 8-YSZ. ZrO_2 in its pure form cannot be used as an electrolyte because of its low ionic conductivity. Therefore, it is doped with Y_2O_3, Equation 1.6, which means substitution of a trivalent cation, Y^{3+}, for the host lattice cation Zr^{4+}. With this substitution, the concentration of oxygen vacancies can be increased [10].

$$Y_2O_3 \xrightarrow{ZrO_2} 2Y'_{Zr} + 3O_o^x + V_o^{\cdot\cdot} \quad (1.6)$$

The oxygen vacancies distribute diffusion of oxide ions through the electrolyte, which provides relatively high oxide ion conductivity. Due to the aim of lowering the operation temperature of the cell, thin electrolyte films on porous electrodes are being fabricated. Three electrolyte systems namely yttria stabilized zirconia (YSZ), strontium, magnesium-doped lanthanum gallate (LSGM), and gadolinium- or samarium-doped ceria (CGO or CSO) have been widely investigated for SOFCs [11].

1.3.1.3. Cathode: The cathode is the air electrode of SOFC where electrochemical reduction of oxygen occurs. For this purpose, the cathode must have high catalytic activity for the oxygen reduction reaction (ORR), sufficient porosity to allow oxygen diffusion, chemical compatibility with the other contacting cell components under operating conditions, stability during both in fabrication and operation of the cell, and high electronic and ionic conductivity [12].

The choice of the cathode material selection is significantly dependent on that of the electrolyte. Care must be given to match the TEC's and prevent undesirable interface chemical reactions. The reaction occurs at the cathode side:

$$\frac{1}{2}\, O_2\ (gas) + 2e^-\ (cathode) \rightarrow O^{2-}(electrolyte) \quad (1.7)$$

In the intermediate temperature SOFCs (IT-SOFCs), the low operating temperature reduces the chemical interaction of materials, thus its power characteristics does not degrade rapidly. When the cell is connected to a load via a closed circuit, a current is produced through the electrochemical reactions and as the working temperature is lowered down, the cell potential is reduced by internal non-reversible voltage losses which means the polarization losses induced by electric current increase. The following three main types of losses are separated: ohmic (η_1), concentration (η_2), and activation (η_3) [12]:

$$E = E_0 - \eta_1 - \eta_2 - \eta_3 \tag{1.8}$$

where E is the voltage on the working fuel cell, E_0 is the open circuit voltage (OCV). Figure 1.2 schematically represents how the cell polarization of typical SOFC changes with the current density withdrawn. The influences of the mentioned types of polarization losses are also shown.

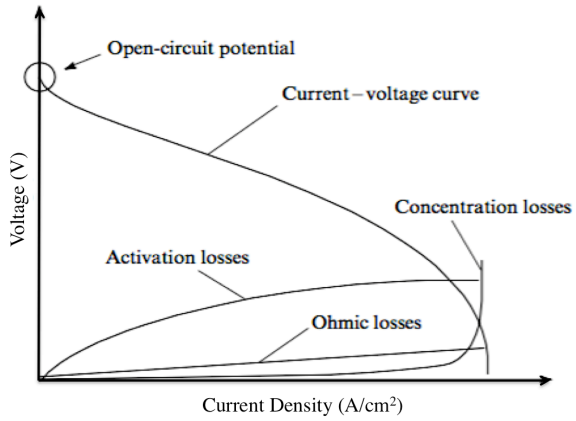

Figure 1.2. Current - voltage curve of a working SOFC.

Ohmic resistance losses occur with the electric resistance of the cell components, and they increase with the increase in the current density likewise in Ohm's Law. The reduction of ohmic losses with the rise of working temperature is associated with that most materials of the cell primary components show conduction of the activation nature so that their resistance increases as the temperature decreases. The general methods of reducing this type of polarization are the employment of high conductivity electrodes and the use of appropriate interconnect materials.

The concentration losses are caused by the reduced potential at the TPBs due to the depletion of charge carrying reactants resulted by slow diffusion from the bulk of the gas chambers/channels through the porous electrodes.

Activation polarization makes the biggest contribution to the polarization losses during SOFC operation. It occurs due to complex nature of electrode half reactions (oxidation-reduction reactions), which contains several stages. Particularly, this is related to the oxygen reduction on the cathode that is along with the breakup of the strong double bond in the oxygen molecule to form O^{2-} ions in vacant sites of the solid oxide. The cathode polarization losses must be minimized by an appropriate cathode material selection and an interface microstructure optimization.

As the state of the art materials, cathodes for SOFCs must have many properties including high electrical conductivity, high catalytic activity for ORR, and compatibility with other cell components. In the first periods of SOFC development, platinum metal was used as cathode since other appropriate materials were not available. However, platinum is expensive and its use in cost-effective commercial SOFCs for power generation is not practical. Low cost alternative to platinum–perovskite oxides also possess the required properties and have consequently attracted much interest [13].

The perovskite materials $La_{1-x}Sr_xMnO_{3-\delta}$ (LSM) with x between 0.15 and 0.50 are the most commonly used and researched cathode material for standard SOFC. Those Sr-doped lanthanum perovskites stay stable both in large oxygen excess-oxidizing atmosphere and in large oxygen deficient-reducing gas atmospheres [14]. Oxygen deficient means the oxygen vacancies while oxygen-excess results on metal vacancies, which is good for electrode properties. However, the ionic conductivity of LSM is extremely low [15]. This causes practical limitations and restrictions to the application of LSM especially at low temperature (<800 ^{o}C).

Cobalt and iron containing perovskite like $La_{1-x}Sr_xCo_{1-y}Fe_yO_{3-\delta}$ (LSCF) is another candidate for cathode materials. Compared with LSM-based materials, LSCF has both higher electrical and ionic conductivity [16]. Thus, in some cases LSM is treated as the electronic conductor while LSCF is generally selected as mixed ionic and electronic conductor (MIEC) [17]. Although the practice of LSCF as cathode can effectively improve the cell performance, LSCF materials have to be selected carefully due to its higher TEC value than the YSZ electrolyte [18].

In order to lower the working temperature of SOFCs, strontium-doped samarium cobaltite with the composition of $Sm_{0.5}Sr_{0.5}CoO_3$ (SSC) has been developed recently. It has

better conductivity values than LSCF and LSM at the intermediate temperatures (500 – 800 ºC) [19]. Instead, just as the LSCF, the TEC value of SSC is also too high and this will affect adversely its compatibility with YSZ electrolyte. But, it is practically compatible with GDC and LSGM electrolyte materials [20].

As mentioned above, the electronic and ionic conductivities of LSCF and SSC are high, however, their TEC are much higher than YSZ. TEC value of LSM is close to YSZ but its ionic conductivity is considerably low. Consequently, many alternative materials have been studied and developed with the aim of improved both electronic and ionic conductivity and obtaining a TEC value close to the YSZ while having desirable catalytic activity under cell working conditions. In this respect, Fe-doped lanthanum strontium cuprate ($La_{0.7}Sr_{0.3}Cu_{0.4}Fe_{0.6}O_{3-\delta}$) was stated to reveal a high conductivity and good TEC match with the electrolyte [21]. $Ba_{0.5}Sr_{0.5}Co_{0.8}Fe_{0.2}O_{3-\delta}$ is another interested cathode material for IT-SOFCs [22].

In summary, in order to make the cell economically practical and available for commercialization, lowering the operating temperature to allow for cheaper materials as well as reduce the degradation problems is on the vital interest. This has initiated a push for the development of new materials.

Crystal structure and properties of perovskite oxides are also two important features in SOFC systems. Perovskite materials have been widely used as cathode materials in SOFCs [23]. It is essential to first investigate the fundamentals of the perovskite structure to better design cathode materials.

As for the crystal structure of perovskite, it has the general formula of ABO_3. The A-site cations with lower valence (such as La, Sr, and Ca) are larger in ionic radius and coordinated to twelve oxygen anions while the B-site cations (such as Fe, Co, Ti, and Cr) accommodate much smaller space and are coordinated to six oxygen anions. Valence sites can be obtained by the full or partial substitution of A or B cations with different valences. When the total valence of the cations sums up to less than six, an anionic charge is formed by introducing vacancies at the oxygen lattice sites [24]. Figure 1.3 prevails the typical structure of the cubic perovskite ABO_3.

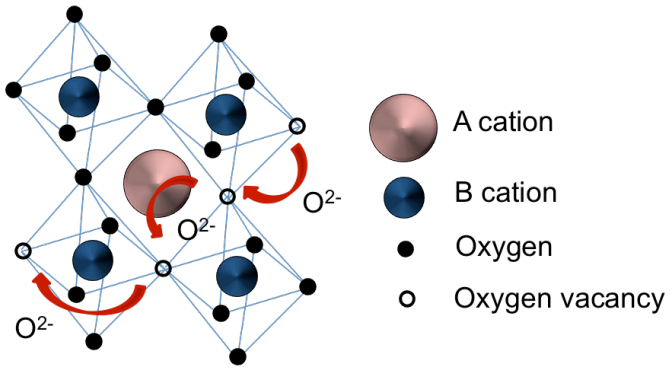

Figure 1.3. Crystal structure of 'ideal' cubic perovskite ABO_3.

A-cations are located at the center of the cube and have coordination number 12; B-cations reside at cube vertices (at the centers of octahedra) and have coordination number 6. Oxygen atoms are at the corners of the octahedra and bulk oxygen transport in perovskite structure is also shown in Figure 1.3.

Many perovskites do not have the 'ideal' cubic symmetry due to their distortion in structure. Because of such reasons such as cation displacements inside the octahedra and also tilting of the octahedra, common distortions related to the properties of the A and B substituted atoms are made up. The degree of the distortion in crystal structure can be determined by the Goldschmidt tolerance factor (t) as follows:

$$t = \frac{(r_A + r_B)}{\sqrt{2}\,(r_B + r_O)} \tag{1.9}$$

Based on the ionic model of the perovskite crystal structure, t value has been derived by using the relationship between the ionic radii of A and B-site cations and oxygen (r_A, r_B and r_O, respectively). When the tolerance factor is near unity, the structure is the ideal cubic. A cation with smaller radius or B cation with larger radius gives rise to a decrease in tolerance factor ($t < 1$). Therefore, the coordination number of the A cation decreases due to tilting of corner sharing BO_6 octahedra to an orthorhombic symmetry. This gives rise to various distortions of the perovskite structure [25].

For the electrical conductivity in perovskites, divalent transition metal substitution for the trivalent A-site cation involves that in order to balance the electro-neutrality in the perovskite, the introduced negative charge is compensated by an increase in valence of the

B-site cation, so called electronic compensation, or by the formation of oxygen vacancies, called as ionic compensation [26]. B-site cations as transition metals can carry out a valence change to compensate the introduced effective charge imbalance and produce B^{4+}/B^{3+} couples that behaves as hopping sites for electrons, i.e. for p-type or n-type conductivity.

When considering the electrical conductivity by the help of Arrhenius plot *ln(σT)* vs *1/T*, linear behavior reveals that the electronic conductivity is because of the small polaron - hopping mechanism which follows the way along the transition metal-oxygen-transition metal chains (B–O–B) in the perovskite structure (e.g. Fe^{3+} – O – Fe^{4+}) [27].

$$\sigma = \left(\frac{C}{T^s}\right) exp\left(\frac{-E_a}{kT}\right) \tag{1.10}$$

Activation energy can be calculated by fitting Equation 1.10, where σ is the electrical conductivity, C is the pre-exponential factor, T is the temperature, k the Boltzmann constant, and E_a is the activation energy expressing the enthalpy of polaron-hopping mechanism [28]. The exponent s equals either 1 or 3/2 for adiabatic or non-adiabatic processes, respectively [29].

For ionic conductivity in perovskites, the oxide-ion conductivity in perovskites ABO_3 progresses by the vacancy mechanism. Oxide ions diffuse from occupied to adjacent vacant sites along the corner of BO_6 octahedra (Figure 1.3) [30]. While jumping from one site to the neighboring vacancy, an oxide ion travels along an arc trajectory rather than along a linear one (the shortest way). During this movement, the oxide ion has to pass through a ‘‘saddle point’’ (Figure 1.4), which is assembled by two A-site cations and one B-site cation.

The radius of the “bottle-neck” (*r’*) centered at the saddle point, calculated from the radius of cations in the perovskite structure and the value of *r’* should be close to the oxygen ionic radius, 1.40 Å [31]. For perovskite materials, the value for the radius does not exceed 1.05 Å [32]. However, because the radius of the oxygen ion is 1.40 Å in the sixfold coordination there must be significant outward shifts from the equilibrium positions of the cations away from the mobile oxygen ion.

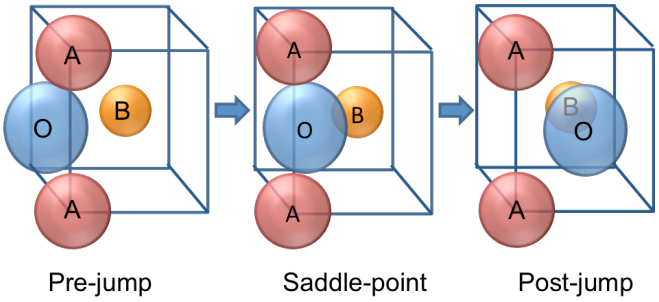

Figure 1.4. Schematic representation of saddle point.

There are also structural properties of perovskite oxides that are related to the oxide-ion conductivity: the tolerance factor (Equation 1.9), the free volume (the difference between the unit cell volume and the volume of ions present in the cell), the metal-oxygen bond and the extent of deviation of cation dimensions from ideal values [30,32]. The latter parameter means that the ionic radii of A-site cation is close to the oxygen ionic radius and also that the radius of the B-site cation is close to the radius of octahedral vacancy in ABO_3 close packing [32]. Most important factor required for oxide ion conduction in perovskite crystalline structure is the lower activation energy for oxide ions and their higher vacancy mobility. That is accomplished by the deteriorating from completely symmetrical crystalline network without any stress. That is why $A^{3+}B^{3+}O_3$ type of perovskite structure has the highest oxide ion mobility due to the lowest interaction with B-site cation [33].

For the kinetics and reaction mechanisms of cathodes, the main requirement to be satisfied by a SOFC cathode is a high reaction rate according to the cathode catalytic multistep reaction. In the overall electrochemical reactions, the molecular species involved must first be transformed to some electro-active intermediate form via multiple processes. Generally, this electrochemically kinetic step is regulated to an area close to TPBs, which are defined as the meeting sites where the oxygen ion conductor, electronic conductor, and the gas phase come in contact. The electrochemical steps contain different bulk and surface steps. The intermediate steps in the overall electrode reaction are usually considered as follows: the reduction of O_2 molecules including adsorption, dissociation, reduction and incorporation of the oxygen anion into the lattice of cathode materials; ionic transport

through the porous cathode towards the electrolyte; and the ion movement into the electrolyte lattice [34]. Among these processes, several steps could be rate limiting for ORR, which is the biggest contributor to the total cell resistance.

For perovskite type materials such as doped $LaMnO_3$, $LaCoO_3$, $SmCoO_3$, or $LaFeO_3$ are largely examined for use as SOFC cathodes, and for these materials three possible paths for the cathodic reaction may be considered that is the electrode surface path, the bulk path and the electrolyte surface path as shown in Figure 1.5 [35].

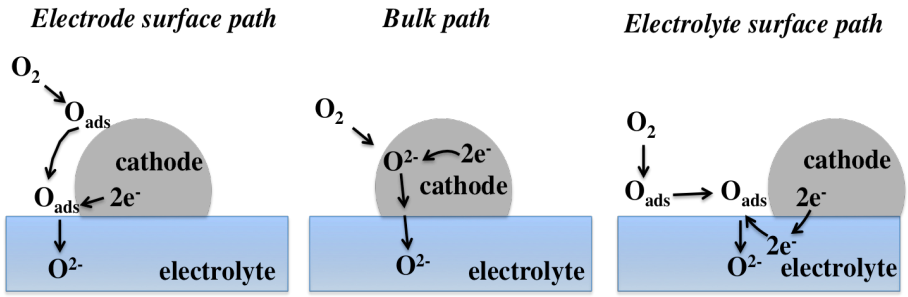

Figure 1.5. Outlines of possible reaction paths of the oxygen reduction and incorporation reaction and some possible rate determining steps.

These three paths are suitable for the cases of an electrical conductive material such as LSM, a mixed electrical and ionic conductive material such as LSCF and a composite such as LSM-YSZ, respectively.

1.3.2. Electrochemical Impedance Spectroscopy

With Electrochemical Impedance Spectroscopy (EIS), properties (physical and chemical processes) of electrochemical systems can be studied. A voltage is applied and the current, which flows through the system, is measured. Resistance is the ability of a

circuit element to resist the flow of electrical current. Ohm's law (Equation 1.11) defines resistance in terms of the ratio between voltage V and current I (ideal resistor).

$$R = {}^{V}/_{I} \tag{1.11}$$

In reality circuit elements show much more complex behavior, so impedance is used. Like resistance, impedance is a measure of the ability of a circuit to resist the flow of electrical current. The Impedance is not limited by the simplification of the ideal resistance, like independence of frequency and in phase of voltage and current [36].

The electrochemical impedance is usually measured by applying an AC potential (sinusoidal) to an electrochemical cell and measuring the current through the cell. The response to this signal is an AC current signal, containing the frequency and it's harmonics (Figure 1.6).

The signal, expressed as a function of time, has the form

$$V(t) = V_o \cos(\omega t) \tag{1.12}$$

Where *V(t)* is the potential at time t, V_o is the amplitude of the signal, and ω is the radial frequency. The relationship between radial frequency ω (rad.s^{-1}) and frequency f (Hz) is:

$$\omega = 2\pi f \tag{1.13}$$

In a system, the response signal, *I(t)*, is shifted in phase (ϕ) and has a different amplitude, I_o:

$$I(t) = I_o \cos(\omega t - \phi) \tag{1.14}$$

Given an expression for Ohm's law to calculate the impedance:

$$Z(\omega) = \frac{V(t)}{I(t)} = \frac{V_o \cos(\omega t)}{I_o \cos(\omega t - \phi)} = Z_o \frac{\cos(\omega t)}{\cos(\omega t - \phi)} \tag{1.15}$$

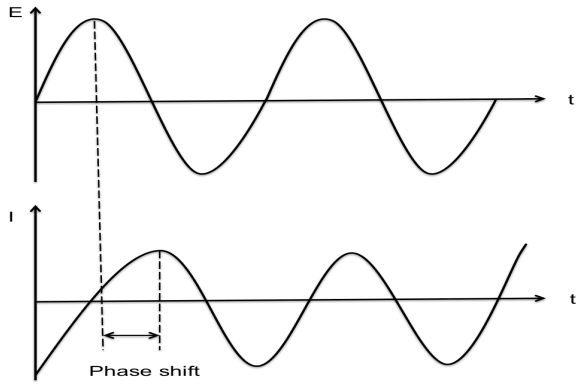

Figure 1.6. Sinusoidal current response in a linear system.

By using Euler's relationship (Equation 1.16), it is possible to express the impedance as a complex function. The potential is described as (Equation 1.17) and the current response as (Equation 1.18). The impedance is then represented as a complex number (Equation 1.19).

$$e^{i\phi} = \cos\phi + i\sin\phi \tag{1.16}$$

$$V(t) = V_o . e^{-i\omega t} \tag{1.17}$$

$$I(t) = I_o . e^{-i(\omega t + \phi)} \tag{1.18}$$

$$Z(\omega) = \frac{V(t)}{I(t)} = Z_o . e^{i\phi} = Z_o\,(\cos\phi + i\sin\phi) = Z_o\,(Z_{re}(\omega) + Z_{im}(\omega)) \tag{1.19}$$

The expression for *Z(ω)* is comprised by a real and an imaginary part (Equation 1.19). When the real part is plotted on the x-axis and the imaginary part on the y-axis a "Nyquist plot" is acquired (Figure 1.7).

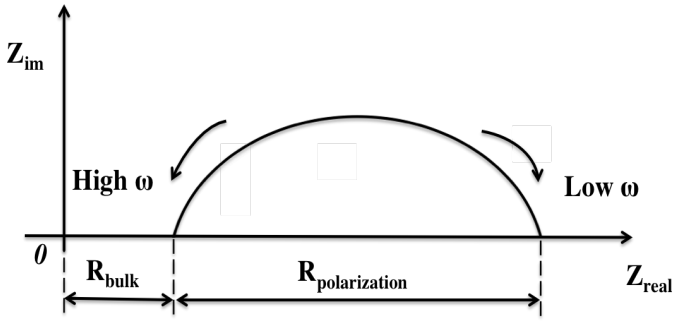

Figure 1.7. Schematic representation of EIS Nyquist plot.

The real part, Z_{real}, on the x-axis shows resistive steps of impedance curve, while the imaginary part, Z_{im}, on the y-axis represents capacitive processes of an impedance curve. The bulk resistance, R_{bulk}, is controlled by both the electrolyte and interconnects and can be measured from the high frequency part on the Nyquist plot. The difference between the low frequency intercept, which is called as the total resistance, R_T, and the R_{bulk} gives the polarization resistance, $R_{polarization}$. All the electrochemical processes related to the electrodes are displayed by $R_{polarization}$. The number of impedance arcs in the plot is associated with processes that contribute to the impedance of electrode reactions.

1.4. Scope of the thesis

There are many requirements on the SOFC cathode that must be fulfilled for the commercialization of this technology to be viable. Up to now, many materials have developed to address all requirements and broad research is enduring in order to find such a material. In addition to that, although a number of experimental studies on cathodes for SOFCs are described, there is still very little fundamental knowledge on both the physical and electrochemical processes occurring inside the oxygen electrode, however there are many discrepancies in the literature. It is therefore of great importance to follow the research on SOFC cathodes.

The main objective of this thesis is the development of novel and superior cathode materials for SOFC applications working at moderate temperatures (500°C<T) with the desired efficiency.

In Chapter 1, a brief introduction is given on fuel cells, especially for SOFCs. Subsequently a general review on SOFC materials, its working principle and kinetics as reported in literature is given. Stress is on the cathode, particularly its chemistry, research and developmental features. A literature review is summarized about the conventional cathode materials such as LSM and LSCF cathodes. In this review a comparison will also be made with several other types of perovskite cathode materials. Moreover, a theoretical background is given on electrochemical impedance spectroscopy (EIS). At the end of the chapter the scope of the master thesis is presented.

The experimental set-up and the design for electrochemical cells are presented in Chapter 2. The study concerned a comparison is made between four different cathode materials under identical conditions. The cathode types investigated LV3SF, LG10SC, LV05SM and LV05SC were successfully synthesized by sol-gel process and are characterized with XRD and XPS. As electrolyte material yttria stabilized zirconia (YSZ) and gadolinium-doped ceria (GDC) were used. For electrical conductivity measurements, rectangular bars of the synthesized materials were prepared and four-probe conductivity method was performed. Also for the electrochemical characterization of the electrodes impedance measurements were completed. The analysis of the measured impedance generally required the use of three to four (RQ) circuits in series in the equivalent circuit model. Of the four cathodes, the LV05SC on YSZ showed the highest are area specific resistance. The results for other cathode materials were in good agreement with literature.

Synthesis and characterization of novel cathode materials for SOFCs are clearly addressed in Chapter 3. Instead of traditional cathode material used for IT-SOFC, new perovskite-based mixed ionic-electronic conductive materials, which can reduce oxygen with higher electrochemical activity yielding better performance was intended for use. Especially, benefiting from the outstanding features of the crystal structure of perovskite, development of IT-SOFC electrodes exhibiting high efficiency and evaluating their efficiency was aimed by employing cheaper and low-order metals (Ti, Fe, Co, Cr, Mn, V, B and Gd). Understanding the oxygen reduction reaction occurring in the perovskite

structure is very crucial for assessing the cathode efficiency in SOFC system. Because oxide-ion forming reaction from the reduction of freely moving oxygen in air on the surface of metal and/or metal oxide is carried out with a complex and multi-step mechanism. This process usually progresses through parallel reactions. This simultaneous accomplishment of the reaction substantially depends on the chemical nature of the ion carrier within the cathode material, the crystal atom sequences and also the microstructure. For these reasons, various metals such as Ti, Fe, Co, Cr, Mn, V, B and Gd were doped into the perovskite structure in a systematic manner and the novel cathode material with the desired properties were expected to be produced.

In Chapter 4, the advance studies of these SOFC cathode materials are explained as realistic SOFC performance tests to better address their challenging features. There is an explanation about the study on the degradation under controlled conditions coupled *in-situ* experiments with analytical techniques such as Raman and XRD in order to expose the degradation mechanisms needs to be carried out. Further studies are needed on how the developed cathode materials work when executed in an operational SOFC when it comes to both electrochemical performance and chemical and mechanical compatibility.

Conclusion as Chapter 5 includes the pronounced evaluations of analysis of these novel SOFC cathode materials. As a result of this study, it is found that LV05SC has the best electrical conductivity value, however, the rest of the materials (LV3SF, LG10SC, and LV05SM) have better ionic conductivity values. Therefore, it is concluded that these cathode materials would be candidates as IT-SOFC cathode materials.

2. EXPERIMENTAL

2.1. Sol-Gel Process

Sols and gels are two forms of matter that have been to known to sustain naturally for a long time and they comprise a number of substances such as blood, serum and milk and various materials like ink and clays. Sols and gels have emerged scientific interests for a long time as the oldest known sols are prepared in 1853 by Faraday and they were only of pure scientific interests [37]. However, because of their immensely high specific area, sols and gels have become increasingly interesting in the field of catalysis. Since the 1970s, the number of publications in this field has been rising and this accelerated the number of applications in high technology ceramics. By the sol-gel techniques, high purity powders, electronic and ionic conductors can be produced and also this technique is very helpful and important for the fabrication of homogeneous complex ceramic products. In point of the fact, sol-gel processing has been considered as the way to better ceramics through chemistry. To give a brief explanation, a sol is a stable suspension of colloidal solid particles within a liquid. In order to exist as a sol, the solid particles, which are denser than the surrounding, must be small enough for the dispersion forces to be greater than those of gravity. Basically, particles in a sol must be between 2nm and 0.2μm in size [38]. When it comes to the gel, it is a porous interconnected homogeneous solid network and forms when the homogeneous dispersion within the initial sol solidifies and this is called as gelation that inhibits the growth of inhomogeneity [39].

Sol-gel processes not only have brought an initial view in the domain of glass and ceramics fabrication but also have enlightened the significance of chemistry along the ultimate fabrication lines of materials, from initial chemical precursors to the final products [40]. The main idea of this process is to steadily form an oxide network by polymerization reactions of chemical precursors dissolved in a liquid medium.

Sol-gel technique has been widely used for synthesis of an inorganic network over a chemical reaction at low temperatures. For the sol-gel synthesis, there are many variations can be brought. This technique actually does not only nominate a single process,

yet a very diverse type of procedures, which concentrates around a simple plan as presented in Figure 2.1.

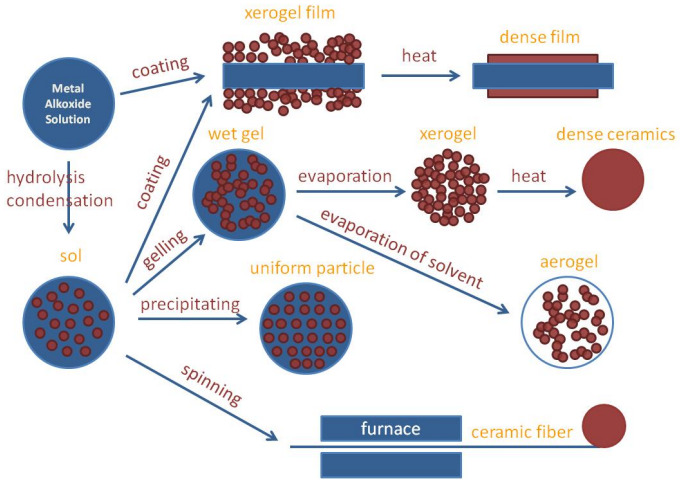

Figure 2.1. Outline of sol-gel processing.

The sol-gel process can briefly be defined as the conversion of a precursor solution into an inorganic solid via inorganic polymerization reactions induced by water. Usually, the precursor or starting compound can be either an inorganic (no carbon) metal salt (chloride, nitrate, sulfate) or a metal organic compound such as an alkoxide.

Production of ceramic oxide materials has been extensively developed and basically the sol-gel process consists of the following steps:

i. Preparation of a homogeneous solution by each of two ways; first one is by dissolution of metal organic precursors in an organic solvent that is miscible with water and the second is by dissolution of inorganic salts in water.
ii. Conversion of the homogeneous solution into a sol with the treatment of a suitable reagent.
iii. Aging
iv. Shaping
v. Sintering/Thermal treatment

The initial step in a sol-gel reaction is the formation of an inorganic polymer by hydrolysis and condensation reactions, such as the transformation of the molecular precursor into a highly cross-linked solid. A sol, a dispersion of colloidal particles in a liquid, is the result of hydrolysis step and further condensation eventuates in a gel which is an interconnected, rigid and porous inorganic network surrounding a continuous liquid phase. This conversion is called as the sol-gel chemistry. In order to desiccate the gels, there are two possibilities. By the removal of the pore liquid, aerogels are produced without any collapse in the network. When the gel drying process is done under ambient conditions, shrinkage of the pores occurs with yielding a xerogel. One of the significant properties of the sol-gel process is the feasibility to give shape to the material into any desired form like monoliths, films, fibers, and mono-sized powders, and following with the conversion into a ceramic material by heat treatment.

2.1.1. Fabrication of SOFC Material Powders with Sol-Gel Process

Sol-gel processes have been practiced to produce SOFC materials with desired physical and chemical properties which traditional solid-state reaction techniques are unable to supply. This method has been applied for synthesis of numerous cathode materials like LSM [41], $(Pr_{0.7}Ca_{0.3})_{0.9}MnO_{3-\delta}$ [42], LSCF [43], Fe-doped LSM [44], La, Pr, Sm and/or Ba co-doped $Ln_{0.58}Sr_{0.4}Fe_{0.8}Co_{0.2}O_{3-\delta}$ [45,46], $Pr_{1-x}Sr_xCo_{0.8}Fe_{0.2}O_{3-\delta}$ [47], BSCF [48] etc. The grain size of the porous cathode material is an important parameter to examine in order to reduce interfacial polarization resistance. By decreasing the grain size or increasing the surface/volume ratio, TPB, i.e. the number of reaction sites can be enlarged considerably. With this method, it has been thought that there will be a significant increase in the number of reaction sites (TPB) in electrode materials or decrease in the sintering temperature of the electrolyte material.

Moreover, the reduction of the working temperature from high temperature (such as 900-1000˚C) to intermediate temperature (500-800˚C) for future applications is one of the most significant goals in SOFC research. Unfortunately, the high polarization resistance of the cathode material, which limits the cell power density, is the main limiting factor at intermediate temperature. The cathode has to be porous in structure with a small grain size

to optimize the active surface area and TPB length [49]. Sol-gel process is ideally suited for assembling such microstructures. The advantages of this process over other techniques consist:

i. The microstructure and composition of electrode materials can be controlled with relative ease,
ii. The electrode and electrolyte adherence is strong,
iii. Low temperature processing is possible.

The microstructures of solid oxide fuel cell components strongly influence its performance. Each component should cover the expectations like specific microstructures further to the requirements on intrinsic features of the materials in order to obtain high efficiency: gas-permeable and porous electrode (cathode and anode) with high surface area to augment the TPB length and gas-tight, thin electrolyte to minimize the ohmic resistance. Sol-gel method is a considerably functional approach to fabricate desired materials and components. The benefits of this process include superior microstructure control and convenience of compositional modification especially at low temperatures with simple and inexpensive equipment [37]. This kind of technique has been used both for powder synthesis as well as for modification of electrode surface and electrode/electrolyte interfaces to adjust the microstructure and electrochemical performance of cell components.

Sol-gel technique has been extensively improved to obtain ceramic oxide materials and arises mainly from three steps:

i. Preparation of starting solution: involves mixing low viscosity solutions of suitable precursors such as metal derivatives. These precursors can in some cases be the metal oxides or metal alkoxide solutions.
ii. Gelling stage: arises from forming a uniform sol and causing it to the gel; this is the key step in the sol-gel process to enable homogeneity on the ceramic product during withering. The conversion of the sol to the gel state can be carried out by three different routes:
    - Growth of polymeric molecules which establish randomly a three dimensional network

- Expansion of individual particles which become larger as they grow together
- Stabilization of colloids by surface charges succeeding interparticle condensation step leads to gelation

iii. Thermal treatment to the final product: giving shape to the ceramic material during or after the gelation stage like bulk materials, hollow spheres, fibers and surface coating.

Metal alkoxide solutions, other forms of metals such as metal oxides, nitrates, acetates (carboxylates) and β-diketonates are the most commonly used precursors for the preparation of multicomponent ceramic materials.

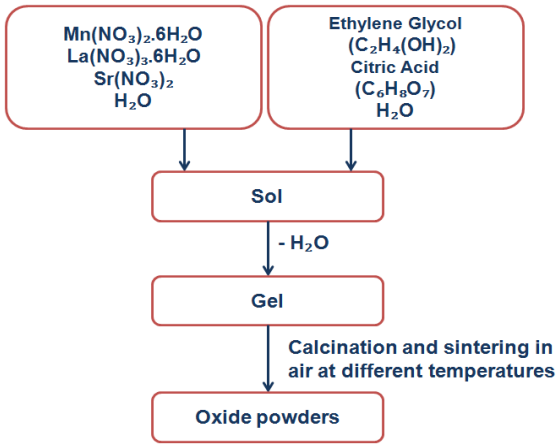

Figure 2.2. A flow scheme illustrating the processing procedure for LSM powder synthesis.

LSM maintains its reputation as the best-known cathode material for SOFCs based on yttria stabilized zirconia electrolyte. Presented in the flow scheme of Figure 2.2 is a classical sol-gel technique for LSM powder synthesis. In this process, the starting materials are $La(NO_3)_3.6H_2O$ (Alfa Aesar, 99.9%), $Mn(NO_3)_2.6H_2O$ (Alfa Aesar, 98%) and $Sr(NO_3)_2$ (Alfa Aesar, 99%) metal nitrate powders. Each was dissolved in deionized water to make the metal nitrate solution. The appropriate ratios of ethylene glycol and citric acid were mixed as polymerization and complexation agents, respectively. The solution was immersed in an oil bath, then was heated and stirred at ~115-120˚C to evaporate excess water on a thermal plate, where polymerization occurs in the solution and leads to in a homogeneous sol. When the acquired sol was further heated, an intermediate resin was

formed. The resulting resin autoignited and produced the desired powder. All calcined powders were initially baked at 400˚C for 1 h with a heating ramp of 0.5˚C.min^{-1} so as to burn out the organic substances present in the cathode and then finally annealed at 1100˚C for 2 h with the same ramping, and with decreasing temperature to 25˚C at a ramp rate of 1˚C.min^{-1} in laboratory air, which is a moisture-containing atmosphere. The resultant cathode powders were characterized by X-Ray diffraction.

During recent decades there has been substantial interest in identifying the best material for application as the cathode material in a solid oxide fuel cell. Materials like $La_{1-x}Sr_xMnO_{3-\delta}$ (LSM), $La_{1-x}Sr_xFeO_{3-\delta}$ (LSF) or $La_{1-x}Sr_xCoO_{3-\delta}$ (LSC) and mixtures thereof, for example $La_{1-x}Sr_xCo_{1-y}Fe_yO_{3-\delta}$ (LSCF) have been investigated in detail and these transition-metal oxides were extensively well-studied due to their excellent catalytic activity [50]. In this respect, different metals were added to Lanthanum Strontium Manganite (LSM) and Lanthanum Strontium Cobalt Ferrite (LSCF) like Vanadium and Gadolinium. These metals were doped with different ratios to LSM and LSCF and then replaced proportionally. In this study, it is aimed to develop a unique SOFC system with better efficiency by producing novel and advanced cathode electrodes, which produces oxide ions sufficiently and transfers these ions efficiently to the electrolyte. The transition metals were doped in the following manner:

Synthesis of $La_{0.6-x}V_xSr_{0.4}CoO_{3-\delta}$ (x = 0.005, 0.01, 0.02, 0.03, 0.04, 0.05, 0.10): All metal nitrates, acetates and starting materials were of analytical grade from the Alfa Aesar and Sigma Aldrich chemical reagent company. The under mentioned developed cathode materials were named by according to the content ratio of cations for lucidity in following.

0.5% (mole) Vanadium doped Lanthanum Strontium Cobalt Oxide ($La_{0.595}V_{0.005}Sr_{0.4}CoO_{3-\delta}$) (LV05SC): 0.573g (1.32x10^{-3} mole) Lanthanum (III) nitrate hexahydrate ($La(NO_3)_3$. $6H_2O$), 3.87x10^{-3}g (1.11x10^{-5} mole) Vanadium (III) acetylacetonate, 0.188g (8.89 x10^{-4} mole) Strontium nitrate $Sr(NO_3)_3$, 0.647g (2.223 x10^{-3} mole) Cobalt (II) nitrate hexahydrate and 0.854g (4.45x10^{-3} mole) Citric acid monohydrate ($C_6H_8O_7.H_2O$) was dissolved in 45ml distilled water with magnetic stirring. Then 1 mL (1.72x10^{-2} mole) ethylene glycol ($C_2H_6O_2$) was added into the beaker after the mixture was dissolved. With constant stirring, the temperature was kept around 115-120˚C and the viscous gel swelled with a rapid evolution of a large volume of gases to produce a

voluminous powder. The formed resin was calcined and the resulting powder was characterized by XRD.

1% (mole) Vanadium doped Lanthanum Strontium Cobalt Oxide ($La_{0.59}V_{0.01}Sr_{0.4}CoO_{3-\delta}$) (LV1SC): The LV1SC samples were synthesized via sol-gel process. 0.935g ($4.45x10^{-3}$ mole) Citric acid monohydrate ($C_6H_8O_7.H_2O$) and 1ml ($1.72x10^{-2}$ mole) ethylene glycol ($C_2H_6O_2$) were used as parallel complexing agents. 0.569g ($1.31x10^{-3}$ mole) Lanthanum (III) nitrate hexahydrate ($La(NO_3)_3.6H_2O$), $7.75x10^{-3}$g ($2.23x10^{-5}$ mole) Vanadium (III) acetylacetonate, 0.188g ($8.90\ x10^{-4}$ mole) Strontium nitrate $Sr(NO_3)_3$ and 0.648g ($2.227\ x10^{-3}$ mole) Cobalt (II) nitrate hexahydrate were used as starting materials. After converting the sample into a viscous gel under heating and stirring conditions, the viscous gel was dried to form a powder precursor which was calcined at 1100˚C for 2h. The crystallographic phases of the sample material were verified using XRD analysis.

2% (mole) Vanadium doped Lanthanum Strontium Cobalt Oxide ($La_{0.58}V_{0.02}Sr_{0.4}CoO_{3-\delta}$) (LV2SC): The cathode powders of LV2SC were prepared by mixing of 0.562g ($1.29x10^{-3}$ mole) Lanthanum (III) nitrate hexahydrate ($La(NO_3)_3.6H_2O$), 0.015g ($4.47x10^{-5}$ mole) Vanadium (III) acetylacetonate, 0.189g ($8.944x10^{-4}$ mole) Strontium nitrate $Sr(NO_3)_3$, 0.650g ($2.236\ x10^{-3}$ mole) Cobalt (II) nitrate hexahydrate and 0.939g ($4.47x10^{-3}$ mole) Citric acid monohydrate ($C_6H_8O_7.H_2O$) in distilled water, along with 1 mL ($1.72x10^{-2}$ mole) ethylene glycol and the mixture was heated and stirred constantly until the reaction was complete. The powders were then calcined at 1100˚C to obtain pure single-phase materials. Phase purity and crystal structure were determined by XRD.

3% (mole) Vanadium doped Lanthanum Strontium Cobalt Oxide ($La_{0.57}V_{0.03}Sr_{0.4}CoO_{3-\delta}$) (LV3SC): High-purity 0.554g ($1.27x10^{-3}$ mole) Lanthanum (III) nitrate hexahydrate ($La(NO_3)_3\ .\ 6H_2O$), 0.023g ($6.72x10^{-5}$ mole) Vanadium (III) acetylacetonate, 0.189g ($8.96\ x10^{-4}$ mole) Strontium nitrate $Sr(NO_3)_3$, 0.651g ($2.24\ x10^{-3}$ mole) Cobalt (II) nitrate hexahydrate and 0.941g ($4.48x10^{-3}$ mole) Citric acid monohydrate ($C_6H_8O_7.H_2O$) were used as starting materials. Then 1 mL ($1.72x10^{-2}$ mole) ethylene glycol ($C_2H_6O_2$) was added into the beaker after the mixture was dissolved. The

solution was stirred and the excess water evaporated on a hot plate at 115-120˚C until the mixture auto-ignited. The following resin was calcined and characterized by XRD.

4% (mole) Vanadium doped Lanthanum Strontium Cobalt Oxide ($La_{0.56}V_{0.04}Sr_{0.4}CoO_{3-\delta}$) (LV4SC): In a typical sol-gel synthesis of LV4SC, 0.545g ($1.26x10^{-3}$ mole) Lanthanum (III) nitrate hexahydrate ($La(NO_3)_3.6H_2O$), 0.031g ($9x10^{-5}$ mole) Vanadium (III) acetylacetonate, 0.190g ($9\ x10^{-4}$ mole) Strontium nitrate $Sr(NO_3)_3$, 0.654g ($2.25x10^{-3}$ mole) Cobalt (II) nitrate hexahydrate and 0.945g ($4.5x10^{-3}$ mole) Citric acid monohydrate ($C_6H_8O_7.H_2O$) were dissolved in 45 ml of distilled water. Then, 1 mL ($1.72x10^{-2}$ mole) ethylene glycol ($C_2H_6O_2$) was added to the solution to obtain a homogeneous gel. After stirring the solution on a hot plate, it became a stiff gel. The resulting gel was calcined at 1100˚C for 2h. Phase structures of the powder were determined using XRD.

5% (mole) Vanadium doped Lanthanum Strontium Cobalt Oxide ($La_{0.55}V_{0.05}Sr_{0.4}CoO_{3-\delta}$) (LV5SC): LV5SC cathode material was prepared by the conventional sol-gel method. 0.539g ($1.24x10^{-3}$ mole) Lanthanum (III) nitrate hexahydrate ($La(NO_3)_3.6H_2O$), 0.039g ($1.13x10^{-4}$ mole) Vanadium (III) acetylacetonate, 0.191g ($9.05\ x10^{-4}$ mole) Strontium nitrate $Sr(NO_3)_3$, 0.658g ($2.263\ x10^{-3}$ mole) Cobalt (II) nitrate hexahydrate, 0.951g ($4.52x10^{-3}$ mole) Citric acid monohydrate ($C_6H_8O_7.H_2O$) and 1 mL ($1.72x10^{-2}$ mole) ethylene glycol ($C_2H_6O_2$) were dissolved in 45 ml of distilled water. The resulting resin was calcined at 1100˚C for characterization analysis by XRD.

10% (mole) Vanadium doped Lanthanum Strontium Cobalt Oxide ($La_{0.5}V_{0.1}Sr_{0.4}CoO_{3-\delta}$) (LV10SC): 0.499g ($1.15x10^{-3}$ mole) Lanthanum (III) nitrate hexahydrate ($La(NO_3)_3.\ 6H_2O$), 0.0804g ($2.309x10^{-4}$ mole) Vanadium (III) acetylacetonate, 0.195g ($9.23x10^{-4}$ mole) Strontium nitrate $Sr(NO_3)_3$, 0.672g ($2.309x10^{-3}$ mole) Cobalt (II) nitrate hexahydrate and 0.970g ($4.62x10^{-3}$ mole) Citric acid monohydrate ($C_6H_8O_7.H_2O$) was dissolved in 45ml distilled water with magnetic stirring. Then 1 mL ($1.72x10^{-2}$ mole) ethylene glycol ($C_2H_6O_2$) was added into the beaker after the mixture was dissolved. With constant stirring, the temperature was kept around 115-120˚C and the viscous gel swelled with a rapid evolution of a large volume of gases to produce a

voluminous powder. The formed resin was calcined and the resulting powder was characterized by XRD.

Synthesis of $La_{0.6-x}V_xSr_{0.4}FeO_{3-\delta}$ (x = 0.01, 0.02, 0.03, 0.04, 0.05, 0.06, 0.07, 0.08, 0.09, 0.10): The below-mentioned developed cathode materials were abbreviated by according to the content ratio of cations for clarity in following.

1% (mole) Vanadium doped Lanthanum Strontium Iron Oxide ($La_{0.59}V_{0.01}Sr_{0.4}FeO_{3-\delta}$) (LV1SF): LV1SF samples were synthesized by mixing of 0.577g ($1.33x10^{-3}$ mole) Lanthanum (III) nitrate hexahydrate ($La(NO_3)_3.6H_2O$), 0.008g ($2.258x10^{-5}$ mole) Vanadium (III) acetylacetonate, 0.191g ($9.032\ x10^{-4}$ mole) Strontium nitrate $Sr(NO_3)_3$, 0.912g ($2.258\ x10^{-3}$ mole) Iron (III) nitrate nonahydrate, 0.867g ($4.516\ x10^{-4}$ mole) Citric acid monohydrate ($C_6H_8O_7.H_2O$) and 1 mL ($1.72x10^{-2}$ mole) ethylene glycol ($C_2H_6O_2$). The precursor solution was subsequently heated at 115-120˚C under stirring to form a viscous gel, and then the gel was baked at 1100˚C for 2h. The phase of samples was characterized with XRD.

2% (mole) Vanadium doped Lanthanum Strontium Iron Oxide ($La_{0.58}V_{0.02}Sr_{0.4}FeO_{3-\delta}$) (LV2SF): The chemicals used for preparing the resulting gel were 0.569g ($1.31x10^{-3}$ mole) Lanthanum (III) nitrate hexahydrate ($La(NO_3)_3.6H_2O$), 0.016g ($4.536x10^{-5}$ mole) Vanadium (III) acetylacetonate, 0.192g ($9.072\ x10^{-4}$ mole) Strontium nitrate $Sr(NO_3)_3$ and 0.916g ($2.268\ x10^{-3}$ mole) Iron (III) nitrate nonahydrate. The nitrates and acetates were dissolved in distilled water at 115-120˚C. 0.871g ($4.536x10^{-4}$ mole) Citric acid monohydrate ($C_6H_8O_7.H_2O$) and 1 mL ($1.72x10^{-2}$ mole) ethylene glycol ($C_2H_6O_2$) were used as polymerization and complexation agents, respectively. The subsequent formed gel was calcined and the phase purity of the powder was checked by X-Ray Diffraction.

3% (mole) Vanadium doped Lanthanum Strontium Iron Oxide ($La_{0.57}V_{0.03}Sr_{0.4}FeO_{3-\delta}$) (LV3SF): LV3SF powders were prepared by sol-gel method. 0.562g ($1.29x10^{-3}$ mole) Lanthanum (III) nitrate hexahydrate ($La(NO_3)_3.6H_2O$), 0.024g ($6.83x10^{-5}$ mole) Vanadium (III) acetylacetonate, 0.193g ($9.108\ x10^{-4}$ mole) Strontium nitrate $Sr(NO_3)_3$, 0.919g ($2.277\ x10^{-3}$ mole) Iron (III) nitrate nonahydrate, 0.875g

($4.554x10^{-4}$ mole) Citric acid monohydrate ($C_6H_8O_7.H_2O$) and 1 mL ($1.72x10^{-2}$ mole) ethylene glycol ($C_2H_6O_2$) were dissolved in 45 ml of distilled water with continuous stirring. The polymeric gel precursor was prepared by heating the stock solution at 115-120˚C. The LV3SF powders were prepared by calcining the precursors at 1100˚C for 2h. XRD spectra determined the crystal structure of the powder.

4% (mole) Vanadium doped Lanthanum Strontium Iron Oxide ($La_{0.56}V_{0.04}Sr_{0.4}FeO_{3-\delta}$) (LV4SF): 0.554g ($1.28x10^{-3}$ mole) Lanthanum (III) nitrate hexahydrate ($La(NO_3)_3 . 6H_2O$), 0.032g ($9.14x10^{-5}$ mole) Vanadium (III) acetylacetonate, 0.193g ($9.14 x10^{-4}$ mole) Strontium nitrate $Sr(NO_3)_3$, 0.923g ($2.286x10^{-3}$ mole) Iron (III) nitrate nonahydrate and 0.878g ($4.57x10^{-4}$ mole) Citric acid monohydrate ($C_6H_8O_7.H_2O$) was dissolved in 45ml distilled water with magnetic stirring. Then 1 mL ($1.72x10^{-2}$ mole) ethylene glycol ($C_2H_6O_2$) was added into the beaker after the mixture was dissolved. With constant stirring, the temperature was kept around 115-120˚C. The viscous gel swelled with a rapid evolution of a large volume of gases to produce a voluminous powder, which was calcined at 1100˚C for 2h. The crystal phases of the sintered specimens were analyzed by X-Ray diffraction.

5% (mole) Vanadium doped Lanthanum Strontium Iron Oxide ($La_{0.55}V_{0.05}Sr_{0.4}FeO_{3-\delta}$) (LV5SF): The LV5SF samples were synthesized via sol-gel process. 0.964g ($4.59x10^{-3}$ mole) Citric acid monohydrate ($C_6H_8O_7.H_2O$) and 1ml ($1.72x10^{-2}$ mole) ethylene glycol ($C_2H_6O_2$) were used as parallel complexing agents. 0.546g ($1.26x10^{-3}$ mole) Lanthanum (III) nitrate hexahydrate ($La(NO_3)_3.6H_2O$), 0.039g ($1.147x10^{-4}$ mole) Vanadium (III) acetylacetonate, 0.194g ($9.18 x10^{-4}$ mole) Strontium nitrate $Sr(NO_3)_3$ and 0.927g ($2.295x10^{-3}$ mole) Iron (III) nitrate nonahydrate were used as starting materials. After converting the sample into a viscous gel under heating and stirring conditions, the viscous gel was dried to form a powder precursor, which was calcined at 1100˚C for 2h. Phase development was determined by XRD analysis.

6% (mole) Vanadium doped Lanthanum Strontium Iron Oxide ($La_{0.54}V_{0.06}Sr_{0.4}FeO_{3-\delta}$) (LV6SF): The cathode powders of LV6SF were prepared by mixing of 0.538g ($1.24x10^{-3}$ mole) Lanthanum (III) nitrate hexahydrate ($La(NO_3)_3 . 6H_2O$), 0.048g ($1.38x10^{-4}$ mole) Vanadium (III) acetylacetonate, 0.195g ($9.2x10^{-4}$ mole)

Strontium nitrate $Sr(NO_3)_3$, 0.929g (2.30×10^{-3} mole) Iron (III) nitrate nonahydrate and 0.966g (4.6×10^{-3} mole) Citric acid monohydrate ($C_6H_8O_7.H_2O$) in distilled water, along with 1 mL (1.72×10^{-2} mole) ethylene glycol and the mixture was heated and stirred constantly until the reaction was complete. The powders were then calcined at 1100°C to obtain pure single-phase materials. Phase purity and crystal structure were determined by XRD.

7% (mole) Vanadium doped Lanthanum Strontium Iron Oxide ($La_{0.53}V_{0.07}Sr_{0.4}FeO_{3-\delta}$) (LV7SF): 0.531g ($1.22 \times 10^{-3}$ mole) Lanthanum (III) nitrate hexahydrate ($La(NO_3)_3 . 6H_2O$), 0.056g (1.62×10^{-4} mole) Vanadium (III) acetylacetonate, 0.195g (9.24×10^{-4} mole) Strontium nitrate $Sr(NO_3)_3$, 0.933g (2.31×10^{-3} mole) Iron (III) nitrate nonahydrate and 0.971g (4.62×10^{-3} mole) Citric acid monohydrate ($C_6H_8O_7.H_2O$) were used as starting materials. Then 1 mL (1.72×10^{-2} mole) ethylene glycol ($C_2H_6O_2$) was added into the beaker after the mixture was dissolved. The solution was stirred and the excess water evaporated on a hot plate at 115-120°C until the mixture auto-ignited. The following resin was calcined and characterized by XRD.

8% (mole) Vanadium doped Lanthanum Strontium Iron Oxide ($La_{0.52}V_{0.08}Sr_{0.4}FeO_{3-\delta}$) (LV8SF): In a typical sol-gel synthesis of LV8SF, 0.523g (1.21×10^{-3} mole) Lanthanum (III) nitrate hexahydrate ($La(NO_3)_3.6H_2O$), 0.065g (1.86×10^{-4} mole) Vanadium (III) acetylacetonate, 0.196g (9.29×10^{-4} mole) Strontium nitrate $Sr(NO_3)_3$, 0.938g (2.323×10^{-3} mole) Iron (III) nitrate nonahydrate and 0.976g (4.65×10^{-3} mole) Citric acid monohydrate ($C_6H_8O_7.H_2O$) were dissolved in 45 ml of distilled water. Then, 1 mL (1.72×10^{-2} mole) ethylene glycol ($C_2H_6O_2$) was added to the solution to obtain a homogeneous gel. After stirring the solution on a hot plate, it became a stiff gel. The resulting gel was calcined at 1100°C for 2h. Phase structures of the powder were determined using XRD.

9% (mole) Vanadium doped Lanthanum Strontium Iron Oxide ($La_{0.51}V_{0.09}Sr_{0.4}FeO_{3-\delta}$) (LV9SF): LV9SF cathode material was prepared by the conventional sol-gel method. 0.515g (1.18×10^{-3} mole) Lanthanum (III) nitrate hexahydrate ($La(NO_3)_3.6H_2O$), 0.073g (2.09×10^{-4} mole) Vanadium (III) acetylacetonate, 0.197g (9.32×10^{-4} mole) Strontium nitrate $Sr(NO_3)_3$, 0.941g (2.33×10^{-3} mole) Iron (III)

nitrate nonahydrate, 0.979g ($4.66x10^{-3}$ mole)Citric acid monohydrate ($C_6H_8O_7.H_2O$) and 1 mL ($1.72x10^{-2}$ mole) ethylene glycol ($C_2H_6O_2$) were dissolved in 45 ml of distilled water. The resulting resin was calcined at 1100˚C for characterization analysis by XRD.

10% (mole) Vanadium doped Lanthanum Strontium Iron Oxide ($La_{0.5}V_{0.1}Sr_{0.4}FeO_{3-\delta}$) (LV10SF): 0.507g ($1.17x10^{-3}$ mole) Lanthanum (III) nitrate hexahydrate ($La(NO_3)_3.6H_2O$), 0.081g ($2.34x10^{-4}$ mole) Vanadium (III) acetylacetonate, 0.198g ($9.37x10^{-4}$ mole) Strontium nitrate $Sr(NO_3)_3$, 0.946g ($2.34x10^{-3}$ mole) Iron (III) nitrate nonahydrate, 0.985g ($4.68\ x10^{-3}$ mole) Citric acid monohydrate ($C_6H_8O_7.H_2O$) and 1 mL ($1.72x10^{-2}$ mole) ethylene glycol ($C_2H_6O_2$) were used as starting materials. These metal nitrates and acetates were dissolved in distilled water and stirred on a hot plate at 115-120˚C to obtain a stiff gel. The gel was calcined in order to achieve a powder precursor. The phase formation of LV05SF was examined by XRD.

Synthesis of $La_{0.6-x}V_xSr_{0.4}CrO_{3-\delta}$ (x = 0.005, 0.01, 0.02, 0.03, 0.04, 0.10): The herein below developed cathode materials were abridged by according to the content ratio of cations for lucidity in following.

0.5% (mole) Vanadium doped Lanthanum Strontium Chromium Oxide ($La_{0.595}V_{0.005}Sr_{0.4}CrO_{3-\delta}$) (LV05SCr): 0.591g ($1.36x10^{-3}$ mole) Lanthanum (III) nitrate hexahydrate ($La(NO_3)_3.6H_2O$), 0.004g ($1.15x10^{-5}$ mole) Vanadium (III) acetylacetonate, 0.194g ($9.176x10^{-4}$ mole) Strontium nitrate $Sr(NO_3)_3$, 0.918g ($2.294x10^{-3}$ mole) Chromium (III) nitrate nonahydrate, 0.881g ($4.58x10^{-3}$ mole) Citric acid monohydrate ($C_6H_8O_7.H_2O$) and 1 mL ($1.72x10^{-2}$ mole) ethylene glycol ($C_2H_6O_2$) were used as starting materials. These metal nitrates and acetates were dissolved in distilled water and stirred on a hot plate at 115-120˚C to obtain a stiff gel. The gel was calcined in order to achieve a powder precursor. The phase formation of LV05SCr was examined by XRD.

1% (mole) Vanadium doped Lanthanum Strontium Chromium Oxide ($La_{0.59}V_{0.01}Sr_{0.4}CrO_{3-\delta}$) (LV1SCr): LV1SCr samples were synthesized by mixing of 0.587g ($1.35x10^{-3}$ mole) Lanthanum (III) nitrate hexahydrate ($La(NO_3)_3.6H_2O$), 0.008g ($2.298x10^{-5}$ mole) Vanadium (III) acetylacetonate, 0.194g ($9.192x10^{-4}$ mole) Strontium nitrate $Sr(NO_3)_3$, 0.919g ($2.298x10^{-3}$ mole) Chromium (III) nitrate nonahydrate, 0.883g

($4.59x10^{-3}$ mole) Citric acid monohydrate ($C_6H_8O_7.H_2O$) and 1 mL ($1.72x10^{-2}$ mole) ethylene glycol ($C_2H_6O_2$). The precursor solution was subsequently heated at 115-120˚C under stirring to form a viscous gel, and then the gel was baked at 1100˚C for 2h. The phase of samples was characterized with XRD.

2% (mole) Vanadium doped Lanthanum Strontium Chromium Oxide ($La_{0.58}V_{0.02}Sr_{0.4}CrO_{3-\delta}$) (LV2SCr): The chemicals used for preparing the resulting gel were 0.579g ($1.34x10^{-3}$ mole) Lanthanum (III) nitrate hexahydrate ($La(NO_3)_3.6H_2O$), 0.016g ($4.62x10^{-5}$ mole) Vanadium (III) acetylacetonate, 0.195g ($9.23x10^{-4}$ mole) Strontium nitrate $Sr(NO_3)_3$ and 0.923g ($2.308x10^{-3}$ mole) Chromium (III) nitrate nonahydrate. The nitrates and acetates were dissolved in distilled water at 115-120˚C. 0.887g ($4.62\ x10^{-3}$ mole) Citric acid monohydrate ($C_6H_8O_7.H_2O$) and 1 mL ($1.72x10^{-2}$ mole) ethylene glycol ($C_2H_6O_2$) were used as polymerization and complexation agents, respectively. The subsequent formed gel was calcined and the phase purity of the powder was checked by X-Ray Diffraction.

3% (mole) Vanadium doped Lanthanum Strontium Chromium Oxide ($La_{0.57}V_{0.03}Sr_{0.4}CrO_{3-\delta}$) (LV3SCr): LV3SCr powders were prepared by sol-gel method. 0.572g ($1.32x10^{-3}$ mole) Lanthanum (III) nitrate hexahydrate ($La(NO_3)_3.6H_2O$), 0.024g ($6.95x10^{-5}$ mole) Vanadium (III) acetylacetonate, 0.196g ($9.26x10^{-4}$ mole) Strontium nitrate $Sr(NO_3)_3$, 0.927g ($2.317\ x10^{-3}$ mole) Chromium (III) nitrate nonahydrate, 0.890g ($4.63x10^{-3}$ mole) Citric acid monohydrate ($C_6H_8O_7.H_2O$) and 1 mL ($1.72x10^{-2}$ mole) ethylene glycol ($C_2H_6O_2$) were dissolved in 45 ml of distilled water with continuous stirring. The polymeric gel precursor was prepared by heating the stock solution at 115-120˚C. The LV3SCr powders were prepared by calcining the precursors at 1100˚C for 2h. XRD spectra determined the crystal structure of the powder.

4% (mole) Vanadium doped Lanthanum Strontium Chromium Oxide ($La_{0.56}V_{0.04}Sr_{0.4}CrO_{3-\delta}$) (LV4SCr): LV4SCr samples were prepared by a sol–gel technique with 0.894g ($4.65x10^{-3}$ mole) Citric acid monohydrate ($C_6H_8O_7.H_2O$) and 1 mL ($1.72x10^{-2}$ mole) ethylene glycol ($C_2H_6O_2$). 0.564g ($1.30x10^{-3}$ mole) Lanthanum (III) nitrate hexahydrate ($La(NO_3)_3.6H_2O$), 0.032g ($9.308x10^{-5}$ mole) Vanadium (III) acetylacetonate, 0.197g ($9.308x10^{-4}$ mole) Strontium nitrate $Sr(NO_3)_3$, 0.931g ($2.327x10^{-3}$ mole)

Chromium (III) nitrate nonahydrate were dissolved in distilled water. The above solutions were mixed together at room temperature under stirring to achieve a clear solution. The obtained solution was stirred at 115-120°C on a heating plate till a gel was formed. The gel was kept in an oven at 1100°C. The phase of the samples was characterized with X-Ray diffraction.

10% (mole) Vanadium doped Lanthanum Strontium Chromium Oxide ($La_{0.5}V_{0.1}Sr_{0.4}CrO_{3-\delta}$) (LV10SCr): 0.516g ($1.19x10^{-3}$ mole) Lanthanum (III) nitrate hexahydrate ($La(NO_3)_3.6H_2O$), 0.083g ($2.38x10^{-4}$ mole) Vanadium (III) acetylacetonate, 0.202g ($9.54x10^{-4}$ mole) Strontium nitrate $Sr(NO_3)_3$, 0.954g ($2.385x10^{-3}$ mole) Chromium (III) nitrate nonahydrate, 1.002g ($4.77x10^{-3}$ mole) Citric acid monohydrate ($C_6H_8O_7.H_2O$) and 1 mL ($1.72x10^{-2}$ mole) ethylene glycol ($C_2H_6O_2$) were used as starting materials. These metal nitrates and acetates were dissolved in distilled water and stirred on a hot plate at 115-120˚C to obtain a stiff gel. The gel was calcined in order to achieve a powder precursor. The phase formation of LV05SCr was examined by XRD.

Synthesis of $La_{0.6-x}V_xSr_{0.4}MnO_{3-\delta}$ (x = 0.005, 0.01, 0.02, 0.03, 0.04, 0.10): The developed cathode materials featured below were abridged by according to the content ratio of cations for clarity in following.

0.5% (mole) Vanadium doped Lanthanum Strontium Magnesium Oxide ($La_{0.595}V_{0.005}Sr_{0.4}MnO_{3-\delta}$) (LV05SM): Phase-pure LV05SM powders were synthesized by a sol–gel method in which 0.583g ($1.35x10^{-3}$ mole) Lanthanum (III) nitrate hexahydrate ($La(NO_3)_3.6H_2O$), 0.004g ($1.132x10^{-5}$ mole) Vanadium (III) acetylacetonate, 0.192g ($9.056x10^{-4}$ mole) Strontium nitrate $Sr(NO_3)_3$, 0.650g ($2.264x10^{-3}$ mole) Manganese (II) nitrate hexahydrate were dissolved in distilled water, 0.869g ($4.53x10^{-3}$ mole) Citric acid monohydrate ($C_6H_8O_7.H_2O$) and 1 mL ($1.72x10^{-2}$ mole) ethylene glycol ($C_2H_6O_2$) served as complexing agents. Mild heating induced gelation of the solution, and the resulting gel was held at 1100˚C for 2 h. The crystal structure of the powder was analyzed by X-Ray diffraction.

1% (mole) Vanadium doped Lanthanum Strontium Magnesium Oxide ($La_{0.59}V_{0.01}Sr_{0.4}MnO_{3-\delta}$) (LV1SM): The starting materials of 0.579g ($1.34x10^{-3}$ mole)

Lanthanum (III) nitrate hexahydrate ($La(NO_3)_3.6H_2O$), 0.008g ($2.268x10^{-5}$ mole) Vanadium (III) acetylacetonate, 0.192g ($9.072x10^{-4}$ mole) Strontium nitrate $Sr(NO_3)_3$, 0.651g ($2.268x10^{-3}$ mole) Manganese (II) nitrate hexahydrate were dissolved in distilled water to form an aqueous solution, which mixed with 0.871g ($4.536\ x10^{-3}$ mole) Citric acid monohydrate ($C_6H_8O_7.H_2O$) and 1 mL ($1.72x10^{-2}$ mole) ethylene glycol ($C_2H_6O_2$) and the mixture was stirred further on a magnetic stirrer. Then the resulting gel was carried out combustion on a hot plate in the fume hood. Then, the formed gel was calcined in a high-temperature furnace at 1100˚C for 2 h to form the black powder. Phase structures of the as-synthesized powders were characterized by X-Ray diffraction measurement.

2% (mole) Vanadium doped Lanthanum Strontium Magnesium Oxide ($La_{0.58}V_{0.02}Sr_{0.4}MnO_{3-\delta}$) (LV2SM): 0.572g ($1.32x10^{-3}$ mole) Lanthanum (III) nitrate hexahydrate ($La(NO_3)_3.6H_2O$), 0.016g ($4.55x10^{-5}$ mole) Vanadium (III) acetylacetonate, 0.193g ($9.108x10^{-4}$ mole) Strontium nitrate $Sr(NO_3)_3$, 0.653g ($2.277x10^{-3}$ mole) Manganese (II) nitrate hexahydrate and 0.874g ($4.55\ x10^{-3}$ mole) Citric acid monohydrate ($C_6H_8O_7.H_2O$) were dissolved in distilled water and later, a suitable volume of ethylene glycol ($C_2H_6O_2$) was added. The gel obtained was dried to obtain a resin, and this resin was then fired at 1100 °C in an oven in air for 2 h. The obtained powders were structurally characterized using XRD.

3% (mole) Vanadium doped Lanthanum Strontium Magnesium Oxide ($La_{0.57}V_{0.03}Sr_{0.4}MnO_{3-\delta}$) (LV3SM): The solution of metal salts was prepared from 0.564g ($1.30x10^{-3}$ mole) Lanthanum (III) nitrate hexahydrate ($La(NO_3)_3.6H_2O$), 0.024g ($6.858x10^{-5}$ mole) Vanadium (III) acetylacetonate, 0193g ($9.14x10^{-4}$ mole) Strontium nitrate $Sr(NO_3)_3$, 0.656g ($2.286x10^{-3}$ mole) Manganese (II) nitrate hexahydrate were dissolved in distilled water, 0.878g ($4.57\ x10^{-3}$ mole) Citric acid monohydrate ($C_6H_8O_7.H_2O$) and 1 mL ($1.72x10^{-2}$ mole) ethylene glycol ($C_2H_6O_2$). The solution was heated to 115-120°C on a heating plate during approximately 3 h to obtain stiff gel and the formed gel was calcined in high temperature oven. The crystalline phases present were investigated by XRD.

4% (mole) Vanadium doped Lanthanum Strontium Magnesium Oxide ($La_{0.56}V_{0.04}Sr_{0.4}MnO_{3-\delta}$) (LV4SM): The LV4SM aqueous solution was prepared by dissolving 0.556g ($1.28x10^{-3}$ mole) Lanthanum (III) nitrate hexahydrate ($La(NO_3)_3.6H_2O$), 0.032g ($9.18x10^{-5}$ mole) Vanadium (III) acetylacetonate, 0.194g ($9.18x10^{-4}$ mole) Strontium nitrate $Sr(NO_3)_3$, 0.658g ($2.295\ x10^{-3}$ mole) Manganese (II) nitrate hexahydrate, 0.882g ($4.59x10^{-3}$ mole) Citric acid monohydrate ($C_6H_8O_7.H_2O$) and 1 mL ($1.72x10^{-2}$ mole) ethylene glycol ($C_2H_6O_2$) in distilled water at 115-120˚C. There resulting gel was calcined and the phase purity was checked by XRD.

10% (mole) Vanadium doped Lanthanum Strontium Magnesium Oxide ($La_{0.5}V_{0.1}Sr_{0.4}MnO_{3-\delta}$) (LV10SM): The starting materials of 0.509g ($1.17x10^{-3}$ mole) Lanthanum (III) nitrate hexahydrate ($La(NO_3)_3.6H_2O$), 0.082g ($2.35x10^{-4}$ mole) Vanadium (III) acetylacetonate, 0.199g ($9.412x10^{-4}$ mole) Strontium nitrate $Sr(NO_3)_3$, 0.675g ($2.353x10^{-3}$ mole) Manganese (II) nitrate hexahydrate were dissolved in distilled water to form an aqueous solution, which mixed with 0.989g ($4.706x10^{-3}$ mole) Citric acid monohydrate ($C_6H_8O_7.H_2O$) and 1 mL ($1.72x10^{-2}$ mole) ethylene glycol ($C_2H_6O_2$) and the mixture was stirred further on a magnetic stirrer. Then the resulting gel was carried out combustion on a hot plate in the fume hood. Then, the formed gel was calcined in a high-temperature furnace at 1100˚C for 2 h to form the black powder. Phase structures of the as-synthesized powders were characterized by X-Ray diffraction measurement.

Synthesis of $La_{0.6-x}V_xSr_{0.4}TiO_{3-\delta}$ (x = 0.005, 0.01, 0.02, 0.03, 0.04, 0.10): The under mentioned cathode materials were named by according to the content ratio of cations for clarity in following.

0.5% (mole) Vanadium doped Lanthanum Strontium Titanium Oxide ($La_{0.595}V_{0.005}Sr_{0.4}TiO_{3-\delta}$) (LV05ST): Briefly, 0.602g ($1.39x10^{-3}$ mole) Lanthanum (III) nitrate hexahydrate ($La(NO_3)_3.6H_2O$), 0.004g ($1.169x10^{-5}$ mole) Vanadium (III) acetylacetonate, 0.198g ($9.35x10^{-4}$ mole) Strontium nitrate $Sr(NO_3)_3$, 0.828g ($2.338x10^{-3}$ mole) Potassium bis(oxalate)-oxotitanate (IV) dihydrate $K_2[TiO(C_2O_4)_2].2H_2O$, 0.983g ($4.67x10^{-3}$ mole) Citric acid monohydrate ($C_6H_8O_7.H_2O$) and 1 mL ($1.72x10^{-2}$ mole) ethylene glycol ($C_2H_6O_2$) were firstly dissolved into distilled water. The mixed solution

was heated at 200°C in sequence to obtain a dark dry foam structure. The precursor was decomposed on a hot plate, followed by calcinations at 1100°C for 2 h in air to yield the desired powders. X-Ray powder diffraction patterns were recorded for the powder.

1% (mole) Vanadium doped Lanthanum Strontium Titanium Oxide ($La_{0.59}V_{0.01}Sr_{0.4}TiO_{3-\delta}$) (LV1ST): In a typical sol−gel synthesis of LV1ST, 0.598g ($1.38x10^{-3}$ mole) Lanthanum (III) nitrate hexahydrate ($La(NO_3)_3.6H_2O$), 0.00816g ($2.34x10^{-5}$ mole) Vanadium (III) acetylacetonate, 0.198g ($9.37x10^{-4}$ mole) Strontium nitrate $Sr(NO_3)_3$, 0.829g ($2.343x10^{-3}$ mole) Potassium bis(oxalate)-oxotitanate (IV) dihydrate $K_2[TiO(C_2O_4)_2].2H_2O$, 0.985g ($4.68x10^{-3}$ mole) Citric acid monohydrate ($C_6H_8O_7.H_2O$) and 1 mL ($1.72x10^{-2}$ mole) ethylene glycol ($C_2H_6O_2$) were dissolved in 45 mL of distilled water. After stirring the solution for 3 h at 115°C on a hot plate, the solution became a stiff gel which was calcined at 1100 °C in air. X-Ray diffraction was used to confirm the crystal structure of the LV1ST powders.

2% (mole) Vanadium doped Lanthanum Strontium Titanium Oxide ($La_{0.58}V_{0.02}Sr_{0.4}TiO_{3-\delta}$) (LV2ST): Lanthanum Strontium Titanium Oxide doped with Vanadium was synthesized by a sol-gel using 0.591g ($1.36x10^{-3}$ mole) Lanthanum (III) nitrate hexahydrate ($La(NO_3)_3.6H_2O$), 0.016g ($4.7x10^{-5}$ mole) Vanadium (III) acetylacetonate, 0.199g ($9.4x10^{-4}$ mole) Strontium nitrate $Sr(NO_3)_3$, 0.833g ($2.353x10^{-3}$ mole) Potassium bis(oxalate)-oxotitanate (IV) dihydrate $K_2[TiO(C_2O_4)_2].2H_2O$, 0.989g ($4.7x10^{-3}$ mole) Citric acid monohydrate ($C_6H_8O_7.H_2O$) and 1 mL ($1.72x10^{-2}$ mole) ethylene glycol ($C_2H_6O_2$). The nitrates were mixed in aforementioned proportions, and citric acid was added to the solution in equivalent molar ratios to the amount of the total metal cations. The mixed solution was heated on a hotplate at 120 °C to form a gel, and then the gel was placed in a high temperature oven to be ignited and combusted. XRD was carried out to examine the phase formation of the powders.

3% (mole) Vanadium doped Lanthanum Strontium Titanium Oxide ($La_{0.57}V_{0.03}Sr_{0.4}TiO_{3-\delta}$) (LV3ST): 0.583g ($1.35x10^{-3}$ mole) Lanthanum (III) nitrate hexahydrate ($La(NO_3)_3.6H_2O$), 0.025g ($7.089x10^{-5}$ mole) Vanadium (III) acetylacetonate, 0.200g ($9.45x10^{-4}$ mole) Strontium nitrate $Sr(NO_3)_3$, 0.837g ($2.363x10^{-3}$ mole) Potassium bis(oxalate)-oxotitanate (IV) dihydrate $K_2[TiO(C_2O_4)_2].2H_2O$ were dissolved in deionized

water . The analytical reagent of 0.993g ($4.72x10^{-3}$ mole) Citric acid monohydrate ($C_6H_8O_7.H_2O$) and 1 mL ($1.72x10^{-2}$ mole) ethylene glycol ($C_2H_6O_2$) were then added to the above solution with constant stirring. A transparent sol was formed via continuous heating at 120 °C and then heated until it was ignited to form precursor powder. The precursor powder was calcined for 2 h at 1100 °C in air. The phase composition was characterized by X-Ray diffraction.

4% (mole) Vanadium doped Lanthanum Strontium Titanium Oxide ($La_{0.56}V_{0.04}Sr_{0.4}TiO_{3-\delta}$) (LV4ST): $La_{0.56}V_{0.04}Sr_{0.4}TiO_{3-\delta}$, which is noted as LV4ST, was prepared by the modified sol–gel method. The starting reagents are 0.575g ($1.33x10^{-3}$ mole) Lanthanum (III) nitrate hexahydrate ($La(NO_3)_3.6H_2O$), 0.033g ($9.49x10^{-5}$ mole) Vanadium (III) acetylacetonate, 0.201g ($9.49x10^{-4}$ mole) Strontium nitrate $Sr(NO_3)_3$, 0.840g ($2.373x10^{-3}$ mole) Potassium bis(oxalate)-oxotitanate (IV) dihydrate $K_2[TiO(C_2O_4)_2].2H_2O$, 0.997g ($4.75x10^{-3}$ mole) Citric acid monohydrate ($C_6H_8O_7.H_2O$) and 1 mL ($1.72x10^{-2}$ mole) ethylene glycol ($C_2H_6O_2$). Under stirring and heating, a clear viscous gel was obtained and the gel was calcined at 1100˚C. The crystal structure of synthesized powders was investigated by X-Ray diffraction.

10% (mole) Vanadium doped Lanthanum Strontium Titanium Oxide ($La_{0.5}V_{0.1}Sr_{0.4}TiO_{3-\delta}$) (LV10ST): Lanthanum Strontium Titanium Oxide doped with Vanadium was synthesized by a sol-gel using 0.527g ($1.21x10^{-3}$ mole) Lanthanum (III) nitrate hexahydrate ($La(NO_3)_3.6H_2O$), 0.085g ($2.43x10^{-4}$ mole) Vanadium (III) acetylacetonate, 0.206g ($9.73x10^{-4}$ mole) Strontium nitrate $Sr(NO_3)_3$, 0.861g ($2.433x10^{-3}$ mole) Potassium bis(oxalate)-oxotitanate (IV) dihydrate $K_2[TiO(C_2O_4)_2].2H_2O$, 1.022g ($4.86x10^{-3}$ mole) Citric acid monohydrate ($C_6H_8O_7.H_2O$) and 1 mL ($1.72x10^{-2}$ mole) ethylene glycol ($C_2H_6O_2$). The nitrates were mixed in aforementioned proportions, and citric acid was added to the solution in equivalent molar ratios to the amount of the total metal cations. The mixed solution was heated on a hotplate at 120 °C to form a gel, and then the gel was placed in a high temperature oven to be ignited and combusted. XRD was carried out to examine the phase formation of the powders.

Synthesis of $La_{0.6-x}Gd_xSr_{0.4}CoO_{3-\delta}$ (x = 0.1): The developed cathode material featured below was abridged by according to the content ratio of cations for lucidity in following.

10% (mole) Gadolinium doped Lanthanum Strontium Cobalt Oxide ($La_{0.5}Gd_{0.1}Sr_{0.4}CoO_{3-\delta}$) (LG10SC): The initial reagents La, Gd, Sr and Co in the form of nitrates were dissolved in distilled water separately in the amount of 0.476 g (1.1 $x10^{-3}$ mole) Lanthanum (III) nitrate hexahydrate ($La(NO_3)_3.6H_2O$), 0.099 g (2.19 $x10^{-4}$ mole) Gadolinium (III) nitrate hexahydrate ($Gd(NO_3)_3.6H_2O$), 0.186 g (8.78 $x10^{-4}$ mole) Strontium nitrate $Sr(NO_3)_3$, 0.640 g (2.19 $x10^{-3}$ mole) Cobalt (II) nitrate hexahydrate. All these solutions were then mixed with 0.925 g (4.40 $x10^{-3}$ mole) Citric acid monohydrate ($C_6H_8O_7.H_2O$) and 1 mL (1.72$x10^{-2}$ mole) ethylene glycol ($C_2H_6O_2$). Later, the homogeneous solution was heated while stirring until the formation of stiff gel. The gel was ignited at 120 °C to yield precursor powder. The powder, thus obtained, was calcined at 1100°C for 2 h. All the sintered samples were characterized by X-Ray diffraction.

Synthesis of $La_{1-x}Sr_xVO_{3-\delta}$ (x = 0.4): The under mentioned cathode material was named by according to the content ratio of cations for clarity in following.

40% (mole) Strontium doped Lanthanum Vanadium Oxide ($La_{0.6}Sr_{0.4}VO_{3-\delta}$) (LS4V): The solution of metal salts was prepared from 1.793g (4.14$x10^{-3}$ mole) Lanthanum (III) nitrate hexahydrate ($La(NO_3)_3.6H_2O$), 2.403g (6.90$x10^{-3}$ mole) Vanadium (III) acetylacetonate and 0.584g (2.76$x10^{-3}$ mole) Strontium nitrate $Sr(NO_3)_3$ were dissolved in distilled water, 2.651g (0.0138 mole) Citric acid monohydrate ($C_6H_8O_7.H_2O$) and 1 mL (1.72$x10^{-2}$ mole) ethylene glycol ($C_2H_6O_2$). The solution was heated to 115-120°C on a heating plate during approximately 3 h to obtain stiff gel and the formed gel was calcined in high temperature oven. The crystalline phases present were investigated by XRD.

2.2. Rectangular Bar Preparation for Four-Probe Conductivity Measurements

The conductivity is a significant element that affects the character of the cathode materials in SOFCs. This property includes electronic and ionic contributions due to the presence of charge carriers and oxygen vacancies, respectively. Nevertheless, it is recognized that the ionic conductivity contribution in perovskite oxides is small compared to the overall conductivity [51]; therefore, the obtained experimental values are just for the electronic conductivity.

For electrical conductivity measurements, the as-synthesized powders were pressed into rectangular bars with nominal dimensions of 20 mm x 5 mm x 2 mm. These were then sintered at 900˚C for 2h with a ramp rate of 0.5 $^{o}C.min^{-1}$. Electrical conductivity measurements were performed using a DC four-probe method over the temperature range from 400 to 800˚C. An interval of 50 ˚C for every test with the same stabilization time was used. Gold conductor paste (Heraeus) was painted onto the edges of the sample to form a current and voltage electrodes. Four gold wires (0.25mm in diameter, Alfa Aesar) were attached to the electrodes using gold conductor paste, of which two acted as current contacts and the remaining wires as voltage contacts with ensuring a homogeneous current flow. The electrical conductivity (σ) was determined from a set of I – V values by taking $\sigma=1/\rho=L/A\times dI/dV$, where L is the distance between voltage contacts, A is the sample cross-section and dI/dV is the internal resistance. A current of 1 – 2 mA was applied to the two current wires and the voltage was recorded on the two voltage wires using GAMRY Interface 1000 Potentiostat/ Galvanostat.

2.3. Symmetric Cell Production for Electrochemical Impedance Analysis

The symmetric cell configuration was chosen to study the cathode processes as the data interpretation is simpler compared to a full SOFC analysis. The electrochemical characterization of the cathode material synthesized was performed by means of impedance spectroscopy using a half-cell configuration, being necessary for construction of symmetrical cells with electrode/electrolyte/electrode. The symmetrical cells based on YSZ (Fuel cell materials) and GDC (Sigma Aldrich) were fabricated as follows. The electrolyte pellets were prepared by pressing commercial powders in a cylindrical stainless steel mold (5mm in diameter) with a uniaxial dry press at a pressure of 400Mpa for

10mins. After that, the prepared electrolyte disks were initially baked at 400 ˚C for 2h and followed by sintering at 1300 ˚C for 2h. For symmetrical cells, cathode samples were mixed thoroughly with organic binder to make the cathode slurry, the paste obtained was painted with a paintbrush on both positions of the pellets (having a diameter of 5 mm and a thickness of about 0.5 mm) which were then dried at 150 ˚C for 1 h and calcined at 1300 ˚C for 1h in air to form porous electrodes well adhered to the electrolytes. The final active area of each cathode was about 0.04 cm^2. Finally, the surface of the pellets was coated with gold paint as collector load. The symmetrical cells were assembled into a lab-designed device that allows performing the experiments in different atmospheres. To determine the resistance of the various cathode processes, the manufactured symmetric cells were characterized by Electrochemical Impedance Spectroscopy (EIS) measurements in ambient air from 400 to 800 ˚C with an increment of 50 ˚C. The oxygen partial pressure (PO_2) around the cell during the measurements was maintained using electronic mass flow controllers and Nitrogen was used as the carrier gas. Impedance spectra were measured in the frequency range of 0.1 Hz to 1 MHz with 10 mV amplitude of the AC signal. The spectra were analyzed using GAMRY Interface 1000 Potentiostat/ Galvanostat, which was interfaced with a computer-controlled program for data acquisition.

2.4. Tape Casting and Screen-Printing Techniques for Intermediate-Temperature SOFC Material Preparation

Tape casting is a well-designed technique for the manufacturing flat sheets of ceramics with thickness in the range of 10 μm - 500 μm [52]. This technique is generally applied to the production of dense materials but recently it has been commonly utilized also for the production of porous ceramic materials for air separations [53], sensors [54] and various components for planar SOFC applications [55]. This ceramic process is a low cost procedure and easily scalable and also provides fabrication of a wide variety of fuel cell components with significant control on morphologies from highly porous to fully dense microstructures like electrodes and electrolytes.

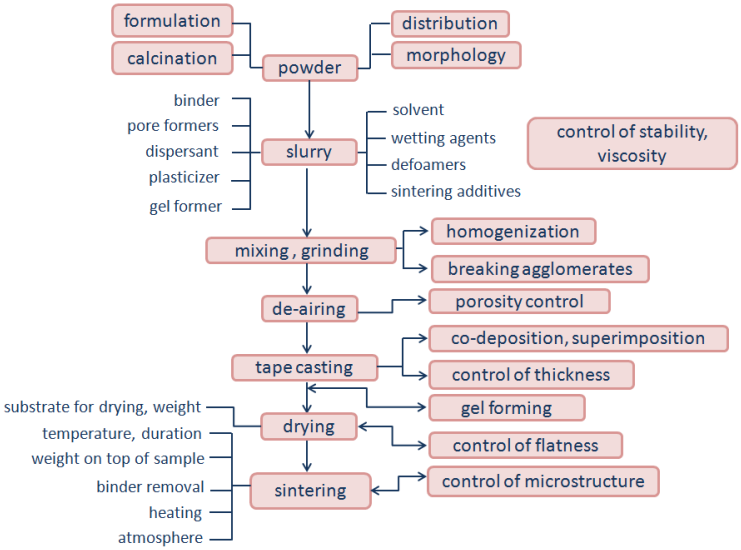

Figure 2.3. Schematic view for tape-casting process.

As shown in Figure 2.3, the whole process assembles sequential steps: the first and the most critical is the modification of the slurry formulation with powder on respect, which is already formulated, calcined and finally meshed to have convenient phase content, grain size distribution and morphology. Organic and/or inorganic additives are added to the powder to form the slurry. The slurry is then mixed and grinded by ball-milling to establish homogenization and destruction of agglomerates. After mixing, the slurry is de-aired under vacuum depending on which level of porosity is desired at the end of the process. The slurry is then ready for the casting and the gap between the blades of the "doctor-blade" defines the wet thickness of the tapes being cast (Figure 2.4).

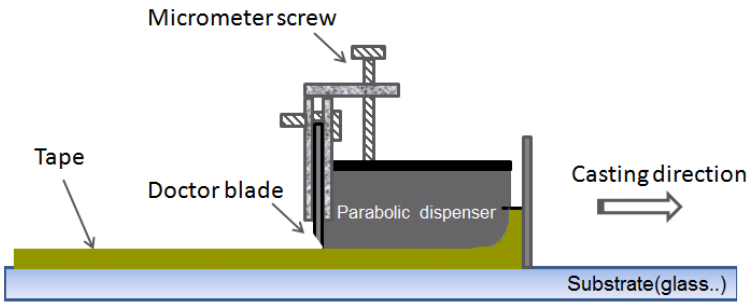

Figure 2.4. Doctor blade profile in tape casting procedure.

The prepared tape is then placed on a temporary support for drying and it can be stripped from the support and fired to form a ceramic layer. Multilayer tapes can be fabricated by sequentially casting one layer on top of another. However, particular importance should be placed to that a good final attachment between two tapes requires that at least one layer is wet. Drying layers or multilayer is also an essential step. Any geometric distortion occurring during the drying process will only deteriorate during sintering. The sintering step is definitely one of the key moments of the whole procedure. This may be effective if a lightweight is deposited on top of the layers to maintain their flatness during sintering. Also, one should give the exact time and temperature not more than what is needed; therefore the most difficult part of sintering duration can be passed easily.

The arrangement, dispersion and homogeneity of the precursor ceramic particles in the slurry determine the final microstructure. Thus, the slurry formulation is a vital step for tape casting; as it is also eligible for related processes like screen-printing, spin coating or dip coating techniques [56]. Practically, a good slurry is the one in which the ceramic grains are electrostatically interacting hence the particles are away from each other, that means there is no agglomerated formed assuming the gravity is negligible. Therefore, no precipitation occurs, and so the viscosity is low enough for casting easily and high enough for the tape to have tolerable resistance in order to keep its geometry [57]. Generally, the slurry involves a mixture of numerous organic substances like binder, dispersant, plasticizer, wetting agents, defoamers and pore formers. The resultant cathode powders form sol-gel process are mixed with solvents (toluene, ethanol, methyl ethyl ketone and xylene) to form an aqueous slurry containing binders (Polyvinyl Butyral, PVB), plasticizers (Polyalkylene Glycol, PAG and Butyl Benzyl Phthalate, BBP) and a dispersant (Fish Oil). The relative amounts of PVB, PAG, BBP, and fish oil are 6%, 5%, 3%, and 3%, respectively, of the total weight of the oxides.

The mixture of toluene (60% wt) and ethanol (40% wt) was used as a solvent. A certain amount of Polyvinyl Butyral (Butvar B79) was added as binder to the solvent mixture in order to have a suitable dispersion medium. The slurry was composed of solvent mixture, fish oil as dispersing agent, Benzyl butyl Phthalate (BBP) and Polyethylene Glycol (PEG) as plasticizers and a required amount of ceramic powder. The slurry was then ball-milled for 24 h continuously. After that, the slurry was transferred into a beaker

to reach the critical viscosity. Finally, the slurry was tape cast on a supporting layer and dried for 3 hours before firing at 1300 °C.

The aforementioned details has been performed for studying the oxygen permeation of a SOFC system having a much thinner electrolyte layer which provides relatively low ohmic losses at operating conditions. There is a wide range of wet forming routes for obtaining thin layer of electrolyte material and other fuel cell components are used and each has its own advantages and disadvantages within. Most researchers use ceramic processing methods such as casting, screen printing, slip casting, direct coagulation or gel casting, and all of them require stable slurries with high solids loading, low-intermediate viscosity and fluidity. These methods are defined as low-cost techniques, which are capable of producing solid oxide fuel cell layers in the desired thickness range (1-200 μm).

In a screen-printing procedure, a highly viscous paste containing a mixture of ceramic powder, organic binder and plasticizer is forced through the open sieves of a screen. Parameters such as grain size and form of the ceramic powder, surface properties and density of the powder have to be optimized. The screen-printed films are dehydrated and sintered at high temperatures (1100-1200 °C) for 2hours in air atmosphere.

3. RESULTS & DISCUSSION

3.1. X-Ray Diffraction (XRD) Results

During the early stage of SOFC development, platinum and some other noble metals were used as the cathode materials. However, the observations summarized in Chapter 1 suggest that by enlarging active area over which chemical processes occur as well as extending the electrochemical interface to include the entire electrode/electrolyte contact area (not just the TPB) could elaborate the transport process of electro active species from the surface to the bulk of the electrode material. Some transition-metal oxides, in addition to being good O_2 catalysts and electronic conductors, exhibit significant ionic conduction while remaining relatively stable at operating conditions. For these mixed conductors (materials which conduct both ions and electrons) the bulk appears to play a significant role in determining the electrode kinetics. As such, these materials provide another useful asymptote to consider when extrapolating to more complex materials such as *perovskites*. One of the first perovskite materials studied was $La_{1-x}Sr_xCoO_{3-\delta}$ (LSC) which is now one of the well-studied mixed conductors and this was followed quickly thereafter by a number of other materials having perovskite crystal structure, including $La_{1-x}Sr_xMnO_{3-\delta}$ (so called LSM), which as became the favored material for SOFC cathodes.

Ideal perovskite crystallizes in cubic close-packed lattice structure. The crystal structure and phase purity of the samples were determined by X-Ray diffraction (XRD).

As seen from Figure 3.1, all the peaks in the pattern can be attributed to the perovskite structure of $La_{1-x}Sr_xMnO_{3-\delta}$ (LSM) with the standard data of JCPDS (49-1808). The X-Ray powder diffraction data (crystal structure and phase composition of the synthesized powders) were collected on a Rigaku D/MAX-Ultima+/PC Diffractometer using Cu-Kα radiation (λ=1.54056Å) for each sample at Boğaziçi University Advanced Technologies Research and Development Center. The XRD measurements were carried out by a step scanning method (2θ range from 0 to 70 deg). The data obtained was compared with reference data for the identification of the crystal structure.

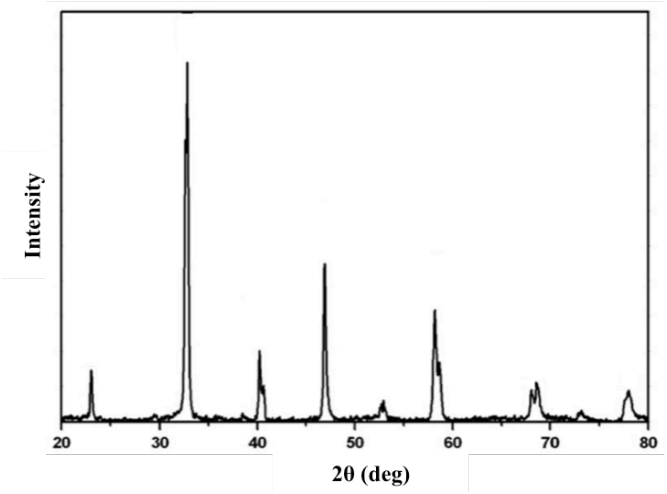

Figure 3.1. X-Ray Diffraction pattern of LSM sample.

XRD Results of $La_{0.6-x}V_xSr_{0.4}CoO_{3-\delta}$: As previously stated $La_{0.6-x}V_xSr_{0.4}CoO_{3-\delta}$ (x = 0.005, 0.01, 0.02, 0.03, 0.04, 0.05, 0.10) samples were prepared by a sol-gel process after calcination at 1100°C in air for 2h. Figure 3.2 shows the XRD patterns of the resulting $La_{0.6-x}V_xSr_{0.4}CoO_{3-\delta}$ powders measured at room temperature.

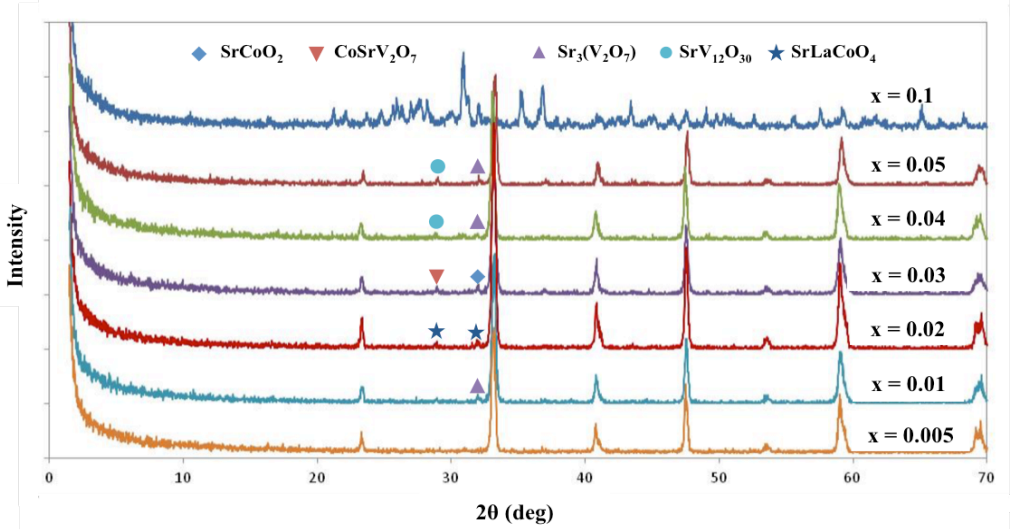

Figure 3.2. XRD patterns of $La_{0.6-x}V_xSr_{0.4}CoO_{3-\delta}$ (x= 0.005 – 0.1) powder calcined at 1100 °C in air for 2h.

It can be seen that the samples with vanadium fractions of $x \leq 0.005$ display a clearly defined single-phase perovskite structure. However, when the doping concentration of vanadium was further increased ($x \geq 0.01$) impure phases like different kinds of oxides could be observed in the $La_{0.6-x}V_xSr_{0.4}CoO_{3-\delta}$ samples. For example, as seen in the above figure for $La_{0.5}V_{0.1}Sr_{0.4}CoO_{3-\delta}$ (LV10SC) sample, two impurities were identified as $Sr_3V_2O_8$ and $SrVO_3$. This suggests that the limit of V doping in this series of $La_{0.6-x}V_xSr_{0.4}CoO_{3-\delta}$ materials should not be more than 0.5 mol %. With increasing V content, the diffraction peaks of $La_{0.6-x}V_xSr_{0.4}CoO_{3-\delta}$ shifted slightly to high-angle direction, as can be seen clearly from Figure 3.2, indicating the shrinkage of crystal parameters. Doping La/Sr site with V, on one hand, may decrease the cell parameter due to the smaller radii of V^{3+} ($r_V{}^{3+}$ = 0.64Å) compare with that of La^{3+} ($r_{La}{}^{3+}$ = 1.36Å) and Sr^{2+} ($r_{Sr}{}^{2+}$ = 1.44Å). On the other hand, it can also result in the reduction of Co ions from Co^{4+} ($r_{Co}{}^{4+}$ (high spin) = 0.53Å) to lower valence state Co^{3+} ($r_{Co}{}^{3+}$ (high spin) = 0.61Å) [31] as charge compensation, thereby, increasing the cell parameter. In view of the changes in the cation radius of A and B sites, the size of V ion had a stronger effect on the crystal structure than its valence state. In addition, there was a loss of intensity of XRD peaks with V-doping level, indicating that the substitution of V decreased the crystallinity of the cubic structure of $La_{0.6-x}V_xSr_{0.4}CoO_{3-\delta}$.

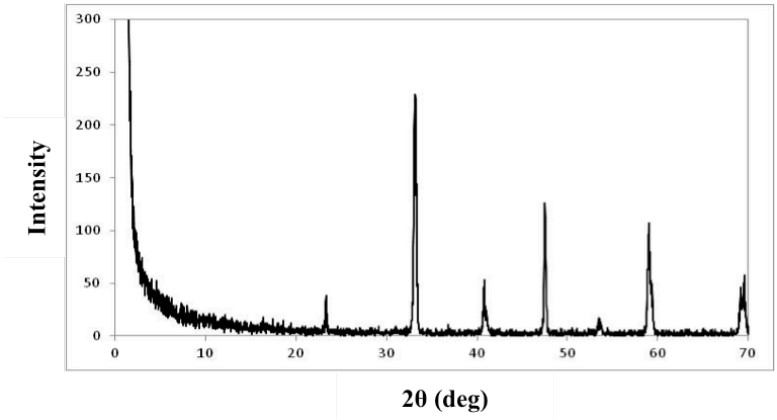

Figure 3.3. Powder XRD patterns of the as-synthesized $La_{0.595}V_{0.005}Sr_{0.4}CoO_{3-\delta}$.

A series of cubic perovskite-type $La_{0.6-x}V_xSr_{0.4}CoO_{3-\delta}$ materials were synthesized and the influence of V doping on the lattice structure was studied in relation to their potential use as cathode materials for SOFC. The solid solution limit of V in $La_{0.6-x}V_xSr_{0.4}CoO_{3-\delta}$ is ca. x=0.005 at 1100 ^oC. As the crystallinity of the cubic structure of $La_{0.6-x}V_xSr_{0.4}CoO_{3-\delta}$ materials decreases with V-doping level, $La_{0.595}V_{0.005}Sr_{0.4}CoO_{3-\delta}$ (LV05SC) was selected as the candidate cathode material on emphasis.

XRD Results of $La_{0.6-x}V_xSr_{0.4}FeO_{3-\delta}$: The ideal oxide perovskite structure ABO_3 consists of a cubic array of corner sharing BO_6 octahedral with the A cation at the body center position. However, non-ideal A and B ionic radii create distortions to the cubic lattice (often orthorhombic or rhombohedral) [58].

Figure 3.4 shows the XRD patterns of the as-synthesized $La_{0.6-x}V_xSr_{0.4}FeO_{3-\delta}$ (x = 0.005 – 0.1), abbreviated as LVxSF correlated with the vanadium content hereafter. All compositions exhibit a perovskite structure, which is either orthorhombic or rhombohedral, and no impurity phase appears. It indicates that partial substitution of V for La does not affect the formation of layered perovskite phase. The slightly different structure variation in our case is due to the cationic radii and the introduction of V^{3+} ions.

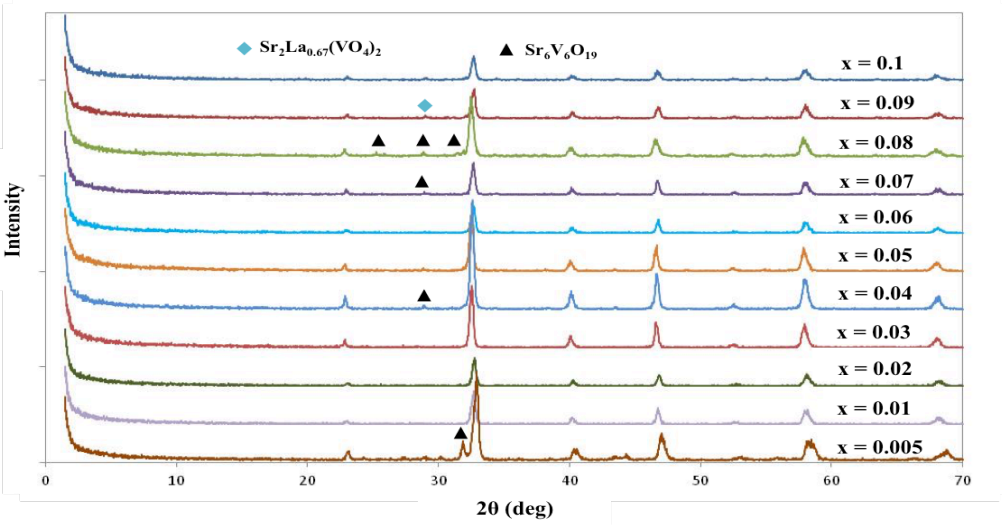

Figure 3.4. Powder X-Ray Diffraction patterns of the as-synthesized $La_{0.6-x}V_xSr_{0.4}FeO_{3-\delta}$ with different V-doping amount.

However, it can be seen that all samples were nearly phase pure, but for the nominal LV05SF (which is $La_{0.6-x}V_xSr_{0.4}FeO_{3-\delta}$ for x = 0.005) sample, a second phase marked with ▲was observed. As indicated in Figure 3.4, the second phase can be indexed to Strontium Vanadium Oxide, $Sr_6V_6O_{19}$. This result emphasizes the solid solution limit of V in $La_{0.6-x}V_xSr_{0.4}FeO_{3-\delta}$ is greater than 0.5%.

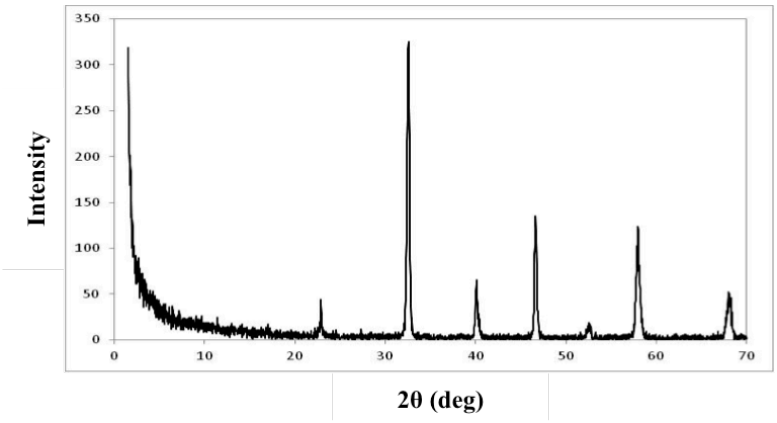

Figure 3.5. X-Ray Diffraction pattern of as-prepared $La_{0.57}V_{0.03}Sr_{0.4}FeO_3$.

Figure 3.5 shows the XRD results for the LV3SF sample. As the LV4SF samples showed a second phase as evidenced by additional peaks at 2θ value of 29.8^o, even though the phase was not unambiguously identified but most closely matched that of $Sr_6V_6O_{19}$, $La_{0.57}V_{0.03}Sr_{0.4}FeO_{3-\delta}$ (LV3SF) was selected as the candidate cathode material on consideration due to its single-phase crystallinity and relatively high peak intensity among others.

XRD Results of $La_{0.6-x}V_xSr_{0.4}MnO_{3-\delta}$: Phase homogeneity of $La_{0.6-x}V_xSr_{0.4}MnO_{3-\delta}$ (x= 0.005 – 0.1) was compared as in Figure 3.6. $La_{0.6-x}V_xSr_{0.4}MnO_{3-\delta}$ like all the $La_{1-x}Sr_xMnO_3$ systems crystallizes in a rhombohedral structure [59]. The rhombohedral distortion of the ideal perovskite octahedra is characterized by the splitting of the principal reflection, which appears as a double peak in the range 2θ= 32–33° [60].

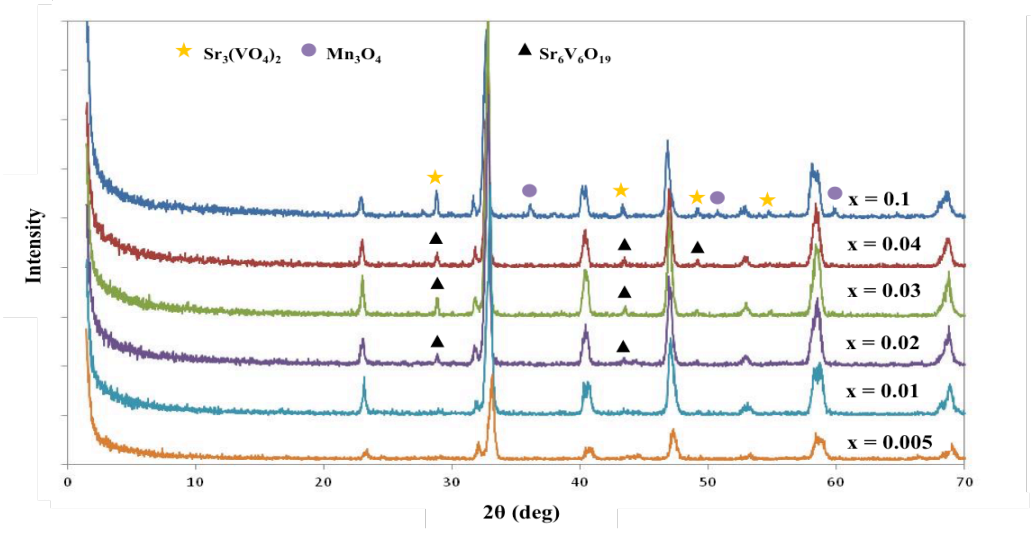

Figure 3.6. XRD patterns of $La_{0.6-x}V_xSr_{0.4}MnO_{3-\delta}$ (x= 0.005 – 0.1) samples.

Figure 3.6 presents typical XRD patterns of $La_{0.6-x}V_xSr_{0.4}MnO_{3-\delta}$ (x = 0.005 – 0.1) fired at 1100 ^oC. The patterns suggest that the LVxSM samples have a single-phase perovskite structure without any detectable impurity phases up to x = 0.01 and the $Sr_6V_6O_{19}$ secondary phase at 2θ values of 29.6° started to form with V content above x = 0.01. This indicates that LVxSM can form a solid solution with V content of $x \leq 0.01$.

No resistive phases, either $La_2Zr_2O_7$ or $SrZrO_3$, are detected by X-Ray diffraction for the LV10SM cathode material. A well-defined perovskite oxide phase can be seen from Figure 3.6. However there are some extra peaks with small size in the XRD pattern. We find they belong to strontium vanadium oxide $Sr_3(VO_4)_2$ by XRD phase analysis software. $Sr_3(VO_4)_2$ is a kind of the perovskite material related mixed ionic-electronic conductor, and not considered to be detrimental to the SOFC cathode. However, it is obvious that there is a distortion from the perovskite crystallinity. This suggests that the limit of V doping in this series of $La_{0.6-x}V_xSr_{0.4}MnO_{3-\delta}$ materials should not be more than 10 mol %.

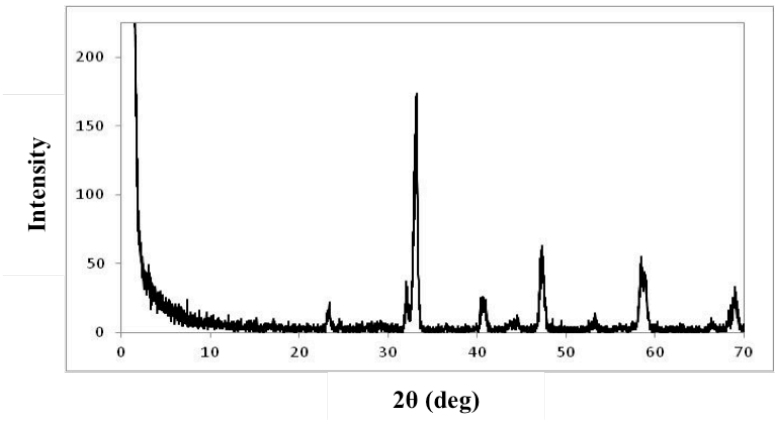

Figure 3.7. X-Ray Diffraction data for $La_{0.595}V_{0.005}Sr_{0.4}MnO_3$.

As can clearly be seen from the Figure 3.7, the diffraction pattern confirms the pure rhombohedral phases of LV05SM ($La_{0.6-x}V_xSr_{0.4}MnO_{3-\delta}$ where x = 0.005) and substitution of V at a level of 0.5 mol % did not change the crystallinity of the sample thus and so LV05SM had potential application as a cathode material.

XRD Results of $La_{0.6-x}Gd_xSr_{0.4}CoO_{3-\delta}$: The room temperature XRD patterns of $La_{0.5}Gd_{0.1}Sr_{0.4}CoO_3$ (LG10SC) compounds synthesized from the sol-gel route followed by a heat-treatment at 1100 ^oC for 2 h in air is shown in Figure 3.8. A perovskite-like structure of LG10SC was certified for the powders and no other phase was found within the sensitivity of XRD.

Lines corresponding to either the initial reagents or any intermediate compound(s) are not present in the Figure 3.8. Moreover, comparing the XRD results of LG10SC with the conventional cathode material LSM in layered perovskite oxide system, the peaks of the LSM are comprised of singlets, while the LG10SC peaks at two-theta values of 33.4° made up of multiplets, as seen in Figure 3.8. These behaviors are identified as specific evidence of a layered perovskite [61].

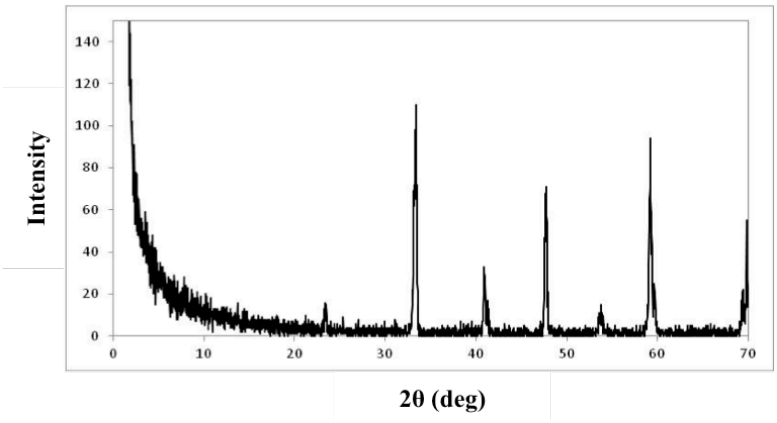

Figure 3.8. XRD pattern of as-synthesized $La_{0.5}Gd_{0.1}Sr_{0.4}CoO_3$ powder.

XRD Results of $La_{0.6-x}V_xSr_{0.4}CrO_{3-\delta}$: It is clear from Figure 3.9 that the $La_{0.6-x}V_xSr_{0.4}CrO_{3-\delta}$ (x = 0.005, 0.01, 0.02, 0.03, 0.04, 0.1) cathode materials sintered at 1100 ^oC have relatively distorted phases from the crystallinity of perovskite structure. There was some observable evidence of impurity or secondary phases like Strontium Chromium Oxide, $SrCrO_4$.

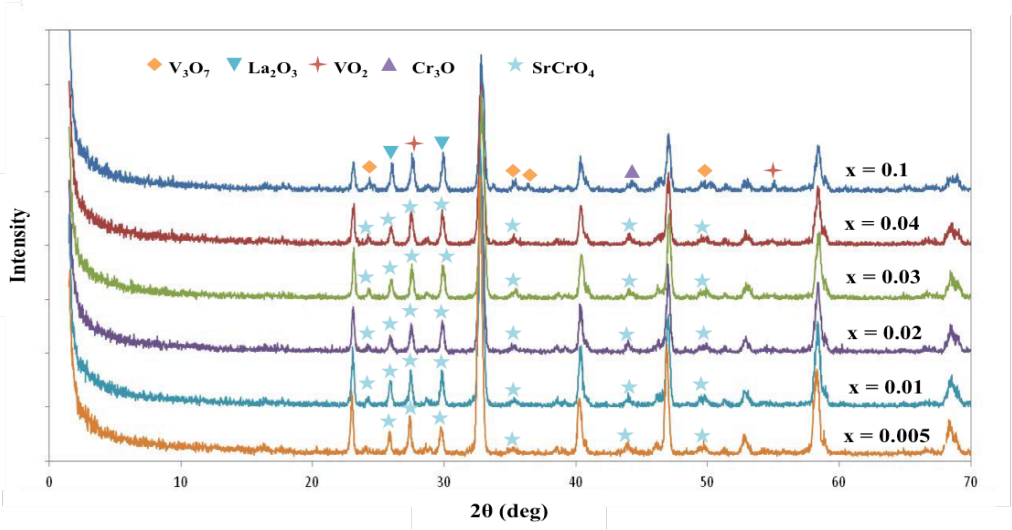

Figure 3.9. XRD peaks of $La_{0.6-x}V_xSr_{0.4}CrO_{3-\delta}$ (x = 0.005, 0.01, 0.02, 0.03, 0.04, 0.1) samples.

Moreover, comparing the XRD results of $La_{0.6-x}V_xSr_{0.4}CrO_{3-\delta}$ (x = 0.10 which is abbreviated as LV10SCr) with the samples of lower V dopant in layered perovskite oxide system, the intensity of impurities and secondary phases were increasing, as seen in Figure 3.9 thereby the material of $La_{0.6-x}V_xSr_{0.4}CrO_{3-\delta}$ was not suitable for as a potential cathode material.

XRD Results of $La_{0.6-x}V_xSr_{0.4}TiO_{3-\delta}$: Figure 3.10 shows the XRD results for the $La_{0.6-x}V_xSr_{0.4}TiO_{3-\delta}$ (x = 0.005, 0.01, 0.02, 0.03, 0.04, 0.1) samples on top of each other for comparison. Each sample showed secondary phases as evidenced by additional peaks at different 2θ values. The phase was not unambiguously identified but most closely matched that of different types of Strontium, Titanium and Vanadium Oxides.

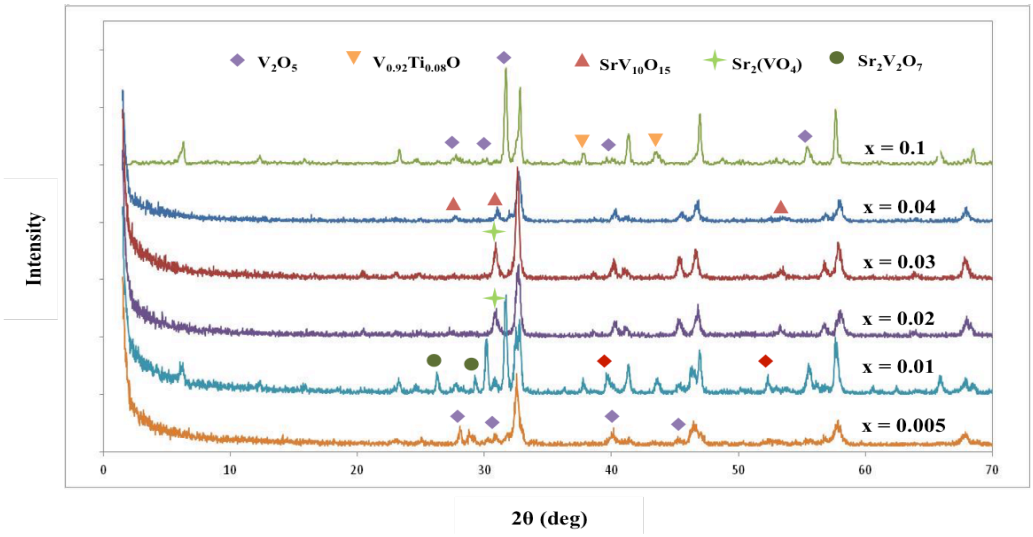

Figure 3.10. X-Ray Diffraction patterns for $La_{0.6-x}V_xSr_{0.4}TiO_{3-\delta}$ (x = 0.005, 0.01, 0.02, 0.03, 0.04, 0.1).

Comparing the XRD results of the samples with lowering in Vanadium content, the intensity of impurities and secondary phases were not in an agreement. While some of the phases were decreasing, some of them were disappearing, as seen in Figure 3.10. At the same time, there were some peaks, which could not match with any defined phase by XRD analysis software. Moreover, some peaks even split half thereby the material of $La_{0.6-x}V_xSr_{0.4}TiO_{3-\delta}$ was not suitable for as a potential cathode material.

XRD Results of $La_{1-x}Sr_xVO_3$: The XRD patterns are presented in Figure 3.11 for the $La_{1-x}Sr_xVO_3$ (x = 0.4) sample obtained by sintering at 1100 ^oC for 2h. It can be obviously seen that the crystal structure of the as-produced cathode material didn't have any peaks correlated with the perovskite crystal structure. Moreover, the sharp peaks form the XRD spectra couldn't match with any identified patterns in the X-Ray Powder Diffraction database.

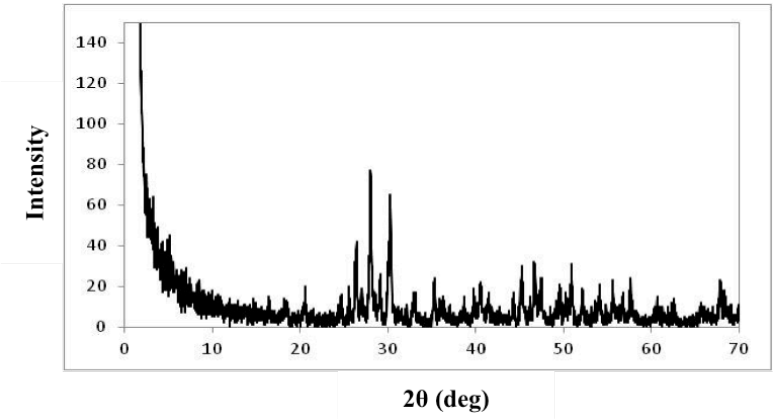

Figure 3.11. XRD patterns of $La_{0.6}Sr_{0.4}VO_3$ cathode powder.

The ionic radius of La^{3+} and Sr^{2+}, A-site cations in the perovskite structure, at the coordination numbers of 12 are 1.36 and 1.44 Å, respectively [31], while the radii of B-site cation V^{5+} at the coordination number of 6 is 0.54 Å, which is significantly smaller than A-site cations. A consideration of the ionic size proposes that V is not incorporated into the lattice.

3.2. X-Ray Photoelectron Spectroscopy (XPS) Results

The major function of the cathode material in SOFC is to contribute reaction sites for the electrochemical reduction of oxygen. Hence, in order to find out the reaction processes and mechanisms, the understanding of the active sites for oxygen reduction

reaction is important. Electrocatalysts and ion transport properties of the cathode samples mostly depend on the adsorption and diffusion of the oxygen. The rate of the reaction, which oxygen is adsorbed from the ambient environment, relies greatly on the structure and composition of the outermost surface of the oxides [62]. The composition and the structure of the surface may vary from that of the bulk. Better understanding of the surface properties of these cathode materials is thus essential. Early studies on cathode samples are mainly centered upon the electrochemical properties [63] and there are few studies done for the view of surface of the sample. In this respect, the X-Ray photoemission spectroscopy (XPS) is a very useful technique for the determination of such important parameters as the chemical state of different metals, their relative concentration and the surface elements ratio.

The XPS experiments were performed using a Thermo Scientific K-Alpha Surface Analysis instrument, a room temperature. An Al K Alpha X-Ray source was used with a spot size of 400 μm and the spectra of powdered samples were recorded with the constant pass energy values at 150eV. The energy step size was set as 0.100 eV and the charge effect was calibrated using the binding energy of C1s (284.5 eV) [64].

XPS Results of $La_{0.6-x}V_xSr_{0.4}CoO_{3-\delta}$ (x = 0.005) – LV05SC: The valance states of elements in the possession and the composition of the surface of the as-synthesized LV05SC sample were further investigated by XPS, as shown in Figure 3.12, and the fitted curves about elements within the powder are illustrated in Figures 3.13, 3.14, 3.15 and 3.16. No peaks of elements other than La, Co, Sr and V except C1s are observed on the survey spectrum (Figure 3.12).

The matched curves about $La3d_{3/2}$ and $La3d_{5/2}$ are illustrated in Figure 3.13. The core level binding energies of $La3d_{3/2}$ and $La3d_{5/2}$ spectra are located at 854.08 and 834.08 eV, respectively, due to the presence of different La atoms.

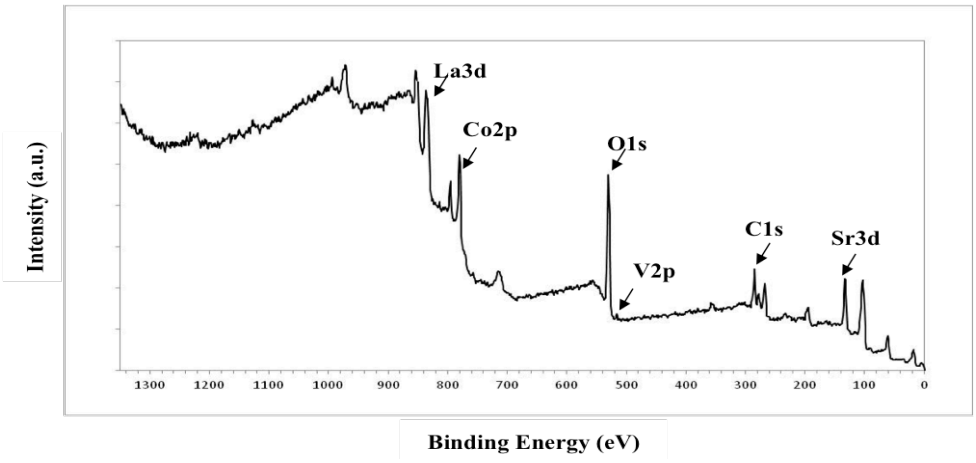

Figure 3.12. XPS survey spectrum of the LV05SC powder.

The reason for the splitting in the La3d states in the XPS is not only due to a spin–orbit interaction into two lines $3d_{5/2}$ and $3d_{3/2}$, but additionally, each line is split due to a transfer of an electron from oxygen ligands to the La4f, which is initially empty [65].

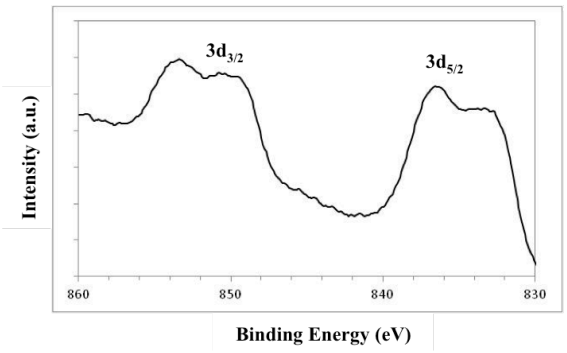

Figure 3.13. The La3d core level XP spectra of LV05SC.

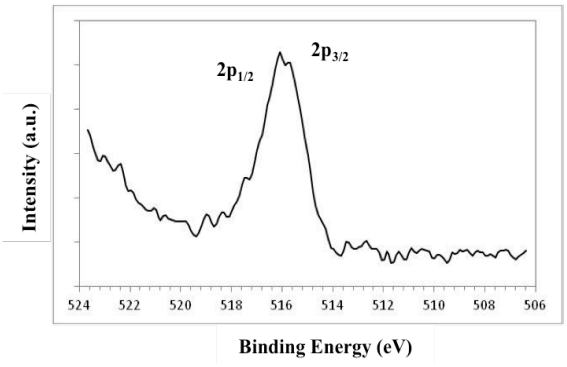

Figure 3.14. The V2p core level XP spectra of LV05SC.

As can be seen from the Figure 3.14, the V2p peak of the sample is divided into two peaks of $V2p_{3/2}$ and $V2p_{1/2}$ at the binding energies of 515.68 and 517.48 eV, assigned to V^{5+} and V^{4+}, respectively [66]. Therefore, the core-level spectra of V2p further confirm that the as-obtained LV05SC sample consist of V^{5+} and V^{4+}.

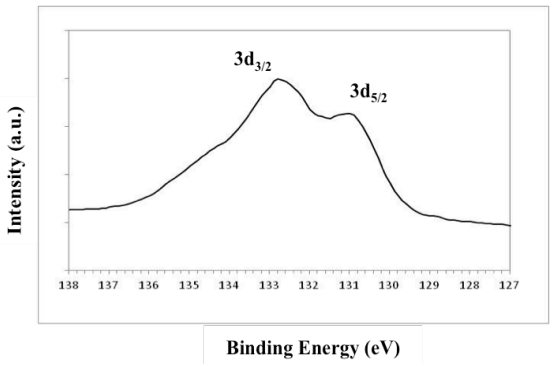

Figure 3.15. The Sr3d core level XP spectra of LV05SC.

The Sr3d X-Ray photoelectron spectra, as shown in Figure 3.15, contains a doublet, whose binding energies are 132.8 and 130.98 eV, which can be assigned as $Sr3d_{3/2}$ and $Sr3d_{5/2}$ lines, respectively. Their binding energies are very close the similar compounds [67], which can be contributed to the Sr^{2+} ions in LV05SC.

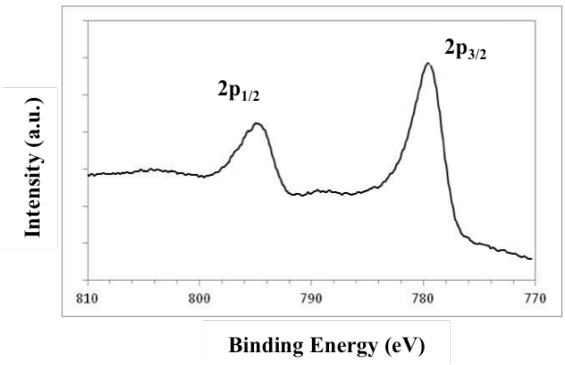

Figure 3.16. The Co2p core level XP spectra of LV05SC.

Figure 3.16 illustrates high resolution spectra of the Co2p XPS region for LV05SC. The peak at 779.58eV arose from $Co2p_{3/2}$, and the one with maxima at 795eV was due to $Co2p_{1/2}$. For the Co2p spectra, a main peak at ca. 779.58eV accompanied by a weak shoulder at ca. 789.5eV is present and this weak shake-up peak indicates the presence of Co^{3+} [68]. For cobalt containing systems, a small shoulder presenting on the high binding energy side of the $Co2p_{3/2}$ spectra at approximately 788eV can be identified as Co^{4+} [69].

XPS Results of $La_{0.6-x}V_xSr_{0.4}MnO_{3-\delta}$ (x = 0.005) – LV05SM: The chemical environments of La, V, Sr, and Mn ions were estimated by curve-fitting of La3d, V2p, Sr3d and V2p spectra, as shown in Figure 3.17.

No peaks of elements other than La, Mn, Sr and V except C1s are observed on the survey spectrum Figure 3.17.

The La3d states of LV05SM are shown in Figure 3.18. The $La3d_{3/2}$ peak of the sample is divided into two peaks at the binding energies of 853.38 and 850.68eV, and the corresponding binding energy of $La3d_{5/2}$ is 837.3 and 833.5eV.

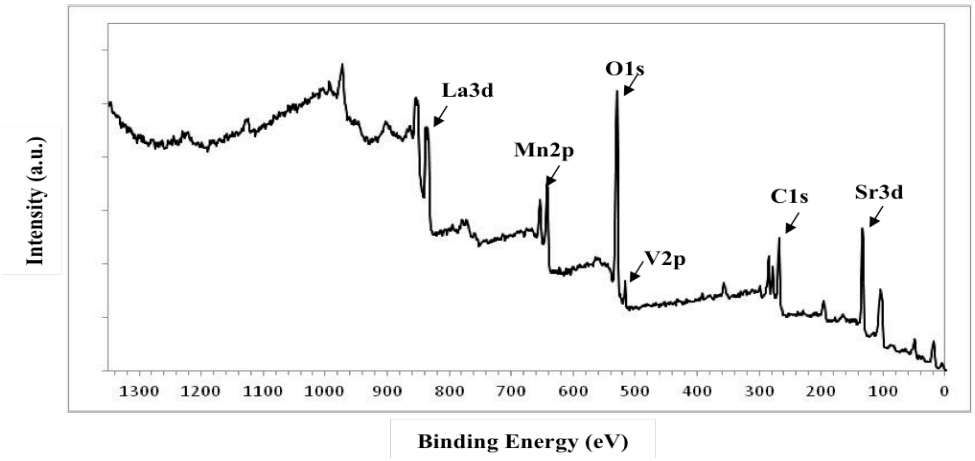

Figure 3.17. XPS spectra survey analysis at room temperature for LV05SM samples.

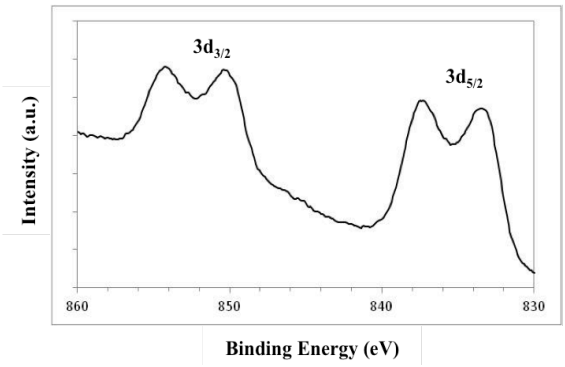

Figure 3.18. XPS spectra of La3d for LV05SM sample.

Energy difference between the $3d_{3/2}$ and $3d_{5/2}$ levels is approximately equal to 17 eV. The binding energies and the multiplet splitting agree well with reported values for La^{3+} compounds [69].

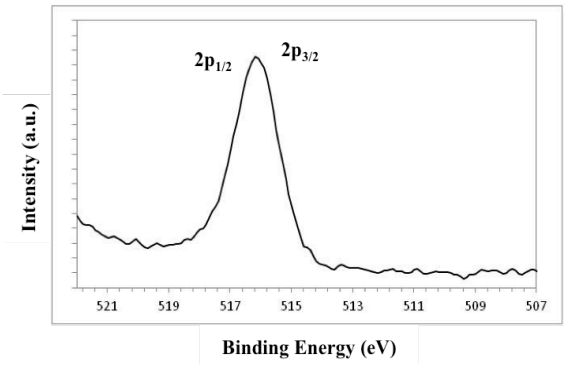

Figure 3.19. XPS spectra of V2p for LV05SM sample.

Figure 3.19 represents an XPS spectrum used for the element chemical environment of V2p. The binding energies of the V2p levels are 515.88 and 516.6eV for $V2p_{3/2}$ and $V2p_{1/2}$, respectively. These are thought to be vanadium in a V^{5+} state and V^{3+} state [70].

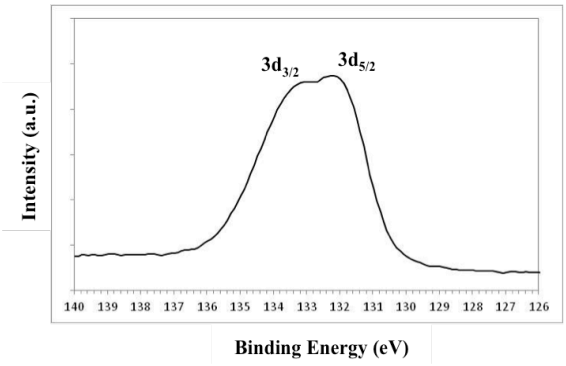

Figure 3.20. XPS spectra of Sr3d for LV05SM sample.

The Sr 3d core-level spectra of the samples contains a doublet as shown in Figure 3.20, whose binding energies are 132.2 and 133.08eV, which can be assigned as $Sr3d_{5/2}$ and $Sr3d_{3/2}$ lines, respectively, indicating that Sr ions are located in two different environments. As regarding the binding energy of $Sr3d_{5/2}$ peak, the component at 132.2 - 132.7eV comes from Sr ions incorporated into the perovskite structure and the one

observed for $Sr3d_{3/2}$ can be assigned to $SrCO_3$ [71]. From the XP spectra, we can conclude that the binding energies are very close to the similar compounds [67], which can be attributed to the Sr^{2+} ions in LV05SM.

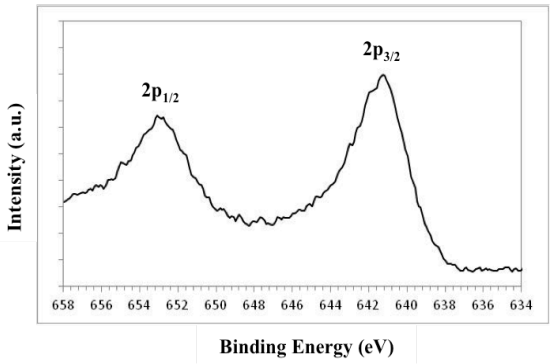

Figure 3.21. XPS spectra of Mn2p for LV05SM sample.

Figure 3.21 shows the Mn2p XP spectra of LV05SM. They display a broad emission line with a maximum near at 641.2eV for $Mn2p_{3/2}$ and 653.08eV for $Mn2p_{1/2}$ emissions. According to the binding energy of $Mn2p_{3/2}$, the oxidation state of Mn ions are between +3 and +4 [64].

XPS Results of $La_{0.6-x}V_xSr_{0.4}FeO_{3-\delta}$ (x = 0.03) – LV3SF: The composition of the surface and the valance states of elements in the as-synthesized LV3SF sample were further investigated by XPS, as shown in Figure 3.22, and the fitted curves about elements within the powder are illustrated in Figures 3.23, 3.24, 3.25, and 3.26.

The Figure 3.22 shows the survey XP spectrum of LV3SF. Only La, Sr, Mn, C and O elements are observed on the sample surface. No additional lines related to the contaminations were detected.

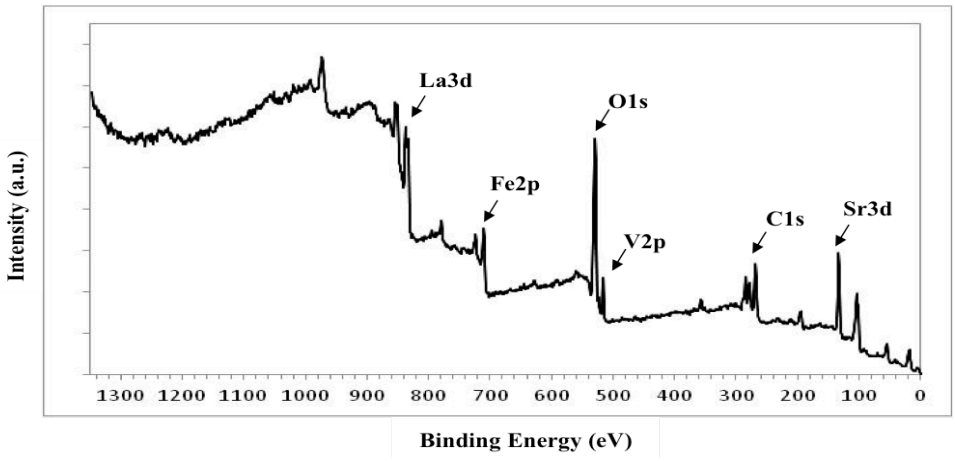

Figure 3.22. XPS survey spectrum of the LV3SF powder.

In Figure 3.23 the La3d states of LV3SF are shown. In studied areas, for La, there are two peaks, one at 833eV, which corresponds to La^{3+} in perovskite phase [72] and, another at 836eV, which is assigned to La^{3+} in La_2O_3 [64]. From the XPS spectra, it can be judged that only La^{3+} ions exist in LV3SF sample.

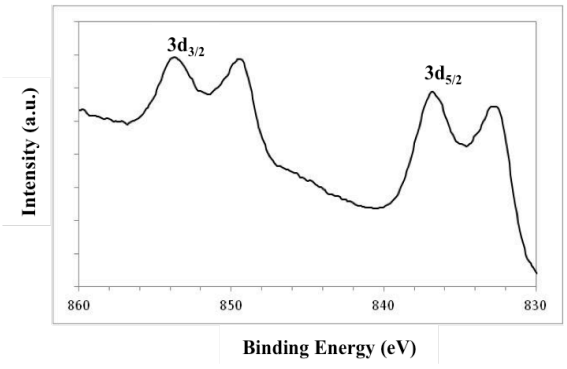

Figure 3.23. XPS spectra of La3d for LV3SF sample.

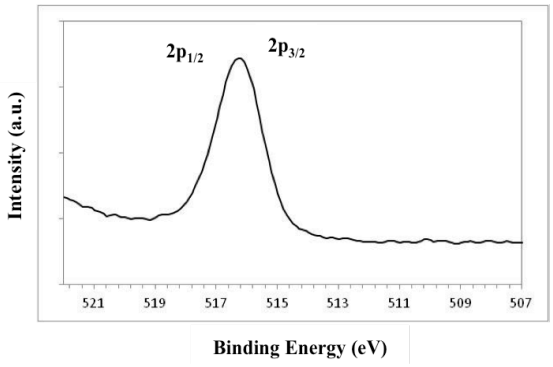

Figure 3.24. The V2p core level XP spectra of LV3SF.

The V2p X-Ray photoelectron spectra, as shown in Figure 3.24, contains a broad peak, whose binding energies are 515.98 and 517eV, which can be assigned as $V2p_{3/2}$ and $V2p_{1/2}$ lines, respectively. These are thought to be vanadium in a V^{5+} state and V^{3+} state [73]. From the spectra, it can be concluded that vanadium exists in a mixed oxidation state.

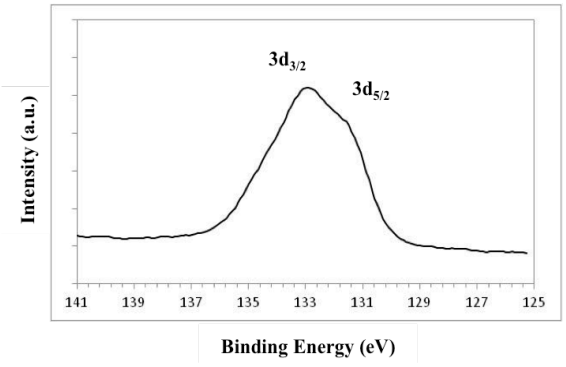

Figure 3.25. The Sr3d core level XP spectra of LV3SF.

The chemical state of the Sr element was revealed by XPS (Figure 3.25). The binding energy for the $Sr3d_{3/2}$ and $Sr3d_{5/2}$ peak of as-prepared LV3SF cathode is 132.8eV and 131.68eV, respectively, corresponding to Sr^{2+} in LV3SF and few SrO, because this binding energy is very close to the similar compounds [74, 67].

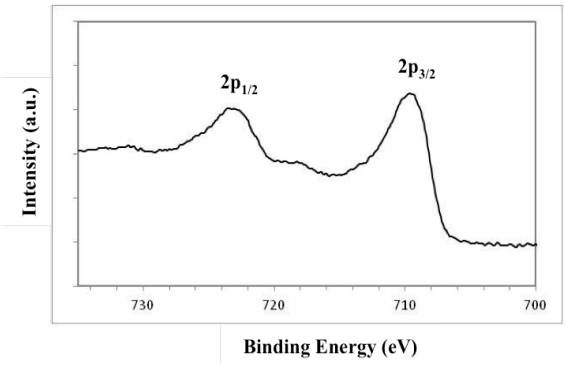

Figure 3.26. The Fe2p core level XP spectra of LV3SF.

Figure 3.26 shows the asymmetric Fe 2p core-level spectra of the LV3SF samples and two different valences, Fe^{3+} and Fe^{4+}. The doublet peaks with binding energy at 719.5 and 723.3eV can be assigned to the Fe^{3+} $2p_{3/2}$ and $2p_{1/2}$ spectrum, respectively. Interestingly, a weak shoulder peak at 718.8eV appears between the above doublet peaks, corresponding to the Fe^{4+} $2p_{3/2}$ [75].

XPS Results of $La_{0.5-x}Gd_xSr_{0.4}CoO_{3-\delta}$ (x = 0.10) – LG10SC: The chemical states and surface proportions of elements for the LG10SC sample were characterized by XPS.

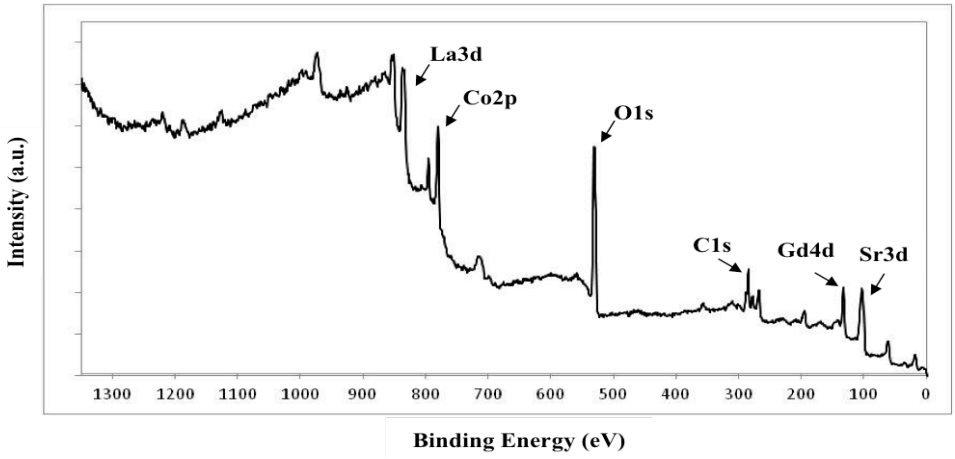

Figure 3.27. XPS survey spectrum of the LG10SC powder.

The XPS survey scan (Figure 3.27) showed that carbon, lanthanum, cobalt, oxygen, strontium and gadolinium were present on the catalyst surface. The La3d states of LG10SC are shown in Figure 3.28.

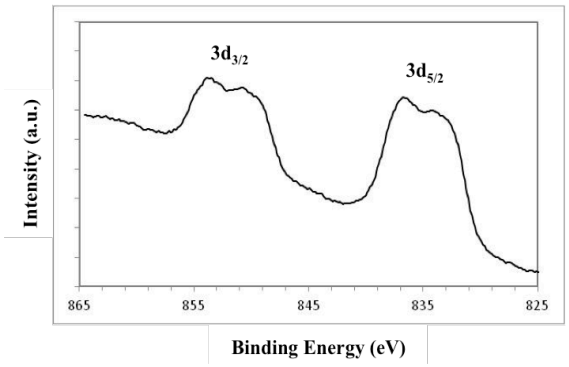

Figure 3.28. XPS spectra of La3d for LG10SC sample.

In the studied areas, the $La3d_{3/2}$ doublet contained components at binding energies of 850 and 853.7eV and for $La3d_{5/2}$ there are two peaks, one at 836.7eV which corresponds to La^{3+} in perovskite phase [76] and, another at 834eV which is also assigned to La^{3+} in La_2O_3 [64].

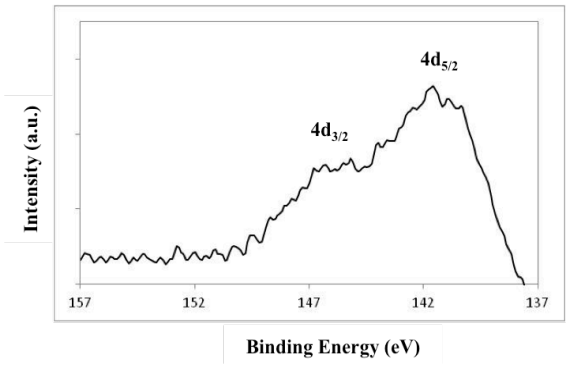

Figure 3.29. XPS spectra of Gd4d for LG10SC sample.

The characteristic peaks of Gd4d region shown in Figure 3.29 were displayed at 141.58 and 146.8eV, which were due to $Gd4d_{5/2}$ and $Gd4d_{3/2}$, respectively, considering two spin–orbit doublet characteristic of Gd^{3+} [77].

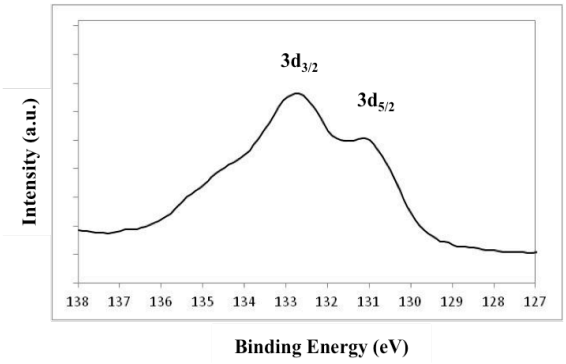

Figure 3.30. XPS spectra of Sr3d for LG10SC sample.

Figure 3.30 shows the measured XPS spectra of $Sr3d_{5/2}$ and $Sr3d_{3/2}$ in LG10SC. Generally, the Sr3d peaks were shown as mainly two distinctive peaks of $3d_{5/2}$ at lower binding energy ranges and $3d_{3/2}$ at relatively higher binding energy ranges [78]. The position of the lower binding energy in the $Sr3d_{5/2}$, which is located at around 131.1eV is originated from the formation of the perovskite phase showing a charge state of Sr^{2+} [79]. Therefore, the main peaks in LG10SC measured at about 131.1eV and 132.8eV were originated from $Sr3d_{5/2}$ and $3d_{3/2}$, which correspond to the perovskite structure.

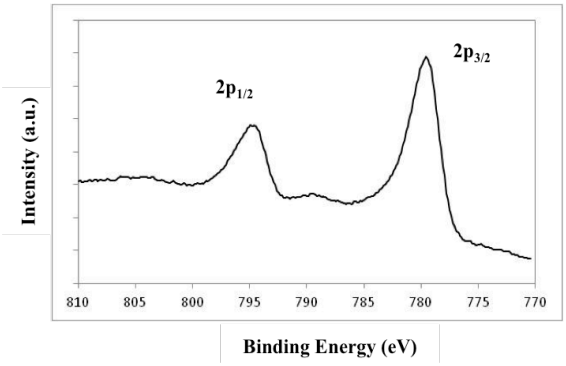

Figure 3.31. XPS spectra of Co2p for LG10SC sample.

As shown in Figure 3.31, the XPS analysis generally results of the Co spectra show that it is comprised of two peaks indicating $Co2p_{3/2}$ at relatively lower binding energy ranges and $Co2p_{1/2}$ at relatively higher binding energy ranges and the peaks between $Co2p_{3/2}$ and $Co2p_{1/2}$ and over the $Co2p_{1/2}$ can be also observed. In the Figure 3.31, the two main peaks located at binding energies of 779.60eV and 795eV are assigned to $Co2p_{3/2}$ and $Co2p_{1/2}$ of LG10SC. According to the Co peaks, the first broad peak, which is related to the mixed Co charge state of Co^{2+} and Co^{4+} in the vicinity of 786.0 - 790.0eV. According to the literatures [80,81], the peaks between 786.0 - 790.0eV were caused by Co^{2+} and the weak peaks observed in the vicinity of 804 - 805eV were related with the coexistence of Co^{3+} and Co^{4+} suggesting that Co is existed as the chemical form of mixed valence state including Co^{3+} and Co^{4+} in LG10SC oxide systems. With the substitution of Gd into the A-site of the perovskite oxide material, probably results in both an increase of the number of oxygen vacancies and an increase of the concentration of Co^{4+} in order to compensate the charge and achieve electro neutrality.

3.3. Electrical Conductivity - Four Probe Measurement Results

The electrical conductivity was measured by the four-probe DC method on the sintered rectangular bars. The measurements were performed upon heating from 400 to 800 °C in air, and with a heating rate of 1 C/min. Four gold (Au) wire contacts were made, which were painted with gold conductor paint. Two current contacts were attached at the bar edges, and two voltage contacts in between at a distance *l*. The sample was then fired at 500 °C for 1 h to allow complete adhesion of the electrodes and reduction of the contact resistance. The sample was then placed in a horizontal tube furnace. In this method an electric current is passed through a bar of the sample and a voltage drop is measured across a distance in the middle of the sample. The sample was left at each temperature at which measurement was taken. The electrical conductivity σ was calculated by the following equation:

$$R = \rho \frac{l}{A} \tag{3.1}$$

where R is the polarization resistance, A is the cross-sectional area of the rod, l is the thickness of the cathode and ρ is the specific resistance. Electrical conductivity values (σ) were obtained through the inverse of the specific resistance. The as-synthesized LV05SC, LV3SF, LV05SM and LG10SC cathode materials were prepared for four-probe DC method and the data obtained is compared with reference data for each sample.

Electrical Conductivity of $La_{0.6-x}V_xSr_{0.4}CoO_{3-\delta}$ (x = 0.005) – LV05SC: Various studies including the electrical conductivity and its dependence on temperature have been reported for LSC cathode material [82]. An explanation of these concepts is complicated in respect to that there are mainly two factors contributed to the electrical conductivity of LSC material. The first one is the distinct parameters of the crystal structure such as interatomic distances and angles and as the second one is the charge carrier concentration which is the concentration of electron holes. In these type of oxides, the oxygen ion transport proceeds through the hopping of oxygen vacancies inside the crystal structure, while the movement of the electrons is along the way B^{n+} – O – B^{n+1} bond due to overlapping between the 3d orbitals of the B-site and 2p orbitals of the oxygen [83].

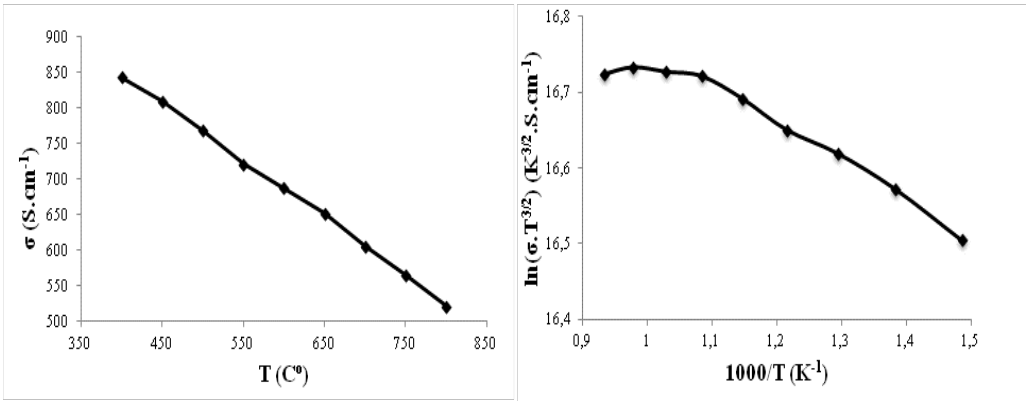

Figure 3.32. Temperature dependance of the electrical conductivity of LV05SC sample sintered at 1100 ^{o}C.

The logarithm of electrical conductivity ($ln\,\sigma T^{s}$) of LV05SC measured upon heating from 400 to 800 °C in air and the electrical conductivity of sample are plotted as a function of temperature in Figure 3.32. The maximum conductivity value reached its

maximum with 843 S/cm at 400 °C and decreased then over 521.50 S/cm at 800 °C. This reflects the expected metal-like conductivity and it refers to the decrease in the electron-hole concentration with increasing temperature. It has been suggested by Petrov in 1995 that the electrical conductivity is directly relevant to the crystal structure [84]. The metal-like conductivity is observed in the cubic phase of $La_{1-x}Sr_xCoO_3$ while the semiconductor-like behavior is examined in the rhombohedral phase. From this point of view, the conductivity is metallic when it decreases with increasing temperature as the increase in conductivity means semiconducting behavior . The temperature dependence of electrical conductivity is generally expressed as:

$$\sigma = \left(\frac{A}{kT^s}\right) \exp\left(-\frac{E_a}{kT}\right) \tag{3.2}$$

in which E_a is the activation energy for electrical conductivity, k is the Boltzmann constant, T is the absolute temperature and A is the pre-exponential factor that contains a number of constants such as the number of charge carriers and the average distance between the B-site ions [16]. The exponent of s equals either 1 or 3/2 for an adiabatic or non-adiabatic hopping process, respectively. The plot of $ln\,\sigma T^s$ versus $1000\ /T$ should give a straight line. The plot for $La_{0.595}V_{0.005}Sr_{0.4}CoO_3$, a somewhat better linear fit was obtained for s = 3/2, suggesting a non-adiabatic hopping process, shown in Figure 3.32.

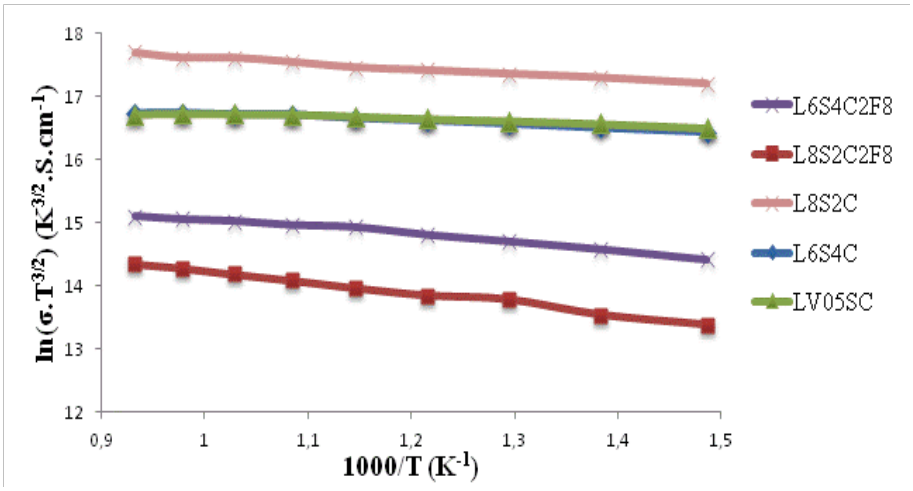

Figure 3.33. Comparison of the total conductivity of various cobalt containing perovskite related materials in air.

The activation energy values are calculated using simple linear regression from the slopes of the linear parts of the $ln\,\sigma T^s$ vs. $1000\,/T$ plots (Figure 3.33). Table 3.1 lists the E_a values obtained over the indicated temperature ranges. The E_a values calculated from the temperature dependence of the electrical conductivity are listed in Table 3.1 varying from 0.045 to 0.15eV. The activation energy of $La_{0.6}Sr_{0.4}CoO_3$ (0.049 eV) is in very good agreement with the value of 0.05eV reported by Sitte, W. [85]. Temperature dependence of the electrical conductivity value in the range of 400 and 800 ^oC was very similar (564 S/cm) with the reported in Montero X., 2009 for $La_{0.8}Sr_{0.2}CoO_3$ structure [86]. The value of 0.10eV obtained for $La_{0.6}Sr_{0.4}Co_{0.2}Fe_{0.8}O_3$ from this measurement agrees perfectly with the value of 0.10eV reported earlier [87]. The activation energy value for $La_{0.8}Sr_{0.2}Co_{0.2}Fe_{0.8}O_3$ was calculated as 0.15eV and L.W. Tai reported an activation energy of 0.14eV between 400 and 800 ^oC [88]. Small variations can be attributed to the differences in the material synthesis and processing methods.

Table 3.1. Calculated σ_{max}, σ_{800^oC} and E_a of specimens sintered at 1100 ^oC.

Composition	σ_{max}(S/cm)	σ_{800^oC} (S/cm)	Temp. Range (^{o}C)	E_a (eV)
$La_{0.595}V_{0.005}Sr_{0.4}CoO_3$	843.43	521.50	400-650	0.045
$La_{0.6}Sr_{0.4}CoO_3$	784.67	525.53	400-800	0.049
$La_{0.8}Sr_{0.2}CoO_3$	1702.31	1389	400-800	0.075
$La_{0.6}Sr_{0.4}Co_{0.2}Fe_{0.8}O_3$	118.75	103.51	400-800	0.10
$La_{0.8}Sr_{0.2}Co_{0.2}Fe_{0.8}O_3$	48.80	48.57	400-800	0.15

Electrical Conductivity of $La_{0.6-x}V_xSr_{0.4}FeO_{3-\delta}$ (x = 0.03) – LV3SF: As a cathode material in SOFCs, the sample must acquire high electrical conductivity at the desired working temperatures since a low electrical conductivity may result in a poor current-collecting efficiency and a large ohmic resistance of cathode.

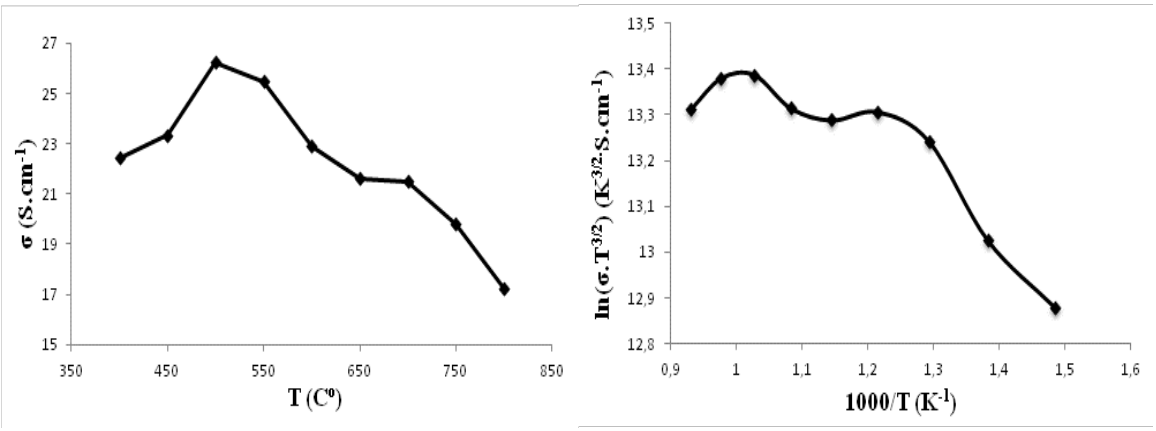

Figure 3.34. Temperature dependance of the electrical conductivity of LV3SF sample sintered at 1100 ^{o}C.

The dependence of conductivity of LV3SF sample on temperature and the Arrhenius plot for the electrical conductivity in air measured by the four-point method is shown in Figure 3.34. This value of total conductivity contains electronic and ionic contributions due to the presence of charge carriers and oxygen vacancies, respectively. However, ionic conductivity in perovskite oxides is known to be small in comparison with the overall conductivity [89]. Therefore, the experimental values of the electrical conductivity are assumed to be correspondant to the electronic conductivity alone. The conductivity increases gradually with increasing temperature, attains a maximum value 26.23 S/cm at around 500 ^{0}C and then decreases with further increase of temperature. This can be explained as the electrical conductivity in Sr-doped $LaFeO_3$ is generally believed to occur by the loss of lattice oxygen, implying a semiconductor behavior [90], associated with the tetravalent state of the iron cations. The decrease in the conductivity at higher temperatures is basically due to the formation of oxygen vacancies, accompanied by reduction of Fe^{4+} to Fe^{3+} that results in a reduction of the charge carrier concentration. The temperature dependence of electrical conductivity is shown in Figure 3.35. The plot of $ln\ \sigma T^{s}$ vs. $1000/T$ for LV3SF suggests that the non-adiabatic mechanism prevails over a wide temperature range (s= 3/2 gives a better linear fit than that of s=1).

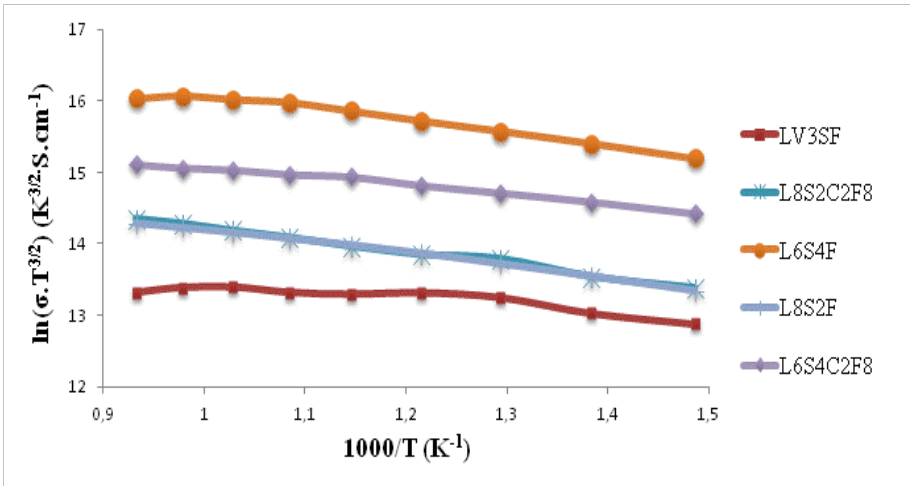

Figure 3.35. Electrical conductivity of $La_{0.57}V_{0.03}Sr_{0.4}FeO_{3-\delta}$ (LV3SF) compared with conventional iron containing cathode materials.

The plots in Figure 3.35 show good linear fit for most compositions. These fits have been used to calculate the activation energies, which are given in Table 3.2. The activation energy values are similar for all compositions, which is in agreement with 0.17eV and 0.13eV for $La_{0.6}Sr_{0.4}FeO_3$ and $La_{0.8}Sr_{0.2}FeO_3$ materials, respectively [91]. These similarities in E_a may be due to the equivalence of the Fe sites responsible of the mobility of charge carriers in all compositions. For $La_{0.6}Sr_{0.4}Co_{0.2}Fe_{0.8}O_3$ the value of 0.10eV obtained from the measurement agrees well with the value of 0.10eV reported earlier [87]. The E_a value for $La_{0.8}Sr_{0.2}Co_{0.2}Fe_{0.8}O_3$ was calculated as 0.15eV and L.W. Tai reported an activation energy of 0.14 eV between 400 and 800 ^oC [88].

Table 3.2. Calculated σ_{max}, σ_{800^oC} and E_a of specimens sintered at 1100 ^oC.

Composition	σ_{max}(S/cm)	σ_{800^oC} (S/cm)	Temp. Range(^{o}C)	E_a (eV)
$La_{0.57}V_{0.03}Sr_{0.4}FeO_3$	26.23	17.22	400-550	0.14
$La_{0.6}Sr_{0.4}FeO_3$	309.75	260.08	400-650	0.16
$La_{0.8}Sr_{0.2}FeO_3$	46.45	45.54	400-800	0.14

Table 3.2. Calculated σ_{max}, $\sigma_{800^{\circ}C}$ and E_a of specimens sintered at 1100 ^{o}C. (cont.)

$La_{0.6}Sr_{0.4}Co_{0.2}Fe_{0.8}O_3$	118.75	103.51	400-800	0.10
$La_{0.8}Sr_{0.2}Co_{0.2}Fe_{0.8}O_3$	48.80	48.57	400-800	0.15

Electrical Conductivity of $La_{0.6-x}V_xSr_{0.4}MnO_{3-\delta}$ (x = 0.005) – LV05SM: The conductivity of LV05SM material under air was measured using a four-probe DC method. The electrical conductivity of LV05SM sample as a function of temperature and the logarithm of electrical conductivity vs. reciprocal temperature in air are shown in Figure 3.36.

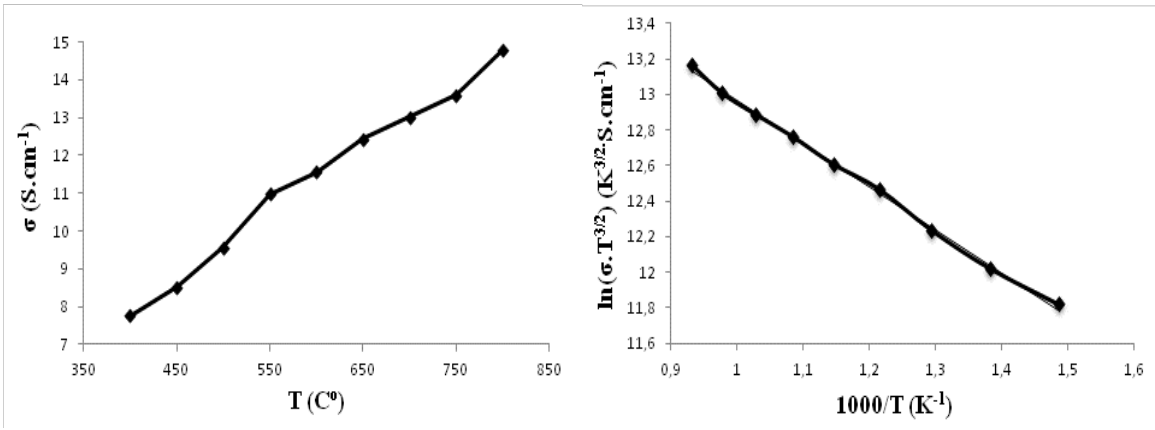

Figure 3.36. Temperature dependance of the electrical conductivity of LV05SM sample sintered at 1100 ^{o}C.

LSM has been known as a p-type semiconductor with electronic holes as charge carriers and essentially this hole motion in the d-orbitals energy levels of manganese is the reason for the electrical conductivity [92]. This is explained by the small polaron hopping of electron holes between Mn^{4+} and Mn^{3+} sites on octahedral corners. The conduction mechanism was completed by the hopping of electrons between multivalent metal ions at

B-site and oxygen ion following the way along B–O–B bonds. The equilibrium between Mn^{4+} and Mn^{3+} ions are controlled by a thermally activated disproportionation of Mn^{3+} in crystalline solids [83]:

$$2Mn_{oct}^{3+} \leftrightarrow Mn_{oct}^{4+} + Mn_{oct}^{2+} \tag{3.3}$$

Mn^{2+} ion is formed due to disproportionation but the conduction process occurs just via the hopping of carriers between Mn^{4+} and Mn^{3+} sites. As a result of charge transfer from Mn^{3+} site to neighboring Mn^{4+} site, the conduction process is assumed to develop, such as jumps of p-type carriers over available sites [93]. Since the electronic conductivity is usually 100-1000 times higher than the ionic conductivity for these kinds of oxides, the measured values reported herein are attributed to the electronic conductivity alone [94]. Generally, the conductivity gradually increases with increasing temperature. However, there is a fluctuation in conductivity at ca. 550 °C, which may be due to the loss of the lattice oxygen leading to more oxygen vacancies as a result of the thermally induced lattice oxygen losses [95], as expressed by Equation 3.4 [96]:

$$O_o^x + 2B_B^{\bullet} \rightarrow V_O^{\bullet\bullet} + 2B_B^x + \frac{1}{2}O_2(g) \tag{3.4}$$

where $B_B^{\bullet}$ refers to B^{4+} localized on B^{3+} site and B_B^x stands for B^{3+}. O_o^x is the lattice oxygen and $V_O^{\bullet\bullet}$ represents the oxygen vacancy. However, the lattice oxygen loss in p-type semiconductors at high temperatures would be the reason for the decrease of electrical conductivity, due to the reduction of charge carrier concentration (electron holes) [95], as expressed by Equation 3.4. There is only electrical conductivity fluctuation at about 550 ^{o}C and no permanent decrease of conductivity is observed in the temperature range of 400-800 ^{o}C. This means that there is a little lattice oxygen loss and thus relatively good structural stability of LV05SM. The temperature dependence of electrical conductivity is shown in Figure 3.37. The E_a value for σT was calculated as 0.20eV for LV05SM sample. This value is slightly high to that reported by R.V. Wandekar et al. as 0.14eV for $La_{0.76}Sr_{0.19}MnO_{3-\delta}$ sample and also to the results of Singanahally T. Aruna et al. where the activation energy of electronic conductivity was reported as 0.155eV for $La_{0.90}Sr_{0.10}MnO_{3-\delta}$ [83,97].

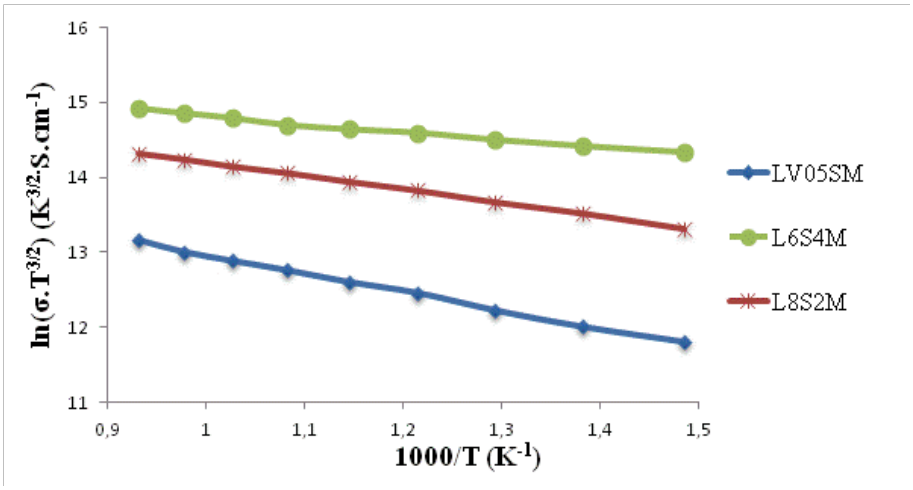

Figure 3.37. Electrical conductivity of $La_{0.595}V_{0.005}Sr_{0.4}MnO_{3-\delta}$ (LV05SM) compared with manganese containing conventional cathode materials.

As shown in Figure 3.37 the conductivity of LV05SM cathode material was compared with our synthesized $La_{0.8}Sr_{0.2}MnO_3$ sample, it is noted that the activation energy is calculated as 0.15eV. This activation energy value is nearly same with measurements on bulk sample of 0.12eV by S. Kuharuangrong [98]. $La_{0.6}Sr_{0.4}MnO_{3-\delta}$ with the higher Sr content material is synthesized in order to examine the conductivity dependence on the doping levels of Sr for $La_{1-x}Sr_xMnO_{3-\delta}$. The electrical conductivity of the sample is measured and calculated as 86 S/cm at 800 ^oC with the E_a (activation energy) of 0.099eV. The value for electrical conductivity is less than the reported by other researchers as 320 S/cm for electrical conductivity [99] but same for activation energy 0.099eV [100]. The reason for different conductivity values is possibly due to the difference in preparation condition such as synthesis methods and calcination conditions. The electrical conductivity at 800 ^oC and the maximum conductivity values, also the activation energy of all compositions are calculated and summarized in Table 3.3.

Table 3.3. Calculated σ_{max}, $\sigma_{800^{\circ}C}$ and E_a of specimens sintered at 1100 ^{o}C.

Composition	σ_{max}(S/cm)	$\sigma_{800^{\circ}C}$ (S/cm)	Temp. Range (^{o}C)	E_a (eV)
$La_{0.595}V_{0.005}Sr_{0.4}MnO_3$	14.8	14.8	400-800	0.20
$La_{0.6}Sr_{0.4}MnO_3$	96.42	86.02	400-800	0.09
$La_{0.8}Sr_{0.2}MnO_3$	46.90	46.90	400-800	0.15

Electrical Conductivity of $La_{0.5-x}Gd_xSr_{0.4}CoO_{3-\delta}$ (x = 0.10) – LG10SC: The electrical conductivity measurements were carried out by the four probe DC method in a tube furnace in air.

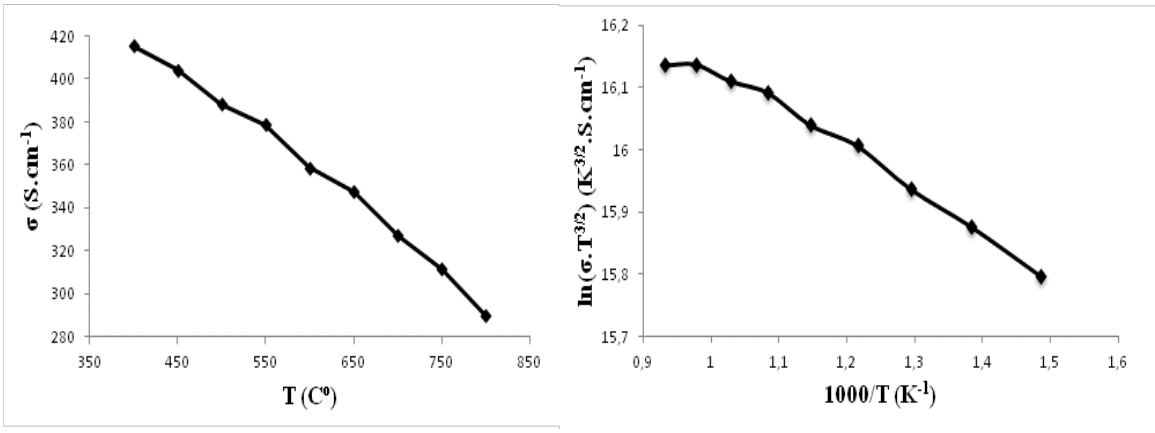

Figure 3.38. Temperature dependance of the electrical conductivity of LG10SC sample sintered at 1100 ^{o}C.

The transition metal elements such as Mn, Fe and Co can be found in compounds with multiple valences. In compounds e.g. $LaCoO_3$, equal numbers of n-and p-type charge carriers are arranged according to

$$2M^{3+} = M^{2+} + M^{4+} \ (M = Mn, Fe, Co) \qquad (3.5)$$

resulting in significantly high conductivity at high temperatures [101]. In the case of Sr substitution for La at A-sites, for example in LSC sample, the Sr^{2+} ions act as acceptors and the reaction $M^{3+} \rightarrow M^{4+}$dominates. Doping Sr for La also forms new oxygen vacancies, which promote ionic conductivity in the compound. As in this case, substitution of Gd^{3+} for A-site alters not only the crystal structure but also it enhances the hopping mechanism, which the conductivity of Sr-doped $LaCoO_3$ has been perfomed by a hopping mechanism [84]. These conductivity data depending on temperature between 400 - 800 ^oC and plot of ln $(\sigma.T^{3/2})$ vs. 1000/T for LG10SC sample covering the entire temperature range studied are plotted in Figure 3.38. The above figure shows that the electrical conductivity of LG10SC sample prefers a metal-like behavior. An increase in conductivity is found for decreasing temperature. This may be due to the charge-transfer between different valence configurations of Co^{3+} ions with the increase of temperature. LG10SC, L6S4C and L8S2C samples were sintered at the same temperature for the purpose of comparison and analysis.

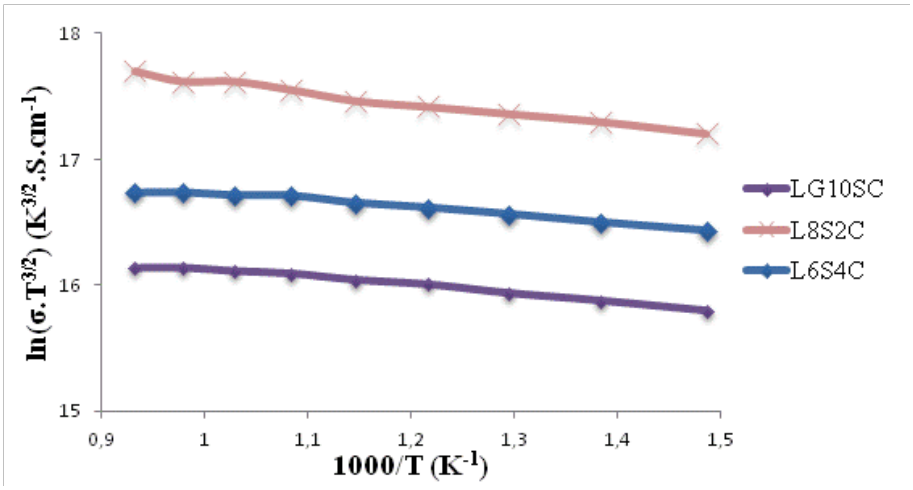

Figure 3.39. Electrical conductivity of $La_{0.5}Gd_{0.1}Sr_{0.4}CoO_{3-\delta}$ (LG10SC) compared with cobalt containing conventional cathode materials.

Figure 3.39 shows the logaritm of the electrical conductivity of these three samples depending on temperature and activation energies were calculated and tabulated in Table

3.4. L8S2C presents the highest conductivity about 1389 S/cm at 800 °C, which is obviously lower than the reported by Petric, A. about 1521 S/cm [27]. The electrical conductivity of L6S4C is about 525 S/cm at 800 °C, which is almost three times smaller than that of 1595 S/cm at 800 °C [27]. LG10SC sample has a lower electrical conductivity than mentioned cathode materials. This may be caused by the limited phase stability or by increasing interactions between point defects (e.g. $V_O^{\bullet\bullet}$ with Sr'_{La} or Co'_{Co}), which reduce the number of mobile oxygen vacancies necessary for electron hopping in LG10SC.

Table 3.4. Calculated σ_{max}, $\sigma_{800^\circ C}$ and E_a of specimens sintered at 1100 °C.

Composition	σ_{max}(S/cm)	$\sigma_{800^\circ C}$ (S/cm)	Temp. Range (°C)	E_a (eV)
$La_{0.5}Gd_{0.1}Sr_{0.4}CoO_3$	415.50	289.83	400-800	0.055
$La_{0.6}Sr_{0.4}CoO_3$	784.67	525.53	400-800	0.049
$La_{0.8}Sr_{0.2}CoO_3$	1702.31	1389	400-800	0.075

Comparison of the electrical conductivity of as-synthesized perovskite materials in air: The electrical conductivity values of LV0SM, LV05SC, LV3SF and LG10SC were measured as function of temperature seen in Figure 3.40.

The ionic conductivity of these materials is lower than 1 S/cm [102], thus the measured electrical conductivity can be approximated as the electronic conductivity of the materials. Figure 3.40 shows the measured electrical conductivity for all four compositions in atmospheric air from 400 to 800 °C. Electrical conduction in these perovskite is believed to occur in the conduction band set up by the overlapping O-2p and metal B-3d orbitals [83]. The materials exhibit high conductivities and all compositions except LV05SC and LG10SC showed metal-like temperature dependences i.e. decrease in conductivity with temperature.

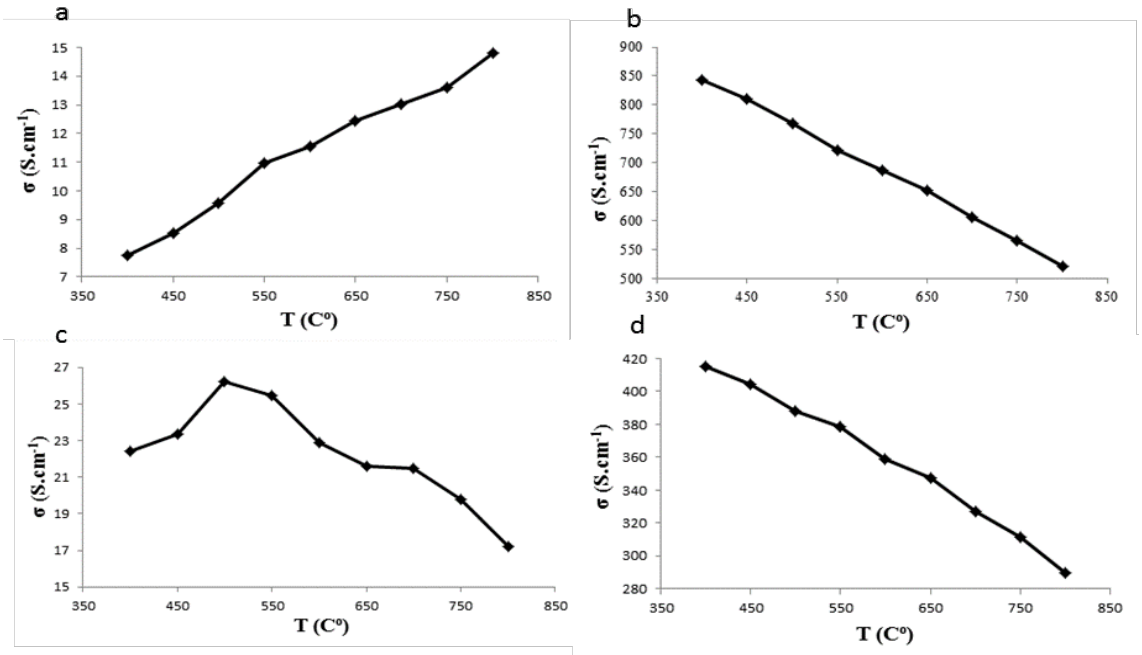

Figure 3.40. The electrical conductivity values of a) LV05SM, b) LV05SC, c) LV3SF, d) LG10SC.

The electronic conductivity of $La_{1-x}Sr_xCoO_{3-\delta}$ is very high as a metal oxide. It is generally not considered rate limiting step for the overall reaction, however, fundamental understanding of the conductive behavior of a material is still of great importance when it is to be used in an electrode. The electronic conductivity of perovskites like $La_{1-x}Sr_xCoO_{3-\delta}$ is closely related to the electronic structure. At increasing temperature cobalt is reduced, which decreases the hole concentration at the same time as the oxygen vacancy concentration increases according to Equation 3.6.

$$O_o^x + 2Co_{Co}^{\bullet} \rightarrow V_O^{\bullet\bullet} + 2Co_{Co}^x + \frac{1}{2}O_2(g) \qquad (3.6)$$

where $Co_{Co}^{\bullet}$ refers to Co^{4+} localized on Co site and Co_{Co}^x stands for Co^{3+}. O_o^x is the lattice oxygen and $V_O^{\bullet\bullet}$ represents the oxygen vacancy. Nakamura et. al. and Petrov et. al. have studied the electrical conductivity of $La_{1-x}Sr_xCoO_{3-\delta}$ as function of temperature using four point dc measurements [84,103]. The studies showed small polaron conduction behavior for $x < 0.3$ with a decreasing temperature at which the conductivity reaches its maximum. Mizusaki found further that σ is dependent on crystal structure as well as the oxygen

vacancy concentration. Mineshige A. have measured the electronic conductivity as function of temperature and showed a metal-insulator transition at x=0.25 at room temperature [104]. Both studies found that $La_{0.6}Sr_{0.4}CoO_{3-\delta}$ is p-type conductor as the conductivity decreased with decreased temperature. Søgaard, M. has derived the mobility of hopping mechanism in $La_{0.6}Sr_{0.4}CoO_{3-\delta}$ and found that the conductivity is inversely proportional to temperature [105]. This indicates that the conductivity of $La_{0.6}Sr_{0.4}CoO_{3-\delta}$ has metallic character. $La_{1-x}Sr_xCoO_{3-\delta}$ is known to have metal-like temperature dependence thus our compositions of LV05SC and LG10SC can be considered metal-like.

$LaMnO_3$ is the present material of choice in commercial SOFCs based on zirconia electrolytes. Electrical conductivity is enhanced by substitution of the La^{3+} site with divalent ions such as strontium or calcium. Of the alkaline earth dopants, Sr substitution is preferred for SOFC applications because the resultant perovskite forms stable compounds with high conductivity in the oxidizing atmosphere found at the cathode [92]. Divalent acceptor substitution (e.g. Sr^{2+}) for the trivalent A-site cation (e.g. La^{3+}) requires a balance in the electroneutrality. The introduced negative charge is compensated by an increase in valence of the B-site cations (electrical compensation) [106]. Transition metals (TM) as B-site cations perform TM^{4+}/TM^{3+} couples which act as hopping sites for electrons/holes, i.e. for n-type or p-type conductivity. When a La^{3+} ion at the A-site is replaced by a Sr^{2+} ion, an electric hole is formed on the B-site to maintain the electroneutrality, leading to the increased electrical conductivity [107]:

$$LaMnO_3 \xrightarrow{xSrO} La_{1-x}^{3+}Sr_x^{2+}Mn_{1-x}^{3+}Mn_x^{4+}O_3 \qquad (3.7)$$

The disproportionation of Mn^{3+} ions into Mn^{2+} and Mn^{4+} (Equation 3.3) pairs seems to provide a compensation mechanism, which is able to account for this apparent buffering of added Sr ions in $LaMnO_3$. $La_{1-x}Sr_xMnO_{3-\delta}$ has electrical properties on the border between that of a p-type semiconductor and a metal [92]. In this temperature range conductivity is increased with increasing temperature for LV05SM, typical of semiconductor behavior.

Lanthanum ferrite derivatives ($LaFeO_3$) have been investigated in detail and provide both electrical and ionic conduction as to be a promising candidate as IT-SOFC cathode material [108]. In LSF perovskites, B-site lattice cations are responsible for the

electron defect creation in perovskite oxides through strong overlapping B–O–B bonds shown as:

$$B^{n+} - O^{2-} - B^{(n+1)+} \Rightarrow B^{(n+1)+} - O - B^{(n+1)+} \Rightarrow B^{(n+1)+} - O^{2-} - B^{n+} \quad (3.8)$$

With increasing temperature, the conductivity for LV3SF sample increases and reaches the maximum at about 500 ^{o}C that corresponds to the metal insulator transition temperature (TMI). The LSF samples exhibit a typical semiconductor-like behavior, which can be ascribed to electron hopping conduction since the localized electronic carriers have a thermally activated mobility [26]. If temperature is higher than TMI, the value of σ begins to decrease with increasing temperature and the sample exhibits a metal-like behavior. This metal-like transport behavior is due to the orbital overlap between Fe 3d and O 2p, which is the characteristic feature for the iron-based perovskite oxides [109]. Thus, our synthesized LV3SF material shows the same trend as LSF.

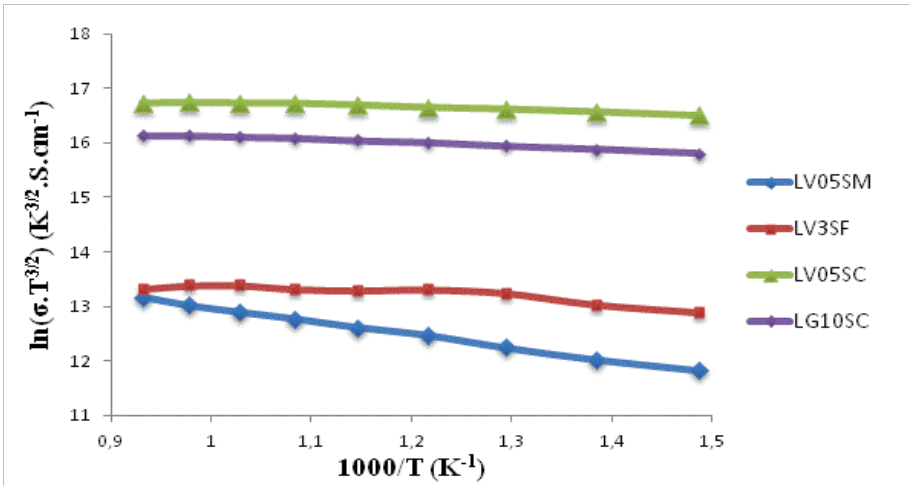

Figure 3.41. Electrical conductivity of LV05SM, LV3SF, LV05SC and LG10SC samples in comparison.

As a comparison between the as-synthesized materials, the Figure 3.41 shows the Arrhenius plots of each samples. The cathode materials LV05SC and LG10SC have better conductivity values of 843.43 and 415.50 S/cm among others, and they have lower activation energies of 0.045 and 0.055eV, respectively. The low value of activation energy

emphasizes the high catalytic activity of the electrode material [110]. Vanadium doped LSM sample has the lowest conductivity value of 14.8 S/cm with activation energy of 0.20eV and it continues with LV3SF material with a value of 26.23 S/cm and E_a of 0.14eV. Although the conductivity values measured are lower than those of other reference cathodes, there are perovskite materials in literature with low conductivity have reported with excellent cathode performance [111, 112]. Therefore, it is believed that in comparison with the electrical conductivity, the higher ionic conductivity should be more important for being a SOFC cathode. In the following section, it is found that synthesized cathodes exhibit attractive electrochemical performances for oxygen reduction.

3.4. Electrochemical Impedance Spectroscopy Results

The results from Four Probe Method measurements show that the conductivity values are lower than expected. However, there are more important expectations than the electrical conductivity like the ionic one, which is one of the main features of the cathode performance for SOFC. The most complex and least understood process in the overall SOFC-cathode mechanism is for the oxygen reduction reaction. This process is often referred to as the surface exchange of oxygen, perhaps because it is still not known which of the many elementary reactions are rate limiting the overall reaction and in which order they occur. The surface exchange reaction is generally believed to consist of the following sub reactions (not elementary): O_2 adsorption, O_2 dissociation, and incorporation of oxygen species into the oxide lattice and the reduction of either diatomic or mono-atomic oxygen species:

$$O_{2\,(g)} + ne^- \rightarrow O_{2,ads}^{n-} \tag{3.9}$$

$$O_{2,ads}^{n-} + me^- \rightarrow 2O_{ads}^{(n+m)-} \tag{3.10}$$

$$O_{ads}^{(n+m)-} + (2-n-m)e^- + V_O^{\cdot\cdot} \rightarrow O_O^X \tag{3.11}$$

The reduction reaction is generally considered to proceed simultaneously with the other reactions to form arbitrarily charged surface species e.g. $O_{2,ads}^{n-}$, O_{ads}^{n-} or O_{O}^{n-}, depending on which reaction is the rate-limiting step and there is much recognition in literature [113]. This topic is still under discussion.

In this section of thesis, to understand the ORR mechanism, the complex impedance measurements were carried out on a selected number of compositions, versus the oxygen partial pressure PO_2 at different temperatures. Figure 3.42 shows the some impedance responses for the single-phase LV05SM electrode on the YSZ electrolyte that is measured under different oxygen partial pressures and collected in every 50 °C in the temperature range from 400 to 800 °C.

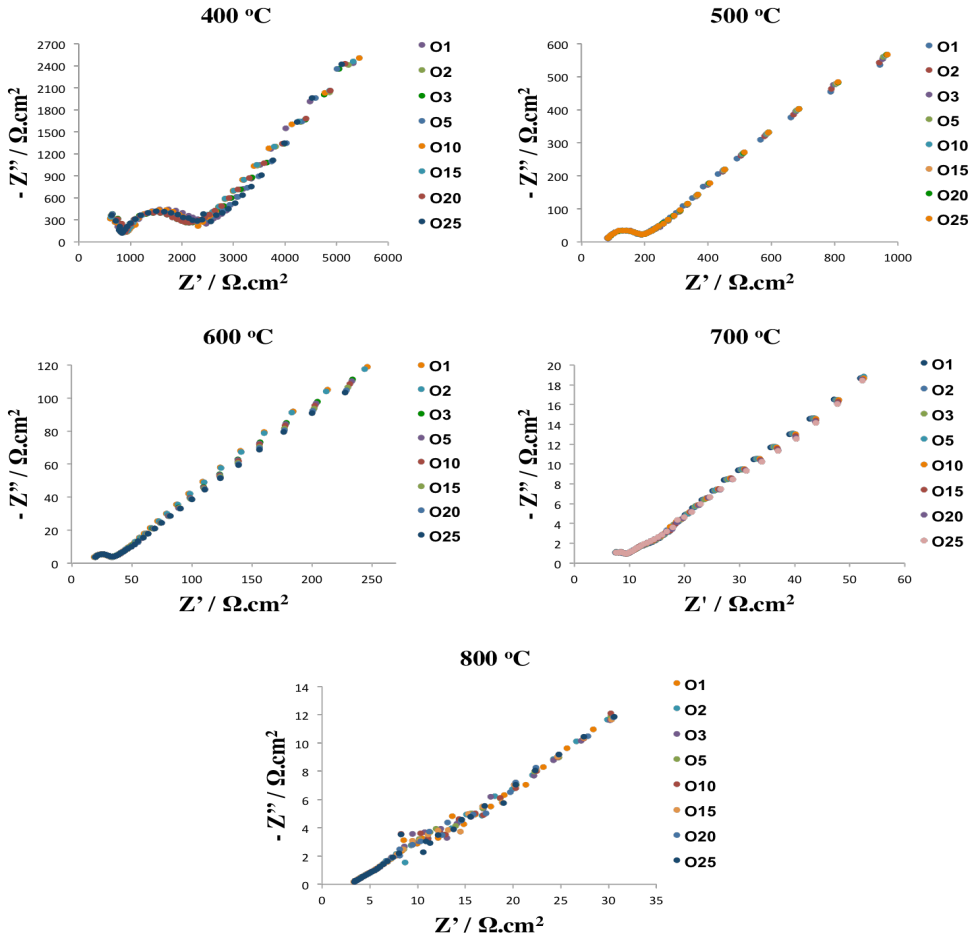

Figure 3.42. Complex impedance plots for LV05SM/YSZ/LV05SM symmetric cell at between 400-800 °C for different oxygen partial pressures.

It is clearly seen in Figure 3.42 that the high frequency part of the two clearly resolved impedance contributions has an apparent shape in the Nyquist plots below the 500 ºC. With increasing operating temperature, the high-frequency arc size decreased noticeably, and the arc was totally disappeared at 500 ºC and higher. An additional arc at the low frequency range appeared when the operating temperature was elevated to 700 ºC. The impedances of a symmetric cell may arise from both the electrodes and electrolyte. The electrolyte typically performs as an ideal resistor and displays only a dot in the Nyquist plots at high temperatures in the investigated frequency range of 10^{6}-10^{-1} Hz. However, a semi-circle associated with the oxide ion diffusion around the grain boundary of the electrolyte also appeared in the high frequency range with the decrease in operation temperature. For example, Zhan et al. observed that the arc associated with the grain boundary ionic diffusion appeared at an operation temperature of 460 ºC in the complex impedance plane plots [114].

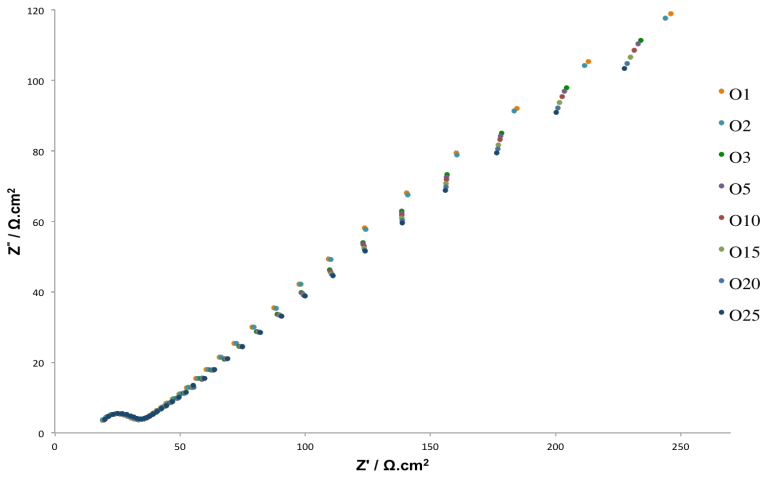

Figure 3.43. Typical EIS of a symmetric LV05SM/YSZ/LV05SM cell measured at 600 ºC while fixing the oxygen partial pressure between 1 – 25%.

As seen from the above Figure 3.43, with decreasing in the partial pressure of oxygen, the impedance arc increases significantly, particular at low frequencies. For most

of the impedance curves, two arcs could be separated at high and low frequency regions. This indicates that at least two electrochemical processes contribute to the overall electrochemical reaction. The electrode impedance responses at high frequencies appears to be independent of oxygen partial pressure at all temperatures, while those at low frequencies, show a significant dependence on the oxygen partial pressure. The magnitude of both arcs changes significantly with the temperature Figure 3.42.

In order to have more information to interpret properly the processes involved in the cathode/electrolyte interface, a study of the influence of oxygen partial pressure in the electrode impedance as a function of temperature was required. The oxygen partial pressure of the atmosphere is varied between 0.01 and 0.25 atm by mixing O_2 with N_2 using mass flow controllers.

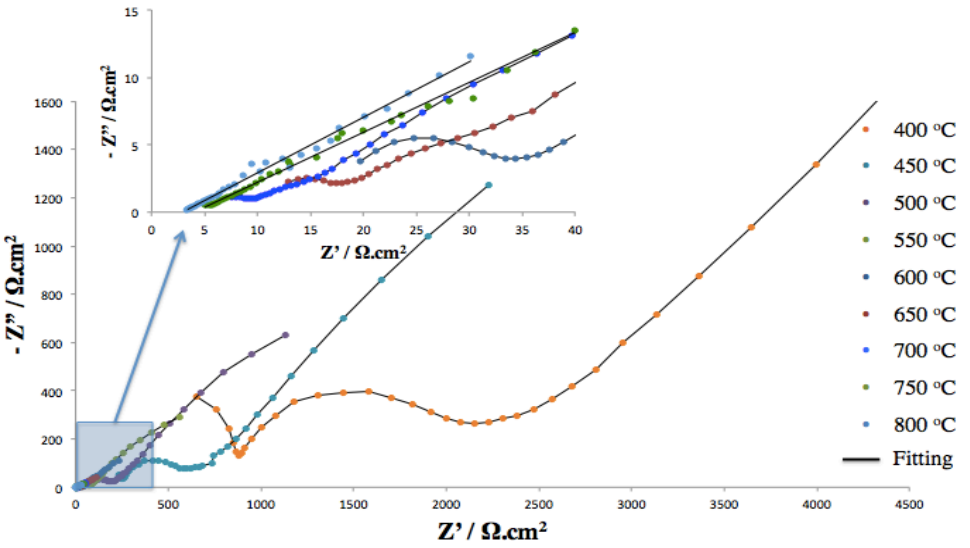

Figure 3.44. Impedance spectra of LV05SM cathode measured in 3% O_2 – 97% N_2 at various temperatures with data fitting.

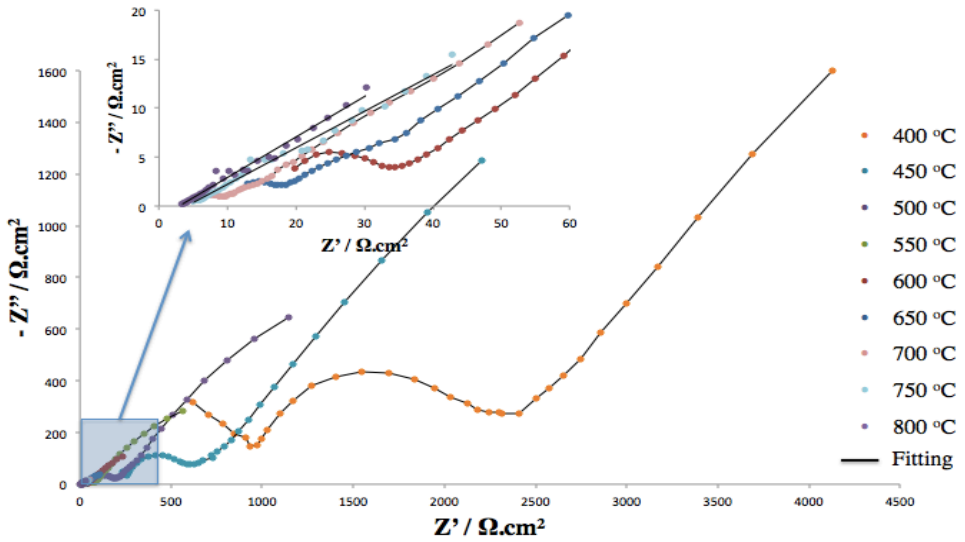

Figure 3.45. Impedance spectra of LV05SM cathode measured in 10% O_2 – 90% N_2 at various temperatures with data fitting.

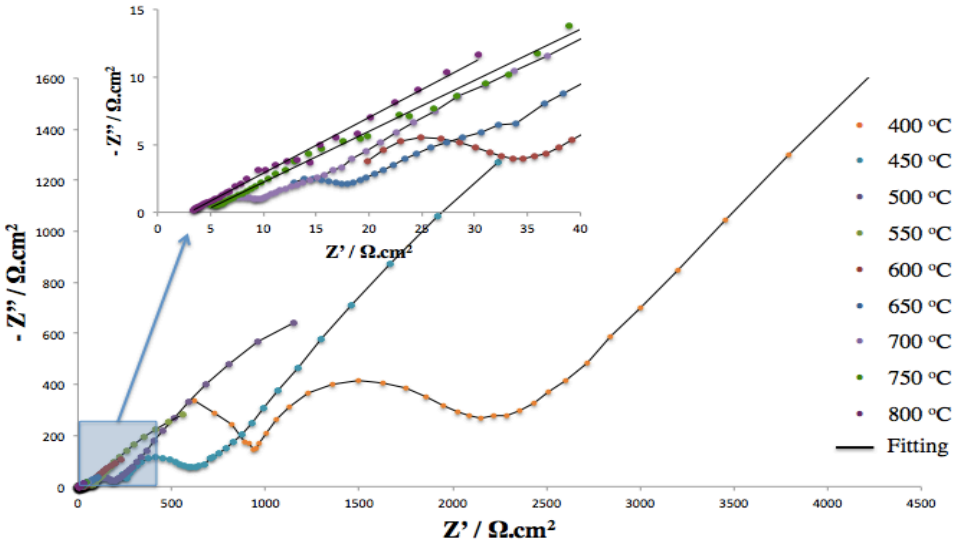

Figure 3.46. Impedance spectra of LV05SM cathode measured in 15% O_2 – 85% N_2 at various temperatures with data fitting.

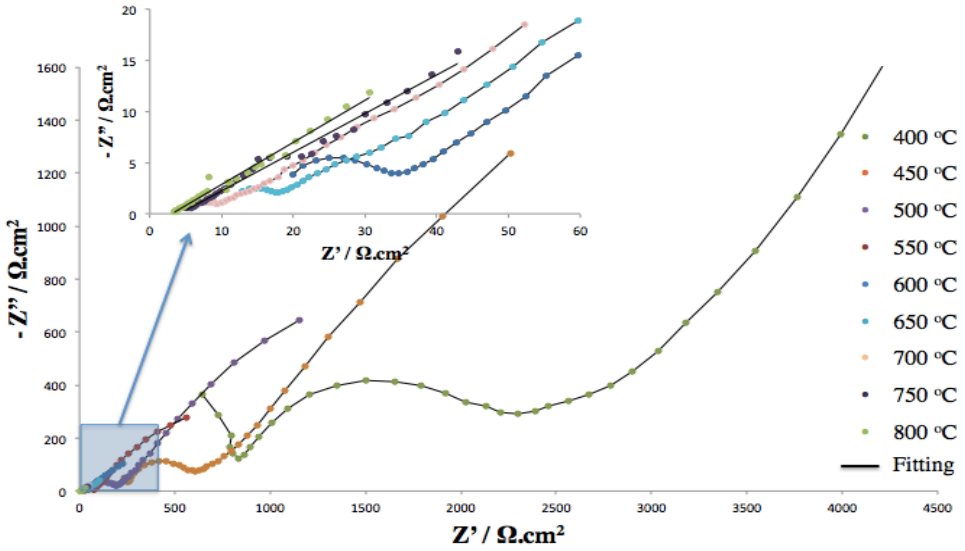

Figure 3.47. Impedance spectra of LV05SM cathode measured in 25% O_2- 75% N_2 at various temperatures with data fitting.

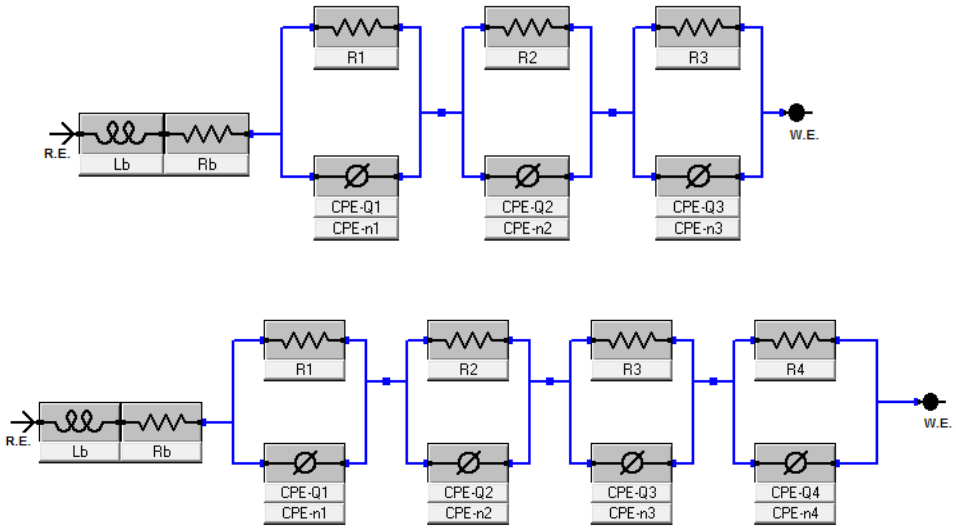

Figure 3.48. The equivalent circuits used for fitting the impedance data for a) 500-600 °C b) 400, 700 and 800 °C.

Figure 3.44, 3.45, 3.46 and 3.47 show some typical EIS diagrams of the LV05SM cathode measured at 400 – 800 ºC in air for 3-10-15-25% O_2. They are composed of a large arc located in between the high frequency and low frequency zones, respectively. All Nyquist plots were fitted to the equivalent circuit of ***L-R_b-(R_1-QPE_1)-(R_2-QPE_2)...(R_i-QPE_i)*** shown in Figure 3.48 by means of the Gamry software. The data fitting contemplates three processes in the electrode reaction; the results show good agreement between the experimental and fitted data. The L is an inductance caused by the device and the connect leads and the R_b is the ohmic resistance of YSZ electrolyte. The remaining components are associated with the electrode where three series connected elements (*RQ*) describe the three processes that contribute to the impedance of electrode/electrolyte interface. The numbers of R_i - QPE_i impedances (made by a resistor R_i in parallel with a constant phase element QPE_i) in series are dependent on operation temperature. The exact equivalent circuits adopted for fitting the EIS data at the temperatures of 500 - 600 ºC are fitted well to an equivalent circuit of *L-R_b-(R_1-QPE_1)-(R_2-QPE_2)-(R_3-QPE_3)* and the temperatures of 400, 700 and 800 ºC are in agreement with an equivalent circuit of *L-R_b-(R_1-QPE_1)-(R_2-QPE_2)-(R_3-QPE_3)-(R_4-QPE_4)*. The first component (R_1QPE_1) appears as a semi-circle at the high-frequency region, the second one (R_2QPE_2) as a semi-circle at the medium-frequency region and the third one (R_3QPE_3) as a semi-circle at the low-frequency region.

With higher operation temperature, the size of the semi-circle at the high frequency decreased. It totally disappeared above 500 ºC. This implies that the well-separated semi-circle in the EIS high frequency range at 400 – 500 ºC may be associated with oxide-ion transfer through YSZ electrolyte grain boundaries. The second semi-circles in the EIS data are contributed from oxygen reduction over the LV05SM electrode. Impedance at high and intermediate frequencies is related to ion and electron transfer at the electrode, electrolyte, and collector/electrode interfaces, while the impedance at low frequencies is associated with non-charge transfer, such as oxygen surface exchange and gas-phase diffusion inside and outside the electrode layer [115].

Table 3.5 summarizes the fitting parameters as a function of temperature for LV05SM/YSZ/LV05SM under different partial pressure of oxygen, as well as the values of area specific resistance (ASR).

Table 3.5. The fitting parameters as a function of temperature for LV05SM/YSZ/LV05SM in PO_2.

PO_2	T (°C)	400	500	600	700	800
O3	*Lb (H)*	5.09×10^{-8}	7.39×10^{-9}	5.31×10^{-6}	1.37×10^{-10}	8.44×10^{-11}
	Rb ($\Omega.cm^2$)	1.0722	0.5108	0.18934	0.0124	0.000381
	R1 ($\Omega.cm^2$)	42040	4048	2334	4.486	1.8522
	R2 ($\Omega.cm^2$)	415.8	36.34	6.19	0.399	0.1723
	R3 ($\Omega.cm^2$)	576.8	60.02	9.802	1.0992	0.1323
	R4 ($\Omega.cm^2$)	3964	-	-	425.2	393
	ASR ($\Omega.cm^2$)	4.69×10^{4}	4144	2349.9	431.18	395.15
O10	*Lb (H)*	1.07×10^{-4}	1.50×10^{-8}	5.10×10^{-6}	7.77×10^{-11}	2.23×10^{-10}
	Rb ($\Omega.cm^2$)	1.0722	0.5108	0.18934	0.0124	0.000381
	R1 ($\Omega.cm^2$)	42040	4042	2312	4.354	1.8304
	R2 ($\Omega.cm^2$)	415.2	36.32	6.158	0.3152	0.1464
	R3 ($\Omega.cm^2$)	576.4	60.02	9.77	0.6538	0.00085
	R4 ($\Omega.cm^2$)	1884	-	-	424.4	363.4
	ASR ($\Omega.cm^2$)	4.48×10^{4}	4138.3	2327.92	429.72	365.37
O15	*Lb (H)*	8.33×10^{-5}	5.47×10^{-9}	4.10×10^{-6}	6.22×10^{-13}	5.03×10^{-9}
	Rb ($\Omega.cm^2$)	1.0722	0.5108	0.18934	0.0124	0.000381
	R1 ($\Omega.cm^2$)	42040	4042	2312	4.344	1.8206
	R2 ($\Omega.cm^2$)	413.2	36.22	6.106	0.3048	0.1403
	R3 ($\Omega.cm^2$)	524.4	59.88	9.756	0.6148	0.00031
	R4 ($\Omega.cm^2$)	581.4	-	-	415.8	363.4
	ASR ($\Omega.cm^2$)	4.35×10^{4}	4138.1	2327.86	421.06	365.36

Table 3.5. The fitting parameters as a function of temperature for LV05SM/YSZ/LV05SM in PO_2. (cont.)

O25	*Lb (H)*	8.35×10^{-9}	2.48×10^{-9}	4.59×10^{-6}	1.83×10^{-11}	5.92×10^{-8}
	Rb ($\Omega.cm^2$)	1.0722	0.5108	0.18934	0.0124	0.000381
	R1 ($\Omega.cm^2$)	42040	4002	2312	4.306	1.8028
	R2 ($\Omega.cm^2$)	164.18	36.22	6.002	0.241	0.1178
	R3 ($\Omega.cm^2$)	225.2	59.7	9.682	0.3094	0.000147
	R4 ($\Omega.cm^2$)	578.4	-	-	415.8	342.6
	ASR ($\Omega.cm^2$)	4.29×10^{4}	4097.92	2327.86	420.65	344.52

The inductance value was shown but not considered, because it is not characteristic of the studied compound. It can be seen that the electrolyte resistance (R_b) as well as the four resistances (R_1, R_2, R_3, R_4) associated with the kinetic of electrode processes decrease with increasing temperature, as expected. It also can be seen that the electrolyte resistance, R_b, does not depend on the oxygen partial pressure, remaining stable at each temperature, which is in agreement with the behavior of a pure ionic conductor as the YSZ electrolyte.

The polarization resistance (R_p) is the purely ohmic part of the electrode resistance. It can be determined as the sum of the resistances of each individual process ($R_p = R_1 + R_2 + R_3 + R_4$). For the symmetrical cell, the measured polarization resistance reflects the sum of the polarization resistance of the two electrodes investigated. Thus, all the cell impedances were normalized by the superficial area (0.04 cm^2), so the R parameters obtained in the fitting for each process were divided by two to consider the contribution of the two electrodes.

It is well known that different processes for oxygen reduction over mixed ionic and electronic conducting electrodes have different relationships with the oxygen partial pressure. The most commonly used parameter to determine the rate-determining step in ORR is n, which indicates the relation between the electrode resistance and oxygen partial pressure [116], as expressed by Figure 3.49:

$$R = R^o(pO_2)^{-n} \quad (3.12)$$

$$n = 1,\ O_2(g) \leftrightarrow O_{2,ads} \quad (3.13)$$

$$n = {}^1/_2,\ O_{2,ads} \leftrightarrow 2O_{ads} \quad (3.14)$$

$$n = {}^3/_8,\ O_{TPB} + e' \leftrightarrow O^-_{TPB} \quad (3.15)$$

$$n = {}^1/_4,\ O_{ads} + 2e' + V_{\ddot{O}} \leftrightarrow O^x_O \quad (3.16)$$

$$n = {}^1/_8,\ O^-_{TPB} + e' \leftrightarrow O^{2-}_{TPB} \quad (3.17)$$

$$n = {}^1/_{10},\ O^{2-}_{TPB} + V_{\ddot{O}} \leftrightarrow O^x_O \quad (3.18)$$

Figure 3.49. The relations of polarization resistance to PO_2 of corresponding ORR processes on the cathode.

The *n* value gives information about the species involved in the electrode reaction (Figure 3.49). The overall ORR can be summarized as ${}^1/_2\,O_2(g) + 2e^- \rightarrow O^{2-}$. It is a complex multi-step process, which practically involves the gas diffusion; surface adsorption/dissociation and charge transfer reaction. For metal oxides with solid electrolytes, $n = 1$ can be attributed to the gaseous diffusions and adsorptions of oxygen molecules as a limiting step; $n = 1/2$ corresponded to the oxygen adsorption-desorption process, involving oxygen diffusion at the interface of gas/cathode and surface diffusion of related intermediate oxygen species as a limiting step; and *n = 3/8* interpreted a reaction controlled by the atomic oxygen diffusion process (along the two phases electrode/electrolyte contact) followed by a charge transfer as a limiting step; $n = 1/4$ related to the charge transfer process on the electrode, occurring at the interfaces of current collector/electrode and the electrode/electrolyte as a limiting step; and *n = 1/8* referred to the formation of oxide ions form the intermediate species as a limiting step; and *n = 1/10* or *n = 0* can been attributed to the oxygen ion diffusion from the triple phase boundary (TPB) to the electrolyte, respectively. Representative profiles for PO_2 dependence of R_1,

R_2, R_3 and $R_2 + R_3$ are shown in Figure 3.50 and the fitting results at various temperatures are listed in Table 3.5.

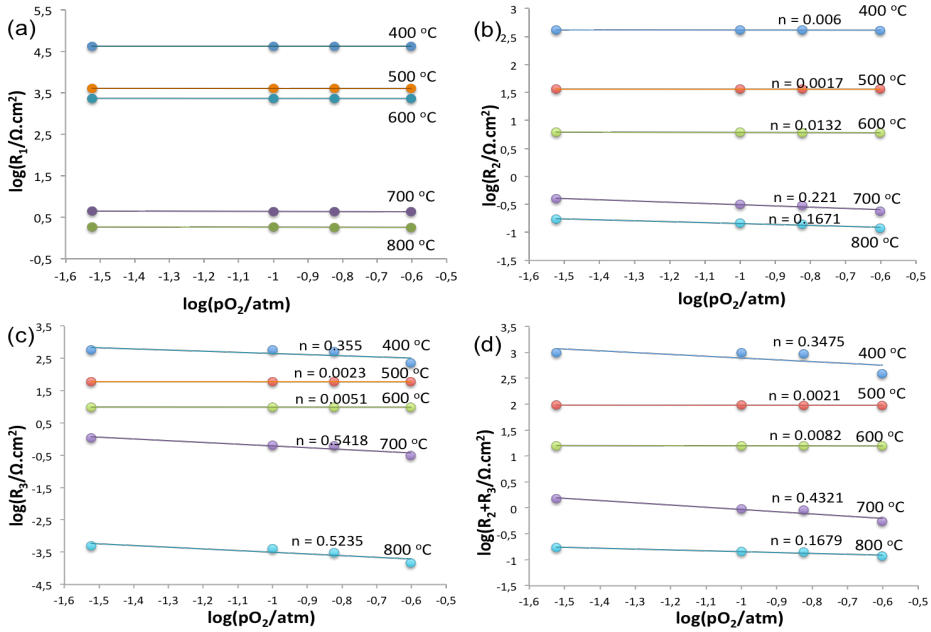

Figure 3.50. Dependence of three resistances at high, medium and low frequency on oxygen partial pressure for LV05SM/YSZ interface between 400 - 800 °C (a) R_1; (b) R_2; (c) R_3 and (d) $R_2 + R_3$.

From the fitted data values, R_1 is independent on the oxygen partial pressure and R_2 and R_3 increases with decreasing PO_2.

It is clearly observed that R_1 did not have a monotonic dependence on oxygen partial pressure. The resistance of the high frequency arc decreases with increasing temperatures, and it is independent of the oxygen partial pressure. The oxygen partial pressure dependence calculated as $n = 0$. These results indicate that this process can be related neither to charge transfer nor to diffusion processes. Therefore, the first arc could be caused by the oxygen ions transferring through the electrolyte/electrode interface.

The polarization resistances R_2 and R_3, associated with Arc2 and Arc3 appearing at intermediate frequency ranges, are found to be highly dependent on oxygen partial

pressure. Both R_2 and R_3 decreased with increased oxygen partial pressure and increased temperature. The values obtained for n are 0.017 - 0.221 for R_2 and 0.0023 - 0.54 for R_3 at the investigated temperatures. Considering the weak oxygen partial pressure, this process could be related to an oxygen atom diffusion followed by a charge transfer.

The process associated with the low-frequency arc presents lowest impedance values. $R_2 + R_3$ was found to be dependent on PO_2 with the value $n = 0.021 – 0.4321$. It suggests that both R_2 and R_3 are associated with electron transfer. In other words, the electron transfer process may be composed of two successive intermediate steps, showing similar importance in the charge transfer process. The polarization resistance of this process quickly reduced with increasing oxygen partial pressure, which is in agreement with the behavior of a gas diffusion process. An increase of oxygen partial pressure results in a sufficient supply of oxygen to the electrode from the gas phase thereby effectively eliminating diffusion polarization resistance.

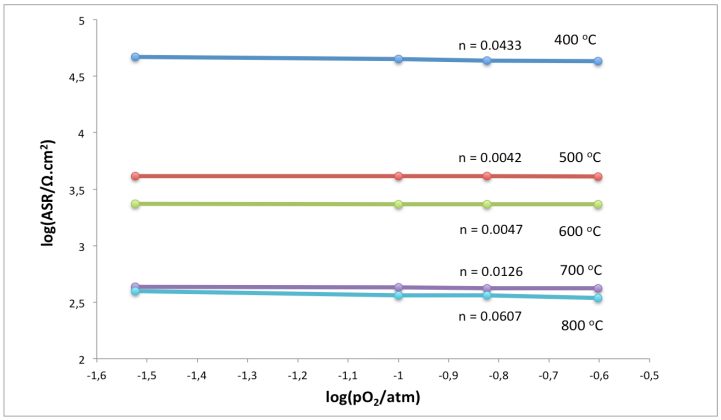

Figure 3.51. The dependence of the ASR of the LV05SM/YSZ interface as a function of oxygen partial pressure at different temperatures.

The ASR values for oxygen reduction reaction are obtained by the sum of individual resistances associated with each process. As expected, the ASR for LV05SM/YSZ interface decreases notably with increasing temperature and slightly with the oxygen partial pressure as shown in Figure 3.51. The characteristic of ASR shows quite

weak PO_2 dependency (n = 0.0042 – 0.0607), which could be related to the oxide ion transfer within the bulk electrode and/or from electrode to YSZ electrolyte through the TPB. Therefore, this process is the major rate-limiting step for LV05SM cathode.

Figure 3.52 shows the impedance responses for the single-phase LV05SM electrode on the GDC electrolyte that is measured under different oxygen partial pressures and collected in every 50 ºC in the temperature range from 400 to 800 ºC.

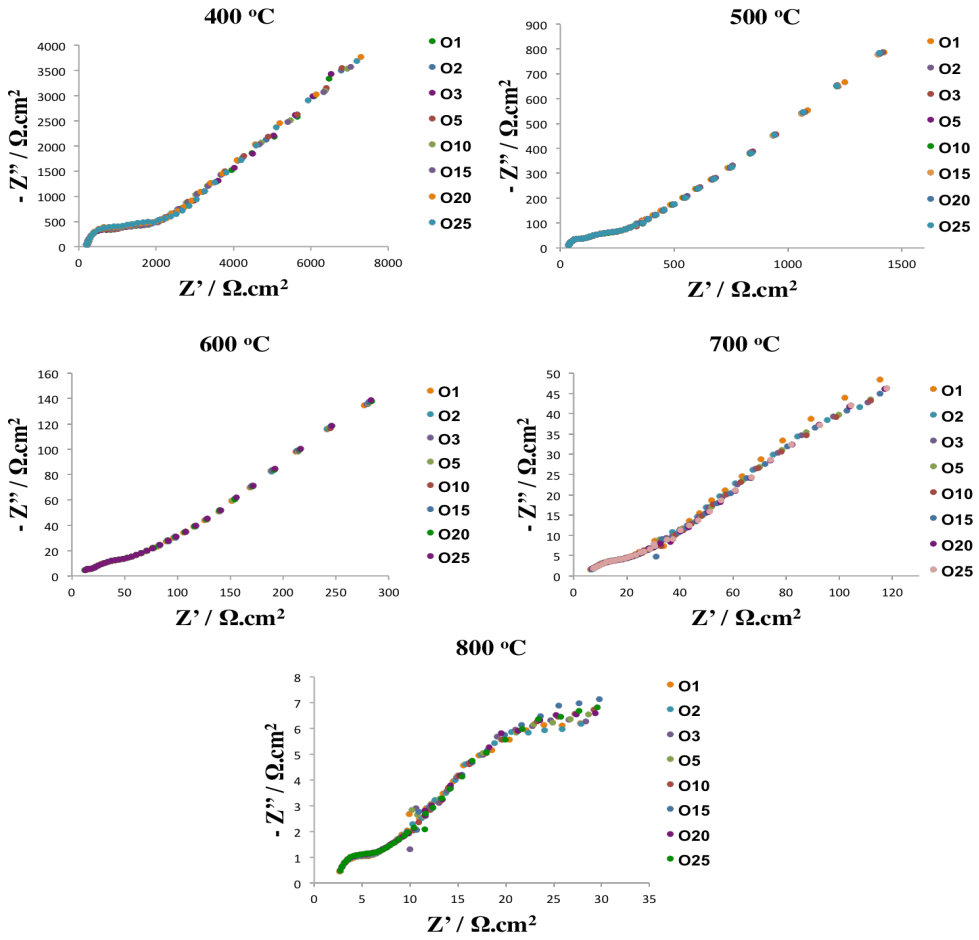

Figure 3.52. Complex impedance plots for LV05SM/GDC/LV05SM symmetric cell at between 400-800 °C for different oxygen partial pressures.

From the above Figure 3.52, EIS diagrams are composed of arcs located in high frequency and low frequency zones, respectively. This indicated that at least two different steps involved in the ORR over the electrode. It is clearly seen that below the 700 ºC, two well-separated semi-circles are observed in the high frequency part of the Nyquist plots. With increasing operating temperature, the high-frequency arc size decreased noticeably, and the arc was totally disappeared at 700 ºC and higher. The impedances of a symmetric cell may arise from both the electrodes and electrolyte. The electrolyte typically performs as an ideal resistor, which represents the intercept value in the impedance diagram at high frequency side with the real axis and it corresponds to the electrolyte resistance, electrode ohmic resistance and lead resistance. With the decrease in operation temperature, a semi-circle associated with the oxide ion diffusion around the grain boundary of the electrolyte appeared in the high frequency range.

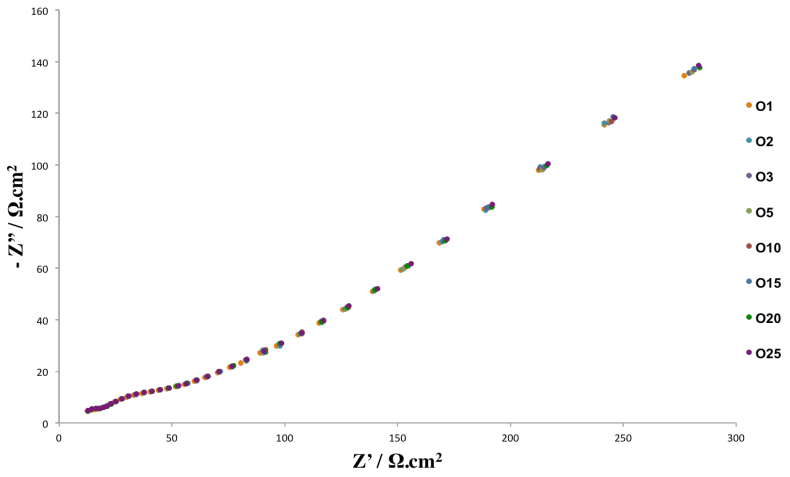

Figure 3.53. Typical EIS of a symmetric LV05SM/GDC/LV05SM cell measured at 600 ºC while fixing the oxygen partial pressure between 1 – 25%.

Figure 3.53 illustrates the impedance diagrams measured at 600 °C under different oxygen partial pressures. Three arcs at high, medium and low frequencies can be observed. In general, the high and medium frequency arcs show little dependence on the oxygen partial pressure, while the amplitude of the low frequency arc increases slightly as

decreasing the oxygen partial pressure. The magnitude of arcs changes significantly with the temperature (Figure 3.52).

In order to determine the processes involved in the ORR, the effect of oxygen partial pressure in the electrode impedance as a function of temperature was further studied. The oxygen partial pressure of the atmosphere was varied between 0.01 and 0.25 atm by mixing O_2 with N_2 using mass flow controllers.

The typical complex EIS plots between 400 - 800 ºC in air at 3-10-15-25% O_2 for the LV05SM cathode with GDC electrolyte are depicted in Figure 3.54, 3.55, 3.56 and 3.57. Two visible semi-circular arcs in the complex impedance plots are evident.

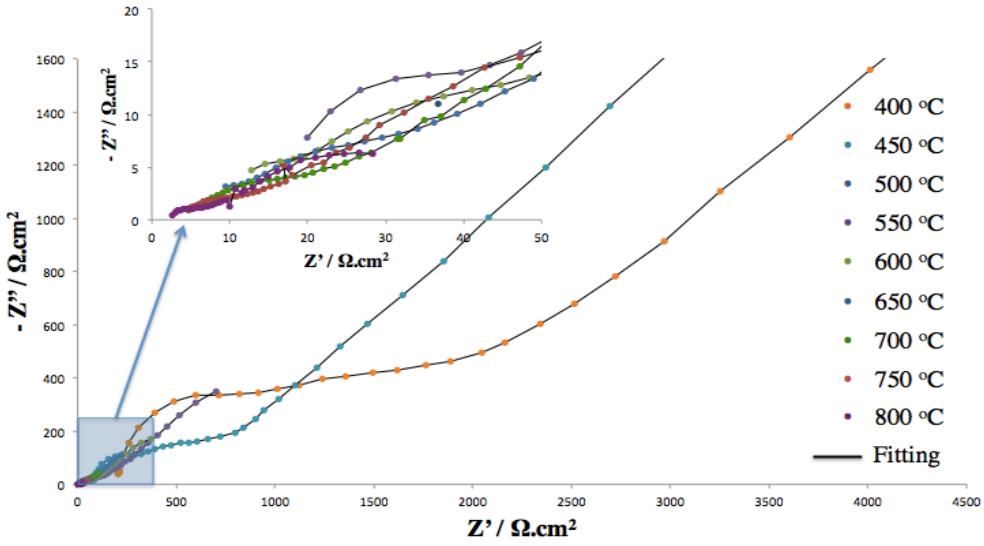

Figure 3.54. Experimental and fit Nyquist plots for a symmetrical LV05SM/GDC/LV05SM cell measured at 3% O_2 – 97% N_2 between 400 – 800 ºC.

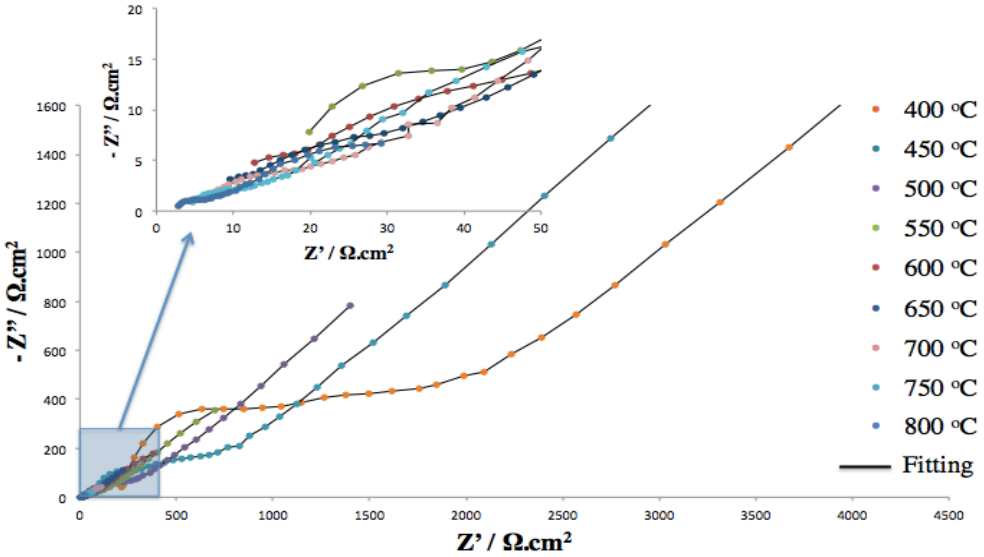

Figure 3.55. Experimental and fit Nyquist plots for a symmetrical LV05SM/GDC/LV05SM cell measured at 10% O_2 – 90% N_2 between 400 – 800 °C.

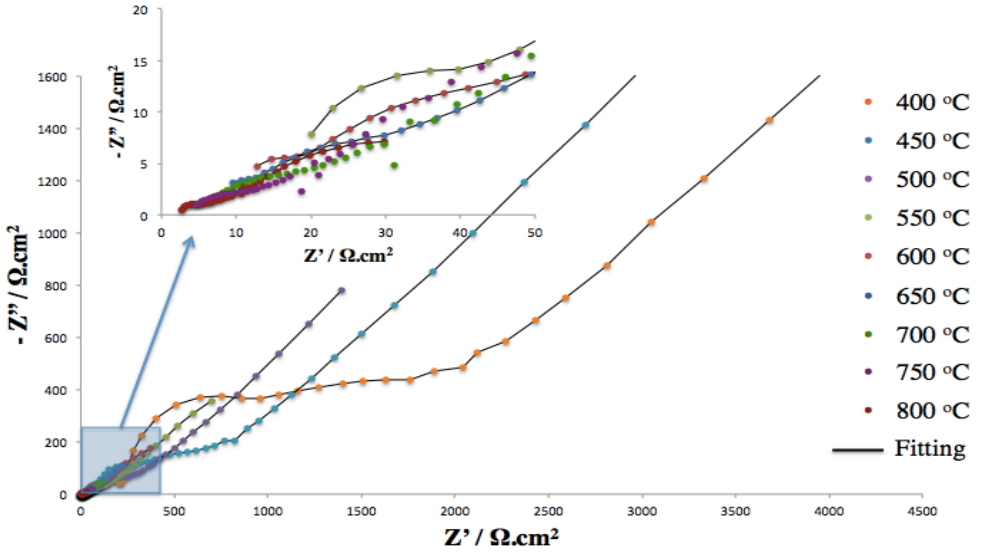

Figure 3.56. Experimental and fit Nyquist plots for a symmetrical LV05SM/GDC/LV05SM cell measured at 15% O_2 – 85% N_2 between 400 – 800 °C.

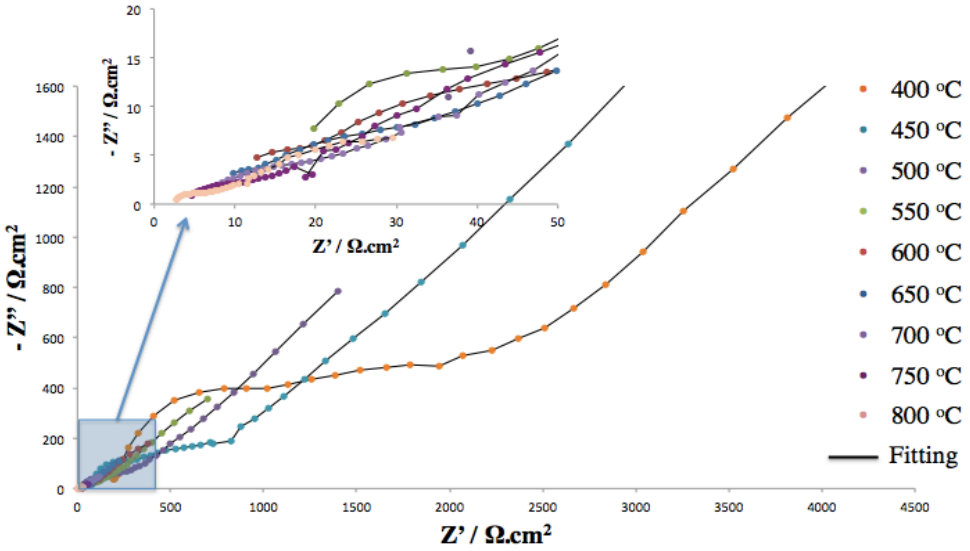

Figure 3.57. Experimental and fit Nyquist plots for a symmetrical LV05SM/GDC/LV05SM cell measured at 25% O_2 – 75% N_2 between 400 – 800 ºC.

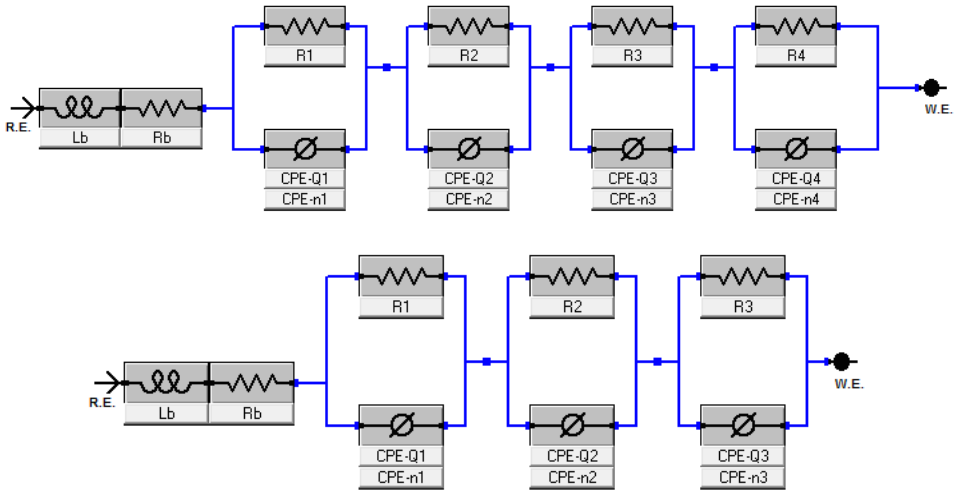

Figure 3.58. The equivalent circuits adopted for fitting the impedance data for a) 400-500 ºC b) 600, 700 and 800 ºC.

Almost similar trends of the complex impedance diagrams were observed. Indeed, several intermediate steps are involved during the overall ORR process. These steps may occur simultaneously on different time scales, which contribute significantly to the total electrode polarization resistance R_p. However, entire frequency response can accurately be described by a mid-frequency (MF) depressed semicircle and a low frequency (LF) skewed semi circular arc. Presence of two semi circular arcs in the complex impedance plane suggests that the oxygen reduction reaction over the electrode was composed of at least two distinct processes. The overall size of the two arcs is generally attributed to the R_p. However, with the decrease in operation temperature, a semi-circle associated with the migration of oxide ion through the grain boundary of the GDC electrolyte also appeared in the high-frequency range [117].

The experimental impedance spectrum, simulated response and electrical equivalent circuit models are shown in Figure 3.54, 3.55, 3.56 and 3.57. The simulated curve (solid line obtained from the electrical equivalent model) fits well with the experimental data. In fact, fewer electrical circuits were considered while obtaining the most accurate fit for the measured data. Customarily, the complex impedance response of a symmetric cell is modeled using the equivalent circuit of $\boldsymbol{L\text{-}R_b\text{-}(R_1\text{-}QPE_1)\text{-}(R_2\text{-}QPE_2)...(R_i\text{-}QPE_i)}$ shown in Figure 3.58 by means of the Gamry software. The data fitting contemplates three processes in the electrode reaction. In the high frequency range a serial inductance L was included to simulate the inductive effects of the setup at high frequencies. A serial R_b was used to simulate the grain boundary contributions of GDC electrolyte at low temperatures and *RQ* elements were fitted as each one being assigned to a specific electrochemical phenomenon. The exact equivalent circuits adopted for fitting the EIS data at the temperatures of 400 - 500 ºC are fitted well to an equivalent circuit of $L\text{-}R_b\text{-}(R_1\text{-}QPE_1)\text{-}(R_2\text{-}QPE_2)\text{-}(R_3\text{-}QPE_3)\text{-}(R_4\text{-}QPE_4)$ and the temperatures between 600, 700 and 800 ºC are fitted well to an equivalent circuit of $L\text{-}R_b\text{-}(R_1\text{-}QPE_1)\text{-}(R_2\text{-}QPE_2)\text{-}(R_3\text{-}QPE_3)$. The first component ($R_1QPE_1$) represents the semi-circle at the high-frequency region, the second one (R_2QPE_2) as a semi-circle at the medium-frequency region and the third one (R_3QPE_3) as a semi-circle at the low-frequency region.

The size of the high frequency arc decreased as the operation temperature decreased and it totally disappeared above 700 ºC. This signifies that the high frequency arc at 400 - 600 ºC is attributed to the migration of oxide ions through the GDC electrolyte. The

oxygen reduction over the LV05SM electrode is responsible for the second semi-circle in the EIS data. Impedance at high and intermediate frequencies are related to ion and electron transfer at the electrode, electrolyte, and collector/electrode interfaces, while the impedance at low frequencies is associated with non-charge transfer, such as oxygen surface exchange and gas-phase diffusion inside and outside the electrode layer [115].

Table 3.6. The fitted parameters as a function of temperature for LV05SM/GDC/LV05SM in PO_2.

PO_2	T (°C)	400	500	600	700	800
O3	*Lb (H)*	$1.38x10^{-9}$	$1.92x10^{-9}$	$1.13x10^{-9}$	$1.44x10^{-7}$	$6.47x10^{-7}$
	Rb ($\Omega.cm^2$)	81.52	15.974	0.8132	0.8096	0.7536
	R1 ($\Omega.cm^2$)	7126	7064	907	228.6	13.542
	R2 ($\Omega.cm^2$)	335.2	25.14	5.926	1.3986	1.125
	R3 ($\Omega.cm^2$)	1864.4	130.66	92.96	16.646	7.04
	R4 ($\Omega.cm^2$)	252.2	85.02	-	-	-
	ASR ($\Omega.cm^2$)	9577.8	7304.82	1005.88	246.64	21.707
O10	*Lb (H)*	$1.54x10^{-9}$	$8.39x10^{-10}$	$2.91x10^{-10}$	$3.83x10^{-7}$	$8.51x10^{-7}$
	Rb ($\Omega.cm^2$)	81.52	15.974	0.8132	0.8096	0.7536
	R1 ($\Omega.cm^2$)	7126	6318	907	228.6	13.54
	R2 ($\Omega.cm^2$)	316.6	25.14	4.074	1.3304	1.1238
	R3 ($\Omega.cm^2$)	1793.4	100.52	92.6	16.646	7.04
	R4 ($\Omega.cm^2$)	252.2	82.62	-	-	-
	ASR ($\Omega.cm^2$)	9488.2	6526.28	1003.67	246.57	21.70

Table 3.6. The fitted parameters as a function of temperature for LV05SM/GDC/LV05SM in PO_2. (cont.)

O15	*Lb (H)*	2.88×10^{-9}	1.75×10^{-8}	5.33×10^{-11}	2.82×10^{-7}	7.76×10^{-7}
	Rb ($\Omega.cm^2$)	81.52	15.974	0.8132	0.8096	0.7536
	R1 ($\Omega.cm^2$)	7126	6318	905.8	228.6	12.732
	R2 ($\Omega.cm^2$)	315.8	24.8	3.94	1.3304	1.1086
	R3 ($\Omega.cm^2$)	1782	99.56	92.36	16.328	6.946
	R4 ($\Omega.cm^2$)	252.2	82.62	-	-	-
	ASR ($\Omega.cm^2$)	9476	6524.98	1002.1	246.26	20.78
O25	*Lb (H)*	2.49×10^{-9}	1.52×10^{-8}	4.74×10^{-8}	3.86×10^{-7}	7.31×10^{-7}
	Rb ($\Omega.cm^2$)	81.52	15.974	0.8132	0.8096	0.7536
	R1 ($\Omega.cm^2$)	7126	5184	905	228.6	12.732
	R2 ($\Omega.cm^2$)	315.8	24.14	3.94	1.1038	1.1038
	R3 ($\Omega.cm^2$)	1782	97.8	92.36	16.28	6.946
	R4 ($\Omega.cm^2$)	252.2	82.62	-	-	-
	ASR ($\Omega.cm^2$)	9476	5388.56	1001.3	245.98	20.78

Table 3.6 summarizes the fitted parameters as a function of temperature for LV05SM/GDC/LV05SM under different partial pressure of oxygen, as well as the values of area specific resistance (ASR). The inductance value was shown but not considered in the present study. It can be seen that the electrolyte resistance (R_b) as well as the four resistances (R_1, R_2, R_3, R_4) associated with the kinetic of electrode processes decrease with increasing temperature, as expected. It also can be seen that the electrolyte resistance, R_b, does not depend on the oxygen partial pressure, remaining stable at each temperature, which is in agreement with the behavior of a pure ionic conductor as the GDC electrolyte.

The expected but invisible right intercept on the real axis at EIS diagram represents the total resistance (R_{tot}) and the left intercept on the real axis corresponds to the ohmic

resistance (R_{ohm}, including the electrolyte and connection wires). The polarization resistance (R_p) is estimated from the difference between R_{tot} and R_{ohm} ($R_p = R_{tot} - R_{ohm}$). Thus, all the cell impedances were normalized by the superficial area (0.04 cm^2), so the R parameters obtained in the fitting for each process were divided by two to consider the contribution of the two symmetric electrodes.

The most commonly used parameter to determine the rate-determining step in the oxygen reduction reaction is the slope of the electrode resistance as a function of oxygen partial pressure. The parameter called n gives information about the species involved in the electrode reaction, inset in Figure 3.49. The overall ORR can be simply described as $^1/_2\, O_2(g) + 2e^- \rightarrow O^{2-}$. In reality, it may involve many sub-steps such as gas diffusion, surface adsorption, dissociation, electron and ion charge transfer, and so on [118]. In order to operate a cell in intermediate temperature range, it is of vital importance to accelerate the ORR in the cathode and the oxygen transport in the cathode and electrolyte. Representative profiles for PO_2 dependence of R_1, R_2, R_3 and $R_2 + R_3$ are shown in Figure 3.59 and the fitting results at various temperatures are listed in Table 3.6.

From the fitted data values, R_1 is slightly dependent on the oxygen partial pressure and R_2 and R_3 increases with decreasing PO_2.

It is clear that R_1 did not have a monotonic dependence on PO_2. The resistance of the high frequency arc decreases with increasing temperatures, and it is independent of the oxygen partial pressure. Therefore, the first arc could be caused by the oxygen ions transferring through the electrolyte/electrode interface.

The polarization resistances R_2 and R_3, associated with Arc2 and Arc3 appearing at intermediate frequency ranges, are found to be dependent on PO_2. Both R_2 and R_3 decreased with increase in PO_2 and increase in temperature. The values obtained for n are 0.0091 - 0.2067 for R_2 and 0.0033 – 0.1434 for R_3 at the investigated temperatures. Considering the weak oxygen partial pressure, this process could be related to an oxygen atom diffusion followed by a charge transfer.

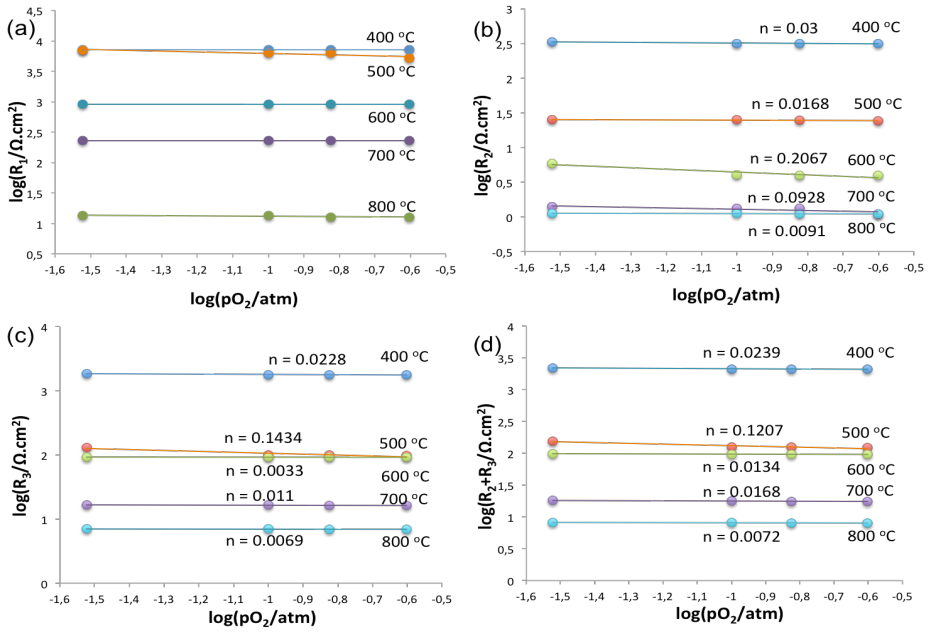

Figure 3.59. Dependence of three resistances at high, medium and low frequency on oxygen partial pressure for LV05SM/GDC interface between 400 - 800 °C (a) R_1; (b) R_2; (c) R_3 and (d) $R_2 + R_3$.

The process associated with the low-frequency arc presents $R_2 + R_3$ which was found to be dependent on PO_2 with the value $n = 0.0072 – 0.1297$. It suggests that both R_2 and R_3 are associated with electron transfer. In other words, the electron transfer process may be composed of two successive intermediate steps, showing comparable importance in the charge transfer process. An increase in PO_2 results in a sufficient supply of O_2 to the electrode from the gas phase thereby effectively eliminating diffusion polarization resistance.

The ASR values for ORR are obtained by the sum of individual resistances associated with each process. As expected, the ASR for LV05SM/GDC interface decreases notably with increasing temperature and slightly with the oxygen partial pressure as shown in Figure 3.60. The characteristic of ASR shows quite weak PO_2 dependency ($n = 0.0012 – 0.1261$), which could be related to the oxide ion transfer within the bulk electrode and/or from electrode to electrolyte through the TPB. Therefore, this process is the major rate-limiting step for LV05SM cathode.

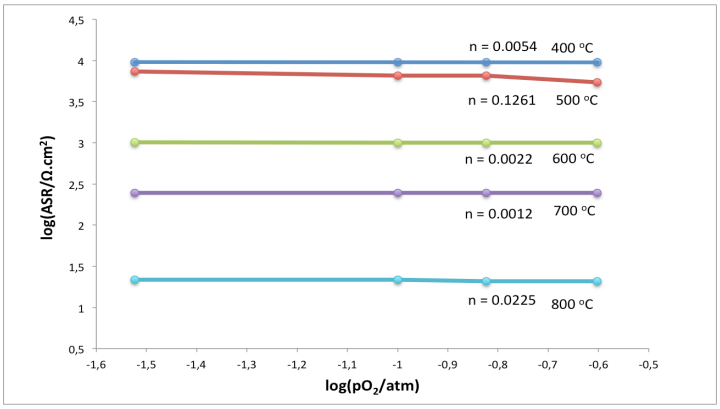

Figure 3.60. The dependence of the area specific resistance of the LV05SM/GDC interface as a function of PO_2 at different temperatures.

Figure 3.61 shows the selected impedance responses for the single-phase LV05SC electrode on the YSZ electrolyte that is measured under different oxygen partial pressures and collected in every 50 ºC in the temperature range from 400 to 800 ºC.

From the above Figure 3.61, EIS diagrams are composed of arcs located in high frequency and low frequency zones, respectively. This indicated that at least two different steps involved in the ORR over the electrode. It is clearly seen that below the 500 ºC, two well-separated semi-circles are observed in the high frequency part of the Nyquist plots. With increasing operating temperature, the high-frequency arc size decreased noticeably, and the arc was totally disappeared at 500 ºC and higher. Both the electrodes and electrolyte shape the impedance spectrum of a symmetric cell. The electrolyte typically exhibits behavior as an ideal resistor, which represents the intercept value in the impedance diagram at high frequency side with the real axis. With the decrease in operation temperature, a semi-circle associated with the oxide ion diffusion around the grain boundary of the electrolyte appeared in the high frequency range.

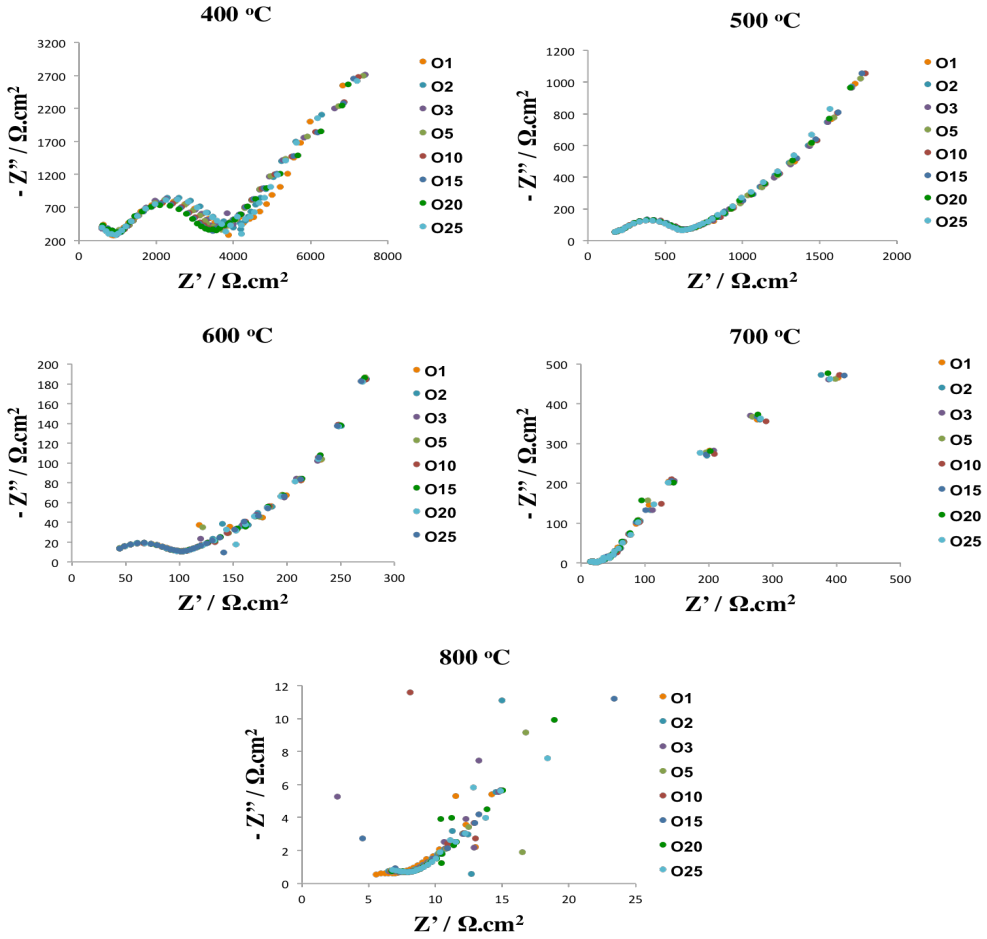

Figure 3.61. Complex impedance plots for LV05SC/YSZ/LV05SC symmetric cell at between 400-800 °C for different oxygen partial pressures.

Figure 3.62 illustrates the impedance diagrams measured at 600 °C under different oxygen partial pressures. In general, the high and medium frequency arcs show little dependence on the oxygen partial pressure, while the amplitude of the low frequency arc increases slightly as decreasing the oxygen partial pressure. The magnitude of both arcs changes significantly with the temperature Figure 3.61.

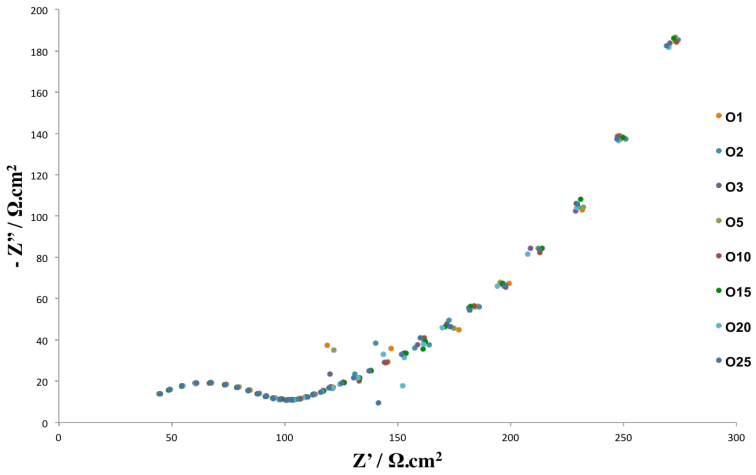

Figure 3.62. Typical EIS of a symmetric LV05SC/YSZ/LV05SC cell measured at 600 ºC while fixing the oxygen partial pressure between 1 – 25%.

In order to have more information to interpret properly the processes involved in the cathode/electrolyte interface, a study of the influence of oxygen partial pressure in the electrode impedance as a function of temperature was required. The oxygen partial pressure of the atmosphere is varied between 0.01 and 0.25 atm by mixing O_2 with N_2 using mass flow controllers.

Figure 3.63, 3.64, 3.65 and 3.66 shows some typical EIS diagrams of the LV05SC cathode measured at 400 – 800 ºC in air for 3-10-15-25% O_2. Two apparent semi-circular arcs in the complex impedance plots are evident. Presence of two semi-circular arcs in the complex impedance plane suggests that the ORR over the electrode was composed of at least two distinct processes.

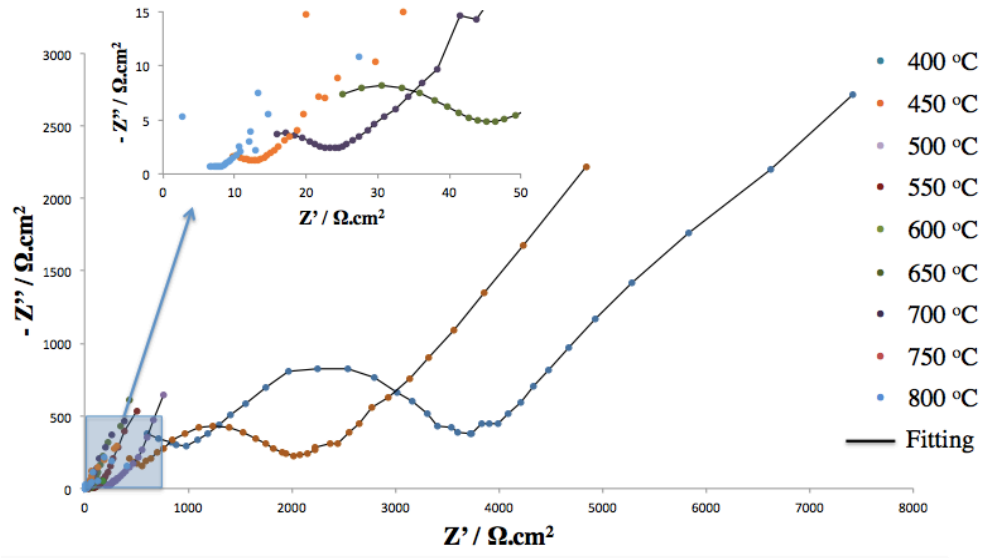

Figure 3.63. Experimental and fit Nyquist plots for a symmetrical LV05SC/YSZ/LV05SC cell measured at 3% O_2 – 97%N_2 between 400 – 800 °C.

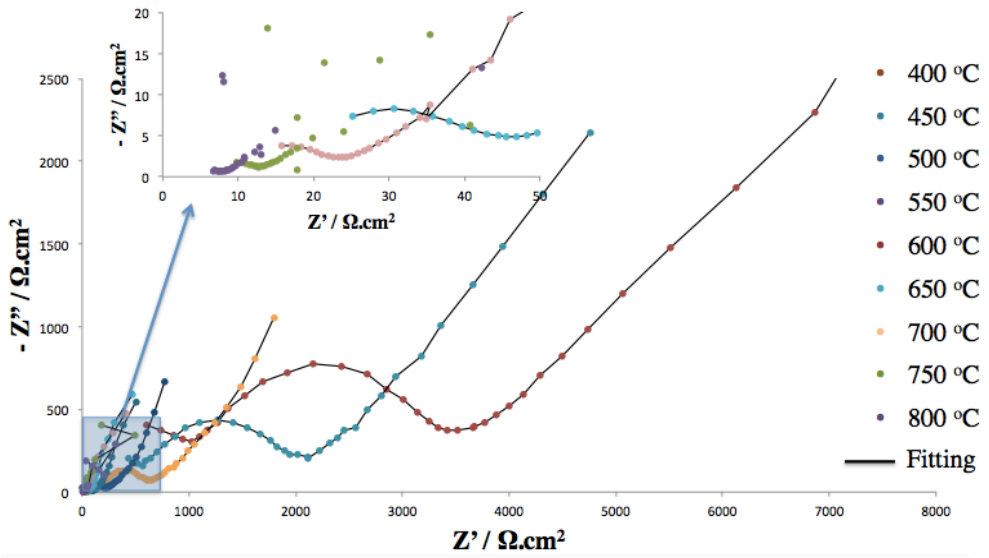

Figure 3.64. Experimental and fit Nyquist plots for a symmetrical LV05SC/YSZ/LV05SC cell measured at 10% O_2 – 90% N_2 between 400 – 800 °C.

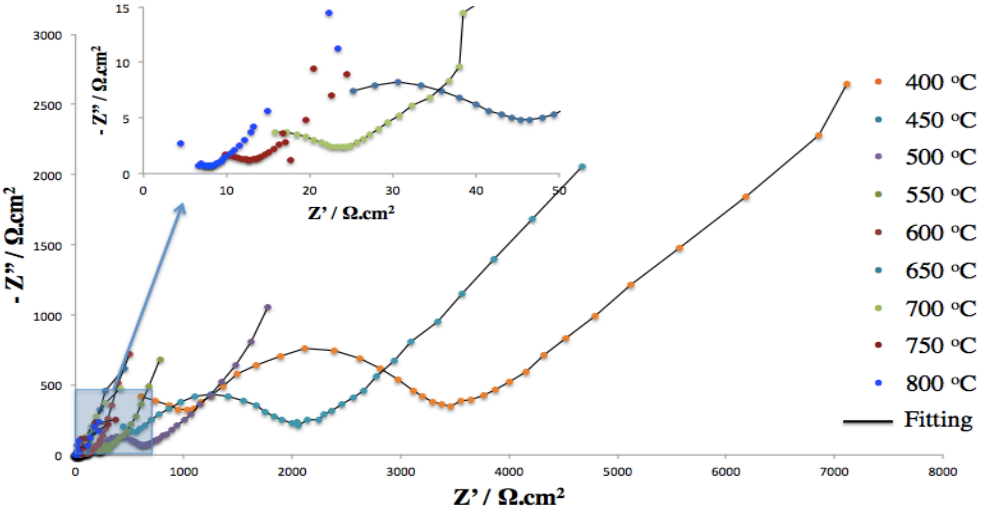

Figure 3.65. Experimental and fit Nyquist plots for a symmetrical LV05SC/YSZ/LV05SC cell measured at 15% O_2 – 85% N_2 between 400 – 800 °C.

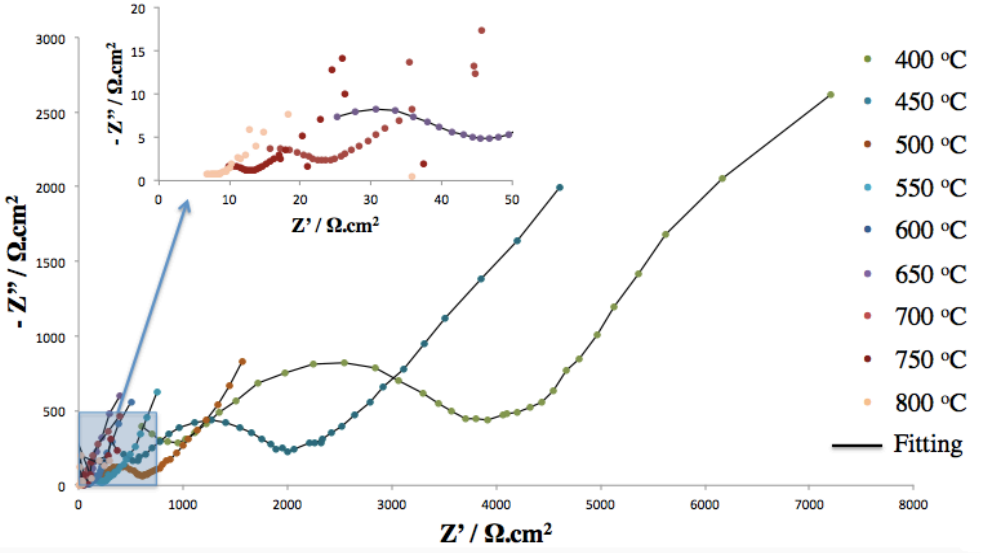

Figure 3.66. Experimental and fit Nyquist plots for a symmetrical LV05SC/YSZ/LV05SC cell measured at 25% O_2 – 75% N_2 between 400 – 800 °C.

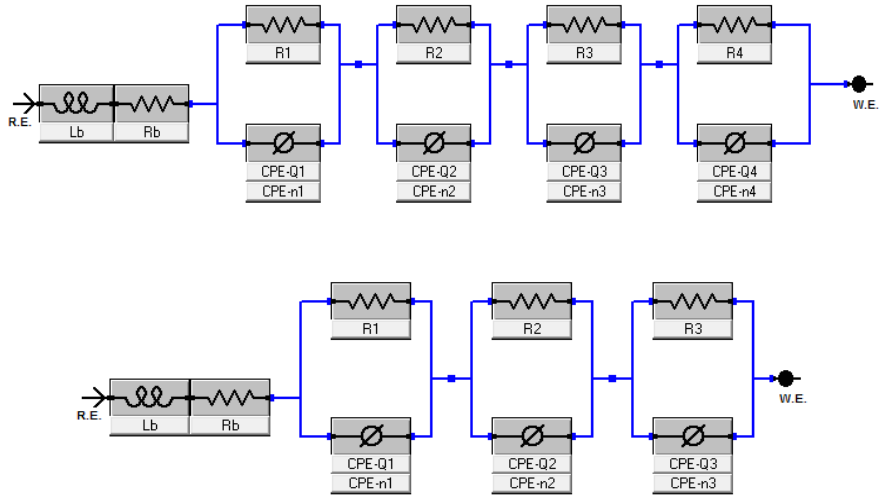

Figure 3.67. The equivalent circuits adopted for fitting the impedance data for a) 400-500 ºC b) 600 - 700 ºC.

Almost similar trends of the complex impedance diagrams were observed. Indeed, several intermediate steps are involved during the overall ORR process. The experimental impedance spectrum, simulated response and electrical equivalent circuit models are shown in Figure 3.63, 3.64, 3.65 and 3.66. All Nyquist plots were fitted to the equivalent circuit of $\boldsymbol{L\text{-}R_b\text{-}(R_1\text{-}QPE_1)\text{-}(R_2\text{-}QPE_2)...(R_i\text{-}QPE_i)}$ shown in Figure 3.67 by means of the Gamry software. The data fitting contemplates three processes in the electrode reaction; the results show good agreement between the experimental and fitted data. The numbers of R_i - QPE_i impedances (made by a resistor R_i in parallel with a constant phase element QPE_i) in series are dependent on operation temperature. The exact equivalent circuits adopted for fitting the EIS data at the temperatures of 600 - 700 ºC are fitted well to an equivalent circuit of $L\text{-}R_b\text{-}(R_1\text{-}QPE_1)\text{-}(R_2\text{-}QPE_2)\text{-}(R_3\text{-}QPE_3)$ and the temperatures of 400 - 500 ºC are in agreement with an equivalent circuit of $L\text{-}R_b\text{-}(R_1\text{-}QPE_1)\text{-}(R_2\text{-}QPE_2)\text{-}(R_3\text{-}QPE_3)\text{-}(R_4\text{-}QPE_4)$. The first component ($R_1QPE_1$) appears as a semi-circle at the high-frequency region, the second one (R_2QPE_2) as a semi-circle at the medium-frequency region and the third one (R_3QPE_3) as a semi-circle at the low-frequency region.

With higher operation temperature, the size of the semi-circle at the high frequency decreased. It totally disappeared above 500 ºC. This implies that the well-separated semi-

circle in the EIS high frequency range at 400 – 500 ºC may be associated with oxide-ion transfer through YSZ electrolyte grain boundaries. The second semi-circles in the EIS data are contributed from oxygen reduction over the LV05SC electrode. Impedance at high and intermediate frequencies are related to ion and electron transfer at the electrode, electrolyte, and collector/electrode interfaces, while the impedance at low frequencies is associated with non-charge transfer, such as oxygen surface exchange and gas-phase diffusion inside and outside the electrode layer [115].

Table 3.7. The fitting parameters as a function of temperature for LV05SC/YSZ/LV05SC in PO_2.

PO_2	T (ºC)	400	500	600	700
O3	*Lb (H)*	$4.39x10^{-8}$	$3.02x10^{-12}$	$1.11x10^{-5}$	$2.97x10^{-9}$
	Rb (Ω.cm²)	66.24	58.82	4.632	4.574
	R1 (Ω.cm²)	$2.72x10^{13}$	$2.05x10^{13}$	$8.31x10^{9}$	2028
	R2 (Ω.cm²)	524	270.6	51	6.646
	R3 (Ω.cm²)	245.6	181.2	64.8	24.74
	R4 (Ω.cm²)	8570	1763.4	-	-
	ASR (Ω.cm²)	$2.72x10^{13}$	$2.05x10^{13}$	$8.31x10^{9}$	2059.38
O10	*Lb (H)*	$7.93x10^{-8}$	$8.69x10^{-7}$	$1.97x10^{-5}$	$1.43x10^{-6}$
	Rb (Ω.cm²)	66.24	58.82	4.632	4.574
	R1 (Ω.cm²)	$2.72x10^{13}$	$2.05x10^{13}$	$1.07x10^{9}$	829.2
	R2 (Ω.cm²)	521.6	263.4	50.94	6.646
	R3 (Ω.cm²)	245.6	180.88	64.72	20.26
	R4 (Ω.cm²)	8380	1729.8	-	-
	ASR (Ω.cm²)	$2.72x10^{13}$	$2.05x10^{13}$	$1.07x10^{9}$	856.106

Table 3.7. The fitting parameters as a function of temperature for LV05SC/YSZ/LV05SC in PO_2. (cont.)

O15	*Lb (H)*	$1.17x10^{-8}$	$6.89x10^{-8}$	$1.06x10^{-5}$	$7.72x10^{-10}$
	Rb ($\Omega.cm^2$)	66.24	58.82	4.632	4.574
	R1 ($\Omega.cm^2$)	$1.73x10^{13}$	$3.73x10^{10}$	$3.17x10^{8}$	829.2
	R2 ($\Omega.cm^2$)	411.2	239.8	51	6.646
	R3 ($\Omega.cm^2$)	245.6	177.2	62.6	20.26
	R4 ($\Omega.cm^2$)	1375.6	1365	-	-
	ASR ($\Omega.cm^2$)	$1.73x10^{13}$	$3.73x10^{10}$	$3.17x10^{8}$	856.106
O25	*Lb (H)*	$9.02x10^{-10}$	$1.23x10^{-14}$	$9.61x10^{-6}$	$3.65x10^{-11}$
	Rb ($\Omega.cm^2$)	66.24	58.82	4.632	4.574
	R1 ($\Omega.cm^2$)	$9.48x10^{10}$	$1.02x10^{10}$	$2.46x10^{8}$	818.6
	R2 ($\Omega.cm^2$)	411.2	239.8	50.92	6.646
	R3 ($\Omega.cm^2$)	245.6	86.4	62.66	19.874
	R4 ($\Omega.cm^2$)	1365	1364.6	-	-
	ASR ($\Omega.cm^2$)	$9.48x10^{10}$	$1.02x10^{10}$	$2.46x10^{8}$	845.12

Table 3.7 summarizes the fitting parameters as a function of temperature for LV05SC/YSZ/LV05SC under different partial pressure of oxygen, as well as the values of area specific resistance (ASR). The inductance value was shown but not considered, because it is not characteristic of the studied compound. It can be seen that the electrolyte resistance (R_b) as well as the four resistances (R_1, R_2, R_3, R_4) associated with the kinetic of electrode processes decrease with increasing temperature, as expected. It also can be seen that the electrolyte resistance, R_b, does not depend on the oxygen partial pressure, remaining stable at each temperature, which is in agreement with the behavior of a pure ionic conductor as the YSZ electrolyte.

The polarization resistance (R_p), which is the ohmic part of the electrode resistance, can be determined as the sum of the resistances of each individual process ($R_p = R_1 + R_2 + R_3 + R_4$). For the symmetrical cell, the measured polarization resistance reflects the sum of the polarization resistance of the two electrodes investigated. Thus, all the cell impedances were normalized by the superficial area (0.04 cm^2), so the R parameters obtained in the fitting for each process were divided by two to consider the contribution of the two symmetric electrodes.

The most commonly used parameter to determine the rate-determining step in ORR is n, which is the slope of the electrode resistance as a function of oxygen partial pressure. The n value indicates the relation between the electrode resistance and oxygen partial pressure [116]. Representative profiles for PO_2 dependence of R_1, R_2, R_3 and $R_2 + R_3$ are shown in Figure 3.68 and the fitting results at various temperatures are listed in Table 3.7.

From the fitted data values, R_1 is independent on the oxygen partial pressure and R_2 and R_3 increases with decreasing PO_2. It is clear that R_1 did not have a monotonic dependence on oxygen partial pressure. The resistance of the high frequency arc decreases with increasing temperatures, and it is independent of the oxygen partial pressure. Therefore, the first arc could be caused by the oxygen ions transferring through the electrolyte/electrode interface.

The polarization resistances R_2 and R_3, associated with Arc2 and Arc3 appearing at intermediate frequency ranges, are found to be highly dependent on oxygen partial pressure. Both R_2 and R_3 decreased with increased oxygen partial pressure and increased temperature. The values obtained for n are 0.0 - 0.1249 for R_2 and 0.0 - 0.1075 for R_3 at the investigated temperatures. Considering the weak oxygen partial pressure, this process could be related to an oxygen atom diffusion followed by a charge transfer.

The process associated with the low-frequency arc presents $R_2 + R_3$ which was found to be dependent on PO_2 with the value n = 0.0134 - 0.043. It suggests that both R_2 and R_3 are associated with electron transfer. In other words, the electron transfer process may be composed of two successive intermediate steps, showing comparable importance in the charge transfer process. An increase of oxygen partial pressure results in a sufficient supply of oxygen to the electrode from the gas phase thereby effectively eliminating diffusion polarization resistance.

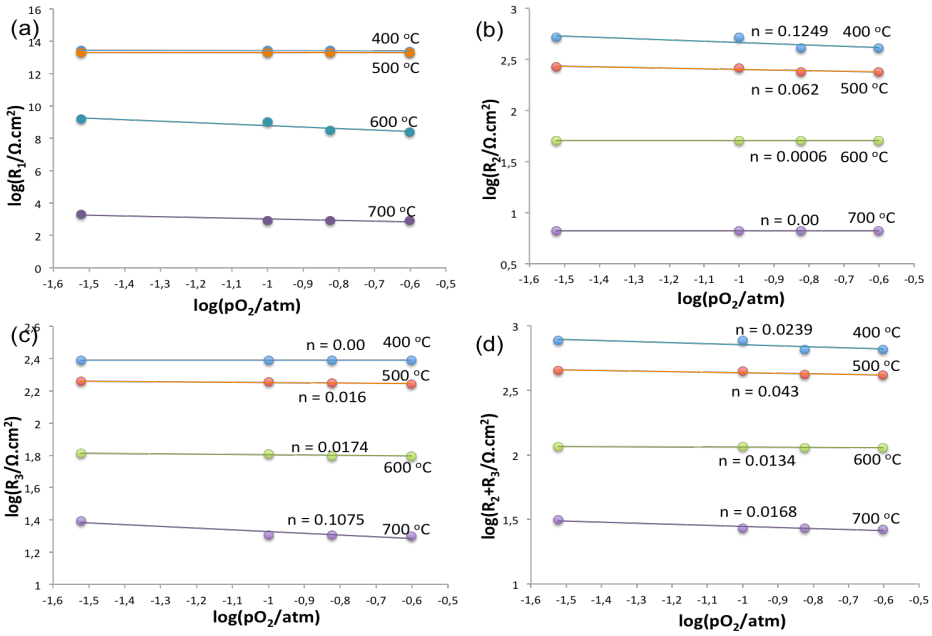

Figure 3.68. Dependence of three resistances at high, medium and low frequency on oxygen partial pressure for LV05SC/YSZ interface between 400 - 800 °C (a) R_1; (b) R_2; (c) R_3 and (d) $R_2 + R_3$.

The ASR values for ORR are obtained by the sum of individual resistances associated with each process. As expected, the ASR for LV05SC/YSZ interface decreases notably with increasing temperature and slightly with the oxygen partial pressure as shown in Figure 3.69. The characteristic of ASR shows quite weak PO_2 dependency (n = 0.3022 – 0.5212), which could be related to oxygen adsorption-desorption process or a reaction controlled by the atomic oxygen diffusion process (along the two phases electrode/electrolyte contact) followed by a charge transfer. Therefore, these two processes are the major rate-limiting steps for LV05SC cathode.

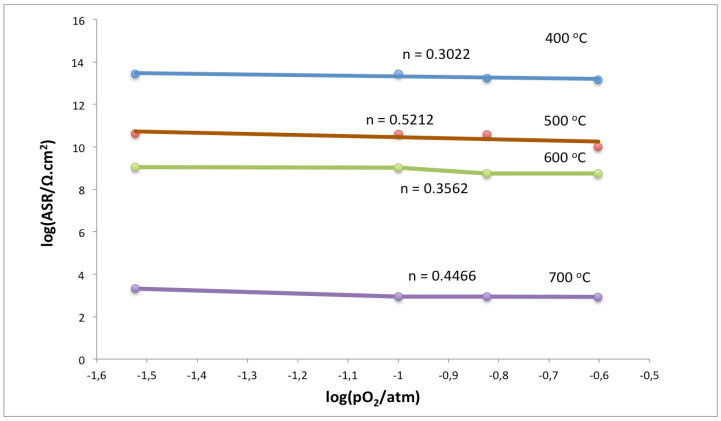

Figure 3.69. The dependence of the area specific resistance of the LV05SC/YSZ interface as a function of oxygen partial pressure at different temperatures.

Figure 3.70 shows the some impedance responses for the single-phase LV05SC electrode on the GDC electrolyte that is measured under different oxygen partial pressures and collected in every 50 ºC in the temperature range from 400 to 800 ºC.

From Figure 3.70, EIS diagrams are composed of arcs located in high and low frequency zones, respectively. This indicates that at least two different steps involved in the ORR over the electrode. It is clearly seen that below the 500 ºC, two well-separated semi-circles are observed in the high frequency part of the Nyquist plots. With increasing operating temperature, the high-frequency arc size decreased noticeably, and the arc was totally disappeared at 500 ºC and higher.

The impedances of a symmetric cell may arise from both the electrodes and electrolyte. The electrolyte typically performs as an ideal resistor, which represents the intercept value in the impedance diagram at high frequency side with the real axis. With the decrease in operation temperature, a semi-circle associated with the oxide ion diffusion around the grain boundary of the electrolyte appeared in the high frequency range.

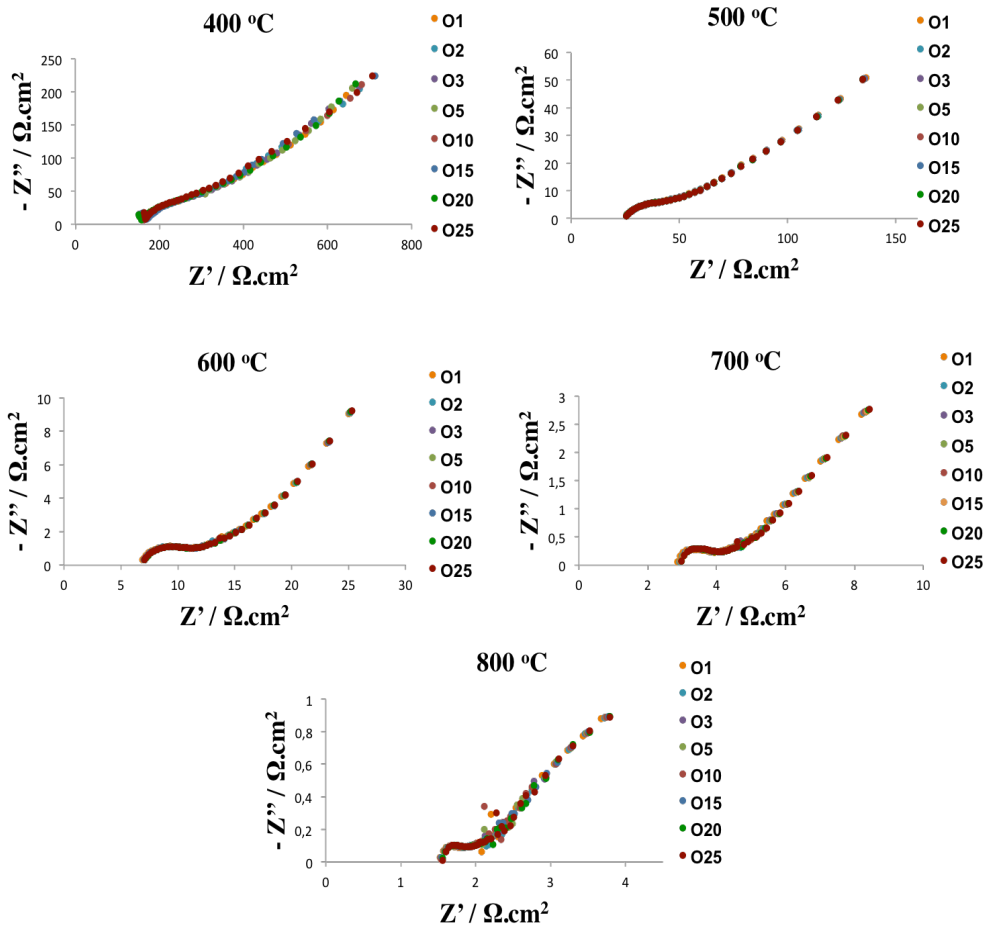

Figure 3.70. Complex impedance plots for LV05SC/GDC/LV05SC symmetric cell at between 400 - 800 °C for different oxygen partial pressures.

Figure 3.71 illustrates the impedance diagrams measured at 600 °C under different oxygen partial pressures. In general, the high and medium frequency arcs show little dependence on the oxygen partial pressure, while the amplitude of the low frequency arc increases slightly as decreasing the oxygen partial pressure. The magnitude of arcs changes significantly with the temperature (Figure 3.70).

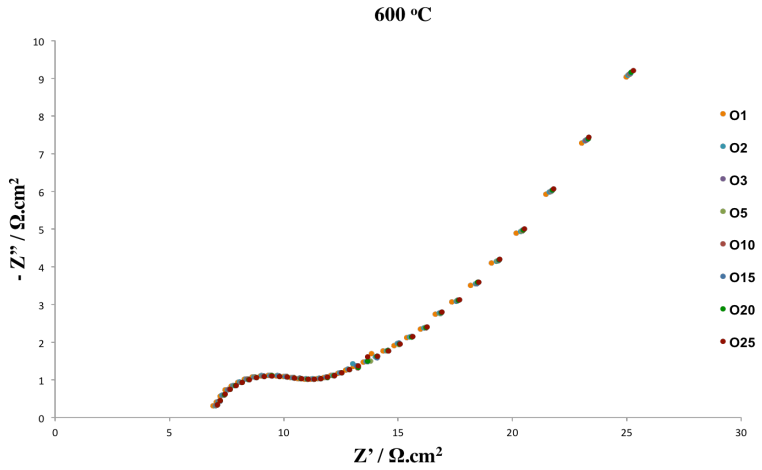

Figure 3.71. Typical EIS of a symmetric LV05SC/GDC/LV05SC cell measured at 600 °C while fixing the oxygen partial pressure between 1 – 25%.

In order to determine the processes involved in the ORR, the effect of PO_2 in the electrode impedance as a function of temperature was further studied. The oxygen partial pressure of the atmosphere was varied between 0.01 and 0.25 atm by mixing O_2 with N_2 using mass flow controllers.

Figure 3.72, 3.73, 3.74 and 3.75 shows some typical EIS diagrams of the LV05SC cathode measured at 400 – 800 °C in air for 3-10-15-25% O_2. Two discernable semi-circular arcs in the complex impedance plots suggest that the ORR over the electrode was composed of at least two distinct processes. Similar trends of the complex impedance diagrams were observed. The experimental impedance spectrum, simulated response and electrical equivalent circuit models are shown in Figure 3.72, 3.73, 3.74 and 3.75. All Nyquist plots were fitted to the equivalent circuit of $\boldsymbol{L\text{-}R_b\text{-}(R_1\text{-}QPE_1)\text{-}(R_2\text{-}QPE_2)...(R_i\text{-}QPE_i)}$ shown in Figure 3.76 by means of the Gamry software. The data fitting contemplates three processes in the electrode reaction; the results show good agreement between the experimental and fitted data.

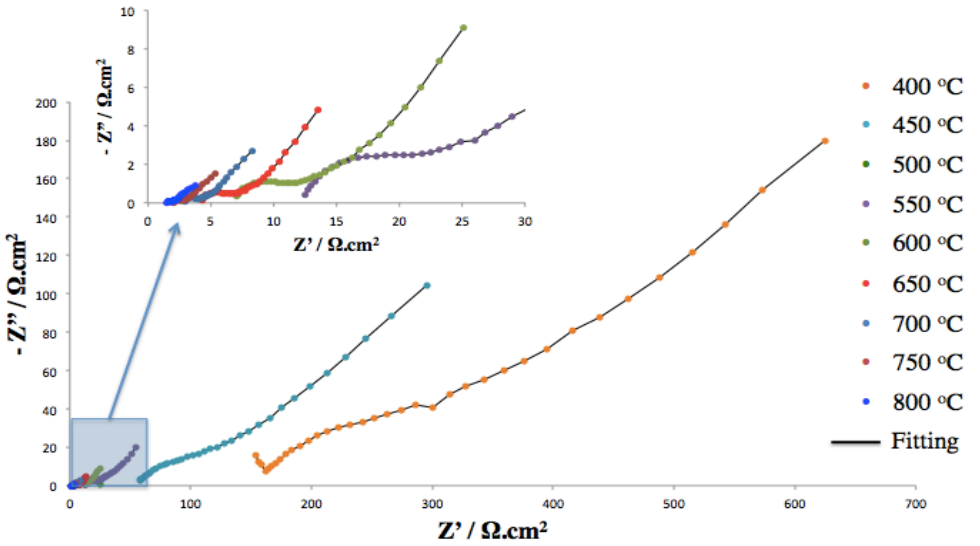

Figure 3.72. Experimental and fit Nyquist plots for a symmetrical LV05SC/GDC/LV05SC cell measured at 3% O_2 – 97% N_2 between 400 – 800 °C.

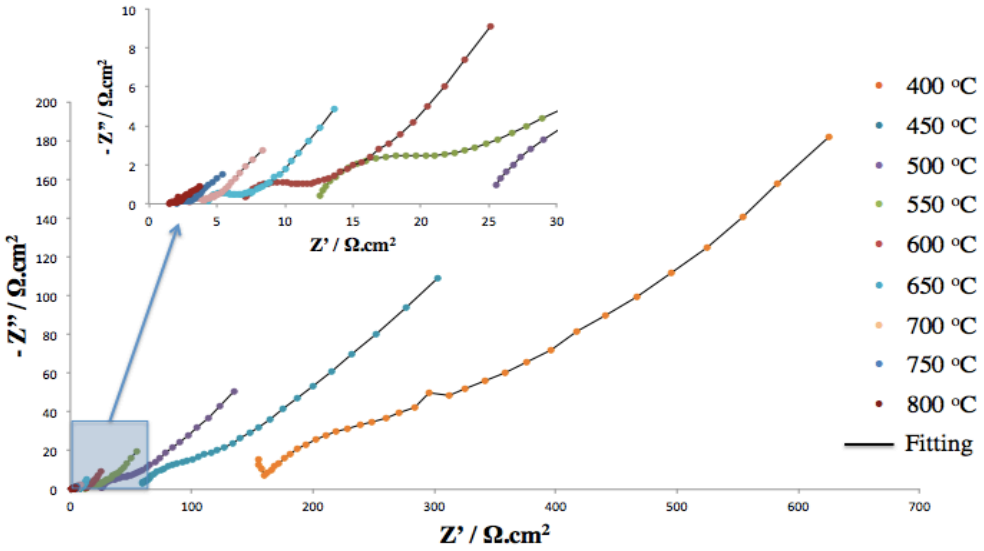

Figure 3.73. Experimental and fit Nyquist plots for a symmetrical LV05SC/GDC/LV05SC cell measured at 10% O_2 – 90% N_2 between 400 – 800 °C.

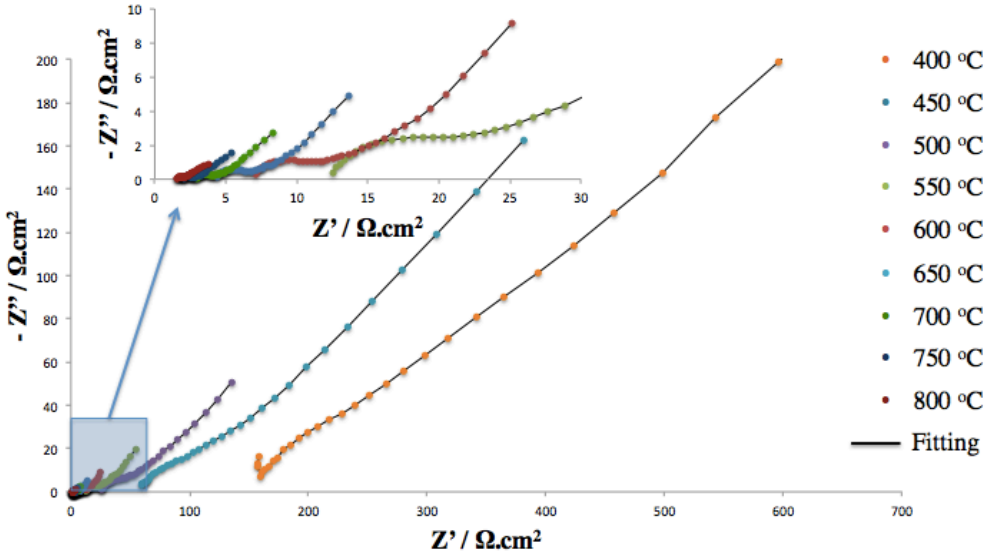

Figure 3.74. Experimental and fit Nyquist plots for a symmetrical LV05SC/GDC/LV05SC cell measured at 15% O_2 – 85% N_2 between 400 – 800 °C.

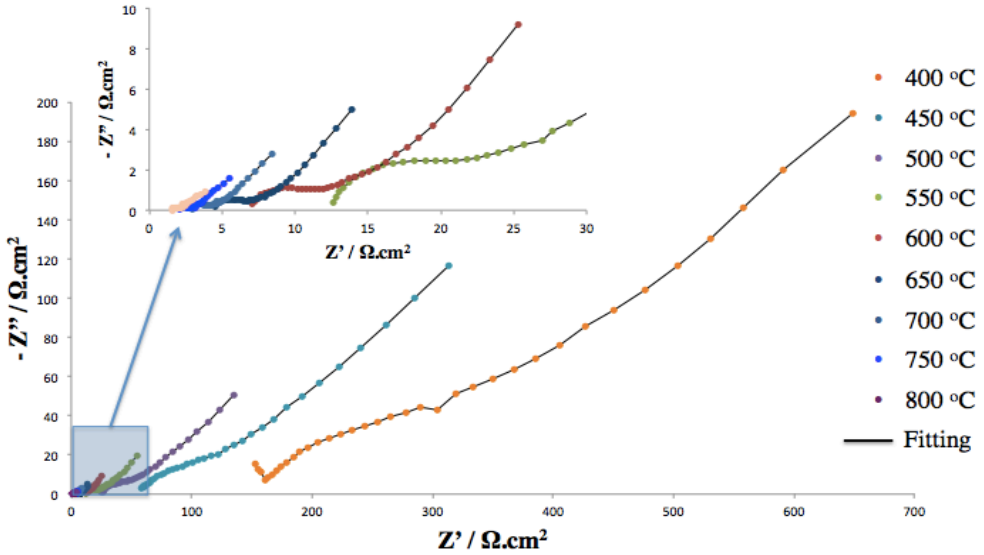

Figure 3.75. Experimental and fit Nyquist plots for a symmetrical LV05SC/GDC/LV05SC cell measured at 25% O_2 – 75% N_2 between 400 – 800 °C.

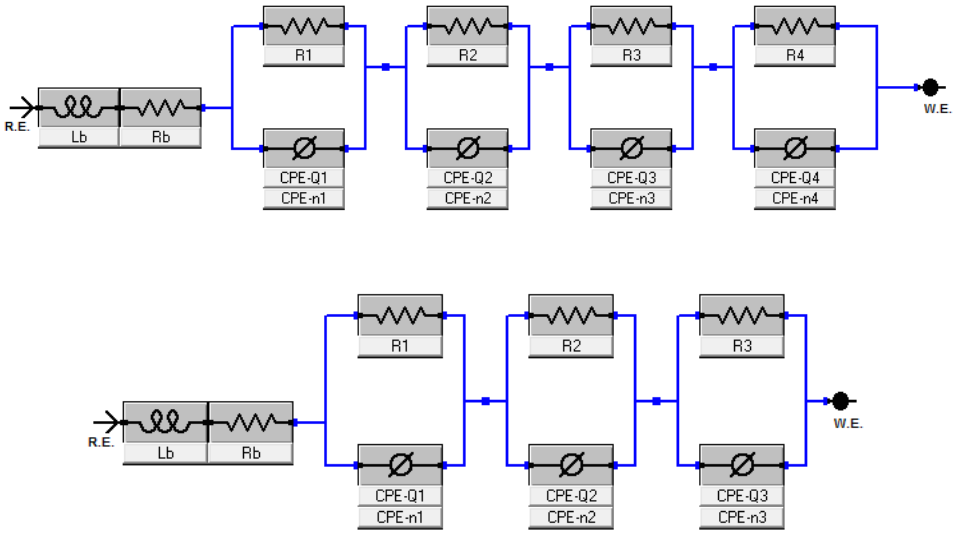

Figure 3.76. The equivalent circuits adopted for fitting the impedance data for a) 400 ºC b) 500 - 800 ºC.

The numbers of R_i - QPE_i impedances (made by a resistor R_i in parallel with a constant phase element QPE_i) in series are dependent on operation temperature. The exact equivalent circuits adopted for fitting the EIS data at the temperatures of 500 - 800 ºC are fitted well to an equivalent circuit of $L\text{-}R_b\text{-}(R_1\text{-}QPE_1)\text{-}(R_2\text{-}QPE_2)\text{-}(R_3\text{-}QPE_3)$ and the temperature of 400 ºC is in agreement with an equivalent circuit of $L\text{-}R_b\text{-}(R_1\text{-}QPE_1)\text{-}(R_2\text{-}QPE_2)\text{-}(R_3\text{-}QPE_3)\text{-}(R_4\text{-}QPE_4)$. The first component ($R_1QPE_1$) appears as a semi-circle at the high-frequency region, the second one (R_2QPE_2) as a semi-circle at the medium-frequency region and the third one (R_3QPE_3) as a semi-circle at the low-frequency region.

The size of the semi-circle at the high frequency decreased and totally disappeared above 500 ºC. This implies that the well-separated semi-circle in the EIS high frequency range at 400 - 500 ºC may be associated with oxide-ion transfer through GDC electrolyte grain boundaries. The second semi-circles in the EIS data are contributed from oxygen reduction over the LV05SC electrode. Impedance at high and intermediate frequencies is related to ion and electron transfer at the electrode, electrolyte, and collector/electrode interfaces, while the impedance at low frequencies is associated with non-charge transfer,

such as oxygen surface exchange and gas-phase diffusion inside and outside the electrode layer [115].

Table 3.8. The fitting parameters as a function of temperature for LV05SC/GDC/LV05SC in PO_2.

PO_2	T (°C)	400	500	600	700	800
O3	*Lb (H)*	$1.53x10^{-7}$	$9.52x10^{-7}$	$9.45x10^{-7}$	$1.11x10^{-6}$	$7.21x10^{-7}$
	Rb (Ω.cm²)	63.62	12.032	3.09	0.5594	0.2114
	R1 (Ω.cm²)	26.42	25.7	2.832	2.822	1.0146
	R2 (Ω.cm²)	23.32	9.116	2.8	1.4418	0.7806
	R3 (Ω.cm²)	2632	430	353	10.298	1.366
	R4 (Ω.cm²)	67.74	-	-	-	-
	ASR (Ω.cm²)	2749.48	464.816	358.632	14.562	3.161
O10	*Lb (H)*	$1.70x10^{-5}$	$5.11x10^{-7}$	$1.02x10^{-6}$	$1.22x10^{-6}$	$1.28x10^{-6}$
	Rb (Ω.cm²)	63.62	12.032	3.09	0.5594	0.2114
	R1 (Ω.cm²)	26.42	25.7	2.808	2.212	1.0146
	R2 (Ω.cm²)	17.94	8.106	2.782	1.255	0.477
	R3 (Ω.cm²)	2632	199.92	183.6	10.298	1.366
	R4 (Ω.cm²)	67.74	-	-	-	-
	ASR (Ω.cm²)	2744.1	233.726	189.19	13.765	2.857
O15	*Lb (H)*	$3.32x10^{-13}$	$8.26x10^{-14}$	$9.75x10^{-7}$	$1.89x10^{-6}$	$1.29x10^{-6}$
	Rb (Ω.cm²)	63.62	12.032	3.09	0.5594	0.2114
	R1 (Ω.cm²)	22.4	22.24	2.778	2.208	0.6204
	R2 (Ω.cm²)	13.81	7.95	2.782	0.935	0.4766
	R3 (Ω.cm²)	2632	199.72	180.28	10.298	1.366

Table 3.8. The fitting parameters as a function of temperature for LV05SC/GDC/LV05SC in PO_2. (cont.)

	R4 ($\Omega.cm^2$)	50.38	-	-	-	-
	ASR ($\Omega.cm^2$)	2718.59	229.91	185.84	13.441	2.463
O25	*Lb (H)*	$1.28x10^{-9}$	$1.59x10^{-16}$	$9.77x10^{-7}$	$1.16x10^{-6}$	$4.22x10^{-7}$
	Rb ($\Omega.cm^2$)	63.62	12.032	3.09	0.5594	0.2114
	R1 ($\Omega.cm^2$)	22.3	21.66	2.772	1.6198	0.4768
	R2 ($\Omega.cm^2$)	13.024	7.462	2.782	0.6074	0.4766
	R3 ($\Omega.cm^2$)	2632	187.7	149.16	10.298	1.366
	R4 ($\Omega.cm^2$)	50.36	-	-	-	-
	ASR ($\Omega.cm^2$)	2717.68	216.82	154.714	12.525	2.319

Table 3.8 summarizes the fitting parameters as a function of temperature for LV05SC/GDC/LV05SC under different partial pressure of oxygen, as well as the values of area specific resistance (ASR). The inductance value was shown but not considered in the present study. It can be seen that the electrolyte resistance (R_b) as well as the four resistances (R_1, R_2, R_3, R_4) associated with the kinetic of electrode processes decrease with increasing temperature, as expected. It also can be seen that the electrolyte resistance, R_b, does not depend on the oxygen partial pressure, remaining stable at each temperature, which is in agreement with the behavior of a pure ionic conductor as the GDC electrolyte.

The expected but invisible right intercept on the real axis at EIS diagram represents the total resistance (R_{tot}) and the left intercept on the real axis corresponds to the ohmic resistance (R_{ohm}, including the electrolyte and connection wires). The polarization resistance (R_p) is estimated from the difference between R_{tot} and R_{ohm} ($R_p = R_{tot} - R_{ohm}$). Thus, all the cell impedances were normalized by the superficial area (0.04 cm^2), so the R parameters obtained in the fitting for each process were divided by two to consider the contribution of the two symmetric electrodes.

The most commonly used parameter to determine the rate-determining step in the ORR is the slope of the electrode resistance as a function of oxygen partial pressure, inset in Figure 3.49. The overall ORR can be simply described as $^1/_2\, O_2(g) + 2e^- \rightarrow O^{2-}$. In reality, it may involve many sub-steps such as gas diffusion, surface adsorption, dissociation, electron and ion charge transfer, and so on [118]. In order to operate a cell in intermediate temperature range, it is of vital importance to accelerate the ORR in the cathode and the oxygen transport in the cathode and electrolyte. Representative profiles for PO_2 dependence of R_1, R_2, R_3 and $R_2 + R_3$ are shown in Figure 3.77 and the fitting results at various temperatures are listed in Table 3.8.

From the fitted data values, R_1 is slightly dependent on the oxygen partial pressure and R_2 and R_3 increases with decreasing PO_2. It is clear that R_1 did not have a monotonic dependence on oxygen partial pressure. The resistance of the high frequency arc decreases with increasing temperatures, and it is independent of the oxygen partial pressure. Therefore, the first arc could be caused by the oxygen ions transferring through the electrolyte/electrode interface.

The polarization resistances R_2 and R_3, associated with Arc2 and Arc3 appearing at intermediate frequency ranges, are found to be highly dependent on oxygen partial pressure. Both R_2 and R_3 decreased with increased oxygen partial pressure and increased temperature. The values obtained for n are 0.0032 - 0.3777 for R_2 and 0.00 - 0.4085 for R_3 at the investigated temperatures. Considering the weak oxygen partial pressure, this process could be related to an oxygen atom diffusion followed by a charge transfer.

The process associated with the low-frequency arc presents $R_2 + R_3$ which was found to be dependent on PO_2 with the value n = 0.0019 - 0.4022. It suggests that both R_2 and R_3 are associated with electron transfer. In other words, the electron transfer process may be composed of two successive intermediate steps, showing comparable importance in the charge transfer process. An increase of oxygen partial pressure results in a sufficient supply of oxygen to the electrode from the gas phase thereby effectively eliminating diffusion polarization resistance.

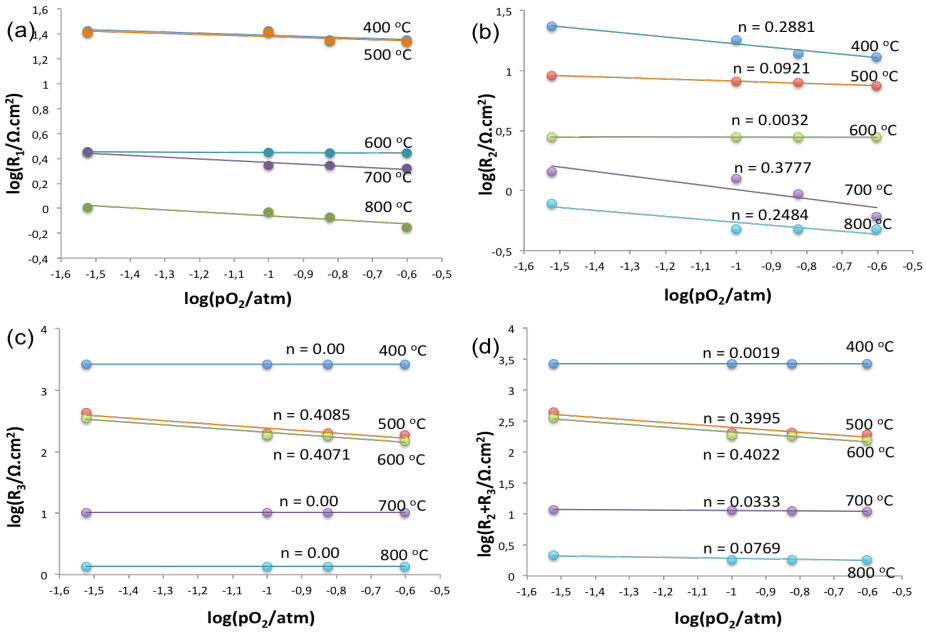

Figure 3.77. Dependence of three resistances at high, medium and low frequency on oxygen partial pressure for LV05SC/GDC interface between 400 - 800 °C (a) R_1; (b) R_2; (c) R_3 and (d) $R_2 + R_3$.

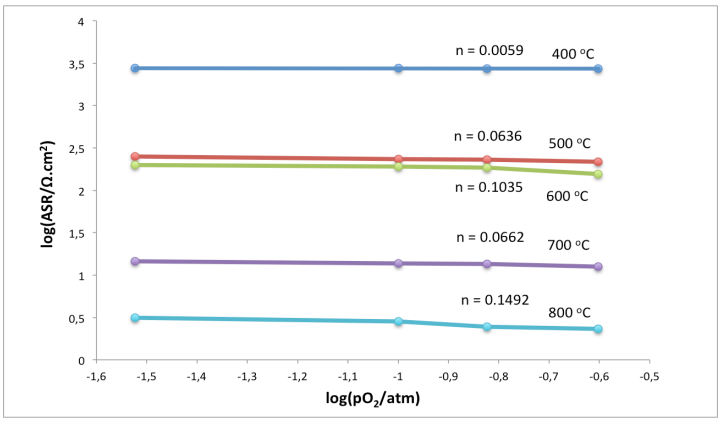

Figure 3.78. The dependence of the area specific resistance of the LV05SC/GDC interface as a function of PO_2 at different temperatures.

The ASR values for ORR are obtained by the sum of individual resistances associated with each process. As expected, the ASR for LV05SC/GDC interface decreases notably with increasing temperature and slightly with the oxygen partial pressure as shown in Figure 3.78. The characteristic of ASR shows a quite weak PO_2 dependency (n = 0.0059 – 0.1492), which could be related to the oxide ion transfer within the bulk electrode and/or from electrode to electrolyte through the TPB. Therefore, this process is the major rate-limiting step for LV05SC cathode.

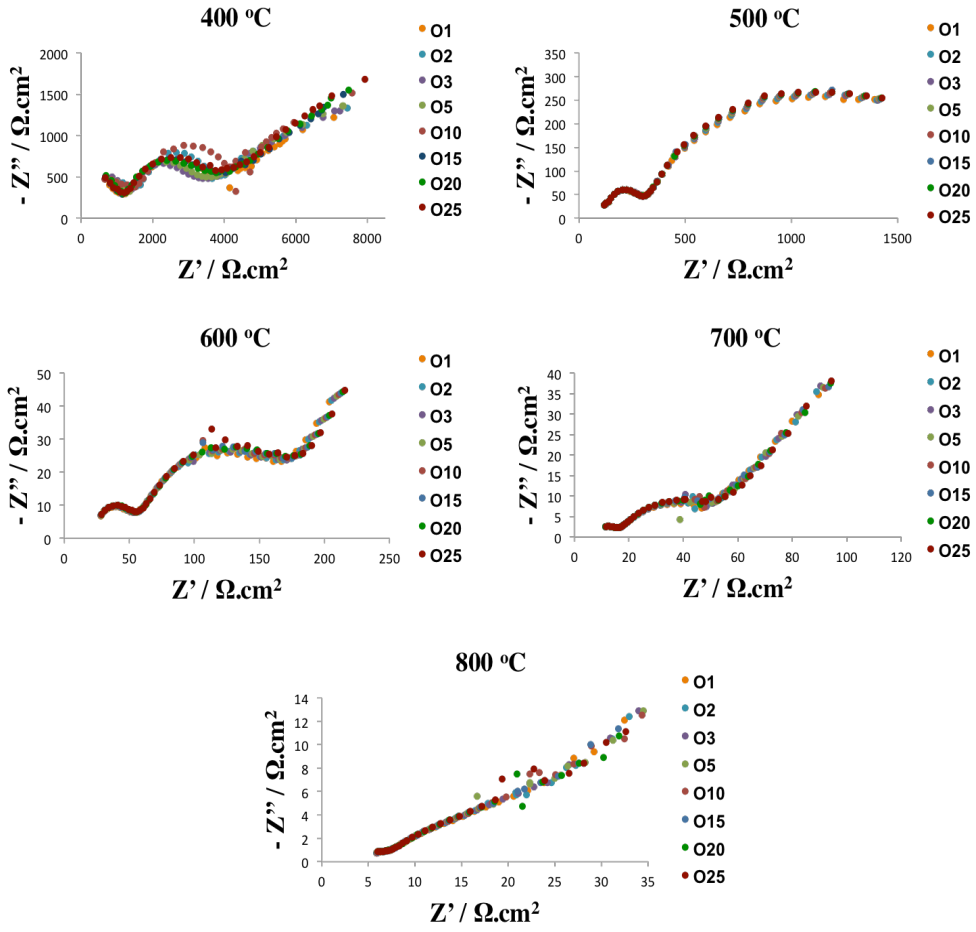

Figure 3.79. Complex impedance plots for LV3SF/YSZ/LV3SF symmetric cell at between 400-800 °C for different oxygen partial pressures.

Figure 3.79 shows the some impedance responses for the single-phase LV3SF electrode on the YSZ electrolyte that is measured under different oxygen partial pressures and collected in every 50 ºC in the temperature range from 400 to 800 ºC.

From the Figure 3.79, it is clearly seen that below the 500 ºC, two impedance contributions has an apparent shape in the high frequency part of the Nyquist plots. With increasing operating temperature, the high-frequency arc size decreased noticeably, and the arc was totally disappeared at 500 ºC. An additional arc at the low frequency range appeared when the operating temperature was elevated to 600 ºC.

The impedances of a symmetric cell may arise from both the electrodes and electrolyte. The electrolyte typically performs as an ideal resistor, which represents the intercept value in the impedance diagram at high frequency side with the real axis. However, with the decrease in operation temperature, a semi-circle associated with the oxide ion diffusion around the grain boundary of the electrolyte also appeared in the high frequency range.

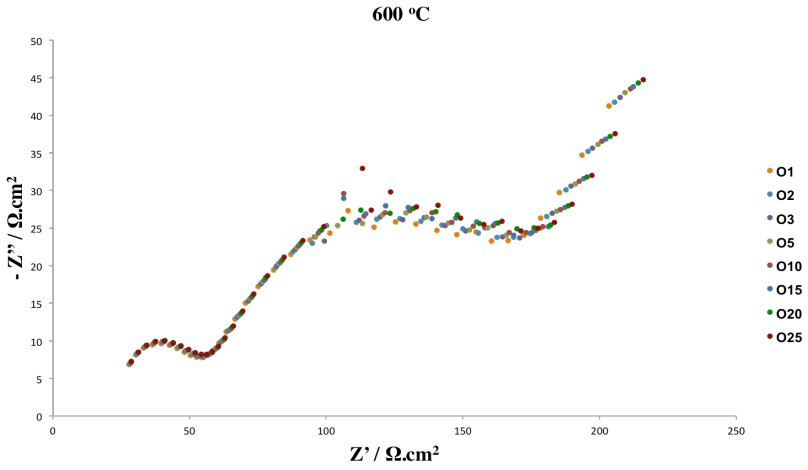

Figure 3.80. Typical EIS of a symmetric LV3SF/YSZ/LV3SF cell measured at 600 ºC while fixing the oxygen partial pressure between 1 – 25%.

Figure 3.80 illustrates the impedance diagrams measured at 600 °C under different oxygen partial pressures. Three arcs at high, medium and low frequencies can be observed.

In general, the high and medium frequency arcs show little dependence on the oxygen partial pressure, while the amplitude of the low frequency arc increases slightly as decreasing the oxygen partial pressure. The magnitude of arcs changes significantly with the temperature Figure 3.79.

In order to have more information to interpret properly the processes involved in the cathode/electrolyte interface, a study of the influence of oxygen partial pressure in the electrode impedance as a function of temperature was required. The oxygen partial pressure of the atmosphere was varied between 0.01 and 0.25 atm by mixing O_2 with N_2 using mass flow controllers.

Figure 3.81, 3.82, 3.83 and 3.84 show some typical EIS diagrams of the LV3SF cathode measured at 400 – 800 ºC in air for 3-10-15-25% O_2. Three noticeable semi-circular arcs in the complex impedance plots are evident. Presence of three semi circular arcs in the complex impedance plane suggests that the ORR over the electrode was composed of at least three distinct processes.

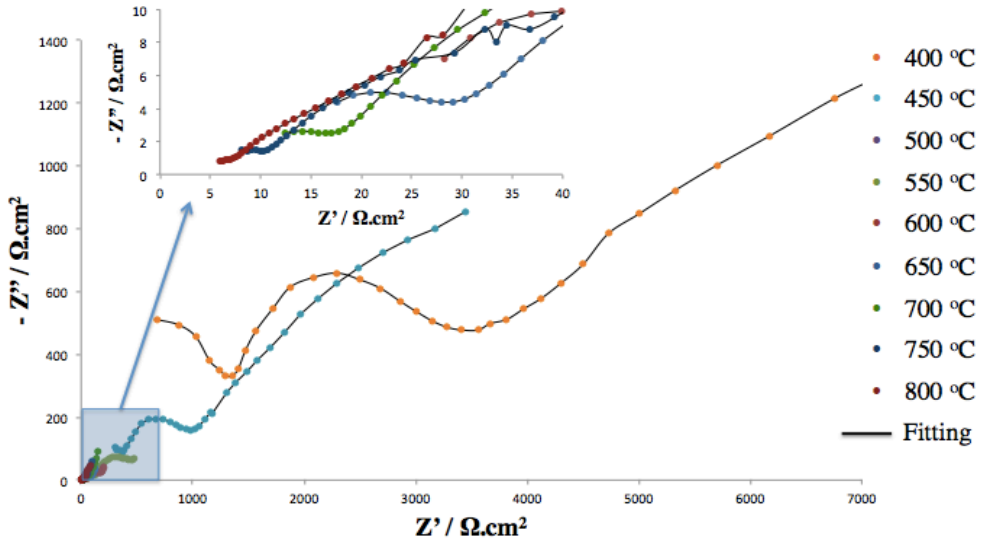

Figure 3.81. Experimental and fit Nyquist plots for a symmetrical LV3SF/YSZ/LV3SF cell measured at 3% O_2 – 97% N_2 between 400 – 800 ºC.

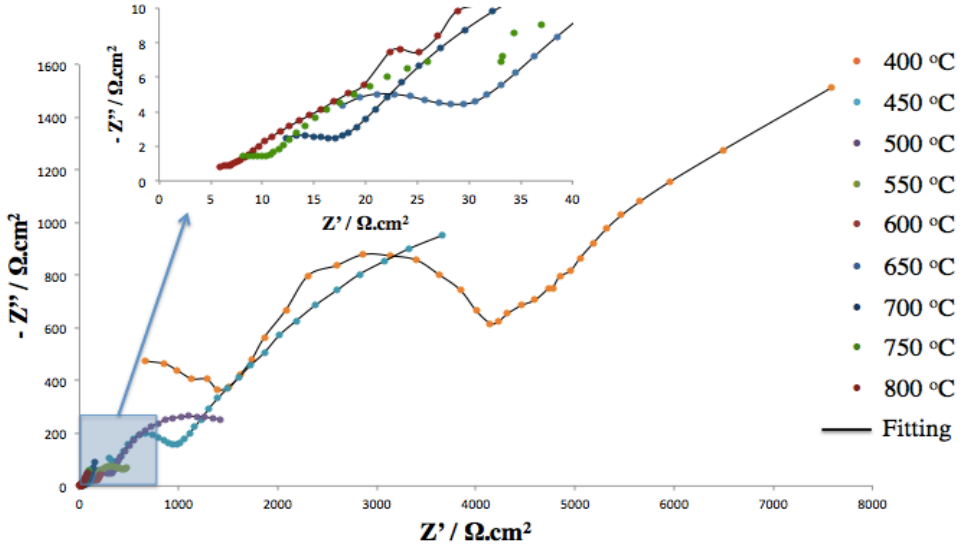

Figure 3.82. Experimental and fit Nyquist plots for a symmetrical LV3SF/YSZ/LV3SF cell measured at 10% O_2 – 90% N_2 between 400 – 800 °C.

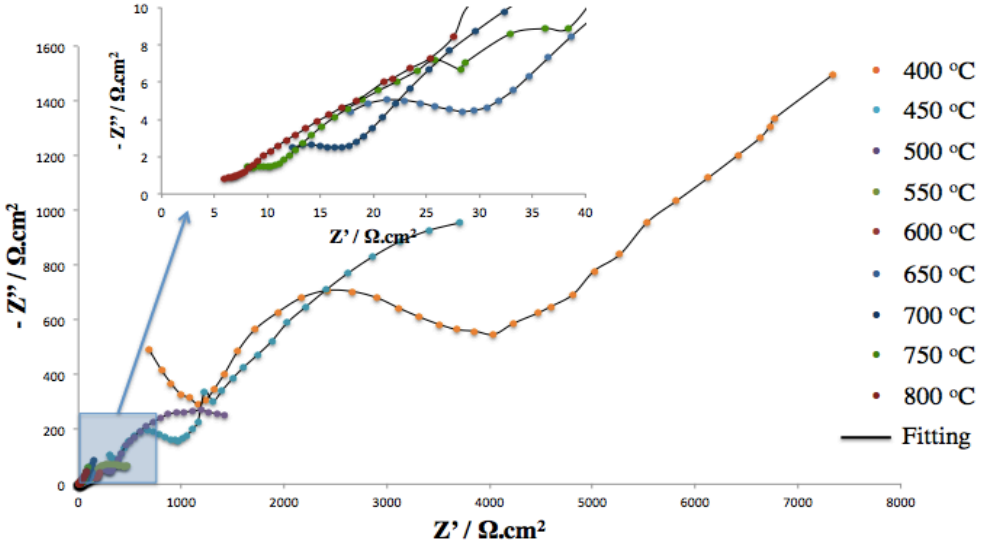

Figure 3.83. Experimental and fit Nyquist plots for a symmetrical LV3SF/YSZ/LV3SF cell measured at 15% O_2 – 85% N_2 between 400 – 800 °C.

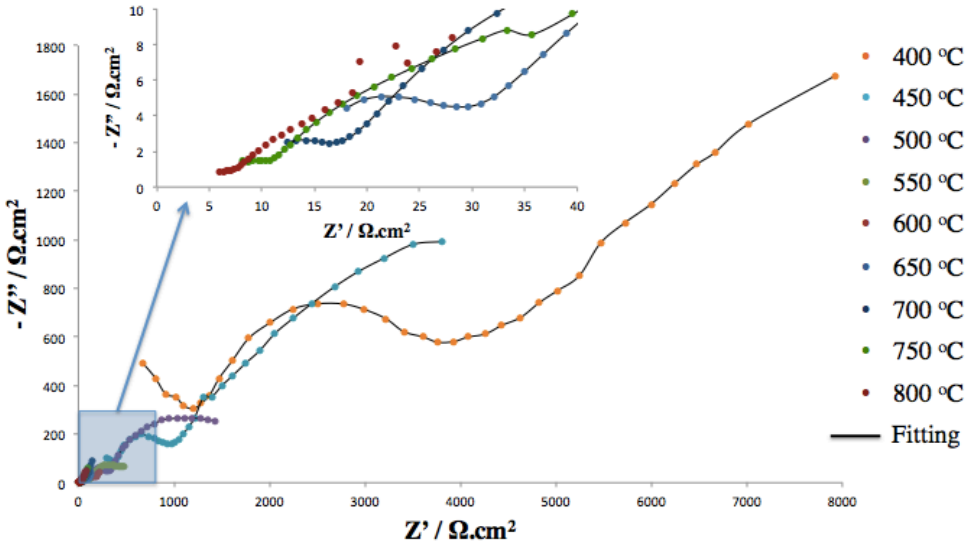

Figure 3.84. Experimental and fit Nyquist plots for a symmetrical LV3SF/YSZ/LV3SF cell measured at 25% O_2 – 75% N_2 between 400 – 800 °C.

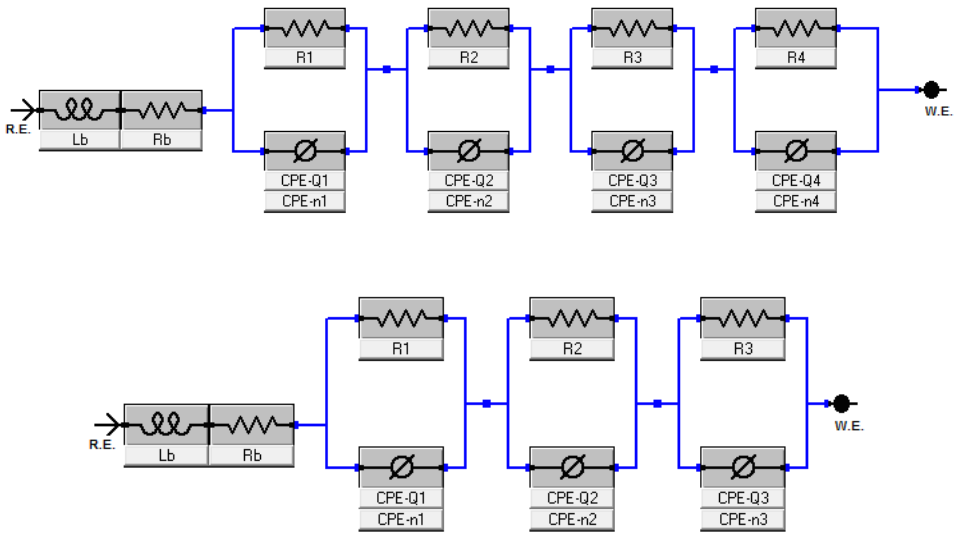

Figure 3.85. The equivalent circuits adopted for fitting the impedance data for a) 400, 600, 700 and 800 °C b) 500 °C.

Almost similar trends of the complex impedance diagrams were observed. Indeed, several intermediate steps are involved during the overall ORR process. The experimental impedance spectrum, simulated response and electrical equivalent circuit models are shown in Figure 3.81, 3.82, 3.83 and 3.84. All Nyquist plots were fitted to the equivalent circuit of $\boldsymbol{L\text{-}R_b\text{-}(R_1\text{-}QPE_1)\text{-}(R_2\text{-}QPE_2)\ldots(R_i\text{-}QPE_i)}$ shown in Figure 3.85 by means of the Gamry software. The data fitting contemplates three processes in the electrode reaction; the results show good agreement between the experimental and fitted data. The numbers of R_i - QPE_i impedances (made by a resistor R_i in parallel with a constant phase element QPE_i) in series are dependent on operation temperature. The exact equivalent circuits adopted for fitting the EIS data at the temperature of 500 ºC is fitted well to an equivalent circuit of $L\text{-}R_b\text{-}(R_1\text{-}QPE_1)\text{-}(R_2\text{-}QPE_2)\text{-}(R_3\text{-}QPE_3)$ and the temperatures of 400, 600, 700 and 800 ºC are in agreement with an equivalent circuit of $L\text{-}R_b\text{-}(R_1\text{-}QPE_1)\text{-}(R_2\text{-}QPE_2)\text{-}(R_3\text{-}QPE_3)\text{-}(R_4\text{-}QPE_4)$. The first component ($R_1QPE_1$) appears as a semi-circle at the high-frequency region, the second one (R_2QPE_2) as a semi-circle at the medium-frequency region and the third one (R_3QPE_3) as a semi-circle at the low-frequency region.

The size of the semi-circle at the high frequency decreased and it totally disappeared at 500 ºC. This implies that the well-separated semi-circle in the EIS high frequency range at 400 – 500 ºC may be associated with oxide-ion transfer through YSZ electrolyte grain boundaries. The second semi-circles in the EIS data are contributed from oxygen reduction over the LV3SF electrode. Impedance at high and intermediate frequencies is related to ion and electron transfer at the electrode, electrolyte, and collector/electrode interfaces, while the impedance at low frequencies is associated with non-charge transfer, such as oxygen surface exchange and gas-phase diffusion inside and outside the electrode layer [115].

Table 3.9 summarizes the fitting parameters as a function of temperature for LV3SF/YSZ/LV3SF under different partial pressure of oxygen, as well as the values of area specific resistance (ASR). The inductance value was shown but not considered, because it is not characteristic of the studied compound.

Table 3.9. The fitting parameters as a function of temperature for LV3SF/YSZ/LV3SF in PO_2.

PO_2	T (°C)	400	500	600	700	800
O3	*Lb (H)*	4.42×10^{-7}	6.15×10^{-8}	3.01×10^{-6}	1.04×10^{-6}	2.22×10^{-10}
	Rb ($\Omega.cm^2$)	71.62	49.1	9.03	3.05	2.046
	R1 ($\Omega.cm^2$)	945.8	348.2	38.58	15.456	10.484
	R2 ($\Omega.cm^2$)	527.2	101.72	17.3	6.024	1.2098
	R3 ($\Omega.cm^2$)	524.6	442.2	323.4	318.8	78.02
	R4 ($\Omega.cm^2$)	2416	-	63.28	17.35	13.186
	ASR ($\Omega.cm^2$)	4413.6	892.12	442.56	357.63	102.89
O10	*Lb (H)*	3.74×10^{-4}	1.66×10^{-9}	4.40×10^{-6}	3.03×10^{-6}	4.53×10^{-7}
	Rb ($\Omega.cm^2$)	71.62	49.1	9.03	3.05	2.046
	R1 ($\Omega.cm^2$)	945.8	322.6	38.14	15.456	9.67
	R2 ($\Omega.cm^2$)	527	89.52	14.148	4.16	1.1002
	R3 ($\Omega.cm^2$)	524.6	442.2	320.4	318.6	76.78
	R4 ($\Omega.cm^2$)	2416	-	53	17.304	12.99
	ASR ($\Omega.cm^2$)	4413.4	854.32	425.688	355.52	100.54
O15	*Lb (H)*	3.74×10^{-8}	8.26×10^{-8}	6.14×10^{-6}	3.87×10^{-6}	1.40×10^{-11}
	Rb ($\Omega.cm^2$)	71.62	49.1	9.03	3.05	2.046
	R1 ($\Omega.cm^2$)	885.8	322.6	23.82	14.378	8.906
	R2 ($\Omega.cm^2$)	464.6	89.52	14.098	4.156	1.0978
	R3 ($\Omega.cm^2$)	524	442.2	320.4	318.4	76.6
	R4 ($\Omega.cm^2$)	2416	-	52.4	17.208	11.178
	ASR ($\Omega.cm^2$)	4290.4	854.32	410.718	354.142	97.78

Table 3.9. The fitting parameters as a function of temperature for LV3SF/YSZ/LV3SF in PO_2. (cont.)

O25	*Lb (H)*	8.88×10^{-7}	1.52×10^{-15}	6.97×10^{-6}	5.46×10^{-6}	7.18×10^{-11}
	Rb ($\Omega.cm^2$)	71.62	49.1	9.03	3.05	2.046
	R1 ($\Omega.cm^2$)	885.8	322.6	20.7	14.378	8.672
	R2 ($\Omega.cm^2$)	464.2	89.38	14	3.966	1.0006
	R3 ($\Omega.cm^2$)	524	442.2	319	318.4	76.12
	R4 ($\Omega.cm^2$)	2416	-	51.9	17.128	11.002
	ASR ($\Omega.cm^2$)	4290	854.18	405.6	353.872	96.794

It can be seen that the electrolyte resistance (R_b) as well as the four resistances (R_1, R_2, R_3, R_4) associated with the kinetic of electrode processes decrease with increasing temperature, as expected. It also can be seen that the electrolyte resistance, R_b, does not depend on the oxygen partial pressure, remaining stable at each temperature, which is in agreement with the behavior of a pure ionic conductor as the YSZ electrolyte.

The polarization resistance (R_p), which is the ohmic part of the electrode resistance, can be determined as the sum of the resistances of each individual process ($R_p = R_1 + R_2 + R_3 + R_4$). For the symmetrical cell, the measured polarization resistance reflects the sum of the polarization resistance of the two electrodes investigated. Thus, all the cell impedances were normalized by the superficial area (0.04 cm^2), so the R parameters obtained in the fitting for each process were divided by two to consider the contribution of the two electrodes.

The most commonly used parameter to determine the rate-determining step in ORR is n, which is the slope of the electrode resistance as a function of oxygen partial pressure. The n value indicates the relation between the electrode resistance and oxygen partial pressure [116]. Representative profiles for PO_2 dependence of R_1, R_2, R_3 and $R_2 + R_3$ are shown in Figure 3.86 and the fitting results at various temperatures are listed in Table 3.9.

From the fitted data values, R_1 is slightly dependent on the oxygen partial pressure and R_2 and R_3 increases with decreasing PO_2.

It is clear that R_1 did not have a monotonic dependence on oxygen partial pressure. The resistance of the high frequency arc decreases with increasing temperatures, and it is independent of the oxygen partial pressure. Therefore, the first arc could be caused by the oxygen ions transferring through the electrolyte/electrode interface.

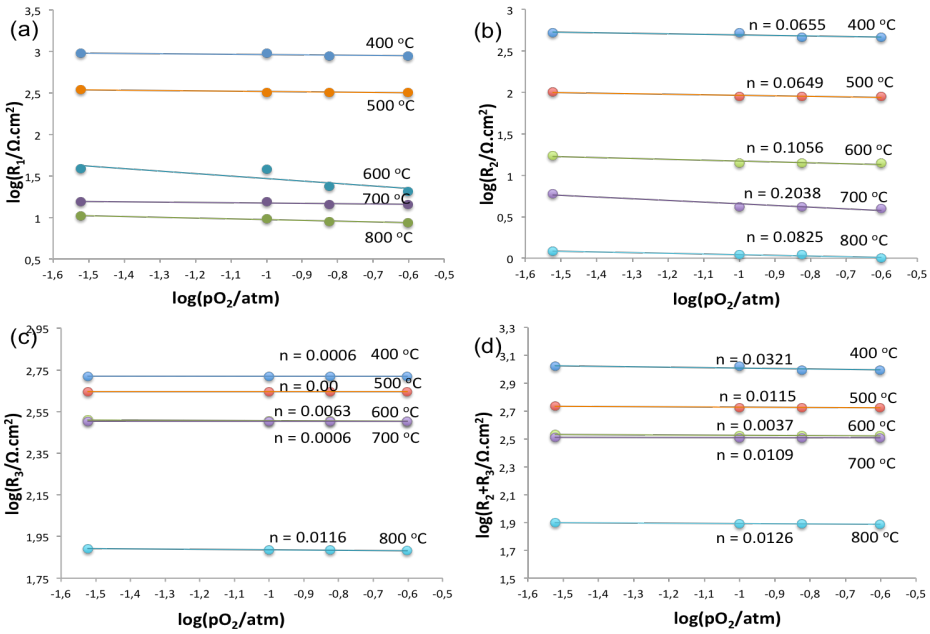

Figure 3.86. Dependence of three resistances at high, medium and low frequency on oxygen partial pressure for LV3SF/YSZ interface between 400 - 800 °C (a) R_1; (b) R_2; (c) R_3 and (d) $R_2 + R_3$.

The polarization resistances R_2 and R_3, associated with Arc2 and Arc3 appearing at intermediate frequency ranges, are found to be highly dependent on oxygen partial pressure. Both R_2 and R_3 decreased with increased oxygen partial pressure and increased temperature. The values obtained for n are 0.0649 - 0.2038 for R_2 and 0.00 - 0.0116 for R_3 at the investigated temperatures. Considering the weak oxygen partial pressure, this process could be related to an oxygen atom diffusion followed by a charge transfer.

The process associated with the low-frequency arc presents R_2 + R_3 which was found to be dependent on PO_2 with the value n = 0.0037 - 0.0321. It suggests that both R_2 and R_3 are associated with electron transfer. In other words, the electron transfer process may be composed of two successive intermediate steps, showing comparable importance in the charge transfer process. An increase of oxygen partial pressure results in a sufficient supply of oxygen to the electrode from the gas phase thereby effectively eliminating diffusion polarization resistance.

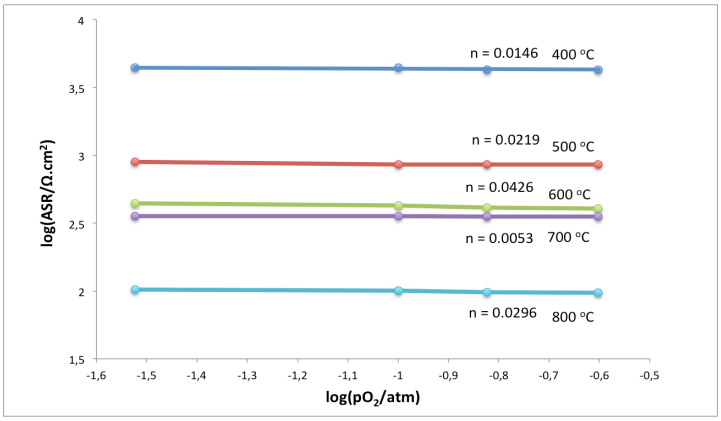

Figure 3.87. The dependence of the area specific resistance of the LV3SF/YSZ interface as a function of oxygen partial pressure at different temperatures.

The ASR values for ORR are obtained by the sum of individual resistances associated with each process. As expected, the ASR for LV3SF/YSZ interface decreases notably with increasing temperature and slightly with the oxygen partial pressure as shown in Figure 3.87. The characteristic of ASR shows quite weak PO_2 dependency (n = 0.0053 – 0.0426), which could be related to the oxide ion transfer within the bulk electrode and/or from electrode to electrolyte through the TPB. Therefore, this process is the major rate-limiting step for LV3SF cathode.

Figure 3.88 shows the some impedance responses for the single-phase LV3SF electrode on the GDC electrolyte that is measured under different oxygen partial pressures and collected in every 50 ºC in the temperature range from 400 to 800 ºC.

From the Figure 3.88, it is clearly seen that below the 500 ºC, the high frequency part of the two clearly resolved impedance contributions has an apparent shape in the Nyquist plots. With increasing operating temperature, the high-frequency arc size decreased noticeably, and the arc was totally disappeared at 500 ºC and higher. An additional arc at the low frequency range appeared when the operating temperature was elevated to 600 ºC.

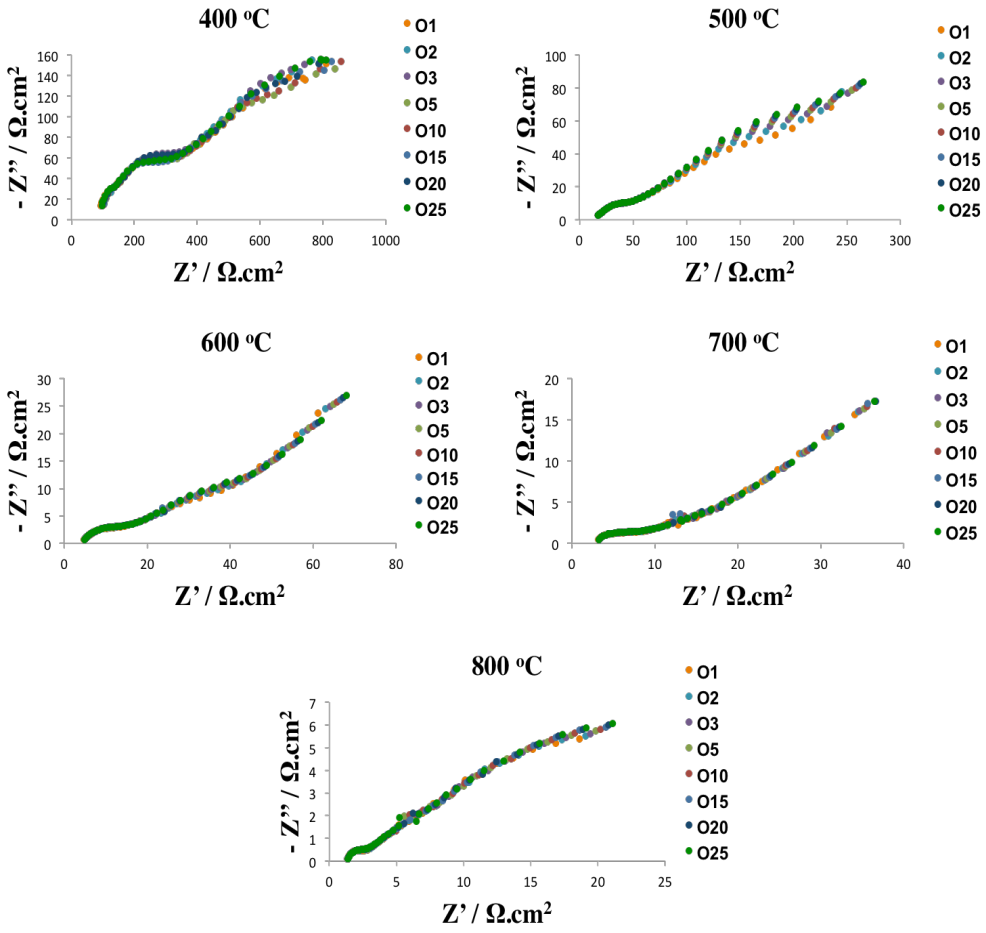

Figure 3.88. Complex impedance plots for LV3SF/GDC/LV3SF symmetric cell at between 400-800 °C for different oxygen partial pressures.

The impedances of a symmetric cell may arise from both the electrodes and electrolyte. The electrolyte typically performs as an ideal resistor and displays only a dot in

the Nyquist plots at high temperatures in the investigated frequency range of 10^{6}–10^{-1} Hz. However, with the decrease in operation temperature, a semi-circle associated with the oxide ion diffusion around the grain boundary of the electrolyte also appeared in the high frequency range.

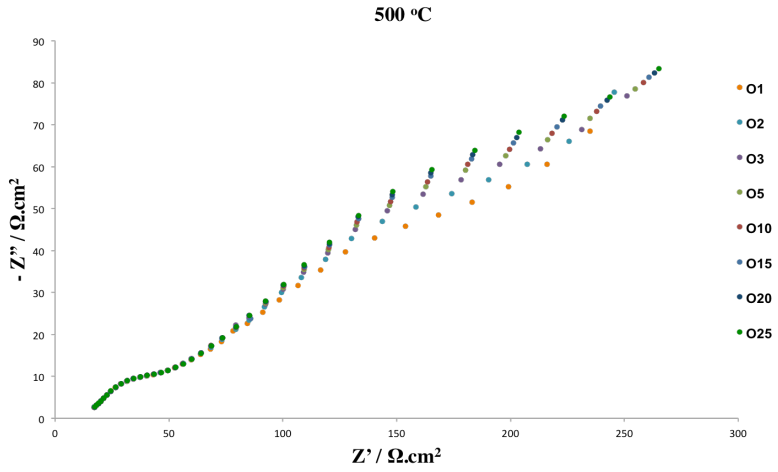

Figure 3.89. Typical EIS of a symmetric LV3SF/GDC/LV3SF cell measured at 500 °C while fixing the oxygen partial pressure between 1 – 25%.

Figure 3.89 illustrates the impedance diagrams measured at 500 °C under different oxygen partial pressures. In general, the high and medium frequency arcs show little dependence on the oxygen partial pressure, while the amplitude of the low frequency arc increases slightly as decreasing the oxygen partial pressure. The magnitude of arcs changes significantly with the temperature (Figure 3.88). In order to determine the processes involved in the ORR, the effect of PO_2 in the electrode impedance as a function of temperature was further studied. The oxygen partial pressure of the atmosphere was varied between 0.01 and 0.25 atm by mixing O_2 with N_2 using mass flow controllers. Figure 3.90, 3.91, 3.92 and 3.93 show some typical EIS diagrams of the LV3SF cathode measured at 400-800 °C in air for 3-10-15-25% O_2. Two discernable semi-circular arcs in the complex impedance plots are evident. Presence of two semi circular arcs in the impedance plane suggests that the ORR over the electrode was composed of at least two distinct processes.

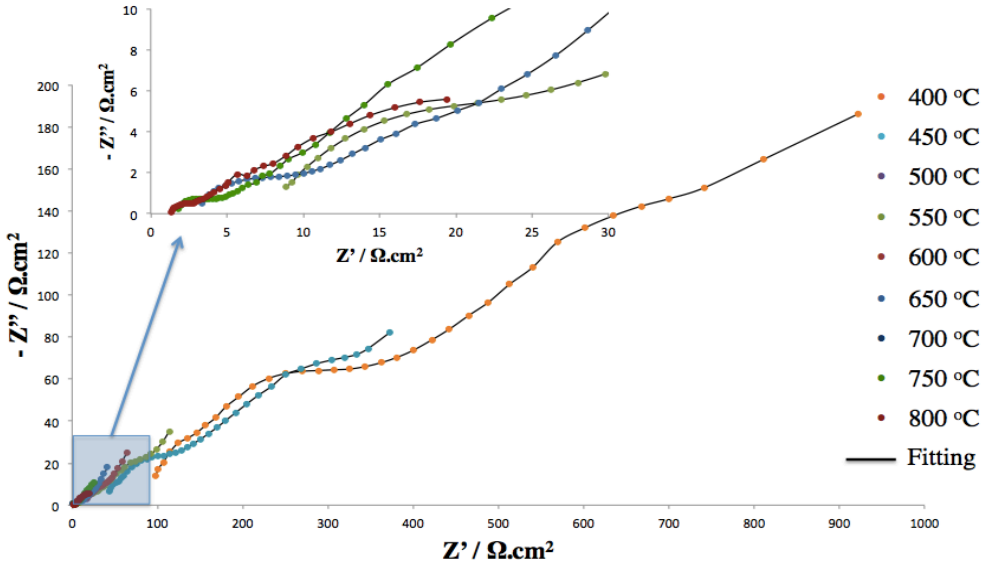

Figure 3.90. Experimental and fit Nyquist plots for a symmetrical LV3SF/GDC/LV3SF cell measured at 3% O_2 – 97% N_2 between 400 – 800 °C.

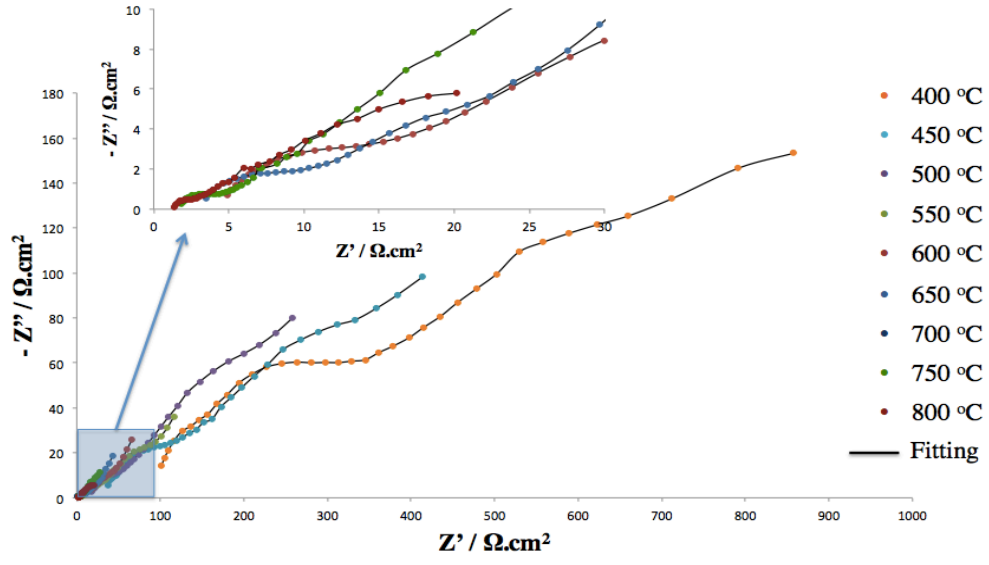

Figure 3.91. Experimental and fit Nyquist plots for a symmetrical LV3SF/GDC/LV3SF cell measured at 10% O_2 – 90% N_2 between 400 – 800 °C.

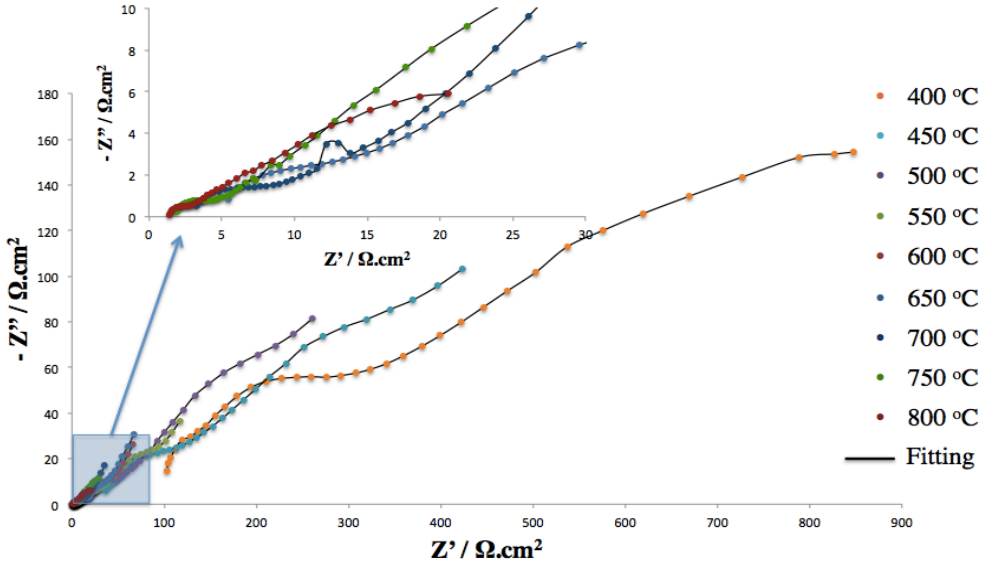

Figure 3.92. Experimental and fit Nyquist plots for a symmetrical LV3SF/GDC/LV3SF cell measured at 15% O_2 – 85% N_2 between 400 – 800 ºC.

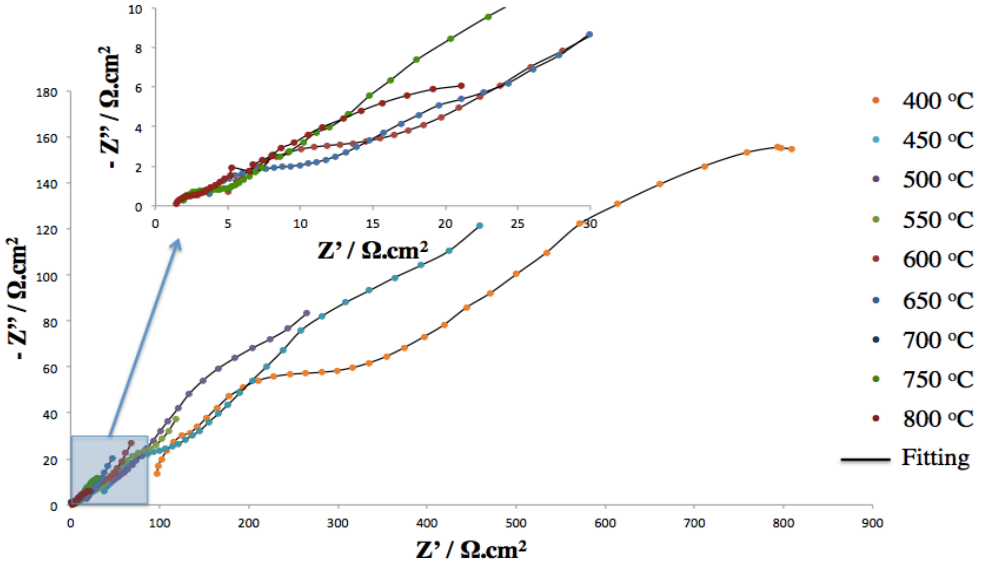

Figure 3.93. Experimental and fit Nyquist plots for a symmetrical LV3SF/GDC/LV3SF cell measured at 25% O_2 – 75% N_2 between 400 – 800 ºC.

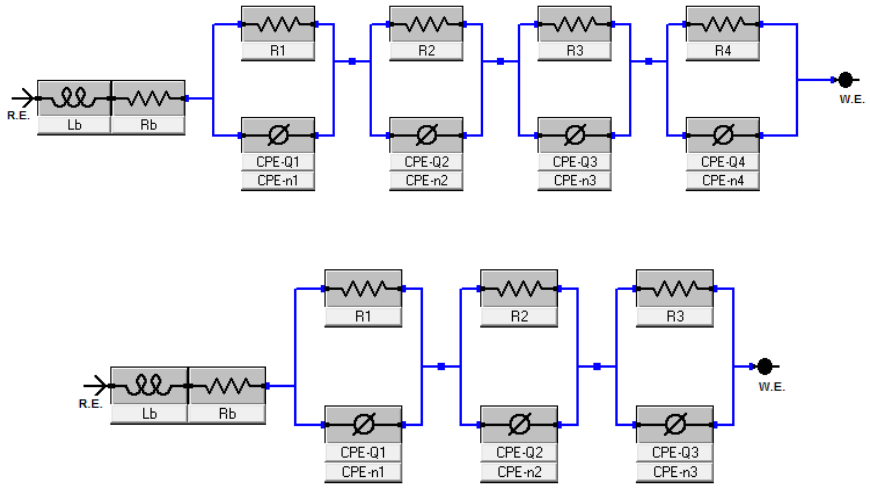

Figure 3.94. The equivalent circuits adopted for fitting the impedance data for a) 400 - 600 ºC b) 700 - 800 ºC.

Almost similar trends of the complex impedance diagrams were observed. The experimental impedance spectrum, simulated response and electrical equivalent circuit models are shown in Figure 3.90, 3.91, 3.92 and 3.93. All Nyquist plots were fitted to the equivalent circuit of ***L-R_b-(R_1-QPE_1)-(R_2-QPE_2)...(R_i-QPE_i)*** shown in Figure 3.94 by means of the Gamry software. The data fitting contemplates three processes in the electrode reaction; the results show good agreement between the experimental and fitted data. The numbers of R_i - QPE_i impedances (made by a resistor R_i in parallel with a constant phase element QPE_i) in series are dependent on operation temperature. The exact equivalent circuits adopted for fitting the EIS data at the temperatures of 700 - 800 ºC are fitted well to an equivalent circuit of *L-R_b-(R_1-QPE_1)-(R_2-QPE_2)-(R_3-QPE_3)* and the temperatures of 400 - 600 ºC are in agreement with an equivalent circuit of *L-R_b-(R_1-QPE_1)-(R_2-QPE_2)-(R_3-QPE_3)-(R_4-QPE_4)*. The first component (R_1QPE_1) appears as a semi-circle at the high-frequency region, the second one (R_2QPE_2) as a semi-circle at the medium-frequency region and the third one (R_3QPE_3) as a semi-circle at the low-frequency region.

The size of the semi-circle at the high frequency decreased and it totally disappeared at 500 ºC. This implies that the well-separated semi-circle in the EIS high

frequency range at 400 – 500 ºC may be associated with oxide-ion transfer through GDC electrolyte grain boundaries. The second semi-circles in the EIS data are contributed from oxygen reduction over the LV3SF electrode. Impedance at high and intermediate frequencies is related to ion and electron transfer at the electrode, electrolyte, and collector/electrode interfaces, while the impedance at low frequencies is associated with non-charge transfer, such as oxygen surface exchange and gas-phase diffusion inside and outside the electrode layer [115].

Table 3.10. The fitting parameters as a function of temperature for LV3SF/GDC/LV3SF in PO_2.

PO_2	T (ºC)	400	500	600	700	800
O3	*Lb (H)*	$3.14x10^{-5}$	$1.04x10^{-6}$	$1.46x10^{-10}$	$4.21x10^{-7}$	$9.12x10^{-15}$
	Rb (Ω.cm²)	28.8	5.842	2.178	0.9288	0.5488
	R1 (Ω.cm²)	1466.6	1423.8	1313.8	65.72	34.58
	R2 (Ω.cm²)	11.902	7.27	2.262	0.8706	0.2286
	R3 (Ω.cm²)	40.82	38.04	31.48	28.06	0.2774
	R4 (Ω.cm²)	37.42	3.202	1.85	-	-
	ASR (Ω.cm²)	1556.742	1472.312	1349.392	94.650	35.086
O10	*Lb (H)*	$2.90x10^{-9}$	$1.22x10^{-6}$	$3.40x10^{-12}$	$3.03x10^{-12}$	$5.20x10^{-7}$
	Rb (Ω.cm²)	28.8	5.842	2.178	0.9288	0.5488
	R1 (Ω.cm²)	1425.6	1399.8	1284.4	63.72	34.58
	R2 (Ω.cm²)	11.702	7.11	2.0	0.8624	0.2286
	R3 (Ω.cm²)	40.8	35.9	30.94	22.74	0.2726
	R4 (Ω.cm²)	37.4	3.164	1.782	-	-
	ASR (Ω.cm²)	1515.502	1445.974	1319.122	87.3224	35.081

Table 3.10. The fitting parameters as a function of temperature for LV3SF/GDC/LV3SF in PO_2. (cont.)

O15	*Lb (H)*	8.63×10^{-9}	1.98×10^{-6}	4.34×10^{-11}	7.42×10^{-14}	5.77×10^{-7}
	Rb ($\Omega.cm^2$)	28.8	5.842	2.178	0.9288	0.5488
	R1 ($\Omega.cm^2$)	1425.4	1321.4	1284.2	60.0	34.58
	R2 ($\Omega.cm^2$)	11.702	7.11	1.7	0.8582	0.224
	R3 ($\Omega.cm^2$)	40.8	34.54	30.94	22.4	0.272
	R4 ($\Omega.cm^2$)	23.98	3.164	1.782	-	-
	ASR ($\Omega.cm^2$)	1501.882	1366.214	1318.622	83.258	35.076
O25	*Lb (H)*	8.91×10^{-9}	7.30×10^{-12}	5.16×10^{-9}	1.46×10^{-8}	5.24×10^{-7}
	Rb ($\Omega.cm^2$)	28.8	5.842	2.178	0.9288	0.5488
	R1 ($\Omega.cm^2$)	1424.4	1313.8	1276.4	44	34.4
	R2 ($\Omega.cm^2$)	11.472	6.766	1.562	0.8016	0.224
	R3 ($\Omega.cm^2$)	40.8	30.94	30.94	20.38	0.2312
	R4 ($\Omega.cm^2$)	20	3.16	1.6216	-	-
	ASR ($\Omega.cm^2$)	1496.672	1354.666	1310.523	65.181	34.855

Table 3.10 summarizes the fitting parameters as a function of temperature for LV3SF/GDC/LV3SF under different partial pressure of oxygen, as well as the values of area specific resistance (ASR). The inductance value was shown but not considered, because it is not characteristic of the studied compound. It can be seen that the electrolyte resistance (R_b) as well as the four resistances (R_1, R_2, R_3, R_4) associated with the kinetic of electrode processes decrease with increasing temperature, as expected. It also can be seen that the electrolyte resistance, R_b, does not depend on the oxygen partial pressure, remaining stable at each temperature, which is in agreement with the behavior of a pure ionic conductor as the GDC electrolyte.

The polarization resistance (R_p), which is the ohmic part of the electrode resistance, can be determined as the sum of the resistances of each individual process ($R_p = R_1 + R_2 + R_3 + R_4$). For the symmetrical cell, the measured polarization resistance reflects the sum of the polarization resistance of the two electrodes investigated. Thus, all the cell impedances were normalized by the superficial area (0.04 cm^2), so the R parameters obtained in the fitting for each process were divided by two to consider the contribution of the two electrodes.

The most commonly used parameter to determine the rate-determining step in ORR is n, which is the slope of the electrode resistance as a function of oxygen partial pressure. The n value indicates the relation between the electrode resistance and oxygen partial pressure [116]. Representative profiles for PO_2 dependence of R_1, R_2, R_3 and $R_2 + R_3$ are shown in Figure 3.95 and the fitting results at various temperatures are listed in Table 3.10.

From the fitted data values, R_1 is slightly dependent on the oxygen partial pressure and R_2 and R_3 increases with decreasing PO_2. It is clear that R_1 did not have a monotonic dependence on oxygen partial pressure. The resistance of the high frequency arc decreases with increasing temperatures, and it is independent of the oxygen partial pressure. Therefore, the first arc could be caused by the oxygen ions transferring through the electrolyte/electrode interface.

The polarization resistances R_2 and R_3, associated with Arc2 and Arc3 appearing at intermediate frequency ranges, are found to be highly dependent on oxygen partial pressure. Both R_2 and R_3 decreased with increased oxygen partial pressure and increased temperature. The values obtained for n are 0.0105 - 0.1764 for R_2 and 0.0002 – 0.1478 for R_3 at the investigated temperatures. Considering the weak oxygen partial pressure, this process could be related to an oxygen atom diffusion followed by a charge transfer.

The process associated with the low-frequency arc presents $R_2 + R_3$ which was found to be dependent on PO_2 with the value n = 0.0037 - 0.1439. It suggests that both R_2 and R_3 are associated with electron transfer. In other words, the electron transfer process may be composed of two successive intermediate steps, showing comparable importance in the charge transfer process. An increase of oxygen partial pressure results in a sufficient supply of oxygen to the electrode from the gas phase thereby effectively eliminating diffusion polarization resistance.

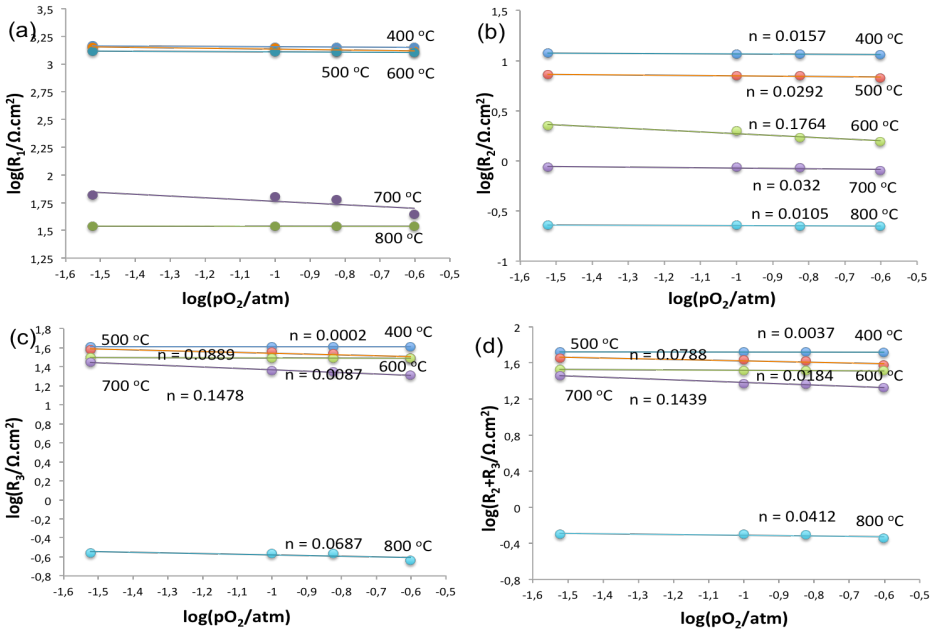

Figure 3.95. Dependence of three resistances at high, medium and low frequency on oxygen partial pressure for LV3SF/GDC interface between 400 - 800 °C (a) R_1; (b) R_2; (c) R_3 and (d) $R_2 + R_3$.

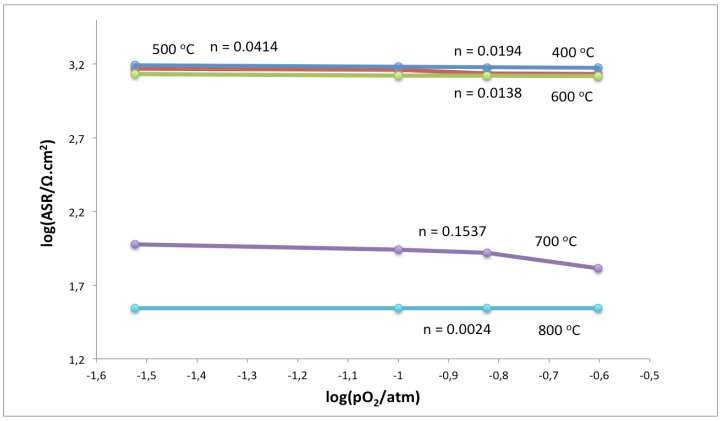

Figure 3.96. The dependence of the area specific resistance of the LV3SF/GDC interface as a function of oxygen partial pressure at different temperatures.

The ASR values for ORR are obtained by the sum of individual resistances associated with each process. As expected, the ASR for LV3SF/GDC interface decreases notably with increasing temperature and slightly with the oxygen partial pressure as shown in Figure 3.96. The characteristic of ASR shows quite weak PO_2 dependency (n = 0.0024 – 0.1537), which could be related to the oxide ion transfer within the bulk electrode and/or from electrode to electrolyte through the TPB. Therefore, this process is the major rate-limiting step for LV3SF cathode.

Figure 3.97 shows the some impedance responses for the single-phase LG10SC electrode on the YSZ electrolyte that is measured under different oxygen partial pressures and collected in every 50 ºC in the temperature range from 400 to 800 ºC.

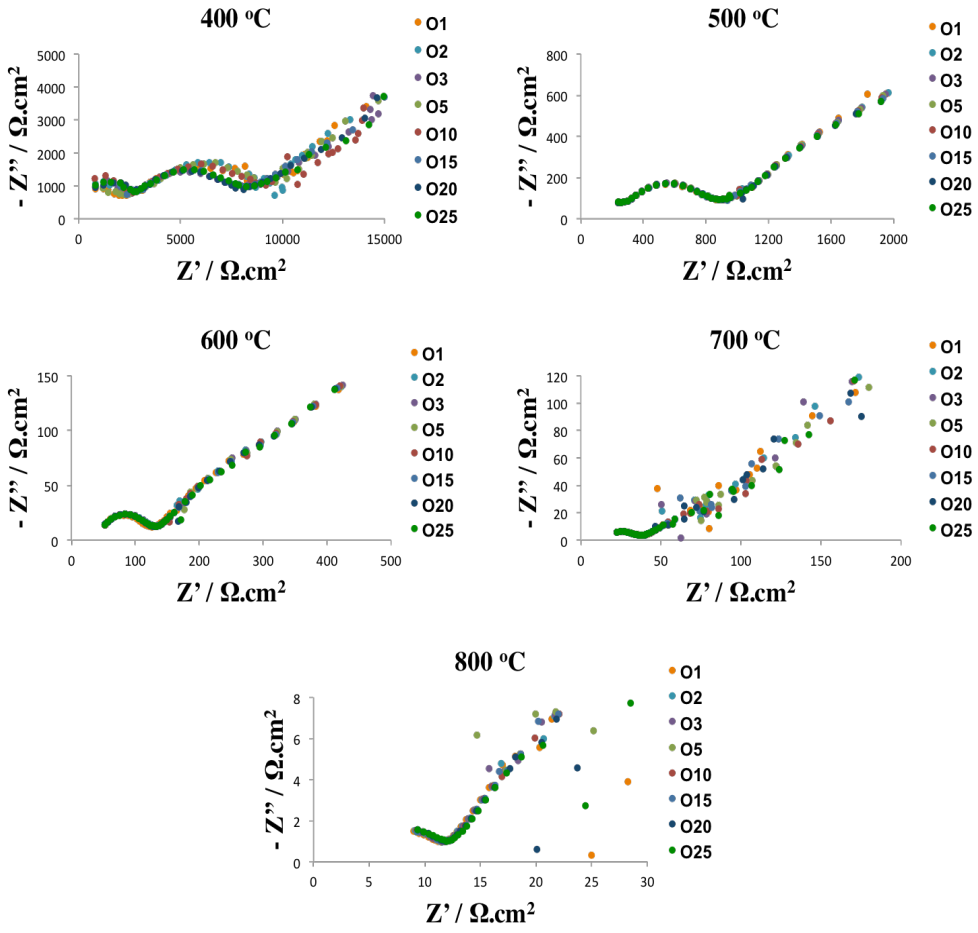

Figure 3.97. Complex impedance plots for LG10SC/YSZ/LG10SC symmetric cell at between 400-800 °C for different oxygen partial pressures.

From the Figure 3.97, it is clearly seen that below the 600 ºC, two impedance contributions has an apparent shape in the high frequency part of the Nyquist plots. With increasing operating temperature, the high-frequency arc size decreased noticeably, and the arc was totally disappeared at 600 ºC. The impedances of a symmetric cell may arise from both the electrodes and electrolyte. The electrolyte typically performs as an ideal resistor, which represents the intercept value in the impedance diagram at high frequency side with the real axis. However, with the decrease in operation temperature, a semi-circle associated with the oxide ion diffusion around the grain boundary of the electrolyte also appeared in the high frequency range.

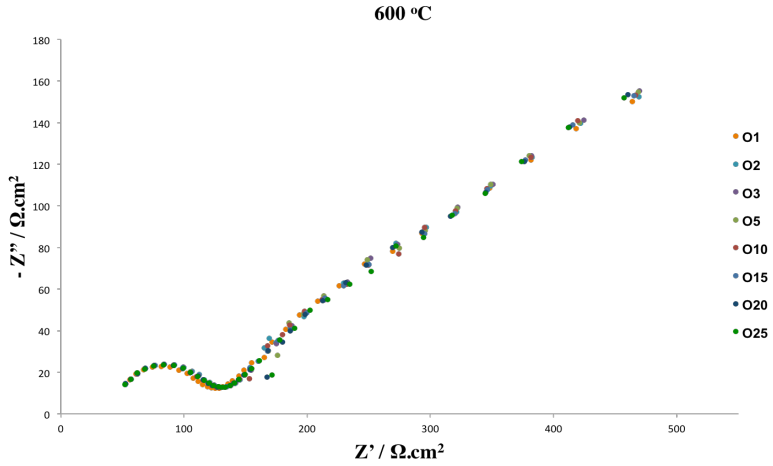

Figure 3.98. Typical EIS of a symmetric LG10SC/YSZ/LG10SC cell measured at 600 ºC while fixing the oxygen partial pressure between 1 – 25%.

Figure 3.98 illustrates the impedance diagrams measured at 600 °C under different oxygen partial pressures. In general, the high and medium frequency arcs show little dependence on the oxygen partial pressure, while the amplitude of the low frequency arc increases slightly as decreasing the oxygen partial pressure. The magnitude of arcs changes significantly with the temperature Figure 3.97. In order to determine the processes involved in the ORR, the effect of PO_2 in the electrode impedance as a function of temperature was further studied. The oxygen partial pressure of the atmosphere was varied between 0.01 and 0.25 atm by mixing O_2 with N_2 using mass flow controllers.

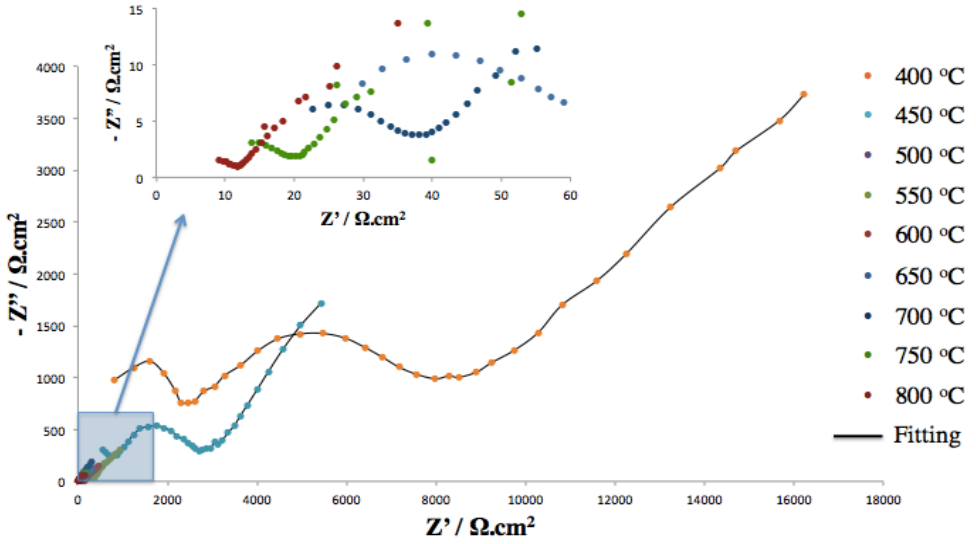

Figure 3.99. Experimental and fit Nyquist plots for a symmetrical LG10SC/YSZ/LG10SC cell measured at 3% O_2 – 97% N_2 between 400 – 800 °C.

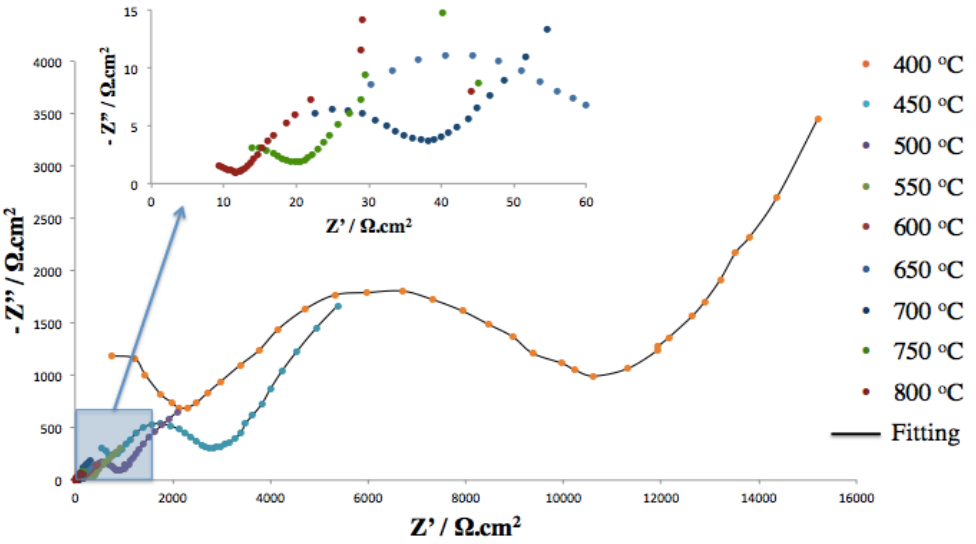

Figure 3.100. Experimental and fit Nyquist plots for a symmetrical LG10SC/YSZ/LG10SC cell measured at 10% O_2 – 90% N_2 between 400 – 800 °C.

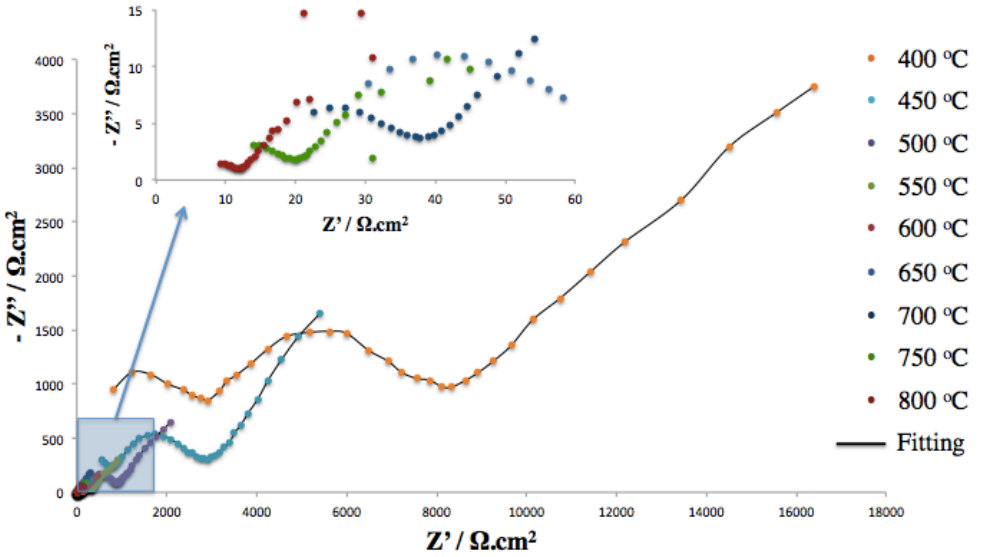

Figure 3.101. Experimental and fit Nyquist plots for a symmetrical LG10SC/YSZ/LG10SC cell measured at 15% O_2 – 85% N_2 between 400 – 800 °C.

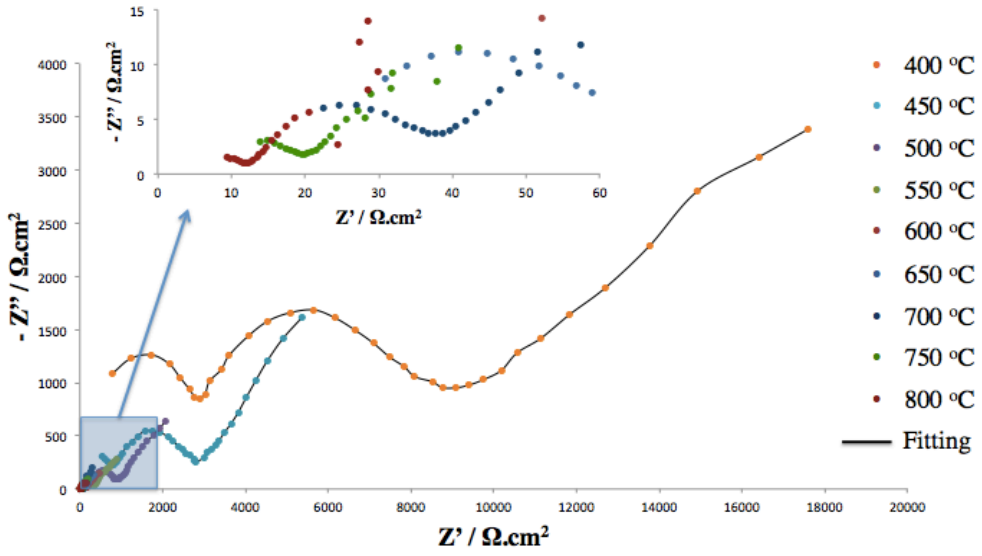

Figure 3.102. Experimental and fit Nyquist plots for a symmetrical LG10SC/YSZ/LG10SC cell measured at 25% O_2 – 75% N_2 between 400 – 800 °C.

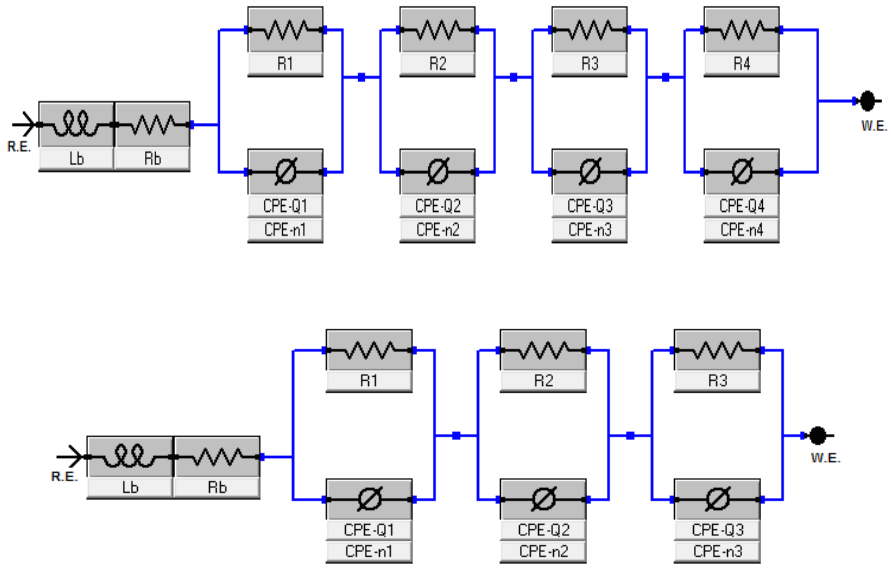

Figure 3.103. The equivalent circuits adopted for fitting the impedance data for a) 400 - 500 ºC b) 600 - 800 ºC.

Figure 3.99, 3.100, 3.101 and 3.102 show some typical EIS diagrams of the LG10SC cathode measured at 400 – 800 ºC in air for 3-10-15-25% O_2. Two discernable semi-circular arcs in the complex impedance plots are evident. Presence of two semi circular arcs in the complex impedance plane suggests that the ORR over the electrode was composed of at least two distinct processes. Almost similar trends of the complex impedance diagrams were observed. Indeed, several intermediate steps are involved during the overall ORR process. The experimental impedance spectrum, simulated response and electrical equivalent circuit models are shown in Figure 3.99, 3.100, 3.101 and 3.102.

All Nyquist plots were fitted to the equivalent circuit of ***L-R_b-(R_1-QPE_1)-(R_2-QPE_2)...(R_i-QPE_i)*** shown in Figure 3.103 by means of the Gamry software. The data fitting contemplates three processes in the electrode reaction; the results show good agreement between the experimental and fitted data. The numbers of R_i - QPE_i impedances (made by a resistor R_i in parallel with a constant phase element QPE_i) in series are dependent on operation temperature. The exact equivalent circuits adopted for fitting the EIS data at the temperatures of 600 - 800 ºC is fitted well to an equivalent circuit of *L-R_b-(R_1-QPE_1)-(R_2-QPE_2)-(R_3-QPE_3)* and the temperatures of 400 - 500 ºC are in agreement with an equivalent

circuit of $L\text{-}R_b\text{-}(R_1\text{-}QPE_1)\text{-}(R_2\text{-}QPE_2)\text{-}(R_3\text{-}QPE_3)\text{-}(R_4\text{-}QPE_4)$. The first component ($R_1QPE_1$) appears as a semi-circle at the high-frequency region, the second one (R_2QPE_2) as a semi-circle at the medium-frequency region and the third one (R_3QPE_3) as a semi-circle at the low-frequency region.

The size of the semi-circle at the high frequency decreased and it totally disappeared at 600 ºC. This implies that the well-separated semi-circle in the EIS high frequency range at 400 – 500 ºC may be associated with oxide-ion transfer through YSZ electrolyte grain boundaries. The second semi-circles in the EIS data are contributed from oxygen reduction over the LG10SC electrode. Impedance at high and intermediate frequencies is related to ion and electron transfer at the electrode, electrolyte, and collector/electrode interfaces, while the impedance at low frequencies is associated with non-charge transfer, such as oxygen surface exchange and gas-phase diffusion inside and outside the electrode layer [115].

Table 3.11. The fitting parameters as a function of temperature for LG10SC/YSZ/LG10SC in PO_2.

PO_2	T (ºC)	400	500	600	700	800
O3	*Lb (H)*	$2.41\text{x}10^{-7}$	$1.30\text{x}10^{-8}$	$1.19\text{x}10^{-7}$	$1.90\text{x}10^{-5}$	$1.01\text{x}10^{-6}$
	Rb ($\Omega.cm^2$)	30	24.8	20.2	2.656	2.636
	R1 ($\Omega.cm^2$)	8672	1946.6	1843	669.4	103.32
	R2 ($\Omega.cm^2$)	2218	282.8	39.16	13.902	3.026
	R3 ($\Omega.cm^2$)	708.6	584.8	556.6	252.4	11.924
	R4 ($\Omega.cm^2$)	1361.4	1361	-	-	-
	ASR ($\Omega.cm^2$)	12960	4175.2	2438.76	935.702	118.27

Table 3.11. The fitting parameters as a function of temperature for LG10SC/YSZ/LG10SC in PO_2. (cont.)

O10	*Lb (H)*	1.32×10^{-7}	3.03×10^{-7}	1.60×10^{-9}	9.23×10^{-6}	2.17×10^{-6}
	Rb ($\Omega.cm^2$)	30	24.8	20.2	2.656	2.636
	R1 ($\Omega.cm^2$)	8666	1903.6	1843	210.4	103.28
	R2 ($\Omega.cm^2$)	2218	282.8	36.34	13.902	2.974
	R3 ($\Omega.cm^2$)	685	583.2	495.6	252.2	11.27
	R4 ($\Omega.cm^2$)	1361.4	1327.4	-	-	-
	ASR ($\Omega.cm^2$)	12930.4	4097	2374.94	476.502	117.524
O15	*Lb (H)*	5.82×10^{-8}	1.38×10^{-9}	2.57×10^{-12}	1.13×10^{-5}	3.47×10^{-6}
	Rb ($\Omega.cm^2$)	30	24.8	20.2	2.656	2.636
	R1 ($\Omega.cm^2$)	8666	1900.6	1104	210.4	94.56
	R2 ($\Omega.cm^2$)	2218	275.2	36.04	13.902	2.974
	R3 ($\Omega.cm^2$)	685	557.6	495.6	252.2	11.27
	R4 ($\Omega.cm^2$)	1361.4	1296	-	-	-
	ASR ($\Omega.cm^2$)	12930.4	4029.4	1635.64	476.502	108.804
O25	*Lb (H)*	5.08×10^{-8}	1.66×10^{-10}	1.23×10^{-9}	4.23×10^{-14}	1.22×10^{-7}
	Rb ($\Omega.cm^2$)	30	24.8	20.2	2.656	2.636
	R1 ($\Omega.cm^2$)	8666	1843	1102.2	154.2	94.56
	R2 ($\Omega.cm^2$)	2218	222.8	36.04	13.9	2.974
	R3 ($\Omega.cm^2$)	684.4	556.6	444	252.2	10.592
	R4 ($\Omega.cm^2$)	1361.4	1286.4	-	-	-
	ASR ($\Omega.cm^2$)	12929.8	3908.8	1582.24	420.3	108.126

Table 3.11 summarizes the fitting parameters as a function of temperature for LG10SC/YSZ/LG10SC under different partial pressure of oxygen, as well as the values of area specific resistance (ASR). The inductance value was shown but not considered in the present study. It can be seen that the electrolyte resistance (R_b) as well as the four resistances (R_1, R_2, R_3, R_4) associated with the kinetic of electrode processes decrease with increasing temperature, as expected. It also can be seen that the electrolyte resistance, R_b, does not depend on the oxygen partial pressure, remaining stable at each temperature, which is in agreement with the behavior of a pure ionic conductor as the YSZ electrolyte.

The expected but invisible right intercept on the real axis at EIS diagram represents the total resistance (R_{tot}) and the left intercept on the real axis corresponds to the ohmic resistance (R_{ohm}, including the electrolyte and connection wires). The polarization resistance (R_p) is estimated from the difference between R_{tot} and R_{ohm} ($R_p = R_{tot} - R_{ohm}$). Thus, all the cell impedances were normalized by the superficial area (0.04 cm^2), so the R parameters obtained in the fitting for each process were divided by two to consider the contribution of the two electrodes.

The most commonly used parameter to determine the rate-determining step in the ORR is the slope of the electrode resistance as a function of oxygen partial pressure, inset in Figure 3.49. The overall ORR can be simply described as $^1/_2\, O_2(g) + 2e^- \rightarrow O^{2-}$. In reality, it may involve many sub-steps such as gas diffusion, surface adsorption, dissociation, electron and ion charge transfer, and so on [118]. In order to operate a cell in intermediate temperature range, it is of vital importance to accelerate the ORR in the cathode and the oxygen transport in the cathode and electrolyte. Representative profiles for PO_2 dependence of R_1, R_2, R_3 and $R_2 + R_3$ are shown in Figure 3.104 and the fitting results at various temperatures are listed in Table 3.11.

From the fitted data values, R_1 is slightly dependent on the oxygen partial pressure and R_2 and R_3 increases with decreasing PO_2. It is clear that R_1 did not have a monotonic dependence on oxygen partial pressure. The resistance of the high frequency arc decreases with increasing temperatures, and it is independent of the oxygen partial pressure. Therefore, the first arc could be caused by the oxygen ions transferring through the electrolyte/electrode interface.

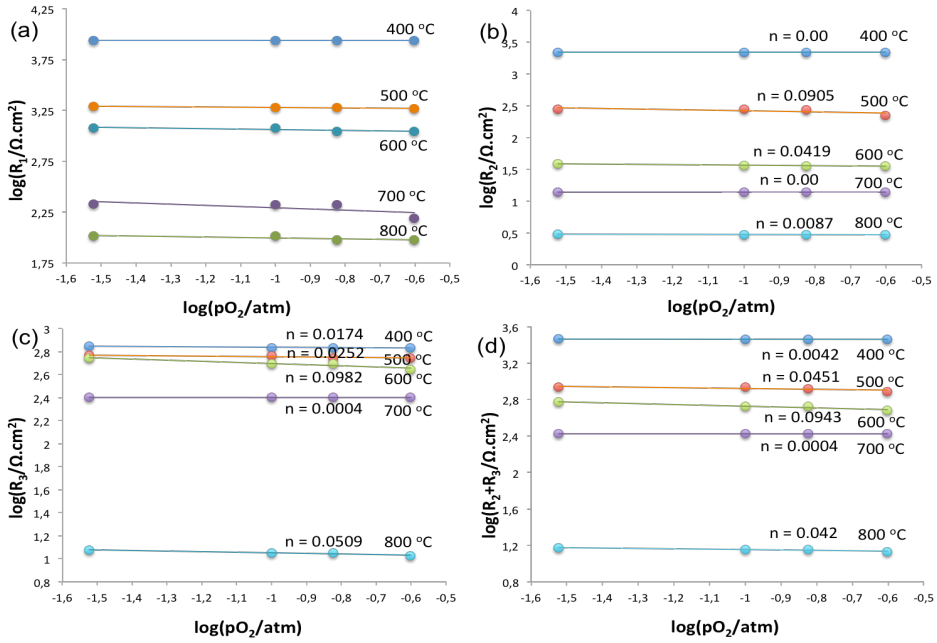

Figure 3.104. Dependence of three resistances at high, medium and low frequency on oxygen partial pressure for LG10SC/YSZ interface between 400 - 800 °C (a) R_1; (b) R_2; (c) R_3 and (d) $R_2 + R_3$.

The polarization resistances R_2 and R_3, associated with Arc2 and Arc3 appearing at intermediate frequency ranges, are found to be highly dependent on oxygen partial pressure. Both R_2 and R_3 decreased with increased oxygen partial pressure and increased temperature. The values obtained for n are 0.00 - 0.0905 for R_2 and 0.0004 – 0.0982 for R_3 at the investigated temperatures. Considering the weak oxygen partial pressure, this process could be related to an oxygen atom diffusion followed by a charge transfer.

The process associated with the low-frequency arc presents $R_2 + R_3$ which was found to be dependent on PO_2 with the value n = 0.0004 - 0.0943. It suggests that both R_2 and R_3 are associated with electron transfer. In other words, the electron transfer process may be composed of two successive intermediate steps, showing comparable importance in the charge transfer process. An increase of oxygen partial pressure results in a sufficient supply of oxygen to the electrode from the gas phase thereby effectively eliminating diffusion polarization resistance.

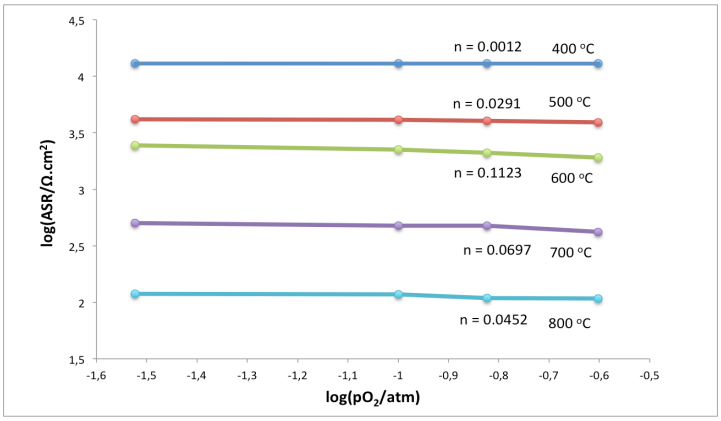

Figure 3.105. The dependence of the area specific resistance of the LG10SC/YSZ interface as a function of PO_2 at different temperatures.

The ASR values for ORR are obtained by the sum of individual resistances associated with each process. As expected, the ASR for LG10SC/YSZ interface decreases notably with increasing temperature and slightly with the oxygen partial pressure as shown in Figure 3.105. The characteristic of ASR shows quite weak PO_2 dependency (n = 0.0012 – 0.1123), which could be related to the oxide ion transfer within the bulk electrode and/or from electrode to electrolyte through the TPB. Therefore, this process is the major rate-limiting step for LG10SC cathode.

Figure 3.106 shows the some impedance responses for the single-phase LG10SC electrode on the GDC electrolyte that is measured under different oxygen partial pressures and collected in every 50 ºC in the temperature range from 400 to 800 ºC.

The typical complex impedance plots at various temperatures for LG10SC symmetric cell are depicted in Figure 3.106. Mainly two discernable arcs in the complex impedance plots are evident. Almost similar trends of the complex impedance plots corresponding to all of the studied cells were observed. In fact, several intermediate steps are involved during the overall oxygen reduction reaction (ORR) process [119]. These steps may occur simultaneously on different time scales.

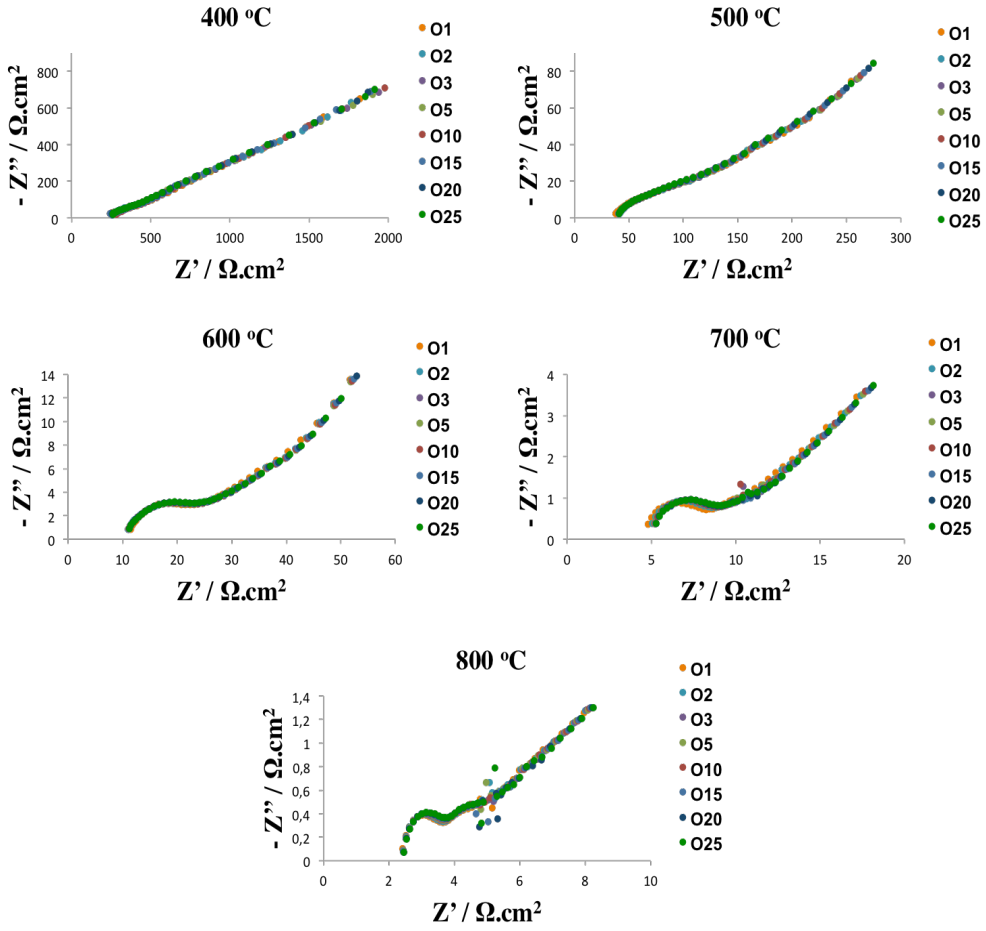

Figure 3.106. Complex impedance plots for LG10SC/GDC/LG10SC symmetric cell at between 400-800 °C for different oxygen partial pressures.

From the above Figure 3.106, it is clearly seen that below the 600 °C, there isn't any clearly resolved impedance contributions has apparent shape in the Nyquist plots. With increasing operating temperature, the high-frequency arc size increased noticeably at 600 °C and higher. The impedances of a symmetric cell may arise from both the electrodes and electrolyte. The electrolyte typically performs as an ideal resistor and displays only a dot in the Nyquist plots at high temperatures.

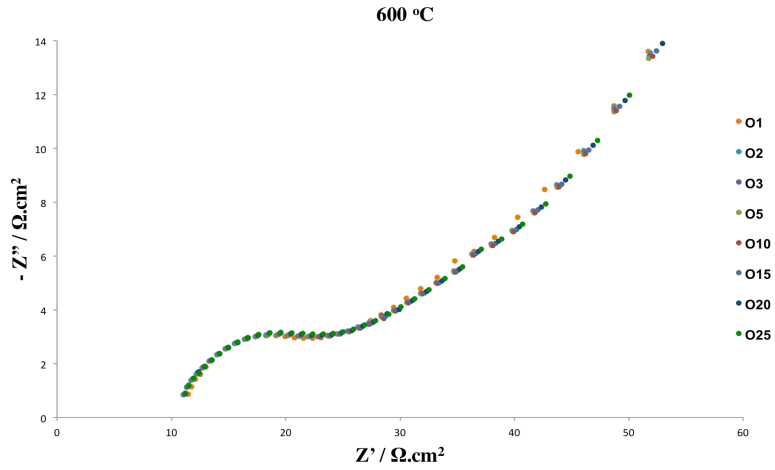

Figure 3.107. Typical EIS of a symmetric LG10SC/GDC/LG10SC cell measured at 600 °C while fixing the oxygen partial pressure between 1 – 25%.

Figure 3.107 illustrates the impedance diagrams measured at 600 °C under different oxygen partial pressures. In general, the high and medium frequency arcs show little dependence on the oxygen partial pressure, while the amplitude of the low frequency arc increases slightly as decreasing the oxygen partial pressure. The magnitude of arcs changes significantly with the temperature Figure 3.106.

In order to determine the processes involved in the ORR, the effect of PO_2 in the electrode impedance as a function of temperature was further studied. The oxygen partial pressure of the atmosphere was varied between 0.01 and 0.25 atm by mixing O_2 with N_2 using mass flow controllers.

Figure 3.108, 3.109, 3.110 and 3.111 show some typical EIS diagrams of the LG10SC cathode measured at 400 – 800 °C in air for 3-10-15-25% O_2. Two discernable semi-circular arcs in the complex impedance plots suggest that the ORR over the electrode was composed of at least two distinct processes. The experimental impedance spectrum, simulated response and electrical equivalent circuit models are shown in Figure 3.108, 3.109, 3.110 and 3.111.

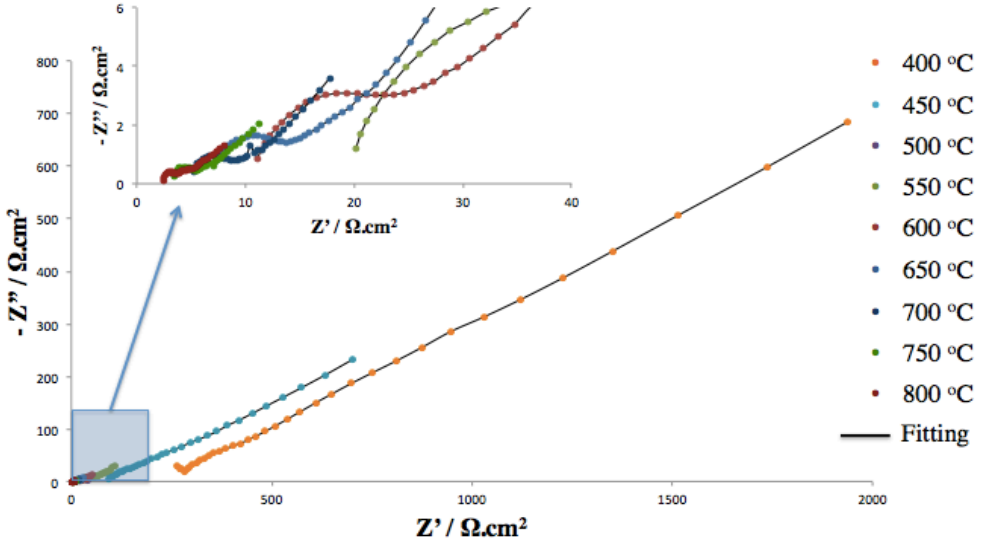

Figure 3.108. Experimental and fit Nyquist plots for a symmetrical LG10SC/GDC/LG10SC cell measured at 3% O_2 – 97% N_2 between 400 – 800 °C.

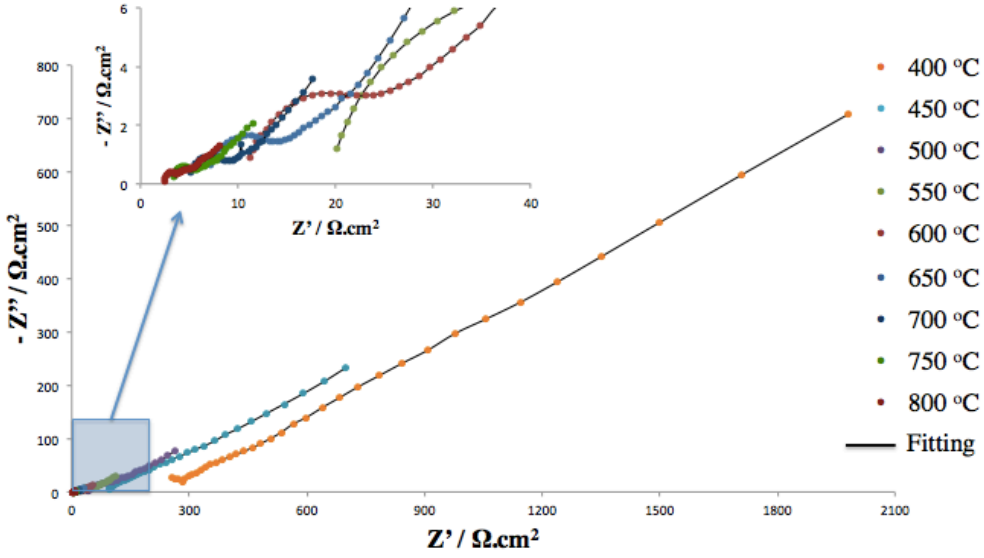

Figure 3.109. Experimental and fit Nyquist plots for a symmetrical LG10SC/GDC/LG10SC cell measured at 10% O_2 – 90% N_2 between 400 – 800 °C.

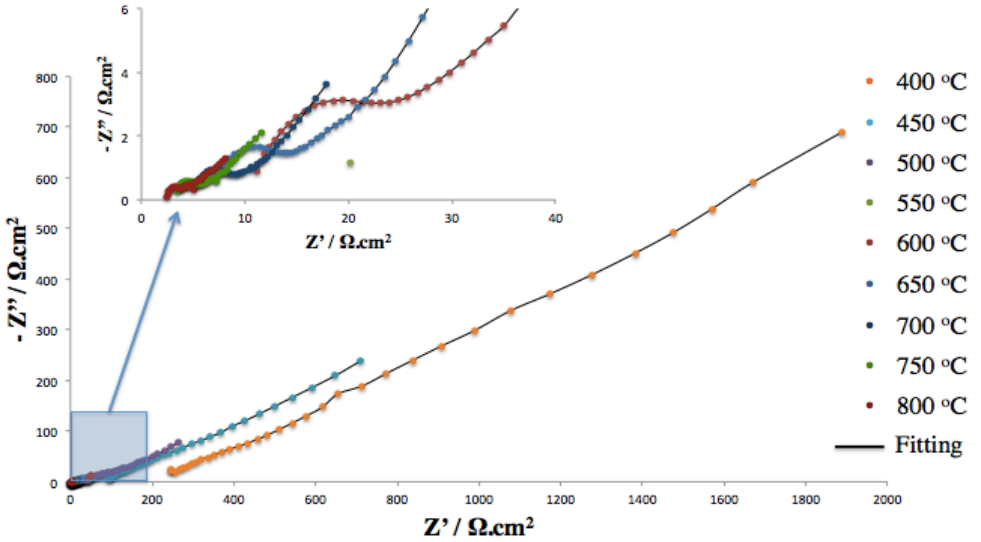

Figure 3.110. Experimental and fit Nyquist plots for a symmetrical LG10SC/GDC/LG10SC cell measured at 15% O_2 – 85% N_2 between 400 – 800 °C.

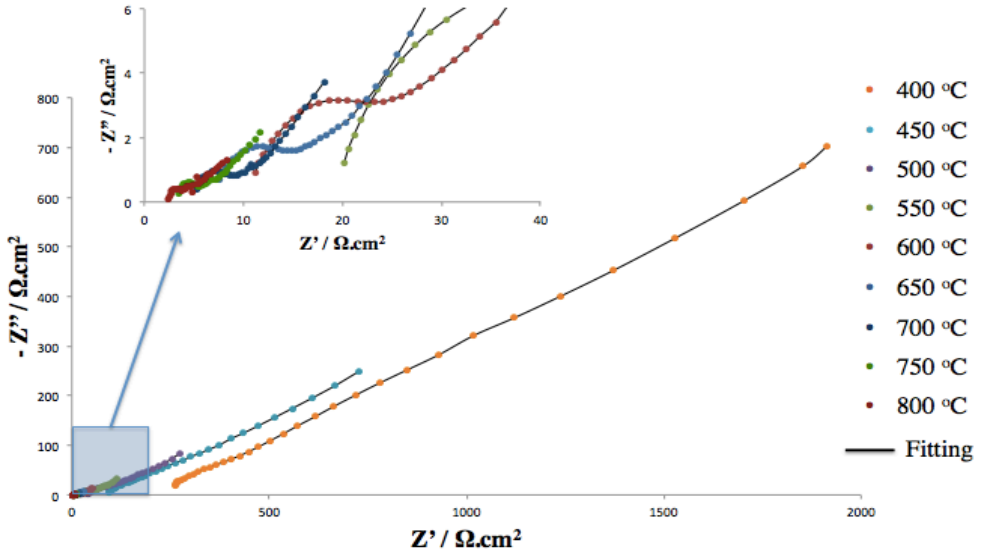

Figure 3.111. Experimental and fit Nyquist plots for a symmetrical LG10SC/GDC/LG10SC cell measured at 25% O_2 – 75% N_2 between 400 – 800 °C.

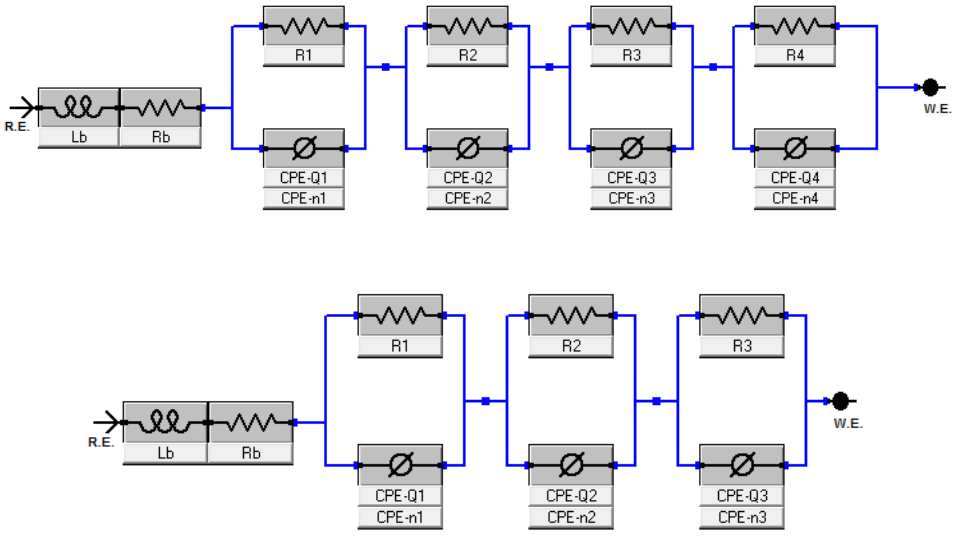

Figure 3.112. The equivalent circuits adopted for fitting the impedance data for a) 400 ºC b) 500 - 800 ºC.

All Nyquist plots were fitted to the equivalent circuit of ***L-R_b-(R_1-QPE_1)-(R_2-QPE_2)...(R_i-QPE_i)*** shown in Figure 3.112 by means of the Gamry software. The data fitting contemplates three processes in the electrode reaction; the results show good agreement between the experimental and fitted data. The numbers of R_i - QPE_i impedances (made by a resistor R_i in parallel with a constant phase element QPE_i) in series are dependent on operation temperature.

The exact equivalent circuits adopted for fitting the EIS data at the temperatures of 600 - 800 ºC are fitted well to an equivalent circuit of L-R_b-(R_1-QPE_1)-(R_2-QPE_2)-(R_3-QPE_3) and the temperature of 400 ºC is in agreement with an equivalent circuit of L-R_b-(R_1-QPE_1)-(R_2-QPE_2)-(R_3-QPE_3)-(R_4-QPE_4). The first component (R_1QPE_1) appears as a semi-circle at the high-frequency region, the second one (R_2QPE_2) as a semi-circle at the medium-frequency region and the third one (R_3QPE_3) as a semi-circle at the low-frequency region.

There is not any clear difference in impedance contributions in the Nyquist plots below 600 ºC. The high-frequency arc size increased noticeably at 600 ºC and higher. Both the electrodes and electrolyte are responsible for the impedances of a symmetric cell. The

electrolyte is generally counted as an ideal resistor, which is represented as the intercept value in the impedance diagram at high frequency side with the real axis. The second semi-circles in the EIS data are contributed from oxygen reduction over the LG10SC electrode. Impedance at high and intermediate frequencies is related to ion and electron transfer at the electrode, electrolyte, and collector/electrode interfaces, while the impedance at low frequencies is associated with non-charge transfer, such as oxygen surface exchange and gas-phase diffusion inside and outside the electrode layer [115].

Table 3.12. The fitting parameters as a function of temperature for LG10SC/GDC/LG10SC in PO_2.

PO_2	T (°C)	400	500	600	700	800
O3	*Lb (H)*	$7.15x10^{-9}$	$8.07x10^{-9}$	$6.66x10^{-7}$	$3.45x10^{-7}$	$1.20x10^{-6}$
	Rb ($\Omega.cm^2$)	97.8	18.728	4.84	2.276	0.5204
	R1 ($\Omega.cm^2$)	56.02	21.7	13.018	0.5444	0.461
	R2 ($\Omega.cm^2$)	43.86	20.92	6.944	1.5556	0.8192
	R3 ($\Omega.cm^2$)	923.2	279.8	43.22	32.94	17.37
	R4 ($\Omega.cm^2$)	428.8	-	-	-	-
	ASR ($\Omega.cm^2$)	1451.88	322.42	63.182	35.04	18.650
O10	*Lb (H)*	$7.21x10^{-5}$	$5.63x10^{-7}$	$7.08x10^{-7}$	$1.41x10^{-7}$	$1.20x10^{-6}$
	Rb ($\Omega.cm^2$)	97.8	18.728	4.84	2.276	0.5204
	R1 ($\Omega.cm^2$)	52.72	20.4	12.796	0.4972	0.4
	R2 ($\Omega.cm^2$)	39.3	20	6.334	1.4394	0.7252
	R3 ($\Omega.cm^2$)	770.2	279.8	43.2	32.94	17.37
	R4 ($\Omega.cm^2$)	428.8	-	-	-	-
	ASR ($\Omega.cm^2$)	1291.02	320.2	62.33	34.876	18.495

Table 3.12. The fitting parameters as a function of temperature for LG10SC/GDC/LG10SC in PO_2. (cont.)

O15	*Lb (H)*	3.80×10^{-5}	7.43×10^{-7}	5.09×10^{-15}	5.51×10^{-7}	3.69×10^{-7}
	Rb ($\Omega.cm^2$)	97.8	18.728	4.84	2.276	0.5204
	R1 ($\Omega.cm^2$)	52.3	20.1	12.408	0.462	0.4
	R2 ($\Omega.cm^2$)	25.92	19.318	6.334	1.4392	0.52
	R3 ($\Omega.cm^2$)	770.2	279.8	43.2	32.94	17.37
	R4 ($\Omega.cm^2$)	419.8	-	-	-	-
	ASR ($\Omega.cm^2$)	1268.22	319.218	61.942	34.841	18.29
O25	*Lb (H)*	1.72×10^{-9}	1.04×10^{-6}	6.99×10^{-7}	5.32×10^{-7}	8.58×10^{-7}
	Rb ($\Omega.cm^2$)	97.8	18.728	4.84	2.276	0.5204
	R1 ($\Omega.cm^2$)	32.28	19.204	12.044	0.4618	0.3832
	R2 ($\Omega.cm^2$)	25.92	19.288	6.114	1.4372	0.5198
	R3 ($\Omega.cm^2$)	770.2	279.8	43.2	32.94	17.37
	R4 ($\Omega.cm^2$)	419.8	-	-	-	-
	ASR ($\Omega.cm^2$)	1248.2	318.292	61.358	34.839	18.273

Table 3.12 summarizes the fitting parameters as a function of temperature for LG10SC/GDC/LG10SC under different partial pressure of oxygen, as well as the values of area specific resistance (ASR). The inductance value was shown but not considered, because it is not characteristic of the studied compound. It can be seen that the electrolyte resistance (R_b) as well as the four resistances (R_1, R_2, R_3, R_4) associated with the kinetic of electrode processes decrease with increasing temperature, as expected. It also can be seen that the electrolyte resistance, R_b, does not depend on the oxygen partial pressure, remaining stable at each temperature, which is in agreement with the behavior of a pure ionic conductor as the GDC electrolyte.

The polarization resistance (R_p), which is the ohmic part of the electrode resistance, can be determined as the sum of the resistances of each individual process ($R_p = R_1 + R_2 + R_3 + R_4$). For the symmetrical cell, the measured polarization resistance reflects the sum of the polarization resistance of the two electrodes investigated. Thus, all the cell impedances were normalized by the superficial area (0.04 cm^2), so the R parameters obtained in the fitting for each process were divided by two to consider the contribution of the two symmetric electrodes.

The most commonly used parameter to determine the rate-determining step in ORR is n, which is the slope of the electrode resistance as a function of oxygen partial pressure. The n value indicates the relation between the electrode resistance and oxygen partial pressure [116]. Representative profiles for PO_2 dependence of R_1, R_2, R_3 and $R_2 + R_3$ are shown in Figure 3.113 and the fitting results at various temperatures are listed in Table 3.12.

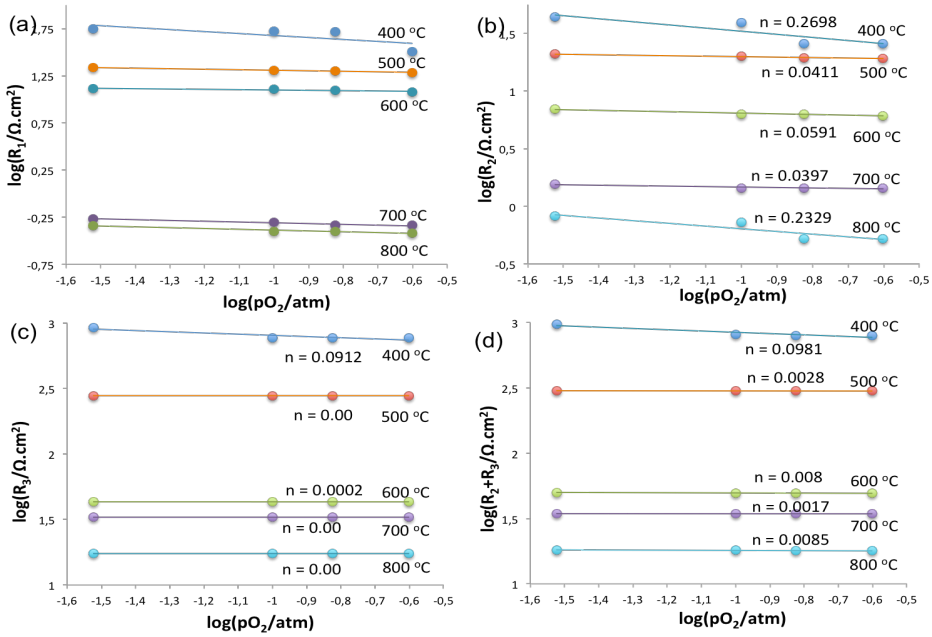

Figure 3.113. Dependence of three resistances at high, medium and low frequency on oxygen partial pressure for LG10SC/GDC interface between 400 - 800 °C (a) R_1; (b) R_2; (c) R_3 and (d) $R_2 + R_3$.

From the fitted data values, R_1 is slightly dependent on the oxygen partial pressure and R_2 and R_3 increases with decreasing PO_2. It is clear that R_1 did not have a monotonic dependence on oxygen partial pressure. The resistance of the high frequency arc decreases with increasing temperatures, and it is independent of the oxygen partial pressure. Therefore, the first arc could be caused by the oxygen ions transferring through the electrolyte/electrode interface.

The polarization resistances R_2 and R_3, associated with Arc2 and Arc3 appearing at intermediate frequency ranges, are found to be highly dependent on oxygen partial pressure. Both R_2 and R_3 decreased with increased oxygen partial pressure and increased temperature. The values obtained for n are 0.0397 - 0.2698 for R_2 and 0.00 – 0.0912 for R_3 at the investigated temperatures. Considering the weak oxygen partial pressure, this process could be related to an oxygen atom diffusion followed by a charge transfer.

The process associated with the low-frequency arc presents $R_2 + R_3$ which was found to be dependent on PO_2 with the value n = 0.0017 - 0.0981. It suggests that both R_2 and R_3 are associated with electron transfer. In other words, the electron transfer process may be composed of two successive intermediate steps, showing comparable importance in the charge transfer process. An increase of oxygen partial pressure results in a sufficient supply of oxygen to the electrode from the gas phase thereby effectively eliminating diffusion polarization resistance.

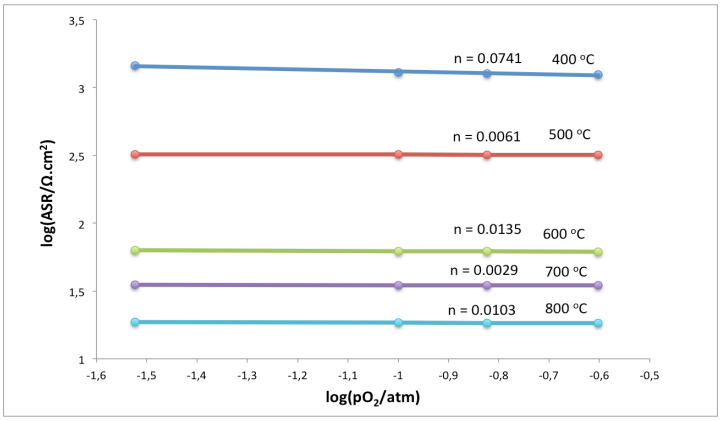

Figure 3.114. The dependence of the area specific resistance of the LG10SC/GDC interface as a function of PO_2 at different temperatures.

The ASR values for ORR are obtained by the sum of individual resistances associated with each process. As expected, the ASR for LG10SC/GDC interface decreases notably with increasing temperature and slightly with the oxygen partial pressure as shown in Figure 3.114. The characteristic of ASR shows quite weak PO_2 dependency (n = 0.0029 – 0.0741), which could be related to the oxide ion transfer within the bulk electrode and/or from electrode to electrolyte through the TPB. Therefore, this process is the major rate-limiting step for LG10SC cathode.

4. FUTURE WORK

It is found that $La_{0.595}V_{0.005}Sr_{0.4}CoO_{3-\delta}$ (LV05SC), $La_{0.595}V_{0.005}Sr_{0.4}MnO_{3-\delta}$ (LV05SM), $La_{0.57}V_{0.03}Sr_{0.4}FeO_{3-\delta}$ (LV3SF) and $La_{0.50}Gd_{0.10}Sr_{0.4}CoO_{3-\delta}$ (LG10SC) have very high activity towards oxygen reduction reaction in SOFC operating conditions. To integrate these materials into a solid oxide fuel cell one needs to better address its challenging features. It is also of great significance to study the degradation behavior. For an electrode produced from the as-synthesized materials to be technically relevant this depends upon more detailed work on various condition.

The powder synthesis, thermal treatment and the electrode fabrication methods and processing parameters deeply affect the electrode performance. The catalytic behavior of mixed ionic and electronic conductive electrodes and their related perovskites are susceptive to dramatic changes in fabrication and storage conditions. A detailed study on these aspects could give possibilities to further optimization of electrode materials.

A study on the degradation not only under controlled conditions but also coupled *in-situ* experiments with analytical techniques such as Raman and XRD in order to expose the degradation mechanisms needs to be carried out. As degradation constitutes a difficulty when it comes to commercialization of SOFC, however, very little is known about degradation phenomena in the electrode materials.

An electrochemical study on the prepared electrodes with known surface chemistry and structure should be performed. The literature is insufficient on associating surface chemistry and electrocatalytic activity, yet the surface structure plays a crucial role. This could include different surface techniques like Raman, XRD, SEM, TEM, and AFM. Raman spectroscopy is an effective method to detect the emerging phase of the cathode and to study the surface of these cathode materials. Also, Raman spectroscopy is capable of fingerprinting the surface species and secondary phases present on the SOFC cathode due to their specific vibration modes. SEM facilitates direct observation of basic morphological characteristics such as global morphologies, particle size and distribution as well as morphological evolution with temperature and current passage. On the other hand, TEM allows examination of a narrow area for the distribution and dispersion of particles on the electrode backbone or through the thickness of catalyst layer. Lastly, AFM offers

high three-dimensional spatial resolution and facilitates mechanistic study of the ORR for the cathode samples.

Thermal stability of the developed materials is a vital property that has not been considered during this thesis. A study examining this property would be of great concern if these materials were to be used within the SOFC technology.

The electrode materials should also be optimized when it comes to microstructure, since there is much in literature about microstructure-performance relationship. More work can be accomplished at the fabrication and testing side in order to experimentally advance the cathode functional layer.

As a whole, the SOFC is a sophisticated technology in which multicomponent gas transport, gas phase reactions, heterogeneous catalytic reactions and charge transfer in electrochemistry are all involved and coupled together. In addition, further studies are needed on how the developed cathode materials work when executed in an operational SOFC when it comes to both electrochemical performance and chemical and mechanical compatibility.

5. CONCLUSION

This study is dealing with fundamental experimental studies on mixed electronic and ionic conducting model perovskite cathode electrodes, intended to improve our understanding of the complex electrochemical processes taking place at SOFC cathodes in general, and in particular for the application as catalytically active cathode in SOFC systems. As an SOFC cathode candidate, the stability of the developed cathode materials with regard to the application was first studied on materials synthesized from the metal nitrates by the sol-gel process. The formed resin was calcined and the resulting powder was characterized by XRD. The XRD diffractograms show a single-phase perovskite structure for all developed samples with a rhombohedral unit cell. All peaks in the XRD pattern of the cathode samples are relatively sharp, indicating good incorporation into the lattice of the metal oxides used in the powder synthesis.

The major function of the cathode in SOFC is to contribute reaction sites for the electrochemical reduction of oxygen. Hence, the understanding of the active sites for ORR is very important to complete the cycle in the SOFC system. Catalytic properties of the cathode mostly depend on the absorption and diffusion of the oxygen. The kinetics of this reaction relies greatly on the structure and composition of the outermost surface of the oxides. Better understanding of the surface properties of the developed cathodes is thus essential. In this respect, XPS analyses were performed and the valance states of elements in the possession and the composition of the surface of the samples were further investigated.

The synthesized four cathode materials were prepared for electrical conductivity measurements (four-probe DC method) as rectangular bars and the data obtained were compared with reference data for each sample. The ionic conductivity of these materials is lower than 1 S/cm. Thus, the measured conductivity can be approximated as the electrical conductivity of the materials. According to advance studies, the materials exhibit high conductivities and all compositions except LV05SC and LG10SC showed metal-like temperature dependences i.e. decrease in conductivity with temperature. While in the studied temperature range, the electrical conductivity is increased with increasing temperature for LV05SM, typical of semiconductor behavior. In the case of LV3SF

sample, with increasing temperature the conductivity increases and reaches its maximum value at about 500 ^{o}C. As a comparison between the as-synthesized materials, LV05SC and LG10SC have better conductivity values of 843.43 and 415.50 S/cm among others, and they have lower activation energies of 0.045 and 0.055 eV, respectively.

The low value of activation energy emphasizes the high catalytic activity of the electrode material. Vanadium doped LSM sample (LV05SM) has the lowest conductivity value of 14.8 S/cm with activation energy of 0.20 eV and it continues with LV3SF material with a value of 26.23 S/cm and E_a of 0.14 eV. Although the measured conductivity values are lower than those from references in the literature, there are perovskite materials reported with low conductivity and excellent cathode performance. Therefore, in comparison with electrical conductivity, it is better to have higher ionic conductivity for being a SOFC cathode.

The most complex and least understood process in the overall SOFC-cathode mechanism is for the ORR. This process is often referred to the surface exchange of oxygen, perhaps because it is still not known which of the many elementary reactions are rate limiting the overall reaction and in which order they occur. Hence, the complex impedance measurements were carried out on a selected number of compositions with symmetric cells, versus the oxygen partial pressure PO_2 at different temperatures in order to complete understanding the ORR mechanism.

The impedances of a symmetric cell may arise from both the electrodes and electrolyte. The electrolyte typically performs as an ideal resistor and the oxide ion diffusion through the electrolyte material could be observed as a semi-circle in the high frequency range inside the impedance spectrum and it is independent of PO_2. However at lower temperatures the electrolyte becomes the limiting factor for SOFC applications.

In order to investigate the effect of partial pressure, impedance responses for the developed materials measured under different oxygen partial pressures and collected in 50 ^{o}C increments. With decreasing in the partial pressure of oxygen, the impedance arc increases significantly, particularly at low frequencies. The number of arcs depends on the reaction steps occurring inside the cathode material. For most of the impedance curves, two arcs could be separated at high and low frequency regions. This indicates that at least two electrochemical processes contribute to the overall electrochemical reaction. In order

to have more information to interpret properly the processes involved in the cathode/electrolyte interface, a study of the influence of both the partial pressure and the temperature in the electrode impedance was performed and the data were fitted to the equivalent circuits. From the fitting parameters, it can be said that the resistances associated with the kinetic of electrode processes decrease with increasing temperature.

The polarization resistance (R_p) is the purely ohmic part of the electrode resistance and the resistance values for ORR are obtained by the sum of individual resistances associated with each process. The characteristic of R_p shows that the oxide ion transfer within the bulk electrode is the major rate-limiting step for the LV05SM, LG10SC and LV3SF cathode samples. The polarization resistance value for LV05SC material was related to the oxygen adsorption-desorption process or a reaction controlled by the atomic oxygen diffusion process. Therefore, these two processes are the major rate-limiting steps for LV05SC cathode.

The comparison of the polarization and impedance behaviour of pronounced cathode materials under identical experimental conditions showed that the much higher electrode performance of LV3SF, LG10SC, and LV05SM compared to that of LV05SC is clearly due to their better ionic conductivity values. As a result of this study, it is concluded that these cathode materials would be candidates as IT-SOFC cathode materials.

REFERENCES

1. Li, B., L. Wang, B. Kang, P.Wang and Y.Qiu, "Review of Recent Progress in Solid-State Dye-Sensitized Solar Cells", *Solar Energy Materials & Solar Cells*, Vol. 90, pp. 549-573, 2006.

2. Kamat, P.V., "Meeting the Clean Energy Demand: Nanostructure Architectures for Solar Energy Conversion", *Journal of Physical Chemistry C*, Vol. 111, pp. 2834-2860, 2007.

3. *Energy Efficiency: A Recipe for Success*, World Energy Council, London, UK, 2010.

4. Grove, W.R., "On Voltaic Series and the Combination of Gases by Platinum", *The London and Edinburgh Philosophical Magazine and Journal of Science*, Vol. 14, pp. 127-130, 1839.

5. Ivers-Tiffee, E., A. Weber and D. Herbstritt, "Materials and Technologies for SOFC-Components", *Journal of the European Ceramic Society*, Vol. 21, pp. 1805-1811, 2001.

6. Minh, N.Q., "Ceramic Fuel Cells", *Journal of American Ceramic Society*, Vol. 76, pp. 563-588, 1993.

7. Zhu, W.Z. and S.C. Deevi, "A Review on the Status of Anode Materials for Solid Oxide Fuel Cells", *Materials Science and Engineering*, Vol. 362, pp. 228-239, 2003.

8. Fergus, J.W., "Oxide Anode Materials for Solid Oxide Fuel Cells", *Solid State Ionics*, Vol. 177, pp. 1529-1541, 2006.

9. Goodenough, J.B., "Alternative Anode Materials for Solid Oxide Fuel Cells", *Journal of Power Sources*, Vol. 173, pp. 1-10, 2007.

10. Badwal, S.P.S., "Stability of Solid Oxide Fuel Cell Components", *Solid State Ionics*, Vol. 143, pp. 39-46, 2001.

11. Lashtabeg, A. And S.J. Skinner, "Solid Oxide Fuel Cells - A Challenge for Materials Chemists?", *Journal of Materials Chemistry*, Vol. 16, pp. 3161-3170, 2006.

12. Singhal, S.C., and K. Kendall, *High Temperature Solid Oxide Fuel Cells: Fundamentals, Design and Applications*, Oxford: Elsevier, 2003.

13. Adler, S.B., "Factors Governing Oxygen Reduction in Solid Oxide Fuel Cell Cathodes", *Chemical Reviews*, Vol. 104, pp. 4791-4843, 2004.

14. Mizusakia, J., N. Mori, H. Takai, Y. Yonemura, H. Minamiue , H. Tagawa , M. Dokiya , H. Inaba , K. Naraya , T. Sasamoto and T. Hashimoto, "Oxygen Nonstoichiometry and Defect Equilibrium in the Perovskite-Type Oxides $La_{1-x}Sr_xMnO_{3-\delta}$", *Solid State Ionics*, Vol. 129, pp.164-177, 2000.

15. De Souza, R.A., J.A. Kilner and J.F. Walker, "A SIMS Study of Oxygen Tracer Diffusion and Surface Exchange in $La_{0.8}Sr_{0.2}MnO_{3-\delta}$", *Materials Letter*, Vol. 43, pp. 43-52, 2000.

16. Richter, J., P. Holtappels, T. Graule, T. Nakamura, and L.J. Gauckler, "Materials Design for Perovskite SOFC Cathodes", *Monatshefte für Chemie*, Vol. 140, pp. 985-999, 2009.

17. Leone, P., M. Santarelli, P. Asinari, M. Cali,and R. Borchiellini, "Experimental Investigations of the Microscopic Features and Polarization Limiting Factors of Planar SOFCs with LSM and LSCF Cathodes", *Journal of Power Sources*, Vol. 177, pp. 111-122, 2008.

18. Srdic, V.V., R.P. Omorjan,and J. Seydel, "Electrochemical Performances of (La,Sr)CoO_3 Cathode for Zirconia-Based Solid Oxide Fuel Cells", *Materials Science and Engineering B*, Vol. 116, pp. 119-124.

19. Xia, C., W. Rauch, F. Chen, and M. Liu, "$Sm_{0.5}Sr_{0.5}CoO_3$ Cathodes for Low-Temperature SOFCs", *Solid State Ionics*, Vol. 149, pp.11-19, 2002.

20. Lv, H., Y. Wu, B. Huang, B. Zhao, and K. Hu, "Structure and Electrochemical Properties of $Sm_{0.5}Sr_{0.5}Co_{1-x}Fe_xO_{3-\delta}$ Cathodes for Solid Oxide Fuel Cells", *Solid State Ionics*, Vol. 177, pp. 901-906, 2006.

21. Ding, X., C. Cui, X. Dub, and L. Guo, "Electrical Conductivity, Thermal Expansion and Electrochemical Properties of Fe-Doped $La_{0.7}Sr_{0.3}CuO_{3-\delta}$ Cathodes for Solid Oxide Fuel Cells", *Journal of Alloys and Compounds*, Vol. 475, pp. 418-421, 2009.

22. Zhou, W., R. Ran, and Z. Shao, "Progress in Understanding and Development of $Ba_{0.5}Sr_{0.5}Co_{0.8}Fe_{0.2}O_{3-\delta}$ Based Cathodes for Intermediate-Temperature Solid-Oxide Fuel Cells: A Review", *Journal of Power Sources*, Vol. 192, pp. 231-246, 2009.

23. Skinner, S.J., "Recent Advances in Perovskite-Type Materials for Solid Oxide Fuel Cell Cathodes", *International Journal of Inorganic Materials*, Vol. 3, pp. 113-121, 2001.

24. Tao, S., and J.T.S. Irvine, "A Redox-Stable Efficient Anode For Solid-Oxide Fuel Cells", *Nature Materials*, Vol. 2, pp.320-323, 2003.

25. Nomura, K., and S. Tanase, "Electrical Conduction Behavior in $(La_{0.9}Sr_{0.1})M^{III}O_{3-\delta}$ (M^{III}=Al, Ga, Sc, In, and Lu) Perovskites", *Solid State Ionics*, Vol. 98, pp. 229-236, 1997.

26. Stevenson, J.W., T.R. Armstrong, R.D. Carneim, L.R. Pederson and W.J. Weber, "Electrochemical Properties of Mixed Conducting Perovskites

$La_{1-x}M_xCo_{1-y}Fe_yO_{3-\delta}$ (M = Sr, Ba, Ca)", *Journal of Electrochemical Society*, Vol. 143, pp. 2722-2729, 1996.

27. Petric, A., P. Huang, and F. Tietz, "Evaluation of La–Sr–Co–Fe–O Perovskites for Solid Oxide Fuel Cells and Gas Separation Membranes", *Solid State Ionics*, Vol. 135, pp. 719-725, 2000.

28. Huang, X., L. Peia, Z. Liua, Z. Lua, Y. Suia, Z. Qiana, and W. Su, "A Study on $PrMnO_3$-Based Perovskite Oxides Used in SOFC Cathodes", *Journal of Alloys and Compounds*, Vol. 354, pp. 265-270, 2002.

29. Kostogloudis, G.C., N. Vasilakos and C. Ftikos, "Preparation and Characterization of $Pr_{1-x}Sr_xMnO_{3-\delta}$ (x = 0, 0.15, 0.3, 0.4, 0.5) as a Potential SOFC Cathode Material Operating at Intermediate Temperatures (500-700 °C)", *Journal of European Ceramic Society*, Vol. 17, pp. 1513-1521, 1997.

30. Cherry, M., M.S. Islam, and C.R.A. Catlow, "Oxygen Ion Migration in Perovskite-Type Oxides", *Journal of Solid State Chemistry*, Vol. 118, pp. 125-132, 1995.

31. Shannon, R.D., "Revised Effective Ionic Radii and Systematic Studies of Interatomie Distances in Halides and Chaleogenides", *Acta Crystallographica A*, Vol. 32, pp.751-768, 1976.

32. Mogensen, M., D. Lybye, N. Bonanos, P.V. Hendriksen, and F.W. Poulsen, "Factors Controlling the Oxide Ion Conductivity of Fluorite and Perovskite Structured Oxides", *Solid State Ionics*, Vol. 174, pp. 279-286, 2004.

33. Hayashia, H., H. Inabaa, M. Matsuyamab, N.G. Lanb, M. Dokiyab, and H. Tagawa, "Structural Consideration on the Ionic Conductivity of Perovskite-Type Oxides", *Solid State Ionics*, Vol. 122, pp. 1–15, 1999.

34. Siebert, E., A. Hammouche, and M. Kleitz, "Impedance $La_{1-x}Sr_xMnO_{3-\delta}$ Yttria-Stabilized Spectroscopy Electrode Kinetics", *Electrochimica Acta*, Vol. 40, pp. 1741-1753, 1995.

35. Fleig, J., "Solid Oxide Fuel Cell Cathodes: Polarization Mechanisms and Modeling of the Electrochemical Performance", *Annual Review of Materials Research*, Vol. 33, pp. 361-382, 2003.

36. Barsoukov, E., and J.R. Macdonald, *Impedance Spectroscopy, Theory Experiment and Applications*, John Wiley & Sons, Inc., Hoboken, New Jersey, 2nd edition, 2005.

37. Brinker, C.J., and G.W. Scherer, *Sol–Gel Science, the Physics and Chemistry of Sol–Gel Processing*, Academic Press, Boston, 1990.

38. Livage, J., and J. Lemerle, "Transition Metal Oxide Gels and Colliods", Vol. 12, pp. 103-122, 1982.

39. Scherer, G.W, "Structure and Properties of Gels", *Cement and Concrete Research*, Vol. 29, pp. 1149-1157, 1999.

40. Corri, R.J.P., and D. Leclercq, "Recent Developments of Molecular Chemistry for Sol-Gel Processes", *Angewandte Chemie International Edition*, Vol. 35, pp. 1420-1436, 1996.

41. Gaudon, M., C. Laberty-Robert, F. Ansart, P. Stevens, and A. Rousset, "Preparation and Characterization of $La_{1-x}Sr_xMnO_{3+\delta}$ ($0 \leq x \leq 0.6$) Powder by Sol–Gel Processing", *Solid State Ionics*, Vol. 4, pp.125-133, 2002.

42. Xiong, L., S. Wang, Y. Wang, and T. Wen, "$(Pr_{0.7}Ca_{0.3})_{0.9}MnO_{3-\delta}$ - SDC Cathode for IT-SOFC", *Journal of Alloys and Compounds*, Vol. 453, pp. 356-360, 2008.

43. Ghouse, M., Y. Al-Yousef, A. Al-Musa, and M.F. Al-Otaibi, "Preparation of $La_{0.6}Sr_{0.4}Co_{0.2}Fe_{0.8}O_3$ Nanoceramic Cathode Powders for Solid Oxide Fuel Cell (SOFC) Application", *International Journal of Hydrogen Energy*, Vol. 35, pp. 9411-9419, 2010.

44. Lenormand, P., S. Castillo, J. Gonzalez, C. Laberty-Robert, and F. Ansart, "Lanthanum Ferromanganites Thin Films by Sol–Gel Process. Influence of the Organic/Inorganic R Ratio on the Microstructural Properties", *Solid State Ionics*, Vol.7, pp. 159-163, 2005.

45. Vert, V.B., and J.M. Serra, "Influence of Barium Incorporation on the Electrochemical Performance of $Ln_{0.58}Sr_{0.4}Fe_{0.8}Co_{0.2}O_{3-\delta}$ (Ln=La, Pr, Sm) Perovskites for Oxygen Activation at Intermediate Temperatures", *Fuel Cells*, Vol. 9, pp. 663-678, 2009.

46. Vert, V.B., and J.M. Serra, "Improvement of the Electrochemical Performance of $Ln_{0.58}Sr_{0.4}Fe_{0.8}Co_{0.2}O_{3-\delta}$ IT-SOFC Cathodes by Ternary Lanthanide Combinations (La-Pr-Sm)", *Fuel Cells*, Vol. 10, pp. 693-702, 2010.

47. Meng, X., S. Lu, Y. Ji, T. Wei, and Y. Zhang, "Characterization of $Pr_{1-x}Sr_xCo_{0.8}Fe_{0.2}O_{3-\delta}$ ($0.2 \leq x \leq 0.6$) Cathode Materials for Intermediate-Temperature Solid Oxide Fuel Cells", *Journal of Power Sources*, Vol. 183, pp. 581-585, 2008.

48. Shao, Z., and S.M. Haile, "A High-Performance Cathode for the Next Generation of Solid-Oxide Fuel Cells", *Nature*, Vol. 431, pp. 170-173, 2004.

49. Seob Song, H., W.H. Kim, S.H. Hyun, J. Moon, J. Kim, and H. Lee, "Effect of Starting Particulate Materials on Microstructure and Cathodic Performance of Nanoporous LSM–YSZ Composite Cathodes, *Journal of Power Sources*, Vol. 167, pp. 258-264, 2007.

50. Li, Y., R. Gemmen, and X. Liu, "Oxygen Reduction and Transportation Mechanisms in Solid Oxide Fuel Cell Cathodes", *Journal of Power Sources*, Vol. 195, pp. 3345-3358, 2010.

51. Julia, A.B., I.A. Leonidov, M.V. Patrakeev, E.B. Mitberg, V.L. Kozhevnikov, and K.R. Poppelmeier, "High-Temperature Ion Transport in $La_{1-x}Sr_xFeO_{3-\delta}$", *Journal of Solid State Electrochemistry*, Vol. 8, pp. 578-584, 2004.

52. Tietz, F., H.P. Buchkremer, and D. Stover, "Components Manufacturing for Solid Oxide Fuel Cells", *Solid State Ionics*, Vol. 152, pp. 373-381, 2002.

53. Juliana, A., E. Justea, P.M. Geffroy, V. Coudert, S. Degot, P.D. Gallo, N. Richet, and T. Chartier, "Elaboration of $La_{0.8}Sr_{0.2}Fe_{0.7}Ga_{0.3}O_{3-\delta}$ /$La_{0.8}M_{0.2}FeO_{3-\delta}$ (M = Ca, Sr and Ba) Asymmetric Membranes by Tape-Casting and Co-Firing", *Journal of Membrane Science*, Vol. 333, pp. 132-140, 2009.

54. Saha, D., R. Giri, K.K. Mistry, and K. Sengupta, "Magnesium Chromate–TiO_2 Spinel Tape Cast Thick Film as Humidity Sensor", *Sensors and Actuators B*, Vol. 107, pp. 323-331, 2005.

55. Liu, Z., M. Liu, L. Nie, and M. Liu, "Fabrication and Characterization of Functionally-Graded LSCF Cathodes by Tape Casting", *International Journal of Hydrogen Energy*, Vol. 38, pp. 1082-1087, 2013.

56. Xia, C., F. Chen, and M. Liu, "Reduced-Temperature Solid Oxide Fuel Cells Fabricated by Screen Printing", *Electrochemical and Solid-State Letters A*, Vol. 4, pp.52-54, 2001.

57. Albano, M.P. and L.B. Garrido, "Aqueous Tape Casting of Yttria Stabilized Zirconia", *Materials Science and Engineering A*, Vol. 420, pp. 171-178, 2006.

58. Nakamura, A., T. Inami, Y. Shimojo, and Y. Morii, "Magnetic and Neutron Diffraction Study on Perovskites $La_{1-x}Sr_xCrO_3$", *Journal of Solid State Chemistry*, Vol. 141, pp. 404-410, 1998.

59. Cao, X.G.,and S.P. Jiang, "Identification of Oxygen Reduction Processes at (La,Sr)MnO_3 Electrode/$La_{9.5}Si_6O_{26.25}$ Apatite Electrolyte Interface of Solid Oxide Fuel Cells", *International Journal of Hydrogen Energy*, Vol. 38, pp. 2421-2431, 2013.

60. Chiba, R., F. Yoshimura, and Y. Sakurai, "An Investigation of $LaNi_{1-x}Fe_xO_3$ as a Cathode Material for Solid Oxide Fuel Cells", *Solid State Ionics*, Vol. 124, pp. 281-288, 1999.

61. Maignan, A., C. Martin, D. Pelloquin, N. Nguyen, and B. Raveau, "Structural and Magnetic Studies of Ordered Oxygen-Deficient Perovskites $LnBaCo_2O_{5+\delta}$, Closely Related to the "112" Structure, *Journal of Solid State Chemistry*, Vol. 142, pp. 247-260, 1999.

62. Adler, S.B., J.A. Lane, and B.C.H. Steele, "Electrode Kinetics of Porous Mixed-Conducting Oxygen Electrode", *Journal of Electrochemical Society*, Vol.143, pp. 3554-3564, 1996.

63. Kim, J.D., G.D. Kim, J. Moon, Y. Park, W. Lee, K. Kobayashi, M. Nagai, and C. Kim, "Characterization of LSM–YSZ Composite Electrode by AC Impedance Spectroscopy", *Solid State Ionics*, Vol. 143, pp. 379-389, 2001.

64. Wagner, C.D., W.M. Riggs, L.E. Davis, J.F. Moulder, and G.E. Muilenberg**,** *Handbook of X-Ray Photoelectron Spectroscopy*, Perkin-Elmer Corporation**,** 1979.

65. Pawlak, D.A., M. Ito, M. Oku, K. Shimamura, and T. Fukuda, "Interpretation of XPS O (1s) in Mixed Oxides Proved on Mixed Perovskite Crystals", *Journal of Physical Chemistry B*, Vol. 106, pp. 504-507, 2002.

66. De, S., A. Dey, and S.K. De, "Electrical Transport and Optical Properties of Vanadyl Phosphate-Polyaniline Nanocomposites", *Journal of Physics and Chemistry of Solids*, Vol. 68, pp. 66-72, 2007.

67. Shichi, Y., Y. Inoue, F. Munakata, and M. Yamanaka, "X-Ray Photoelectron Spectroscopy Analysis of $Bi_2Sr_2Ca_{1-x}Y_xCu_2O_y$", *Physical Review B*, Vo. 42, pp. 939-942, 1990.

68. Wang, P., L. Yao, M. Wang, and W. Wu, "XPS and Voltammetric Studies on $La_{1-x}Sr_xCoO_{3-\delta}$ Perovskite Oxide Electrodes", *Journal of Alloys and Compounds*, Vol. 311, pp. 53-56, 2000.

69. Gunasekaran, N., N. Bakshi, C.B. Alcock, and J.J. Carberry, "Surface Characterization and Catalytic Properties of Perovskite Type Solid Oxide Solutions, $La_{0.8}Sr_{0.2}BO_3$ (B = Cr, Mn, Fe, Co or Y)", *Solid State Ionics*, Vol.83, pp. 145-150, 1996.

70. Nefzi, H., and F. Sediri, "Vanadium Oxide Nanotubes VOx-NTs: Hydrothermal Synthesis, Characterization, Electrical Study and Dielectric Properties", *Journal of Solid State Chemistry*, Vol. 201, pp. 237-243, 2013.

71. Falcon, H., J.A. Barbero, J.A. Alonso, M.J. Martinez-Lope, and J.L.G. Fierro, "$SrFeO_{3-\delta}$ Perovskite Oxides: Chemical Features and Performance for Methane Combustion", *Chemistry of Materials*, Vol. 14, pp. 2325-2333, 2002.

72. Moran-Ruiz, A., K. Vidal, A. Larranaga, M.A. Laguna-Bercero, J.M. Porras-Vazquez, P.R. Slater, and M.I. Arriortua, "$LaNi_{0.6}Co_{0.4}O_{3-\delta}$ Dip-Coated on Fe-Cr Mesh as a Composite Cathode Contact Material on Intermediate Solid Oxide Fuel Cells", *Journal of Power Sources*, Vol. 269, pp. 509-519, 2014.

73. Weisentein, A.J., N. Childs, R. Amendola, D. Driscoll, S.W. Sofie, P. Gannon, and R. Smith, "Processing and Characterization of $Sr_{2-x}VMoO_{6-\delta}$ Double Perovskites", *Materials Chemistry and Physics*, Vol. 139, pp. 706-718, 2013.

74. Wu, Q.H., M. Liu, and W.Jaegermann, "X-Ray Photoelectron Spectroscopy of $La_{0.5}Sr_{0.5}MnO_3$", *Materials Letters*, Vol. 59, pp. 1980-1983, 2005.

75. Jung, J., and D.D. Edwards, "X-Ray Photoelectron (XPS) and Diffuse Reflectance Infra Fourier Transformation (DRIFT) Study of $Ba_{0.5}Sr_{0.5}Co_xFe_{1-x}O_{3-\delta}$ (BSCF: x = 0-0.8) Ceramics", *Journal of Solid State Chemistry*, Vol. 184, pp. 2238-2243, 2011.

76. Bin, F., C. Song, G. Lv, J. Song, C. Gong, and Q. Huang, "$La_{1-x}K_xCoO_3$ and $LaCo_{1-y}Fe_yO_3$ Perovskite Oxides: Preparation, Characterization, and Catalytic Performance in the Simultaneous Removal of NO_x and Diesel Soot", *Industrial & Engineering Chemistry Research*, Vol. 50, pp. 6660-6667, 2011.

77. Du, W., Y. Zhang, Y. Wang, J. Liu, H. Lu, S. Hou, and X. Zhang, "Designing Synthesis and Photocatalytic Activities of Gd/ZrO_2 Nanocomposite", *Journal of Nanoparticle Research*, Vol. 16, pp. 2241-2251, 2014.

78. Liu, Q., X. Dong, G. Xiao, F. Zhao, and F. Chen, "A Novel Electrode Material for Symmetrical SOFCs", *Advanced Materials*, Vol. 22, pp.5478-5482, 2010.

79. Galenda, A., M.M. Natile, V. Krishnan, H. Bertagnolli, and A. Glisenti, "LaSrCoFeO and Fe_2O_3/LaSrCoFeO Powders: Synthesis and Characterization", *Chemistry of Materials*, Vol. 19, pp. 2796-2808, 2007.

80. Tan, B.J., K.J. Klabunde, and P.M.A. Sherwood, "XPS Studies of Solvated Metal Atom Dispersed Catalysts. Evidence for Layered Cobalt-Manganese Particles on Alumina and Silica", *Journal of American Chemical Society*, Vol. 113, pp. 855-861, 1991.

81. Nitadori, T., M. Muramatsu, and M. Misono, "Valence Control, Reactivity of Oxygen, and Catalytic Activity of $La_{2-x}Sr_xCoO_4$", *Chemistry of Materials*, Vol. 1, pp. 215-220, 1989.

82. Heel, A., P. Holtappels, and T. Graule, "On the Synthesis and Performance of Flame-Made Nanoscale $La_{0.6}Sr_{0.4}CoO_{3-\delta}$ and its Influence on the Application as an Intermediate Temperature Solid Oxide Fuel Cell Cathode", *Journal of Power Sources*, Vol. 195, pp. 6709-6718, 2010.

83. Wandekar, R.V., B.N. Wani, and S.R. Bharadwaj, "Crystal Structure, Electrical Conductivity, Thermal Expansion and Compatibility Studies of Co-Substituted Lanthanum Strontium Manganite System", *Solid State Ionics*, Vol. 11, pp. 240-250, 2009.

84. Petrov, A.N., O.F. Kononchuk, A.V. Andreev, V.A. Cherepanov, and P. Kofstad, "Crystal Structure, Electrical and Magnetic Properties of $La_{1-x}Sr_xCoO_{3-y}$", *Solid State Ionics*, Vol. 80, pp. 189-199, 1995.

85. Sitte, W., E. Bucher, and W. Preis, "Nonstoichiometry and Transport Properties of Strontium-Substituted Lanthanum Cobaltites", *Solid State Ionics*, Vol. 154, pp. 517-522, 2002.

86. Montero, X., W. Fischer, F. Tietz, D. Stöver, M. Cassir, and I. Villarreal, "Development and Characterization of a Quasi-Ternary Diagram Based on $La_{0.8}Sr_{0.2}(Co,Cu,Fe)O_3$ Oxides in View of Application as a Cathode Contact Material for Solid Oxide Fuel Cells", *Solid State Ionics*, Vol. 180, pp. 731-737, 2009.

87. Tai, L.W., M.M. Nasrallah, H.U. Anderson, D.M. Sparlin, and S.R. Sehlin, "Structure and Electrical Properties of $La_{1-x}Sr_xCo_{0.2}Fe_{0.8}O_3$. Part 2. The System $La_{1-x}Sr_xCo_{0.2}Fe_{0.8}O_3$", *Solid State Ionics*, Vol. 76, pp. 273-283, 1995.

88. Tai, L.W., M.M. Nasrallah, H.U. Anderson, D.M. Sparlin, and S.R. Sehlin, "Structure and Electrical Properties of $La_{1-x}Sr_xCo_{1-y}Fe_yO_3$. Part 1. The System $La_{0.8}Sr_{0.2}Co_{1-y}Fe_yO_3$", *Solid State Ionics*, Vol. 76, pp. 259-271, 1995.

89. Meng, X., B. Meng, X. Tan, N. Yang, Z. Ma, "Synthesis Properties of $Ba_{0.5}Sr_{0.5}(Co_{0.6}Zr_{0.2})Fe_{0.2}O_{3-\delta}$ Perovskite Cathode Material for Intermediate Temperature Solid-Oxide Fuel Cells", *Materials Research Bulletin*,Vol. 44, pp.1293-1297, 2009.

90. Vidal, K., L.M. Rodríguez-Martínez, L. Ortega-San-Martín, M.L. Nó, T. Rojo, and M.I. Arriortua, "Effect of the A Cation Size Disorder on the Properties of an Iron Perovskite Series for Their Use as Cathodes for SOFCs", *Fuel Cells*, Vol. 11, pp. 51-58, 2011.

91. Vidal, K., L.M. Rodríguez-Martínez, L. Ortega-San-Martín, E. Díez-Linaza, M. Luisa, T. Rojo, A. Laresgoiti, and M.I. Arriortua, "Isolating the Effect of Doping in the Structure and Conductivity of $(Ln_{1-x}M_x)FeO_{3-\delta}$ Perovskites", *Solid State Ionics*, Vol. 178, pp. 1310-1316, 2007.

92. Kamata, H., Y. Yonemura, J. Mizusaki, H. Tagawa, K. Naraya, and T. Sasamoto, "High Temperature Electrical Properties of The Perovskite-Type Oxide $La_{1-x}Sr_x MnO_{3-\delta}$", *Journal of Physics and Chemistry of Solids*, Vol. 56, pp. 943-950, 1995.

93. Raffaelle, R., H. U. Anderson, D. M. Sparlin, and P. E. Parris, "Transport Anomalies in the High-Temperature Hopping Conductivity and Thermopower of Sr-Doped La(Cr, Mn)O_3", *Physical Review B*, Vol. 43, pp. 7991-8000, 1991.

94. Zhang, K., R. Ran, L. Ge, Z. Shao, W. Jin, and N. Xu, "Systematic Investigation on New $SrCo_{1-y}Nb_yO_{3-\delta}$ Ceramic Membranes with High Oxygen Semi-Permeability", *Journal of Membrane Science*, Vol. 323, pp. 436-443, 2008.

95. Zhao, H., Y. Cheng, N. Xu, Y. Li, F. Li, W. Ding, and X. Lu, "Oxygen Permeability of A-site Nonstoichiometric $Ba_xCo_{0.7}Fe_{0.2}Nb_{0.1}O_{3-\delta}$ Perovskite Oxides", *Solis State Ionics*, Vol. 181, pp. 354-358, 2010.

96. Zhao, H., D. Teng, X. Zhangb, C. Zhanga, and X. Li, "Structural and Electrochemical Studies of $Ba_{0.6}Sr_{0.4}Co_{1-y}Ti_yO_{3-\delta}$ as a New Cathode Material for IT-SOFCs", *Journal of Power Sources*, Vol. 186, pp. 305-310, 2009.

97. Aruna, S.T., M. Muthuraman, and K.C. Patil, "Combustion Synthesis and Properties of Strontium Substituted Lanthanum Manganites $La_{1-x}Sr_xMnO_3$ ($0 \leq x \leq 0.3$)", *Journal of Materials Chemistry*, Vol. 7, pp. 2499-2503, 1997.

98. Kuharuangronga, S., T. Dechakupt, and P. Aungkavattan, "Effects of Co and Fe Addition on the Properties of Lanthanum Strontium Manganite", *Materials Letters*, Vol. 58, pp. 1964-1970, 2004.

99. Mizusaki, J., Y. Yonemura, H. Kamata, K. Ohyama, N. Mori, H. Takai, H Tagawa, M. Dokiya, K. Naraya, T. Sasamoto, H. Inaba, T. Hashimoto, "Electronic Conductivity, Seebeck Coefficient, Defect and Electronic Structure of Nonstoichiometric $La_{1-x}Sr_xMnO_3$", *Solid State Ionics*, Vol. 132, pp. 167-180, 2000.

100. Yang, C.T., W.J. Wei, and A. Roosen, "Electrical Conductivity and Microstructures of $La_{0.65}Sr_{0.3}MnO_3$-8 mol% Yttria-Stabilized Zirconia", *Materials Chemistry and Physics*, Vol .81, pp. 134-142, 2003.

101. Halc, J., D. Kuscer, M. Hrovat, S. Bernik, and D. Kolar, "Electrical and Microstructural Characterization of $(La_{0.8}Sr_{0.2})(Fe_{1-x}Al_x)O_3$ and $(La_{0.8}Sr_{0.2})(Mn_{1-x}Al_x)O_3$ as Possible SOFC Cathode Materials", *Solid State Ionics*, Vol. 95, pp. 259-268, 1997.

102. Teraoka, Y., T. Nobunaga, K. Okamoto, N. Miura, and N. Yamazoe, "Influence of Constituent Metal Cations in Substituted $LaCoO_3$ on Mixed Conductivity and Oxygen Permeability", *Solis State Ionics*, Vol. 48, pp. 207-212, 1991.

103. Nakamura, T., D. Hemmi, K. Iwamoto, N. Hirai, M. Sase, A. Unemoto, F. Horikiri, Y. Mori, K. Sato, K. Yashiro, T. Kawada, and J. Mizusaki, "Evaluation of High-Temperature Electronic and Electrochemical Properties of the Strained

$La_{1-x}Sr_xCoO_{3-\delta}$ Films Prepared by a Pulsed Laser Deposition Technique", *Electrochemistry*, Vol. 82, pp. 884-890, 2014.

104. Mineshige, A., M. Kobune, S. Fujii, Z. Ogumi, M. Inaba, T. Yao, and K. Kikuchi, "Metal–Insulator Transition and Crystal Structure of $La_{1-x}Sr_xCoO_3$ as Functions of Sr-Content, Temperature, and Oxygen Partial Pressure", *Journal of Solid State Chemistry*, Vol. 142, pp. 374-381, 1999.

105. Søgaard, M., P.V. Hendriksen, M. Mogensen, F.W. Poulsen, E. Skou, "Oxygen Nonstoichiometry and Transport Properties of Strontium Substituted Lanthanum Cobaltite", *Solid State Ionics*, Vol. 177, pp. 3285-3296, 2006.

106. Flores, J.C.P., D.P. Coll, S.G. Martín, C. Ritter, G.C. Mather, J.C. Vazquez, M.G. Sanchez, F.G. Alvarado, and U. Amador, "A- and B-Site Ordering in the A-Cation-Deficient Perovskite Series $La_{2-x}NiTiO_{6-\delta}$ ($0 \leq x < 0.20$) and Evaluation as Potential Cathodes for Solid Oxide Fuel Cells", *Chemistry of Materials*, Vol. 25, pp. 2584-2494, 2013.

107. Jiang, S.P., "Development of Lanthanum Strontium Manganite Perovskite Cathode Materials of Solid Oxide Fuel Cells: A Review", *Journal of Materials Science*, Vol.43, pp. 6799-6833, 2008.

108. Bongıo, E.V. H. Black, F.C. Raszewski, D. Edwards, C.J. McConville, and V.R.W. Amarakoon, "Microstructural and High-Temperature Electrical Characterization of $La_{1-x}Sr_xFeO_{3-\delta}$", *Journal of Electroceramis*, Vol. 14, pp. 193-198, 2005.

109. Kharton, V.V., A.V. Kovalevsky, M.V. Patrakeev, E.V. Tsipis, A.P. Viskup, V.A. Kolotygin, A.A. Yaremchenko, A.L. Shaula, E.A. Kiselev, and J.C. Waerenborgh, "Oxygen Nonstoichiometry, Mixed Conductivity, and Mo¨ssbauer Spectra of $Ln_{0.5}A_{0.5}FeO_{3-\delta}$ (Ln = La-Sm, A = Sr, Ba): Effects of Cation Size", *Chemistry of Materials*, Vol. 20, pp. 6457-6467, 2008.

110. Fu, Y.P., "$Sm_{0.5}Sr_{0.5}Co_{0.4}Ni_{0.6}O_{3-\delta}$-$Sm_{0.2}Ce_{0.8}O_{1.9}$ as a Potential Cathode for Intermediate-Temperature Solid Oxide Fuel Cells", *International Journal of Hydrogen Energy*, Vol. 35, pp. 8663-8669, 2010.

111. Wei, B. Z. Lu, X. Huang, J. Miao, X. Sha, X. Xin, and W. Su, "Crystal Structure, Thermal Expansion and Electrical Conductivity of Perovskite Oxides $Ba_xSr_{1-x}Co_{0.8}Fe_{0.2}O_{3-\delta}$ ($0.3 \leq x \leq 0.7$)", *Journal of the European Ceramic Society*, Vol. 26, pp. 2827-2832, 2006.

112. Huang, C., D. Chen, Y. Lin, R. Ran, and Z. Shao, "Evaluation of $Ba_{0.6}Sr_{0.4}Co_{0.9}Nb_{0.1}O_{3-\delta}$ Mixed Conductor as a Cathode for Intermediate-Temperature Oxygen-Ionic Solid-Oxide Fuel Cells", *Journal of Power Sources*, Vol. 195, pp. 5176-5184, 2010.

113. De Souza, R.A., and J.A. Kilner, "Oxygen Transport in $La_{1-x}Sr_xMn_{1-y}Co_yO_{3-\delta}$ Perovskites Part II. Oxygen Surface Exchange", *Solid State Ionics*, Vol. 126, pp. 153-161, 1999.

114. Zhan, Z.L., T.L. Wen, H.Y. Tu, and Z.Y. Lu, "AC Impedance Investigation of Samarium-Doped Ceria", *Journal of Electrochemical Society*, Vol. 148, pp. 427-432, 2001.

115. Adler, S.B., X.Y. Chen, and J.R. Wilson, "Mechanisms and Rate Laws for Oxygen Exchange on Mixed-Conducting Oxide Surfaces", *Journal of Catalysis*, Vol 245, pp. 91-109, 2007.

116. Escudero, M.J., A. Aguadero, J.A. Alonso, and L. Daza, "A Kinetic Study of Oxygen Reduction Reaction on La_2NiO_4 Cathodes by Means of Impedance Spectroscopy", *Journal of Electroanalytical Chemistry*, Vol. 611, pp. 107-116, 2007.

117. Chaudhari, V.N., A.P. Khandale, and S.S. Bhoga, "An Investigation on Strontium Doped $Sm_2NiO_{4+\delta}$ Cathode for Intermediate Temperature Solid Oxide Fuel Cells", *Journal of Power Sources*, Vol. 248, pp. 647-654, 2014.

118. Chen, D., R. Ran, K. Zhang, J. Wang, and Z. Shao, "Intermediate-Temperature Electrochemical Performance of a Polycrystalline $PrBaCo_2O_{5+\delta}$ Cathode on Samarium-Doped Ceria Electrolyte", *Journal of Power Sources*, Vol. 188, pp. 96-105, 2009.

119. Istomin, S.Y., and E.V. Antipov, "Cathode Materials Based on Perovskite-Like Transition Metal Oxides for Intermediate Temperature Solid Oxide Fuel Cells", *Russian Chemical Reviews*, Vol. 82, pp. 686-700, 2013.